Atomic structural studies of graphene interfaces with 0 and 2D materials

Sapna Sinha

Lady Margaret Hall & Linacre College

Supervised by:

Prof. Jamie H. Warner

Prof. Kyriakos Porfyrakis

Dr. Edward Laird

DPhil Thesis

Department of Materials, University of Oxford

Hilary Term 2020

Declaration

The material contained within this thesis has not previously been submitted for a degree at the University of Oxford or any other university. The research reported within this thesis has been conducted by the author unless indicated otherwise.

Copyright Notice

Dedicated

To

My mother Prof. Sangeeta Sinha

My father Prof. Sanjay Kumar

My grandparents

&

My beloved sister Srishti Sinha

Abstract

Integration and Role of Graphene in studying 1- and 2-Dimenional Crystals

Sapna Sinha, Lady Margaret Hall, University of Oxford

Abstract of thesis submitted for the degree of D.Phil., Hilary 2020

Supervised by Professor Jamie H. Warner; Prof. Kyriakos Porfyrakis; Dr. Edward A. Laird

The discovery of graphene has attracted significant attention and research on the material as well as providing avenues of research into other two-dimensional (2D) materials. Expanding the properties of graphene requires integration with other systems, such as molecules, or other low dimensional materials, to provide new functionalities and applications. In particular, the strong sp^2 bond between carbon atoms in graphene gives a unique opportunity for adatom adsorption. Decorating the surface of graphene with adatoms and nanoclusters is one approach that can alter the band structure of graphene and introduce dopants that can modify the p-type and n-type behavior. Moreover, the integration of other 2D materials with graphene can significantly alter their properties and also lead to observation of new structure or phenomenon.

The first chapter is based on synthesizing, extracting and separating endohedral metallo-fullerenes (EMFs) and their integration with 2D graphene systems. Optimal set of process parameters for the arc discharge apparatus for the production of EMFs was identified along with the best solvent extraction and separation methodologies. The EMFs studied were $La@C_{82}$, $Y@C_{82}$, $Sc_3N@C_{80}$ and $Gd_3N@C_{80}$. EPR was used to confirm purity and characteristics of the EMFs. Gd based metallofullerene ($Gd_3N@C_{80}$) molecules was then used to integrate with the graphene system and used to create single adatoms and nanoclusters on a graphene surface. An *in-situ* heating holder within an aberration corrected scanning transmission electron microscope was used to track the adhesion of endohedral metallofullerenes to the surface of graphene, followed by Gd metal ejection and diffusion across the surface. Hydrogen was shown to be used to reduce the temperature of EMF fragmentation and metal ejection, enabling Gd nanocluster formation on graphene surfaces at temperatures as low as 300^oC.

The second part of the project was to study the other 2D materials in their heterostructures with graphene. Lead Iodide (PbI_2) is a large band gap 2D layered material that has potential for 2D semiconductor applications. However, atomic level imaging of PbI_2 monolayer crystal structure and its fundamental defects has been limited due to challenges in obtaining suitable quality thin crystals. In this work, liquid-exfoliation was used to produce monodisperse 2D monolayer PbI_2 nanodisks (30-40nm in diameter and >99% monolayer purity) and deposit them onto suspended graphene supports that have high electron beam transparency to enable atomic resolution annular dark field scanning transmission electron microscopy (ADF-STEM) of PbI_2. Strong epitaxial alignment of PbI_2 monolayers with the underlying graphene lattice occurred, with PbI_2 zig-zag edge commensurate with the graphene arm-chair edge direction, leading to a phase shift from the 1T to 1H structure to increase the level of commensuration in the two lattice spacings (PbI_2 and graphene). Then the fundamental point vacancy structures in PbI_2 monolayers were imaged directly, showing rapid vacancy migration to the edges and self-healing. Zig-zag edges were also observed to dominate the PbI_2 nanodisks. Nanopores were produced by electron beam irradiation of the PbI_2 nanodisks and they underwent migration as an intact entity throughout the lattice. These results provided a

detailed insight into the atomic structure and defects in monolayer PbI_2, and the impact of the strong van der Waals interaction with graphene, which has importance for future applications in opto-electronics.

The third chapter studies the role of graphene in another newly emerging 2D material, Palladium Diselenide ($PdSe_2$). Technologically challenging, controllable transformation between the semiconducting and metallic phases of transition metal chalcogenides (TMDs) is of particular importance. Here, controlled laser irradiation could be used to ablate $PdSe_2$ thin films using high power, or trigger the local transformation of $PdSe_2$ into a metallic phase $PdSe_{2-x}$ using lower laser power. $PdSe_2$ material demonstrated strong sensitivity to laser exposure where high laser power resulted in local material degradation and formation of Pd nanoparticles (NPs), while lower laser power could be used to controllably modify the $PdSe_2$ phase, making it Se-deficient and resulting in a $PdSe_{2-x}$ phase. Four regions within the film were observed after laser exposure (1) hole region where the $PdSe_2$ film and graphene were fully damaged, (2) $PdSe_2$ film was modified forming Pd NPs; (3) the phase change of the material was observed where $PdSe_2$ transforms into $PdSe_{2-x}$ and (4) unmodified area of $PdSe_2$. The presence and absence of graphene considerably changed the hole formation area and the phase transformation.

Publications

Presented here is a list of works published during the course of this DPhil project, which has either been published or is in the process of being published. Some of the co-author works listed here lie beyond the purview of this thesis.

Chapter 2

Sapna Sinha, Jamie Warner. Recent progress in the applications for graphene as a transparent support for electron microscopy. *Small Struct.* 2000049, 2021

Chapter 4

Sapna Sinha, Yuewen Sheng, Ian Griffiths, Neil P. Young, Si Zhou, Angus I. Kirkland, Kyriakos Porfyrakis, and Jamie H. Warner. In Situ Atomic-Level Studies of Gd Atom Release and Migration on Graphene from a Metallofullerene Precursor. *ACS Nano*, 12 (10), 10439-10451, 2018

S. Sinha, P. Dallas, K. Porfyrakis. Process Parameters Optimization for Endohedral Metallofullerene Synthesis via the Arc-Discharge Method *(to be submitted, Chem. Phys. Rev.)*

Chapter 5

Sapna Sinha, Taishan Zhu, Arthur France-Lanord, Yuewen Sheng, Jeffrey C. Grossman, Kyriakos Porfyrakis, Jamie H. Warner. Atomic Structure and Defect Dynamics of 2D Monolayer Lead Iodide Nanodisks with Epitaxial Alignment on Graphene. *Nature Comms*. 11:823, 2020

Chapter 6

Viktoryia Shautsova, **Sapna Sinha**, Linlin Hou, Qianyang Zhang, Martin Tweedie, Yang Lu, Yuewen Sheng, Benjamin F. Porter, Harish Bhaskaran, Jamie H. Warner Direct Laser Patterning and Phase Transformation of 2D $PdSe_2$ Films for On-Demand Device Fabrication *ACS Nano*, 13 (12), 14162-14171, 2019

Co-Author

(1) Mihael A. Gerkman, **Sapna Sinha**, Jamie H. Warner, and Grace G. D. Han. Direct Imaging of Photoswitching Molecular Conformations Using Individual Metal Atom Markers *ACS Nano*, 13 (1) 87-96, 2018

(2) Romain Lhermerout, Christophe Diederichs, **Sapna Sinha**, Kyriakos Porfyrakis, and Susan Perkin. Are Buckminsterfullerenes "Molecular Ball Bearings"? *The Journal of Physical Chemistry B*, 123 (1), 310-316, 2018

(3) Yuewen Sheng, Tongxin Chen, Yang Lu, Ren-Jie Chang, **Sapna Sinha**, and Jamie H. Warner. High-Performance WS_2 Monolayer Light-Emitting Tunneling Devices Using

2D Materials Grown by Chemical Vapor Deposition; *ACS Nano*, 13 (4), 4530-4537, 2019

(4) Gyeong Hee Ryu, Taishan Zhu, Jun Chen, **Sapna Sinha**, Viktoryia Shautsova, Jeffrey C. Grossman, Jamie H. Warner Striated 2D Lattice with Sub-nm 1D Etch Channels by Controlled Thermally Induced Phase Transformations of $PdSe_2$; *Advanced Materials*, 31, 1904251, 2019

(5) Syed Ghazi Sarwat, Zengguang Cheng, Nathan Youngblood, Mohd Sharizal Alias, **Sapna Sinha**, Jamie H. Warner, and Harish Bhaskaran Strong Opto-structural coupling in low dimensional $GeSe_3$ films; *Nano Letters*, 19 (10), 7377-7384, 2019

(6) Jun Chen, Gyeong Hee Ryu, **Sapna Sinha**, and Jamie H. Warner Atomic Structure and Dynamics of Defects and Grain Boundaries in 2D Pd_2Se_3 Monolayers; *ACS Nano*, 13 (7), 8256-8264, 2019

(7) P. Dallas, E. Laird, S. Zhou, **S. Sinha**, S. Cornes, I. Rasovic, R. Harding, K. Porfyrakis. Magnetic properties of Endohedral Fullerenes: Applications and Perspectives *(Accepted book chapter, 21st Century Nanoscience - A Handbook, 1st Edition, CRC Press, in press)*

Abbreviations

ADF-STEM	annular dark-field scanning transmission electron microscopy
AFM	atomic force microscope
CNT	carbon nanotube
ESR	electron spin resonance
DLS	dynamic light scattering
DMF	N,N-Dimethylformamide
DWNT	double walled carbon nanotube
EMF	endohedral metallofullerene
GNRs	graphene nanoribbons
HAADF-STEM	high-angle annular dark-field scanning transmission electron microscopy
HPLC	high performance liquid chromatography
HRTEM	high resolution transmission electron microscopy
LPE	liquid phase exfoliation
MALDI	matrix-assisted laser desorption ionization
MS	mass spectrometry
nc-AFM	non-contact atomic force microscopy
NMP	N-methyl-2-pyrrolidone
SEM	scanning electron microscope
STEM	scanning transmission electron microscopy
STM	scanning tunnelling microscopy
SWNT	single walled carbon nanotube
TEM	transmission electron microscopy
UV/Vis	ultraviolet-visible

Acknowledgement

First and foremost, I want to thank my family for their love and support in my life. I am incredibly grateful for the unwavering encouragement that I have received from my parents, my sister and my maternal grandparents – you mean the world to me. None of this would have been possible without them and this thesis is dedicated to them.

This work has, by no means, been a solo effect and there are a number of people I would like to thank for their contributions and for making this is memorable journey. Firstly, I would like to express my gratitude to my supervisor Prof. Jamie H. Warner for providing me the scholarship needed to start my DPhil project and for providing me the opportunity to work on some very interesting projects in his research group. His encouragement, mentorship and knowledge has been invaluable, and I look forward to working with him in future. I would also like to thank my other supervisor Prof. Kyriakos Porfyrakis for his enthusiasm for the project, support and feedback throughout my DPhil.

I would like to express my sincere gratitude to Women in Science Scholarship, (sponsored by Linacre College and the MPLS division) and EPSRC Studentship for funding my DPhil studies. I would like to mention a special thanks to Dr. Sue Whitting for donations to Linacre College, which made it possible for founding the Women in Science Scholarship. Her enthusiasm and support - both financially and individually - is greatly appreciated.

A huge thankyou goes to my collaborators Dr. Taishan Zhu, Prof. Grace Han, Dr. Ghazi Sarwat, Robert Heinz and Prof. Kitaura Ryo – with whom I had the chance to conduct interesting collaborative work outside my research group. I would also like to thank Rob for collaborative work on DLS, despite the fact that it never came to fruition and to P. Gyring for trying to teach me how to use R, although I may have already forgotten most of it by now. I would also like to thank Ms. Christina Foldbjerg–Holloway from Kyriakos lab; Paul Pattinson from the cleanroom in physics; Ian Griffiths and Neil Young from the EM facilities - for helping me out during many failed experiments and bringing humour to the conversations.

I have thoroughly enjoyed my time as a member of both Prof. Kyriakos' group and Prof. Warner's group and this is entirely due to the amazing group of people I have worked with, who I know will be lifelong friends. I am thankful to Martin, Jun, Yingqui, Sha, Viktoryia, Pablo, Matthew, Stuart, Masha, Federico, Shen and Shanshan for the interesting discussions in the lab about science as well as personal life. Westgate lunches with Warner's group; drink socials and going to theatre with Kyriakos' group will be missed.

I would also like to mention a special thanks to Dr. Natalia Ares for being a great mentor throughout my DPhil. I cannot thank enough for the number of dinners you have taken me out to and for career advice. I would also like to say thank you to Dr. Alex Robertson for being a great mentor, especially in the last year of my DPhil, and for taking the time to proofread my thesis (plus for all the drinks in the Royal Oaks on Monday afternoons).

I would like to thank various people from 12/13 Parks Road, especially the people from office 40.12 for as long as I stayed there. Reuben's conversations and cynicism will be sorely

missed and so will the conversations between him, Jake, Achim and Yutian – although usually very dark, they provided interesting topics of discussion at odd hours of the day. I would also like to thank Achim and Jake for helping me out in the cleanroom and sharing their knowledge of fabrication. Monday lunch ritual with Achim will be sorely missed and so will the complaint sessions about work and life, which generally followed afterwards – It was a great start to the week and made my DPhil journey all the more enjoyable.

I was fortunate enough to be a part of two colleges at the University of Oxford during my DPhil – Linacre College & Lady Margaret Hall. I have been involved with the community and social life at both these colleges and cannot appreciate how much it has contributed to my personal growth. I am grateful to the colleges for being so welcoming and providing a big graduate community where I could meet brilliant people and build a life outside work. I am thankful to have made great friends – especially Dan and Derek at Linacre and Alasdair at LMH – with whom I also worked for a year and who I started my DPhil journey with. I am also incredibly thankful to the wonderful and friendly Kitchen staff at both Linacre and LMH who cracked jokes and made my day nicer.

My job at LMH as a Junior Welfare Dean during my DPhil, has been extremely fulfilling and rewarding and I would like to sincerely thank the college nurse - Anne Harpin; the Welfare Fellow - Prof. Helen Barr; the previous Dean - Prof. Aziz Aboobaker; the current Dean - Dr. Michael Fraser; and the Assistant Dean – (soon to be Dr.) Vania Pinto; for the incredible support over the years and making it an amazing welfare team to work with. I would also like to thank them for letting me stay at Linacre whilst being involved as a student at LMH. A special thanks also goes to the wonderful team of porters at the lodge – Alastair, Ade, Toyin, Alex and Aik – who have not only helped me sort out the college issues but have also patiently listened to my daily complaints about work. My heartfelt gratitude goes to Vania who has been an incredible friend and listener and with who I share a lovely cat – Benny D. Cat. I truly believe that I would not have had an as successful DPhil and happy personal life if it were not for her. I have no words to express my gratitude.

I am especially thankful to the strong and amazing ladies that made up Linacre Ladies that Lift. LLtL provided me with strength – both physically and emotionally - and gave me the much-needed escape from DPhil life. I am thankful to all members of LLtL for making the sport fun and enjoyable; and I am particularly thankful to Catherine and Shez who pushed me to explore my personal limits and challenge the way I viewed my physical and inner strength. And I am grateful that along with LLtL, I also managed to develop great friendships with some incredible women that I met at Oxford. Rahel, Nehir, Diana, Carmen, Vania, Charlie, Lina, Oana, Lena, Gilly, Viktoryia and Sarah – You have been my most valuable circle of support during my DPhil. Thank you for building me up, challenging me and listening to me whenever I needed it. You have pushed me to be strong and always reminded me of my capabilities. You have had a remarkable positive effect in my life and the time spent with you all would be one of my best memories of DPhil.

Outside Oxford, there are many whom I wish to thank for their friendship and support. The list is long, so my apologies to those not named herein. I am the third generation in my family to hold a PhD degree. I realize the privileges that I have had, and I hope to use it to create a positive impact in the world we live in.

Sapna Sinha,
9th July, 2020

Contents

Chapter 1 Introduction

1.1 Project Aims

The objective of this doctorate project is to systematically synthesize and characterize various low dimensional material and understand their van der Waals interaction with graphene using annular dark field scanning transmission electron microscopy.

1.2 The Scope of this Thesis

This thesis includes the research I have conducted over the span of my three years of DPhil study in the Department of Materials, University of Oxford. Chapter 2 provides a broad overview of the importance of using TEM for the study of nanomaterials and the rise of graphene as a superior substrate for the study of different kinds of low-dimensional materials. A review of the study and characterization of various nanomaterials using TEM and the use of graphene and the influence of its interaction with nanomaterials under TEM, are the main sections of this chapter. The methodology and the instruments used for carrying out the research are introduced in Chapter 3. Chapter 4 focuses on my work on synthesizing, extracting and separating endohedral fullerenes (EMFs) and their integration into 2D graphene systems. An Optimal set of process parameters for the arc discharge apparatus for the production of EMFs was identified along with the best solvent extraction and separation methodologies. Gd based metallofullerene ($Gd_3N@C_{80}$) molecules were then used to integrate

with the graphene system and *in-situ* heating as well as H_2 annealing was used to create single adatoms and nanoclusters on a graphene surface. Chapter 5 focuses on the study of other 2D materials, i.e. Lead Iodide (PbI_2) in its heterostructure with graphene. Here, liquid-exfoliation was used to produce monodisperse 2D monolayer PbI_2 nanodisks (30-40nm in diameter and >99% monolayer purity) and deposit them onto suspended graphene supports that have high electron beam transparency to enable atomic resolution annular dark field scanning transmission electron microscopy (ADF-STEM) of PbI_2. Strong epitaxial alignment of PbI_2 monolayers with the underlying graphene lattice occurred, with the PbI_2 zig-zag edge matching the graphene arm-chair direction, leading to a phase shift from the 1T to 1H structure to increase the level of commensuration in the two lattice spacings (PbI_2 and graphene). Then the fundamental point vacancy structures and nanopores in PbI_2 monolayers were imaged directly, showing rapid vacancy and pore migration to the edges and self-healing. Chapter 6 studies the role of graphene in another newly emerging 2D material, Palladium Diselenide ($PdSe_2$). Here, controlled laser irradiation was used to directly ablate $PdSe_2$ thin films using high power, or trigger the local transformation of $PdSe_2$ into a metallic phase $PdSe_{2-x}$ using lower laser power. $PdSe_2$ material demonstrated strong sensitivity to laser exposure where high laser power resulted in local material degradation and formation of Pd nanoparticles (NPs), while lower laser power could be used to controllably modify the $PdSe_2$ phase, making it Se-deficient and resulting in a $PdSe_{2-x}$ phase. The presence and absence of graphene considerably changed the hole formation area and the phase transformation. Chapter 7 highlights the summary of my DPhil work, and also presents the challenges and opportunities with prospects of future research on the study of nanomaterials via TEM by integrating them with graphene.

Chapter 2 Literature Review

2.1 Introduction

TEM has long been used as the ultimate characterization technique for nanomaterials at the atomic level, as discussed briefly in this chapter. Here, the importance of the use of graphene in TEM is also presented to introduce the properties that makes it indispensable for the characterization of other nanomaterials and studying their properties and van der Waals interactions. In this chapter, a review of the study of morphology, properties and behaviour of a range of nanomaterials is presented, with a specific focus on how graphene facilitates these studies due to its unique influence and interaction with individual materials.

2.2 Graphene: The Ultimate TEM Microscope Slide

2.2.1. Advantages of using TEM

With increasing interest in nanomaterials and small molecules, there has also been rapid developments in various imaging and characterization techniques used to study their properties, such as, nc-AFM[1],(1,2) STM[2],(3–6) etc. STM is one of the most popular tools used for imaging surfaces at the atomic scale. However, despite being heavily used for imaging molecules as well as polymers, STM provides lower resolution, which makes it difficult to

[1] Non-Contact Atomic Force Microscopy
[2] Scanning Tunneling Microscopy

image individual atoms and is limited by sample conductivity, cleanliness and acquisition time. In addition, it often requires cryogenic temperatures to be able to record atomic resolution images. Similarly, even though nc-AFM provides higher resolution to image atoms and even bondings,(7,8) its long acquisition time (i.e. 15-30min), makes it a challenge for statistical and dynamic analysis of the molecules. Therefore, one of the major characterization tools with the capability to characterize and study the atomic level structure and properties of nanomaterials is the transmission electron microscope (TEM). State-of-the-art TEM enables imaging and studying nanomaterials with atomic resolution whilst at the same time enabling the use of other characterization techniques simultaneously. TEM has witnessed rampant development which was timely with development in the field of nanomaterials, in the sense that aberration correction allowed operation of the microscope at high resolution, even at lower acceleration voltages, so that the damage to the nanomaterials was minimized.(9) Both transmission electron microscopy (TEM) and scanning transmission electron microscopy (STEM)[3]are extensively used for the characterization of nanomaterials(10) because they are reliable, whilst at the same time, offer various other ways of characterization, such as elemental analysis through EDS[4] and EELS[5].(11–13)

With the advancement of TEM and improved resolution and capabilities in imaging, the bottlenecks for obtaining high resolution images has been shifted from the instrument to sample preparation. Therefore, it is increasingly being recognized that the optimization of sample preparation technique as well as minimizing the background noise from the sample support is very important for obtaining high-resolution images and study nanoparticles and atoms.

[3] Sometimes also referred to as (S)TEM or ADF-STEM.
[4] Energy Dispersive X-ray Spectroscopy
[5] Electron Energy Loss Spectroscopy

2.2.2. Properties of Graphene and Microscopy

Since the discovery of graphene in 2004, it has spawned massive interest in its two-dimensional sp^2-hybridized carbon structure.(14) A single sheet of graphene is comprised of a single atom thick carbon layer with regular and periodic structure. Its excellent electrical properties were first highlighted by Novoselov et. al.(15) and since then, a tremendous amount of research has been carried out to study its morphology, defects, electrical and mechanical properties, etc. An increasing number of applications of graphene have also emerged in the past decade, exploiting its exceptional properties.(16) TEM is one such area where graphene is proving its worth as a sample support for electron microscopes. In this section, some of the properties of graphene are presented which showcase the unique capabilities of the material as a sample support in TEM.

Graphene is the thinnest possible material with high crystalline morphology. A purely crystalline, pristine graphene is also electron ‘‘transparent’’[6] to TEM up to the resolution of 2.13Å.(17) It also shows excellent electron transparency because of the single atom thick carbon layer.(18) The single atomic thickness of 0.34nm also contributes to very little background noise and even when the lattice is completely resolved, the signal can be easily filtered through its FFT[7], if necessary.(19,20) This makes it easy to focus and study other nanomaterials on its surface, because either the graphene is completely invisible at higher voltages, or otherwise its lattice can be completely filtered out from the images. Graphene is also known to be remarkably strong, both mechanically and elastically(21–23), which gives it the ability to withstand high vacuum conditions inside TEM. Moreover, it is known to be a

[6] The atomic level structure of graphene is not resolved in TEM, at resolutions down to 2.13Å, because the crystalline periodicity of 2.13Å is higher than the periodicity of graphene. Therefore, as a substrate, it effectively provides a completely ‘‘transparent’’ background. In addition, transmission coefficient of graphene can be obtained as the ratio of current on graphene to the current passing through it. This can vary a lot between 0.95 to 0.05, effectively making it transparent at specific accelerating voltages.
[7] Fast Fourier Transform

good electrical conductor, with a conductivity which is six orders of magnitude higher than that of amorphous carbon, and therefore does not charge up from the e-beam.(24–26)

TEM is known to create damage in the material. However, it has been reported that graphene can effectively self-repair ion damages in the temperature range that are currently been used for its CVD[8] synthesis, which can now also be achieved inside the microscope, by using *in-situ* heating.(27) This indicates the durability of graphene even against electron beam damage and shows its importance as the ultimate thin sputtering shield under electron beam irradiation. Aside from conventional TEM, graphene supports are also starting to get used in *in-situ* TEM to enable the imaging and investigation of other specimens. Transitioning from 3-dimensional bulk structures to low 0- or 2-dimensional materials has a significant influence on the nature of damage under the electron beam.(28) Therefore, graphene encapsulation of nanomaterials is yet another area (**Section 2.3.2** and **Section 2.3.10**) which has grown tremendously to study beam-sensitive materials in TEM.

Comparing conventional amorphous carbon and graphene as a substrate for TEM grid, graphene is one-atom thick whilst the amorphous carbon sheets can range anywhere between 3 and 20 nm in thickness. Moreover, the chemical inertness of graphene makes it less reactive than the amorphous carbon substrates at lower accelerating voltages. In addition, as discussed above, crystalline graphene can be easily masked by Fourier filtering of the images, which is not possible for amorphous substrates. The conductive properties of graphene give it an additional advantage of possessing a homogenous surface potential that reduces phase distortions of the electron waves.(29) Monolayer graphene oxide is another related material that is widely used as a substrate for microscopy. In the beginning, when it was still difficult to synthesize and transfer large areas of monolayer graphene, graphene oxide could be

[8] Chemical Vapor Deposition (CVD) – A popular technique to synthesize graphene. Discussed in further details in **Chapter 3**.

prepared easily and also transferred onto different kinds of substrates. However, although it has atomic layer thickness, it has limited electrical conductivity that is dependent on the degree of oxidization.(30) With the advent of CVD synthesis of graphene(31), large area graphene can be synthesized and transferred easily as a substrate for TEM purposes, thereby alleviating the limitations inherent to the use of graphene oxide membranes. The availability of large area graphene allows for the easy transfer of graphene from copper substrate to TEM grids, which results in freestanding graphene(17), providing ample surrounding space with sufficient contrast for tuning the microscope and focusing away from the region of interest.

Another membrane which has been popularly used for imaging individual nanoscale particles or molecules is Carbon Nanotubes (CNTs). The development in the area of CNTs preceded that of graphene, and thus a lot of *in-situ* TEM research using CNT substrate was performed much earlier on.(32) Molecules, ions or atoms can be easily confined inside CNTs, which can be exploited to use it as a nano-container to study the properties of individual species in 1-Dimension. CNTs are strong, thermally stable and mechanically robust(33) and can be atomically thin[9], which facilitates the study of the molecules directly, in real space through the nanotube wall. In the past 20 years, dozens of different types of nanomaterials have been encapsulated across the mesh of CNTs and subsequently studied using TEM(34), such as molecules,(35,36) nanoparticles,(37) fullerenes,(38) organic or biomolecules(39), etc. Extending the application of CNTs beyond nanocontainers, it has also been used as a chamber to carry out nanoreactions[10].(40) CNTs provide highly efficient platform for holding complex molecules and its highly stable and robust nature enables control over the encapsulated nanomaterials whilst providing the real-space for imaging and studying the chemical reactions at a molecular level.(41,42) The mechanical robustness, high thermal stability and the

[9] In case of single walled carbon nanotubes (SWCNTs), frequently also referred to as SWNTs
[10] CNTs have been recorded in Guinness Book of World Records as world's tiniest test tubes.(396)

chemical inertness, because of the absence of dangling bonds inside the tube, allow reactions to be carried out inside the tube in harsh conditions without the CNTs being damaged or participating in it itself. Khlobystov et. al. developed a new approach, called chemTEM, which follows the chemical transformations at the single-molecule level with the electron beam inside TEM.(43) The different uses of CNTs in TEM have been shown in **Figure 2.1**.

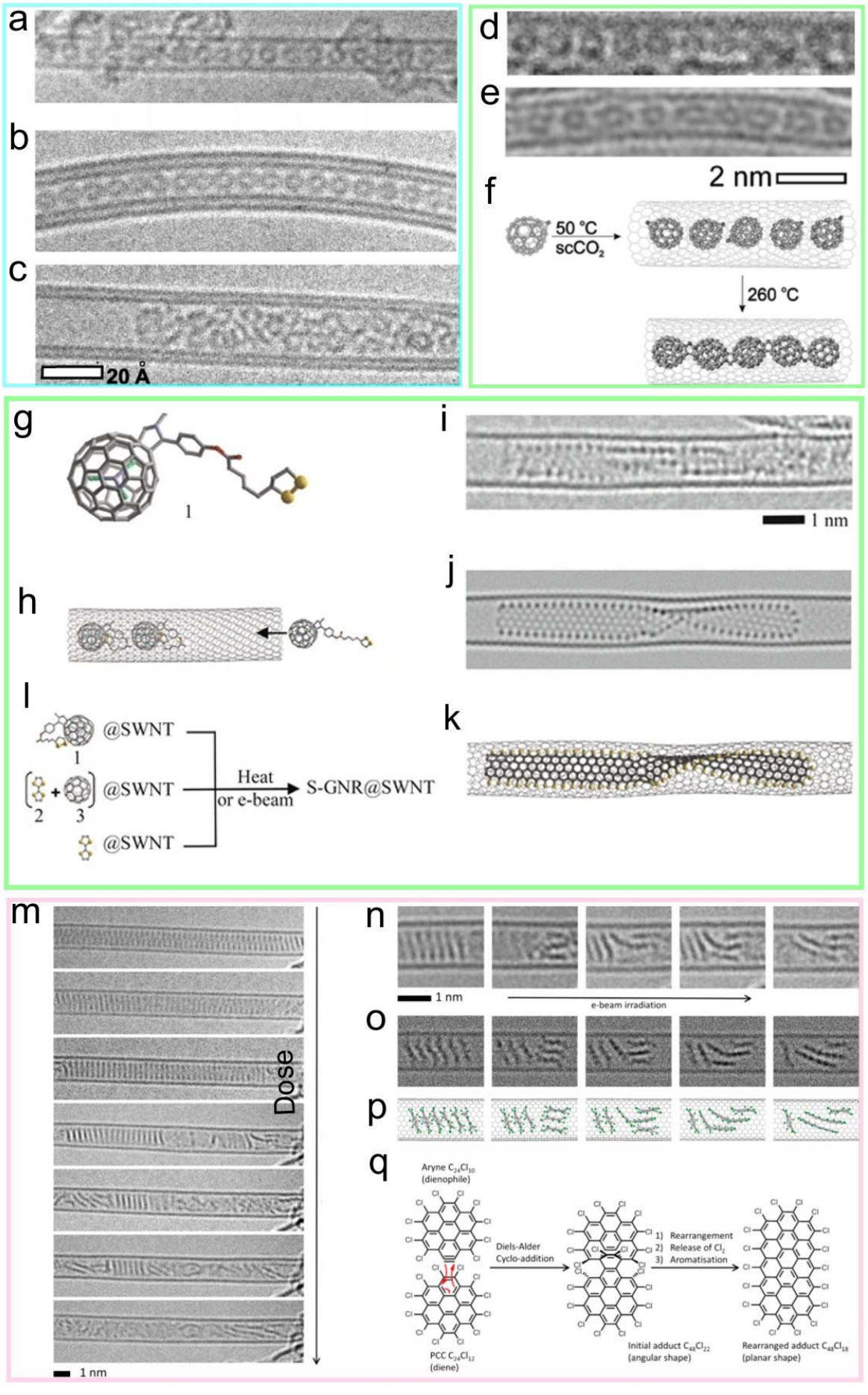
a
b
c
20 Å
d
e
2 nm
f
50 °C
scCO2
260 °C
g
1
i
1 nm
h
j
l
@SWNT
1
@SWNT
2
3
@SWNT
Heat
or e-beam
S-GNR@SWNT
k
m
Dose
1 nm
n
1 nm
e-beam irradiation
o
p
q
Aryne C24Cl10
(dienophile)
Diels-Alder
Cyclo-addition
1) Rearrangement
2) Release of Cl2
3) Aromatisation
PCC C24Cl12
(diene)
Initial adduct C48Cl22
(angular shape)
Rearranged adduct C48Cl18
(planar shape)

Figure 2.1. CNTs as nanovessels (a-c), nano test-tubes for transforming molecules (d-l) and performing chemTEM (m-q). (a-c) HRTEM images of completely filled C_{60}@SWNTs, C_{60}@DWNTs[11] and partially filled C_{60}@DWNTs respectively. (d-f) HRTEM images of unreacted $C_{60}O$, $(C_{60}O)_n$ polymer after heating (d) at 260°C in high vacuum, schematic of the reaction respectively. (g-k) Functionalized fullerene in (g), re-assembly of fullerenes owing to stron van der Waals interactions between fullerene cage and interior of host-nanotubes in (h), experimental TEM image in (i), simulation of (i) in (j) and its model of S-GNR@SWNT[12] in (k) and the different templates of reactions in (l). (m-q) chem TEM of PCC in CNTs showing dose dependent AC-HRTEM time series from 2.0 x 10^6 e^-/nm^2 to 8.0 x 10^6 e^-/nm^2 taken at 80keV in (m), close examination of experimental image in (n), its simulation in (o) and the corresponding generated structural model in (p). The schematic of Diels-Alder cycloaddition and rearrangement of the adduct taking place inside the CNT, as predicted by DFT calculations in (q). Figures reprinted (adapted) with permission from: (a-c), ref.(44), © 2004 American Physical Society; (d-f), ref.(45), © 2005 The Royal Society of Chemistry; (g-k), ref.(46), © 2011 Springer Nature; (m-q), ref.(43), © 2017 American Chemical Society.

However, the limited space and only one accessible direction of motion in CNTs does not provide any information on the behaviour of molecules in 2-dimensions. Graphene overcomes these factors as it provides a 2-dimensional surface for the free motion of nanomaterials on the surface, as compared to CNTs which provide only one degree of translational freedom.

The graphene membrane thus provides the ultimate sample support for TEM, and has helped refresh experimental TEM approaches(47) and renewed interest in TEM supports(48).

2.2.3. Graphene as a Sample Support & More

The application of graphene as a sample support in TEM has been demonstrated widely in the literature, especially with the advent of aberration correction in TEM.(48) Mc Bride et. al. and Meyer et. al.(49) reported the first application of few-layer graphene films for nanocrystal imaging.(47) Their studies showed the high sensitivity that graphene membranes provide in TEM to facilitate imaging of sub 2nm CdSe nanocrystal(49), and detect adsorbates as light as hydrogen atoms(47), using TEM with nearly background-free imaging. It was shown that lower carbon background from graphene particularly benefitted the study of the

[11] Double walled carbon nanotubes (DWNTs)
[12] Graphene nanoribbons (GNRs)

CdSe using EELS. The results show that graphene supports could help investigate the dynamics of small nanoparticles and molecules in real time and provide insights into complex chemical reactions. Although the results were based on few-layer graphene, it opened doors to many possibilities. Now that it is feasible to prepare single layer large area graphene, much research has been carried out in this direction. Thus far, graphene sheets have been used as a support for TEM studies of various different materials such as, nanoparticles, organic molecules, bio-molecules, etc., which has been discussed in details in **Section 2.3**.

The use of graphene as a substrate in TEM can be widely divided into five categories – (i) Imaging the adsorbates and light weight atoms by themselves and their interaction with graphene.(9) (ii) Use of graphene as an inert and mechanically stable substrate for *in-situ* experiments.(50) (iii) Straightforward use as a substrate for high resolution imaging of nanomaterials that cannot be otherwise obtained in a freestanding form for TEM observations.(29) (iv) As an encapsulation cell for imaging highly electron beam sensitive materials like biomolecules, organic compounds, etc. (v) As a unique material to lead research towards creating and studying hybrid interfaces with other materials or specimens(51) with the use of electron beams, by exploiting the presence of dangling bonds from carbon residues on the surface. (52)

2.3 State of the art Microscopy with Graphene Substrate

2.3.1. Fullerene study and encapsulation

The study of 0-dimensional materials[13], such as fullerenes, is a significant area of nanomaterials research that has benefitted from the use of graphene in TEM as a substrate.

[13] '0' dimensional materials are broadly referred to as the nanomaterial which is a few nanometers in size in all its dimensions. In the scientific community, fullerenes and nanoparticles are referred to as 0D nanomaterials.

Carbon supports that are only a single atom thick provide ideal surfaces to study and serve as encapsulation containers for studying fullerenes. Since the discovery of CNTs in late 20th century, single-walled carbon nanotubes (SWNTs) have been used as a molecular test-tubes or nanoreactor capsule to encapsulate fullerenes in order to study it, within high resolution TEM, with reduced radiation damage.(53) Numerous studies have been conducted on empty cage fullerenes and endohedral metallofullerenes (EMFs) inside SWNTs, studying their synthesis(54), structure(55), dynamics(56), reactions(57), defects(58) and damage(59). However, the CNT is a 1-dimensional system that only allows studying the dynamics or reactions of fullerenes in a singular dimension. Graphene on the other hand, provides a similar environment with a single atom thick encasement for fullerenes, whilst at the same time, offering them two degrees of freedom. Graphene encapsulation[14] of small metal particles(60), colloidal nanocrystals(61) or other 2D materials systems(62,63) have shown to reduce the rate of radiation damage(62,63). Extending that encapsulation process to fullerenes gives fullerenes a similar protection from radiation whilst at the same time, providing a reaction chamber that is less constrained than a 0D fullerene cage(64) or SWNT test tubes. This provides new avenues for the study of fullerenes, their reaction and dynamics on a large flat surface.

Choe et. al.(65) used aberration corrected TEM to demonstrate that the molecular rotational motion of anchored C_{60} on graphene can be monitored at a single molecular level. The interaction of C_{60} with graphene also leads to preferential registry of the rotation (**Figure 2.2**a-c), which they explained through the stacking-dependent energy landscape between the two systems. Moreover, it was also shown that the energy barrier for rotational-angle configurations could be estimated by simply analysing the molecular dynamics of the

[14] Graphene encapsulation here refers to graphene sandwich structure with different materials, i.e. graphene-material-graphene structure.

fullerenes. They carried out another investigation(66) on the structural disordering and heterogenous dynamics of C_{70} deposited on graphene (**Figure 2.2**h-l). Their experiments showed interesting results on e-beam induced first-order transition-like crystal melting of the disordered C_{70} molecular system on graphene, as shown in **Figure 2.2**m. The observed heterogenous dynamics of C_{70} after e-beam radiation bore similarity to the dynamical heterogeneity in supercooled liquids that are close to their glass transition. The unprecedented real-time high resolution imaging, opens doors to completely new possibilities of using various types of fullerenes and EMFs on graphene to study molecular glass and supercooled liquids. However, the images obtained of the C_{60} on the graphene are not as clear and the e-beam defect induced on C_{70} was easier to obtain because of the lack of encapsulation. This encapsulation process and its effect was recently studied by Mirzayev et. al.(67), by fabricating 0D/2D heterostructure that incorporated C_{60} molecules between two graphene layers to form a buckyball sandwich (**Figure 2.2**d-e). They showed interesting results on clean and ordered C_{60} islands with one molecule thickness incorporated between two graphene sheets. The graphene layers allowed the study of the structure and dynamics of C_{60} at atomic resolution, and at the same time proved to be successful in shielding C_{60} molecules from radiation damage during STEM imaging (**Figure 2.2**d-g).

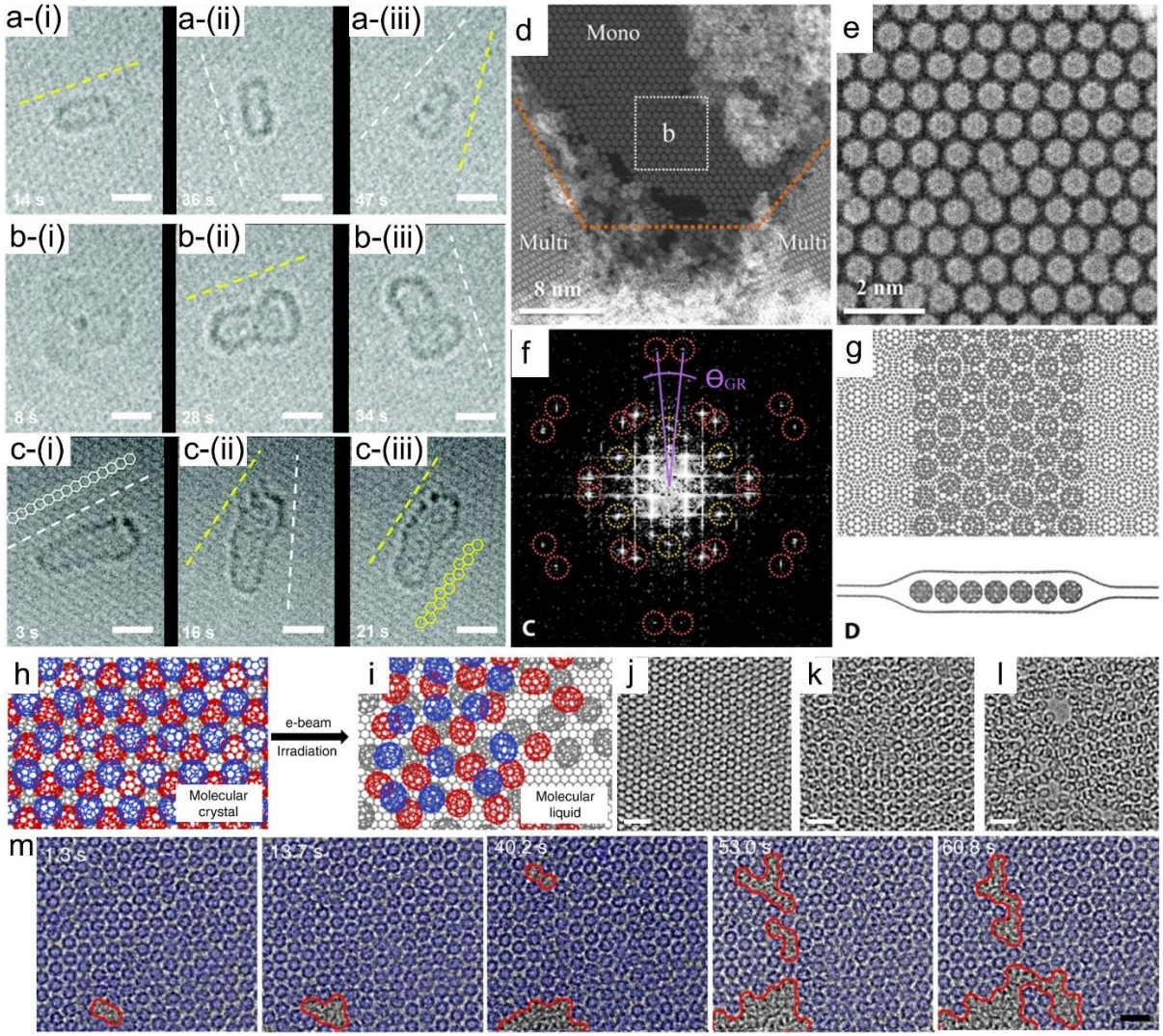

Figure 2.2. (a-c) Sequential TEM images of rotating C_{60} molecules anchored on graphene. The white and yellow dashed lines represent the graphene zigzag and armchair directions respectively. Scale bar corresponds to 1nm. (d-g) Monolayer area of a C60 sandwich between two graphene layers showing both monolayer and multilayer regions (d), higher magnification of monolayer region (e), FFT of (e) with graphene shown with red circles, and some fullerene shown in yellow circle (f) and schematics of a buckyball sandwich with top and side view in (g). (h-i) Atomic models of C_{70} deposited on graphene before and after structural transition under e-beam, respectively. (j-l) TEM images of C_{70} arrangement showing increasing structural disorder from (j) to (l) on prolonged exposed to e-beam. Scale bar corresponds to 2nm. (m) Sequential TEM images taken in the first 60s of e-beam exposure, showing the structural transition from molecular C_{70} crystal phase (enclosed in blue) to liquid phase (enclosed in red). The disordered molecular regions of C_{70} come together slowly whilst showing apparent phase boundaries with the initial homogeneous crystalline C_{70} phase. Scale bar, 2 nm. Figures reprinted (adapted) with permission from: (a-c), ref.(65), © 2016 The Royal Society of Chemistry; (d-g), ref.(67), © 2017 AAAS; (h– m), ref.(66), © 2019 Springer Nature.

Whether anchoring the fullerenes to the graphene surfaces, or depositing them on top, or encapsulating them on either side with graphene, all possibilities show interesting results

and help investigate their crystal phase and motions at low and high temperatures. Further research in the area can provide valuable information on the dynamics and energetics for various types of fullerenes, which have not been studied before and potentially open doors for novel applications.

2.3.2. 2D Materials & Encapsulation

The advances in TEM has enabled high resolution imaging of 2D materials, which has increased our understanding of these materials at the atomic level.(68) However, the electron beam, especially at accelerating voltages above 80kV, causes irradiation damage[15] such as breaking of bonds, mass loss etc., yielding difficulties in studying the intrinsic properties of the 2D materials. Moreover, lower voltages lead to reduced resolution and more difficulty with aberration corrections in recording the information required. The use of graphene with these 2D materials functions as an ideal substrate as well as encapsulation material (28) for clean and radiation damage free study these 2D materials via TEM at lower voltages.

Dozens of different techniques have been reported in the past decade for fabricating 2D lateral heterostructures to facilitate study of their intrinsic electrical properties.(69) However, little study has been carried out to encapsulate 2D materials with graphene to study their structural morphology via TEM. In some cases, it has been shown that encapsulation eliminates damage, almost entirely(62), facilitating clean atomically resolved morphology of the intrinsic structure. In addition, 'sandwich' structures can also enhance recombination rates, because of reduced atomic diffusion, which is also said to be the rate-limiting step of the damage(70) within the atomic structure of the 2D crystal. Zan et al.(63) showed that detailed understanding of the crystallography, reconstruction and stacking order of 2D atomic crystals and their heterostructures can only be studied through direct imaging and identification of each

[15] Radiation damage above 80kV is prominent because of the high energy electrons which can cause knock-on effect on the material of interest.

atom in a protected environment. They showed that MoS_2 crystals have the highest durability and lowest defect formation within two graphene layers (i.e. three-layer stack of graphene/MoS_2/graphene), as compared to when they are left pristine or placed on top of a graphene substrate, and it also allowed the use of TEM to carefully control the nature of formation of defects in the crystal. The results demonstrate that both knock-on damage and ionization effects induced by the e-beam can be reduced dramatically, allowing defect-free chemical analysis of the material. Quantitative experiments were carried out by Algara-Siller et. al. on using different configurations (**Figure 2.3**a-d) of graphene protective layers on $MoSe_2$(71), where they found that protective layers could provide up to 600-fold reduction in the rate of damage with total encapsulation (**Figure 2.3**d), which is ideal for studying its properties. Interestingly, they also found that although a graphene protective layer on top of the 2D crystal (**Figure 2.3**b) would be expected to reduce the inelastic damage to the material, having it underneath the 2D material (**Figure 2.3**c) led to increased elimination of damage, to up to 24% more. They attributed the phenomenon to reduction of the surface sputtering which is generally caused by the direct knock-on damage from the e-beam. Similar results of WS_2 on top of graphene has been reported by Kim et. al.(72), where they showed that simply utilizing the graphene as a substrate, instead of encapsulating it completely, can also result in substantial improvement in long term stability of the material. This can also be a result of reduced backscattering due to the presence of graphene underneath the 2D material.

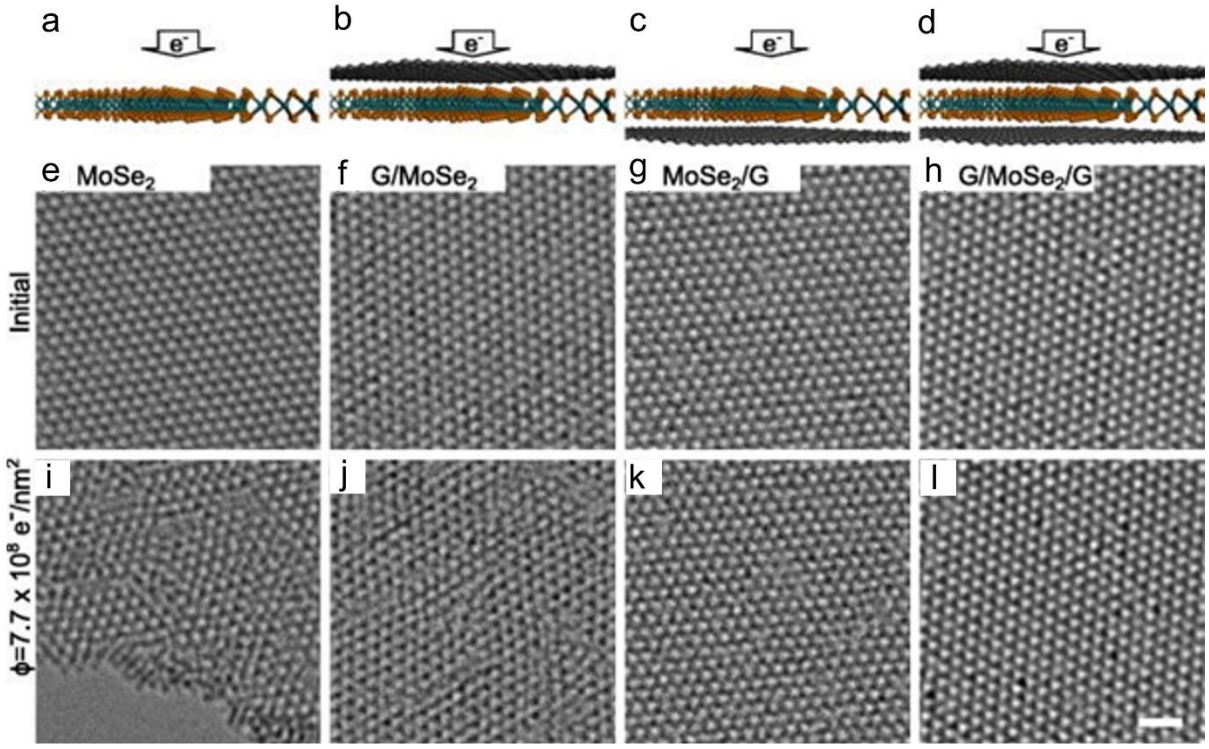

Figure 2.3. (a-d) Schematic of different heterostructure configurations of $MoSe_2$ and graphene – free standing MoS_2 (a), $MoSe_2$ protected by graphene from the top (b), $MoSe_2$ with graphene layer underneath (c), $MoSe_2$ encapsulated with graphene on both sides. (e-h) The initial HRTEM images of the heterostructures shown in (a-d) respectively. (i-l) HRTEM images of the heterostructure (e-h) respectively after exposure to the e-beam of a dose of $\phi=7.7\times10^8 e/nm^2$. The HRTEM images after the exposure (i-l) showed an increase in resistance against radiation damage, going from (i) to (l). The scale bar corresponds to 1 nm. Figures reprinted (adapted) with permission from: (a-l). ref.(71), © 2017 AIP Publishing.

It's also been shown that different kinds of analysis particular to the 2D crystals can be conducted within TEM without damage to the crystal, such as crystal orientation(73), EELS(63,74), EDS(75) and elemental mapping(75), with easy elimination of signals from the protective graphene sheet. Graphene has also been shown to act as a protective layer to assist layer-by-layer thinning of phosphorene samples using TEM, rendering high-quality monolayer and bilayer regions.(76) They also reported that phosphorene shows increased stability and reduction in radiolysis damage when exposed to e-beam. Graphene has also been shown to have influenced the epitaxial alignment of 2D materials, which is attributed to the van der Waals interaction between the two materials. For instance, when amorphous MoS_2

was deposited on graphene, it showed restructuring into crystalline domains when irradiated with electron beam.(77)

2.3.3. Biological Materials

Thus far, carrying out TEM of biological cells has been an important challenge in research. Biological cells are known to be hygroscopic, permeable, as well as electron-absorbing, thus leading to a structural decay when exposed to the electron beams.(78,79) Also, when imaged under high vacuum condition, the reduced pressure leads to contraction in size and volume of the wet cells as well as electrostatic charging in TEM.(80)

With the recent use of graphene in TEM, Mohanty et. al. showed that the problems mentioned above can be solved by encasing the beam-sensitive biological cells in graphene. Graphene is not only electron transparent, but its high electrical(81,82) and thermal conductivity(82,83) facilitates imaging and protection of fluidic samples without electrical charging or heating of the cells. Mohanty et. al.(84) showed that bacteria cells encased within graphene layers could be imaged well under TEM whilst withstanding very low pressure, i.e. 10^{-5} Torr, as well as high beam current up to 150A/cm^2. Pantelic et. al.(17) showed that positively stained DNA can be imaged in high contrast under STEM by the use of pristine graphene which is difficult to achieve with the use of a conventional substrates such as amorphous carbon or graphene oxide. Subsequent study by Cerf et. al.(85) showed that even plasmid DNA, which is made up of only light atoms (C, N, O and some H and P), can be imaged as well as arranged across graphene, and STEM can be used for a complete genetic and epigenetic mapping by reading single molecular system. The use of graphene as a transparent conductive support in TEM for studying nanobio materials has been extended and shown to work exceptionally for many different specimens, such as viruses,(18) insulin amyloid fibrils,(86) DNA assembled Au nanoparticles,(87) etc.

Moreover, the extraordinarily large area of graphene provides ample space for carrying out purposeful reaction with living organisms.(88) Graphene can interact with the biological molecules, opening up a whole new field of science impacting the biological systems. With the use of STEM, Kabiri et. al.(89) imaged both stained and unstained DNA origami nanoplatelets on graphene as well as amorphous carbon with good contrast. However, they found that when these nanoplates were put on top of graphene, they had structural distortion. This can be attributed to the π–π interaction of the DNA with the substrate underneath, which points towards interesting field of science where the biological molecules can interact and form new structures with graphene. This also opens-up interesting area of studying interactions of biological samples by functionalization of the graphene substrate. It has also been shown that functionalization of graphene to render it hydrophilic, can help mount the biological samples well, whilst at the same time keeping the other properties of graphene intact, which facilitates imaging under TEM.(90) Progress in this direction would also lead to real time imaging of biological samples as well as potentially also help study their biochemical activities under controlled conditions.[16]

2.3.4. Organic Compounds

A longstanding challenge in characterization of organic compounds is to understand their distribution and be able to image atomic structures of single molecular compounds which are usually made up of light elements. Graphene serves as an excellent substrate by providing transparent and large surface ultra-clean area to image them and to study their mobility and structures of their conformers. Janicek et. al.(91) showed that EELS can be used in STEM mode of imaging to directly visualize and quantify ligand distributions on gold nanorods, when

[16] Currently, the sample prep and the high energy electrons are known to kill the samples. Therefore, the studies are limited to proteins, DNA or other biological materials which are not alive anymore. However, with the betterment of technology and progress in sample preparation, it may be possible to image live bio-organisms in the future one day.

deposited on graphene. The results showed ligand binding densities between individual nanoparticles and the impact of electron spectroscopy to understand the molecular distributions. Ke et. al.(92) showed that a single Ru_4POM[17] molecule on graphene depicted dynamic rotation without any influence from the graphene surface, and can be monitored by time sequence TEM studies. The authors showed that both the morphology and the reactivity of Ru_4POM-graphene hybrid can be tuned by the right selection of functionalization. The study is key to understanding the nano-graphene modification and applications. Similarly, other research has been carried out on different kinds of organic compounds and ligands on graphene, such as mobility of single polyoxometalate ions(93), monomolecular transformations of perchlorocoronene molecules(43), characterization of magic-sized CdSe and CdTe nanocrystal ligands(94), molecular reactions on graphene(41), etc. Another way of studying these large organic molecules is by anchoring them to the surface of graphene. Merkevich et. al.(95) reported that the structure and dynamics of PCC[18] can be studied by using e-beam to anchor it on graphene. When the molecule is dropped on graphene it initially forms a face-on orientation on the surface, but after being irradiated for a few to hundreds of seconds (doses between 2×10^6 and 13×10^6 $e^- nm^{-2} s^{-1}$), the molecules stand up vertically on the surface. The e-beam initiates a two-step chemical reaction where one of the C-Cl bonds in PCC breaks to form a covalent bond with C from the graphene surface. Further *in-situ* experiments on this system was conducted by Chamberlain et. al.(43) and Skowron et. al.(41) to deduce that Diels-Adler reaction takes place with PCC and graphene on the surface when irradiated with e-beam. Further experimental work on e-beam driven organic-graphene reactivity could help develop hybrid materials with new functionalities.

[17] Polyoxometalates (POMs)
[18] Perchlorocoronene ($C_{24}Cl_{12}$)

Recently, the use of individual heavy metal atoms as a marker in studying complex structural change of organic molecules has also been demonstrated. HAADF-STEM[19] is an excellent imaging mode for identifying and monitoring the heavy metals in the organic molecules as they appear as bright spots during imaging, and graphene can provide transparent support to easily identify and study the transient molecular movement of these heavy metal atom-decorated single molecules. Gerkman et. al.(96) studied photoswitching azobenzene derivatives on graphene support and were able to identify photoisomeric states of the molecule, as shown in details in **Figure 2.4**a-k. Lee et. al.(97) also showed the similar use of heavy metal Pt-atom markers in linear porphyrin hexamer (Pt-L6) for studying the 2D monolayer self-assembly of the molecule on graphene. The results demonstrate how the metal markers in complex organic molecules on top of graphene can be exploited to study large scale structure, alignment, chain bending and packing at individual molecule level (**Figure 2.4**l-r). Incorporating such HAADF-STEM imaging has potential to study dynamically changing device structures incorporating both organic molecules and 2D graphene.

[19] High-angle annular dark-field imaging, also sometimes referred to as HAADF, is a STEM technique where annular dark field images are formed by very high angle, incoherently scattered electrons.

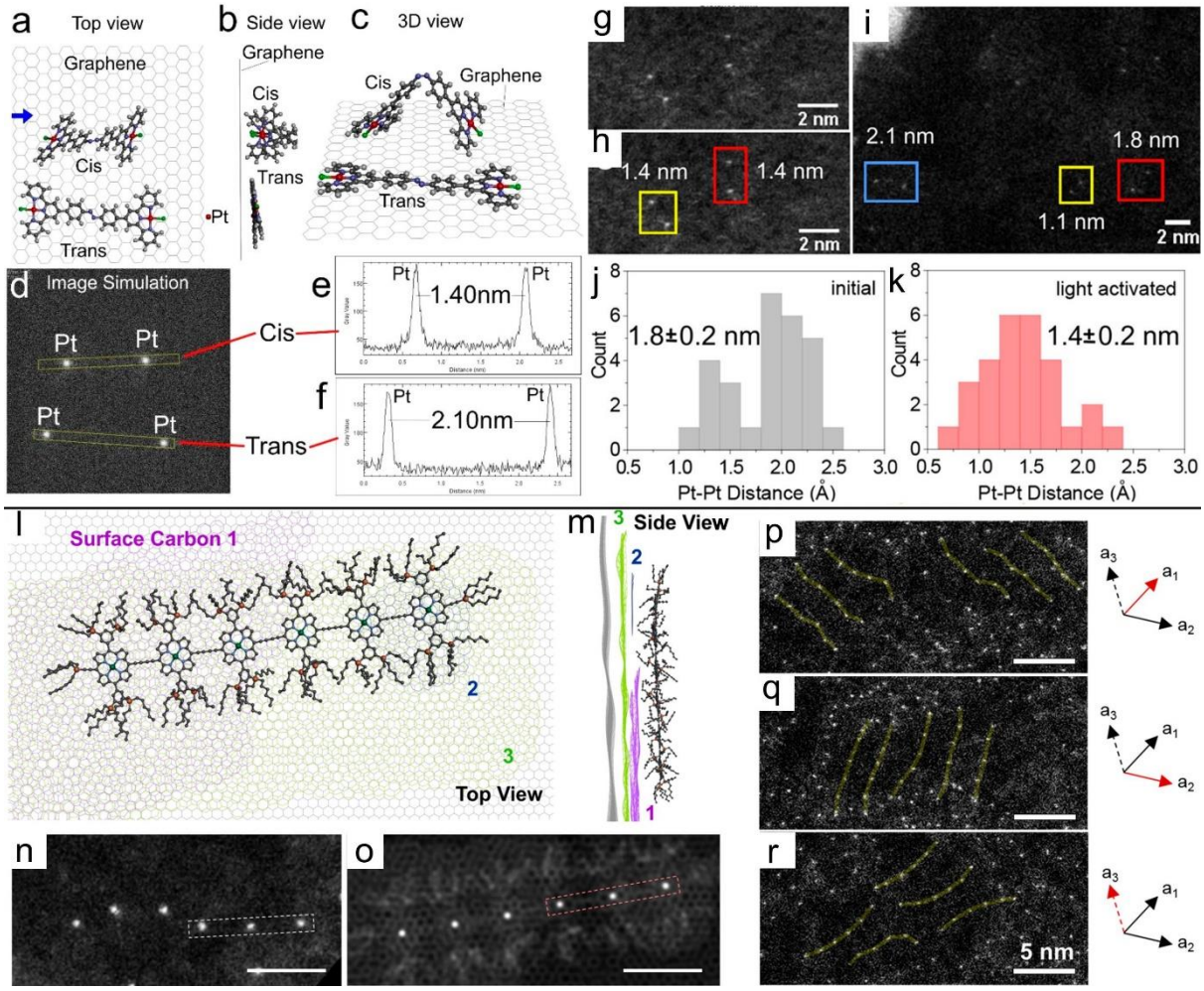

Figure 2.4. (a-l) ADF-STEM study of azobenzene molecule on graphene. (a-c) Top, side and 3D views respectively of *cis* and *trans* isomers of the molecule. (d) Multislice HAADF image simulation of the atomic model from (a). Bright white spots correspond to the heavy Pt atoms. (e-f) Line profiles of *cis* and *trans* form shown in figure (d), indicating Pt–Pt distances which is measurable at high resolution. (g–i) ADF-STEM image of molecules after photoactivation on graphene substrate. (j-k) Histogram of Pt–Pt distances with average standard deviation, measured in 28 isolated molecules before and after light activation respectively. (l-r) Molecular self-assembly of linear porphyrin hexamer on graphene. (l-m) Top and side view of the Pt-porphyrin hexamers on top of graphene. 1-3 denotes the amorphous carbonaceous layers on graphene. (n-o) High resolution images of the hexamers with stark contrast of heavy atoms. (p-r) ADF-STEM images showing hexamer epitaxial alignment and self-assembly on graphene, as highlighted with the yellow colour. Figures reprinted (adapted) with permission from: (a-k), ref.(96), © 2019 American Chemical Society; (l-r), ref.(97), © 2019, American Chemical Society.

Not only big organic compounds and ligands, but single light weight molecules have also been studied on graphene using TEM. In fact, TEM of the dynamics of molecular-scale adsorbates on graphene has been studied well since the beginning of research in graphene, which is not unusual, since studying molecules did not require as much of high resolution as

does the study of single atoms.(98) Much research has been carried out into characterizing the behaviour, stability and dynamics of different kind of organic molecules on graphene surface, such as carbon and other light adatoms.(19) One of the earliest studies described the structural reorganization of hydrocarbon adsorbates on graphene to initiate crystallization, in order to form amorphous carbon monolayers, through *in-situ* heating above 1000K.(99) In this investigation, Westenfelder et. al.(99) showed that graphene not only serve as a quasi-transparent substrate, but also as an in situ heater. The physisorbed hydrocarbons later form polycrystalline graphene at temperatures above 2000K. Other studies have also been carried out on small atoms and molecules such as H, O, NH_4, etc. to predict their mobility, diffusion and dynamics on graphene.(100,101) Such studies have the potential to lead the way to understanding diffusion barriers and chemical activity of single molecules on graphene for applications in graphene based catalysts.

2.3.5. Molecular Self-Assembly

STM studies have shown that the deposition of organic molecules on graphene can either lead to formation of well-ordered organic layers which are influenced by the epitaxy of graphene, or lead to charge transfer between the two materials.(102) The use of molecules and exploiting their self-assembly is a fast and scalable way to realize nanoscale architectures with tailored properties. A lot of research has been conducted on using graphene as a substrate to predict and control the synthesis of these 2D supramolecular organization.(103) Graphene can provide the 2D domain to control the surface-confined molecular states and their self-assembly. However, most of the research that's been carried out in the field in the past several years have utilized AFM or STM as the characteristic tool. Compared to other characterization techniques, imaging via high resolution TEM[20] can be used to study nanometer sized materials as well as very thin samples. And with the use of clean and transparent graphene substrate, the

[20] High resolution TEM is also abbreviated as HRTEM.

organic crystals and thin films can stay suspended during imaging. Here, the review will present the atomic level studies conducted on these self-assembly of molecules on graphene via high resolution TEM.

As we have already seen in the previous section, metals self-assemble on graphene when driven by high energy electron beam. Similarly, it has been reported that with the activation energy transferred, amorphous materials(104), adatoms or clusters(105) can also assemble into crystalline monolayers on graphene. Moreover, Borrnert et. al.(104) showed that with different high resolution imaging modes, amorphous carbon can show different behaviour on graphene under 80keV electron radiation. They showed that in the HRTEM mode, the amorphous carbon on graphene graphitizes in a planar manner due to the van der Waals interactions with the graphene underneath. However, in the STEM mode, the amorphous carbon supported on graphene evaporates off the surface or sometimes re-condenses in amorphous form, instead of graphitizing[21]. This provides a unique opportunity to use different imaging modes for fabricating unique quasi-2D materials and explore their morphologies. The interesting thing to note is that graphene can influence the alignment and packing structure of the organic molecules. Thin film behaviour of strained pentacene film was studied on graphene as a molecular assembly template by Kim et. al.(106) The crystals of pentacene showed directional morphology where they were mostly aligned in one direction. They also showed two distinct molecular packing structures of pentacene, including a new polymorph phase which has never been studied before. Kim et. al. deduced that the unusual polymorph could potentially exhibit enhanced transport in the vertical direction of pentacene-graphene system owing to the shorter vertical distance in the strained crystal. This demonstrates a possibility to

[21] In contrast to HRTEM mode, in the STEM mode, the amorphous carbon can also evaporate. This phenomenon occurs because in STEM, a raster scanning process is used where the high intensity beam hits a small surface leading to removal of amorphous carbon from the surface. Amorphous carbon has also been shown to graphitize in STEM mode, but that happens when the sample is heated *in-situ*.

study and control the packing and strain of molecular crystals on graphene. Similar results on supramolecular assembly of benzene-1,4-dicarboxylic acid (TPA)[22] and benzene-1,3,5-tricarboxylic acid (TMA)[23] on graphene have been reported in literature.(107) Both these molecules were found to self-assemble on graphene to form well-ordered crystals all the way up from atomically monolayer sheets to thin 3-D films with thickness of several nanometers. The authors speculated the epitaxial structure and orientation of these molecules is a result of both inter-molecular hydrogen bonding as well as their interaction with graphene. In a subsequent study carried out by Robertson et. al.(108) on metal-ligand interaction, they synthesized PbTe nanocrystals terminated with oleic acid and trioctylphosphine and studied their behaviour via TEM. They found that the PbTe nanocrystals self-assembled to form packed arrays of HCP structure. The authors then conducted ligand exchange on the surface which resulted in disintegration of the HCP crystalline structure into irregular agglomeration of nanocrystals. The results show that use of graphene can help broaden our understanding of self-assembly while also facilitating controlled manipulation of their structures, tailored to our use.

2.3.6. Metal-Graphene Interaction

High resolution microscopy, especially HAADF-STEM can be employed to study activity of heavy metals, their dynamics in 2-Dimension and interactions with graphene.(109) Westenfelder et. al.(110) found the first phenomenon of atomically resolved structural reorganization of novel gold structures on graphene upon *in-situ* heating. They found periodic arrangements of monolayers and bilayers of gold atoms on graphene as they form rectangular atomic structure at temperatures up to 1300K. Here. graphene served as a transparent substrate to monitor the formation of gold monolayers, in situ heater, and also as a source of carbon

[22] TPA: benzene-1,4-dicarboxylic acid or also known as terephthalic acid
[23] TMA: benzene-1,3,5-tricarboxylic acid or also known as trimesic acid

which led to the formation of crystalline zincblend structures of gold and carbon compound. Many studies have been conducted on studying the dynamics of single metals on 2D surface and their self-assembly by using graphene as a substrate and *in-situ* heater, such as, translation motion of Fe atoms on graphene (111,112), migration of individual Au ad Pt atoms(113), nanoclusters formation and motion of individual Pb and Te atoms(114), formation of Au nanostructures(115), HCP[24] packing of Co on graphene(116) and defects and interface of Si nanocrystals(117). Some of the structures and dynamics are shown in **Figure 2.5**. The common observation that can be drawn from all these results is that the metal particles diffuse easily on the surface of graphene to only end up being stable at either the edge of graphene or on the amorphous carbon layers on top of graphene. They also tend to aggregate to form monolayer 2-D structures, either driven by electron beam or heated *in-situ*.

[24] Hexagonal close packing

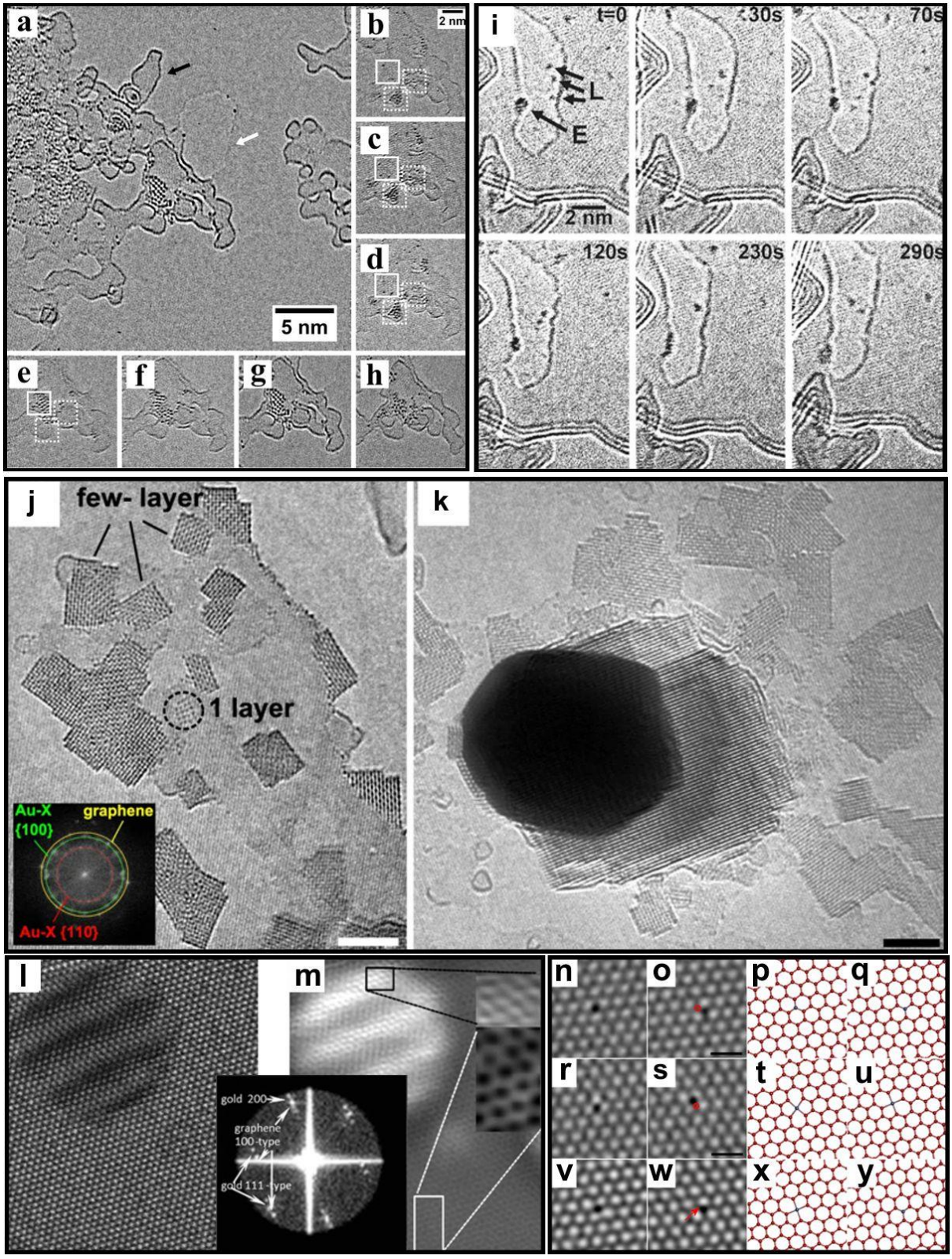

Figure 2.5. (a-h) AC-TEM image of the graphene showing (a) heavy atoms on top and (b-h) time sequence of translation motion of Pb and Te atoms aggregating together on graphene. Time frame between two images is 10s. (i) Sequential images showing Pt atoms diffusion on graphene at 600^{o}C. The region marked with 'L' shows 2-dimensional migration of Pt whereas the region marked with 'E' shows the dispersion of Pt atoms along the edges of graphene. The time frame between two images is indicated in the image. (j-k) AC-HRTEM image at 80keV

of 1-2nm sized cubic structures of Au-X monolayer structures formed at 1300K (j) and a thicker new 3-D structure growing on the Au particles, serving as a feedstock for Au. Scale bars correspond to 2nm. (l-m) Au clusters on graphene, revealed by Moire effects in images taken by atomic-resolution BF-STEM (l) and Noise-filtered HAADF-STEM (m). The bottom inset shows the FFT of the HAADF image that was used as a low-pass filter for (l). The top inset shows the Au/graphene lattice orientation relationship. (n-y) AC-TEM images showing the mobility of Fe atoms and their corresponding atomic models. Red circles or arrows correspond to the position in the previous frame. The color blue in the atomic models correspond to Fe. Figures reprinted (adapted) with permission from: (a-h), ref.(114), © 2014 The Royal Society of Chemistry; (i), ref.(113), © 2008 WILEY-VCH Verlag GmbH & Co.; (j-k), ref.(110), © 2015, Springer Nature; (l-m), ref.(115), © 2011 WILEY-VCH Verlag GmbH & Co; (n-y), ref.(111), © 2013 American Chemical Society.

Surface defects can be quantified by EPR[25](118) but only TEM imaging can exactly determine the type, number and exact location of defects in the lattice structures of the metal particles. Aside from the nanocrystal formation and motion of the particles on the graphene surface, there are other phenomenon that can occur between the nanoparticles and graphene, such as e-beam driven effusion, rotation or structural change.(119,120)

Other interesting observations of metal atoms, such as crystalline phase transition and rotations(121), local strain accumulation(122) and epitaxial orientation of self-assembled metal particles(123) on a 2-D surface (provided by graphene) have been carried out systematically using aberration corrected high resolution TEM. A series of results on Au nanobelts on graphene were were published by Xin et. al.(124–126) to investigate their structure, growth mechanism and kinetics of nanoplate formation using TEM. These results provide insight for using TEM for studying behavior of metallic atoms on a plane and fabricate dimension-controllable metal nanocrystals to inspire development in the field of graphene-based nanocomposites and catalysts.

2.3.7. Nanoparticles and Clusters

Aside from single atom metals and organic molecules, a vast range of nanoparticles, clusters and oxides have also been studied on graphene via TEM and have also been reported

[25] Electron Paramagnetic Resonance

to show various range of phenomenon such as rotation and translation motion, alignment, effusion, etc. when irradiated by e-beam. Warner et. al.(116) showed that electron beam irradiation provides the energy to $CoCl_2$ nanocrystals to exhibit both rotational and translational motion on graphene. The authors claimed that the coalescence of the nanocrystals, when driven by the e-beam, indicates that the energy imparted through the e-beam leads to heating up of the region that in turn promotes continual rearrangement and formation of uniform crystal structure. Similar observation of cluster rotation driven by e-beam was reported by Chen et. al.(127) on crystalline anisotropic nanoclusters. The clusters containing 6-10 Si atoms showed out-of-plane rotation and eventually lined up in rows to achieve stable Si-C bonds. Aside from rotation, dynamic effusion has also been reported in ZnO and CuO nanoparticles when they are trapped in few layer graphene folds.(128) It is interesting to note that the effusion process of these two nanoparticles was found to be distinctly different, where CuO transverses on amorphous phase before effusing out of the rupture in graphene and recrystallizing outside, whereas ZnO maintains its crystalline structure throughout the effusion process out of the graphene by gliding through the vacancies and dislocations. In addition, the crystalline phase of the ZnO changes from the wurtzite to graphene-like ZnO phase after the effusion. These results shed light upon the interface between metal oxide and graphene and their interactions with the e-beam. Apart from cluster motion and effusion under e-beam, thin layers of other materials can also grow on graphene when irradiated under e-beam. Hong et. al.(129) showed that monolayer ZnO layer can grow heteroepitaxially, atom by atom, when irradiated with e-beam. They speculated that formation energies of ZnO, especially at the O- and Zn- terminated edges, decreases rapidly as the growth step increases. This study could lead to a new class of 2D lateral heterostructures, fabricated with high spatial control over epitaxial growth.

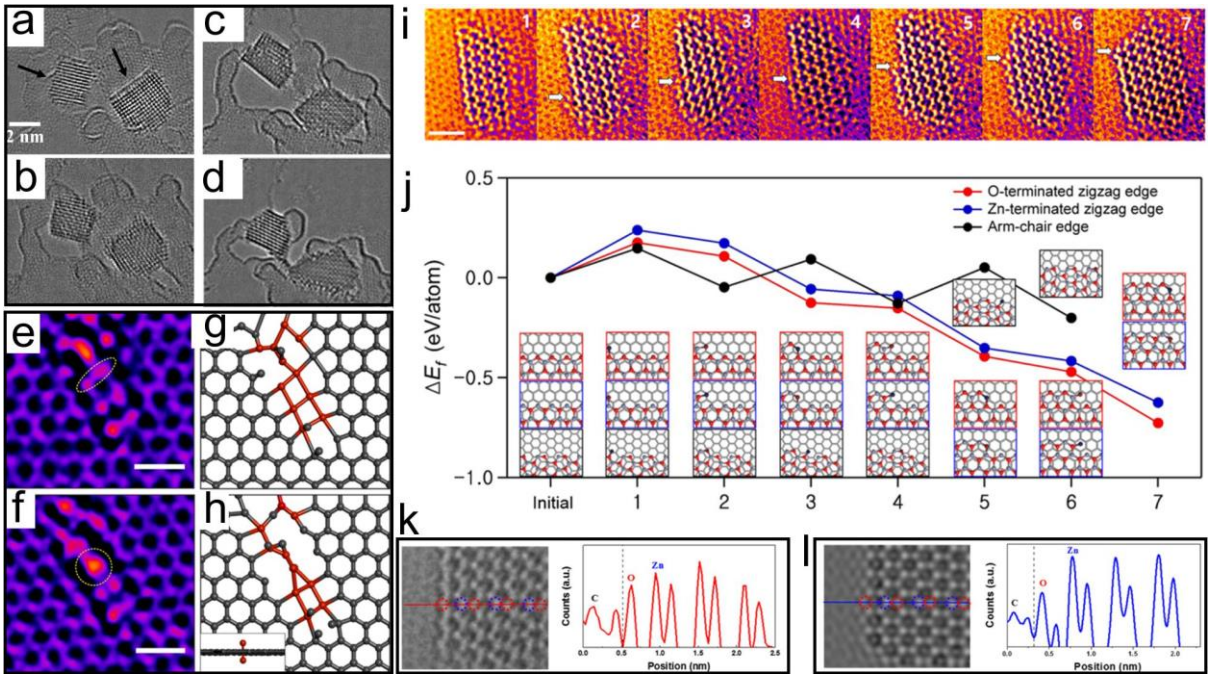

Figure 2.6. (a-d) Sequential time-frame of HRTEM images, taken every 20s, of $CoCl_2$ nanocrystals, showing their rotating on graphene. Graphene lattice has been removed by 2D FFT filtering. (e-h) Si nanocluster and out-of-plane rotation of Si atoms showing small Si nanocrystals in (e) and its atomic structural model in (g), two Si atoms rotating highlighted in yellow in (f) and its atomic structural model in (h). Time duration between (e) and (f) is 8s. Scale bar corresponds to 0.5nm. (i-l) Lateral growth of ZnO over graphene along the zigzag edges. Sequential time-frame TEM images showing growth of epitaxial ZnO in from fram 1 to frame 7 in (i). The scale bar corresponds to 1 nm. Relative formation energy (i.e., $\Delta E_f = E_{f\_growth\ step} - E_{f\_initial}$) of the growth of monolayer ZnO with O- and Zn- terminated zigzag and armchair edges in (j). Red, blue and grey balls correspond to oxygen, zinc and carbon atoms (from graphene) respectively. (k-l) Raw image of part a at final step 7 and its image simulation respectively. Intensity profile shows the intensity from the experiment (red line) and the image simulation (blue line) respectively. Figures reprinted (adapted) with permission from: (a-d), ref.(116), © 2009 American Chemical Society; (le-h), ref.(127), © 2015 American Chemical Society; (i-l), ref.(129), 2016 American Chemical Society.

2.3.8. Free Standing Monolayers

Graphene is known to have defects.(130) Nanopores can be created in graphene either during synthesis or when the defects congregate under the exposure to e-beam. These nanopores show some stability and the smaller ones have been reported to be often stabilized by light weight atoms such as H and Si that act as a bridge between the dangling bonds around the perimeter of the hole.(131) The interesting phenomenon to note in graphene substrate is that even these defective regions in graphene can contribute to the formation of monolayer atomic thick metals or metal oxides. Zhao et. al.(132) showed that Fe atoms gets diffused on

the surface of graphene to the edges and then self-assemble in a graphene nanopore to form freestanding crystalline single-atom-thick layer with either BCC[26] or HCP[27] structure, as shown in **Figure 2.7**a-g. The diffusion of Fe on graphene membrane can be said to be largely electron driven. Even metal oxide showed similar phonomenon when introduced to graphene system.(128,133) When driven by the e-beam, small clusters of CuO_x forms monolayer CuO nanosheets with a square Cu sub-lattice. The sheets were formed on graphene as well as suspended in a graphene nanopore, as shown in **Figure 2.7**l-n. The authors used theoretical calculations to predict that standing CuO monolayers have indirect band gap of around 3eV, which is significantly higher than bulk CuO whose indirect bandgap is of around 1.5eV. By employing precisely controlled e-beam to sputter atoms, if half of the O atoms are further removed from the CuO crystal cells, then CuO may transform into free standing monolayer Cu_2O, which is another stable material but with a direct bandgap. Manipulation and tuning of the structural morphologies of such materials holds promises in applications in the area of optoelectronics. Similar findings of membrane formation, restructuring and atomic diffusion was found for freestanding monolayer and bilayers of ZnO on graphene.(128,133) Structure of planar ZnO had been predicted theoretically and studied via STM(134,135) on a surface but the study of freestanding monolayer ZnO via TEM sheds light upon its actual lattice parameter, structure and stability.(133) Similar to what has been observed for Fe and CuO membranes, the ZnO sheet was also found to be relatively stable under electron irradiation, as shown in **Figure 2.7**o-v. Ta et. al.(128) also showed that when ZnO is introduced to graphene, it can effuse out of the material through small rupture to then also form free standing monolayers. Theoretical works conducted on the free standing 2D metal monolayers in graphene nanopores predict that the metal monolayers can be stable in area up to $\sim 8\ nm^2$ areas and serve as a

[26] Body-centrerd cubic packing
[27] Hexagonal close packing

platform for a number of applications such as catalysis, bioimaging, photovoltaics, sensing, etc.(136) Actual experimental work on this area would pave way for formations of potentially novel 2D structures within the graphene membrane.

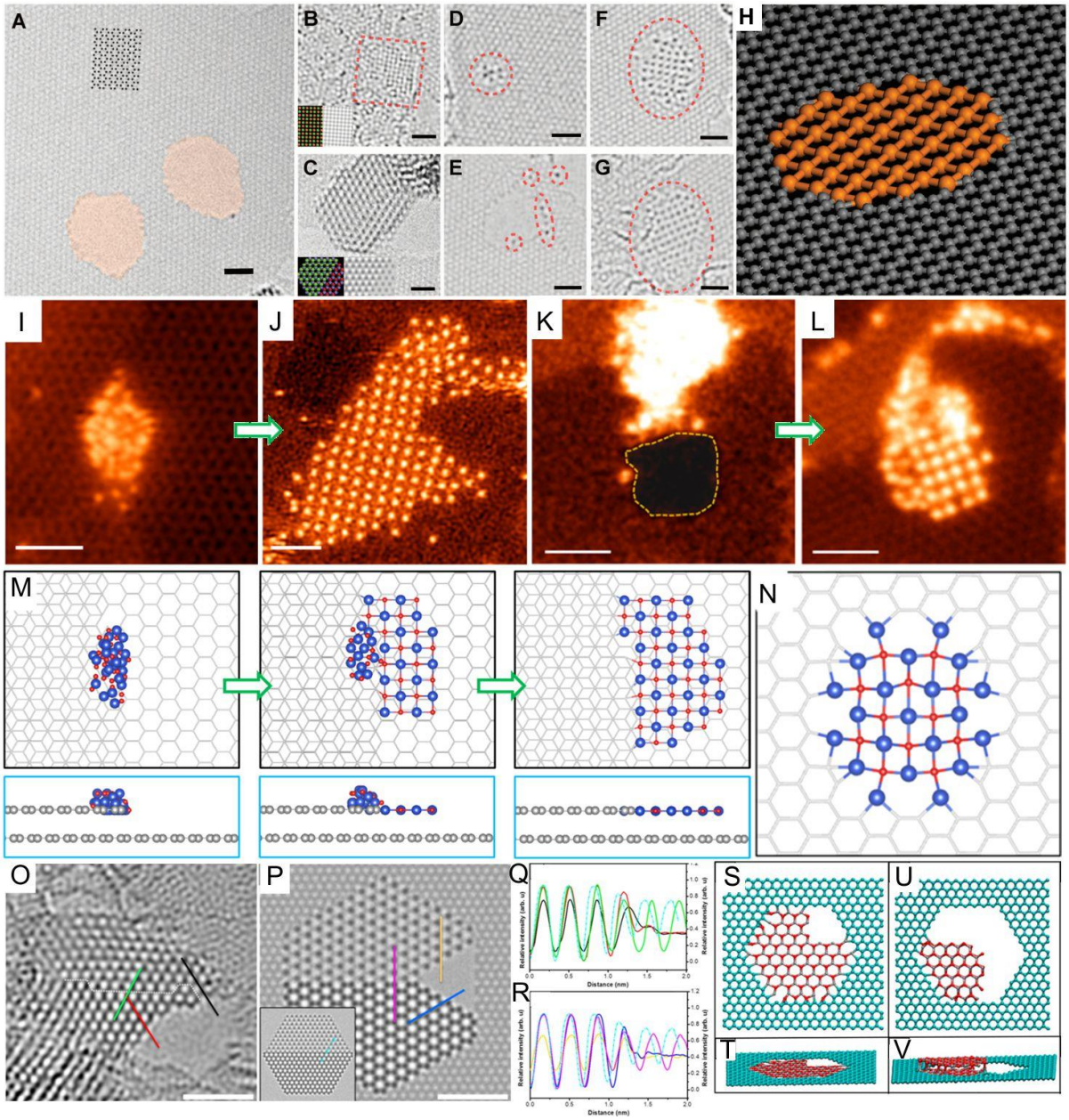

Figure 2.7. (a-h) TEM images of free-standing Fe monolayers on graphene nanopores taken at 80keV acceleration voltage. Graphene nanopores are highlighted in (a), BCC type monolayer Fe packing in (b), HCP type monolayer Fe packing in (c), clusters of atoms embedded in graphene in (d), individual Fe atoms at the edges in (e), free standing Fe monolayers suspended across graphene nanopore in (f-g) and schematic atomic model of monolayer suspension of Fe atoms in graphene (h). All scale bars correspond to 1nm. (l-n) CuO monolayers on graphene surface. ADF-STEM image of CuO_x clusters at the step edge of graphene (l) restructuring into monolayer CuO sheets (j) and CuO_x cluster at the edge of a graphene nanopore (k) diffusing into the nanopore to form freestanding CuO monolayers in

the nanopore (l). Schematic atomic model with top and side view showing the formation process of CuO monolayer on top of graphene (m) and a theoretical model of a freestanding CuO sheet. The blue, red and grey balls correspond to copper, oxygen and carbon respectively. Scale bars correspond to 1nm. (o-v) Free-standing mono- and bi- layer ZnO membranes. TEM image (o) and its image simulation (p) of mono and bilayer ZnO regions. Inset in (p) shows the quartzite structure. Normalized intensity profiles (q-r) for the experimental image and its simulation respectively showing bi-monolayer (green/pink line), bilayer in vacuum (red/dark blue line), monolayer in vacuum (black/yellow line) and wurtzite structure in the inset (light blue/light blue line) respectively. Top view and 3D view of DFT simulated free-standing monolayer (s-t) and bilayer (u-v) ZnO growth on graphene. All scale bars correspond to 2nm. Figures reprinted (adapted) with permission from: (a-h), ref.(132), © 2014 American Chemical Society; (l-n), ref.(105), © 2016 IOP Publishing Ltd; (o-v), ref.(133), 2016 American Chemical Society.

2.3.9. Electrocatalyst

In the emerging field of heterogenous catalysis, where the phase of the catalysts are different to the phase of the reactant or products, the structural parameters of a catalyst play a huge role which directly affects its catalytic performance.(137) These parameters include the size and shape of the catalyst, its chemical composition and accurate atomic structure, bonding between the atoms, charge transfer within and outside the catalyst, etc.(137) With the advent of HAADF-STEM, it has become feasible to easily and directly image catalytic nanometal particles or clusters, which gives a lot of information about their size,(138) structure,(139) composition,(140) numbers and distribution on the surface(141). As most of the catalyst nanoparticles consist of heavy metal atoms, HAADF-STEM is especially beneficial to carry out their characterization(142) as the image intensity is proportional to the atomic number square (Z^2) leading to bright Z-contrast. Moreover, STEM also provides precise mapping of the positions of the atoms on the substrate, especially if the substrate is graphene, whose thinness allows feasible mass measurement of individual atoms or clusters.(143)

Another important parameter affecting the catalytic performance is its interaction with the surface layer or the support material and this is yet another avenue where the use of graphene can yield interesting results. The large surface area, chemical stability and electrical conductivity of graphene also makes it an attractive substrate for single atom electrocatalysts.

Nanocatalysts, whose electrochemical activity is closely connected to the substrate interaction, can be studied easily on top of graphene and the catalytic reactions can also be studied using *in-situ* STEM observations on top of thermaly stable graphene.(144)

Some studies have also indicated direct graphene interaction with nanocatalysts. Miramontes et. al.(145) used STEM to characterize and configure atomic clusters of Rhenium, up to 2-13 atoms per unit and studied their octahedral and tetrahedral morphologies to predict more complex morphologies on top of graphene. They indicated that higher catalytic effect could be expected when these Re clusters where adsorbed on graphene, as compared to individual atoms. Similar study by Bulusheva et. al.(146) proposed that pyridine-type nitrogen atoms located at the edge of graphene sheets were essential to stabilizing single atom catalysts on graphene substrate. This not only changed the interactions of the metal species with the graphene support, but also changed the electronic state of the catalysts. These results are very useful to study further control of the chemical activities of nanocatalysts, either as a single atom or in clusters, with the use of graphene. Numerous other studies of single atom metal and clusters catalysts supported on graphene substrate have been conducted via HAADF-STEM till date, such as, Re(145), Pt-group metals(146), Pt(146–148), Pt clusters(149), Pd(150), Pt/Pd particles(151), Ru(152), on their synthesis, characterization and applications.

2.3.10. Liquid Cells

Liquid-cell TEM has historically been very important in carrying out ground-breaking research in understanding the kinetically dominated nanocrystal reactions(153) and their growth, nucleation and other dynamic activities,(154,155) as it allows for the direct imaging of the structural transformations at single atomic level in a liquid.(156,157) It has also been used for studying numerous other dynamic activities of nanomaterials in hydrated state including, and not limited to, their morphology, structural evolution, intermediate self-

assembly stages, etc.(158) Pu et. al. published a review article describing the different architectures used till date to fabricate liquid cells for microscopy purposes (**Figure 2.8**).(159)

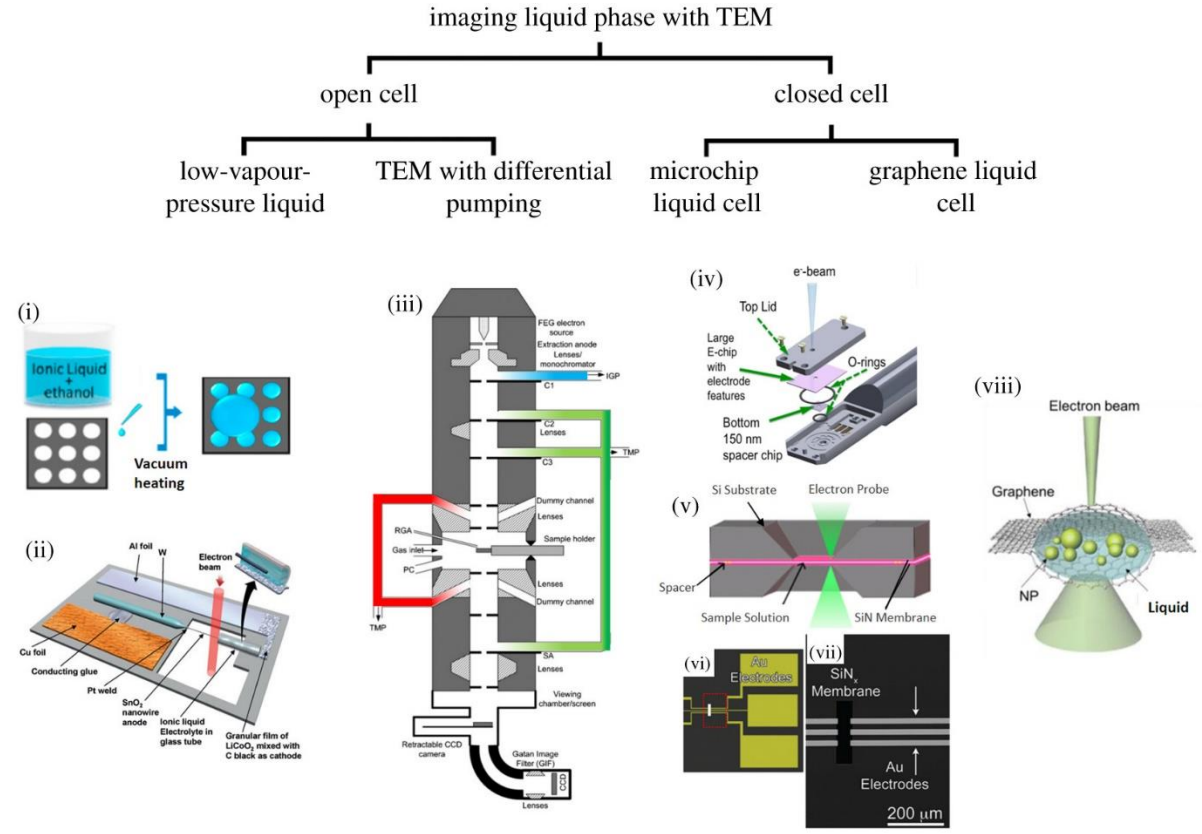

Figure 2.8. Schematic showing different architectures of liquid cells being used for the purpose of liquid phase TEM imaging. (i) Ionic liquid films stabilizing on micrometre-sized holes through surface tension interaction. (ii) Miniature battery sized liquid cell with ionic-liquid electrolyte. (iii) Differentially pumped TEM column with three different pumping stages. (iv) *In situ* liquid TEM stage on the tip of a TEM holder. (v) Silicon/silicon nitride chips assembled liquid cell. (vi) microfabricated electrodes mounted on silicon chip. (vii) Magnified SEM image of the boxed region in (v). (viii) Graphene liquid cell with two graphene sheets for encapsulation. Figures reprinted with permission from: ref.(159), © 2020 Royal Society.

Amongst all the approaches, the use of graphene as a window material for the fabrication of liquid cells, also known as graphene liquid cells (GLCs), has been used extensively and has consistently been proved to be a better candidate than conventional windows for high resolution imaging of beam-sensitive specimens.(87) The architecture of such cells comprises of only layers of graphene to encapsulate liquid specimens. In addition to the properties of graphene that make it an excellent substrate for TEM, its highly

impermeable property doesn't even allow small helium atoms to permeate.(160) Moreover, the graphene sheets are highly inert and flexible and show strong van der Waals interaction to tightly wrap around the liquid inside(161,162) whilst at the same time withstanding the massive amount of pressure difference within and outside the liquid cell.(21) Therefore, the use of graphene also provides a wider variety of choice in terms of using different kinds of liquid whilst at the same time providing the ability to carry out microscopy using the usual TEM holder. The exceptional spatial resolution provided by the use of the ultrathin material opens doors for studying nanostructures dynamics at an atomic scale in a liquid environment.(161) For instance, Hauwiller et. al. recently showed exciting etching phenomenon on gold nanocrystals in GLCs, shedding light upon the presence of high-energy intermediate shaped in a kinetically controlled reaction which was not known previously.(60) As a result, there's been a massive progress in this field of GLCs in the past few years, leading to understanding towards the dynamic behaviours of nanomaterials inside a liquid.(163)

GLCs have also facilitated exciting research and findings in the field of nanoscience, such as crystallization and *in situ* crystal growth,(164) nucleation and shape formation of crystals,(165) study of molecular structure of water and ice,(166) lithium transfer in battery materials,(167) high resolution study of beam-sensitive biological cells,(168) study of intermediate states during the self-assembly of DNA double helices(169) and exceptional spatial resolution study of nanocrystal etching on a single particle level.(170)

One of the biggest advantages of graphene based liquid imaging is that it allows the highest possible resolution, whereas at the same time providing a flexible covering to the liquid inside. It has been especially shown to have brought deep understanding in the area of beam sensitive biological specimens(171) and atomic scale reactions occurring in new energy materials through the study of *in situ* TEM of anodes, cathodes and lithium transfer.(172) Graphene cells combined with emerging microscopy techniques have the potential to study

new science and shed light on the dynamics of nanostructures at the lowest possible atomic scale.

2.4 Conclusion

Experiments have shown exciting results on the dynamics, chemistry and behaviour of nanomaterials in TEM facilitated by the use of graphene as a substrate (**Figure 2.9**). The work carried out in this field also provides new avenues of research in the area of graphene-hybrid materials and their interactions with the e-beam, especially with ADF-STEM. Electron beam driven chemistry in and around graphene demonstrates how it can also serve as a platform for growth of new nanocrystals and in-plane epitaxial alignment of molecules. This is one of the applications of graphene where it actually proved to be facile to handle and superior to other substrates currently in use. It is astonishing how much has already been achieved in the field which is only a few years old. One can anticipate many new exciting e-beam reactions, without the use of any other external stimuli, which would ultimately allow studying and engineering of new heterosstructures inside TEM with the use of graphene.

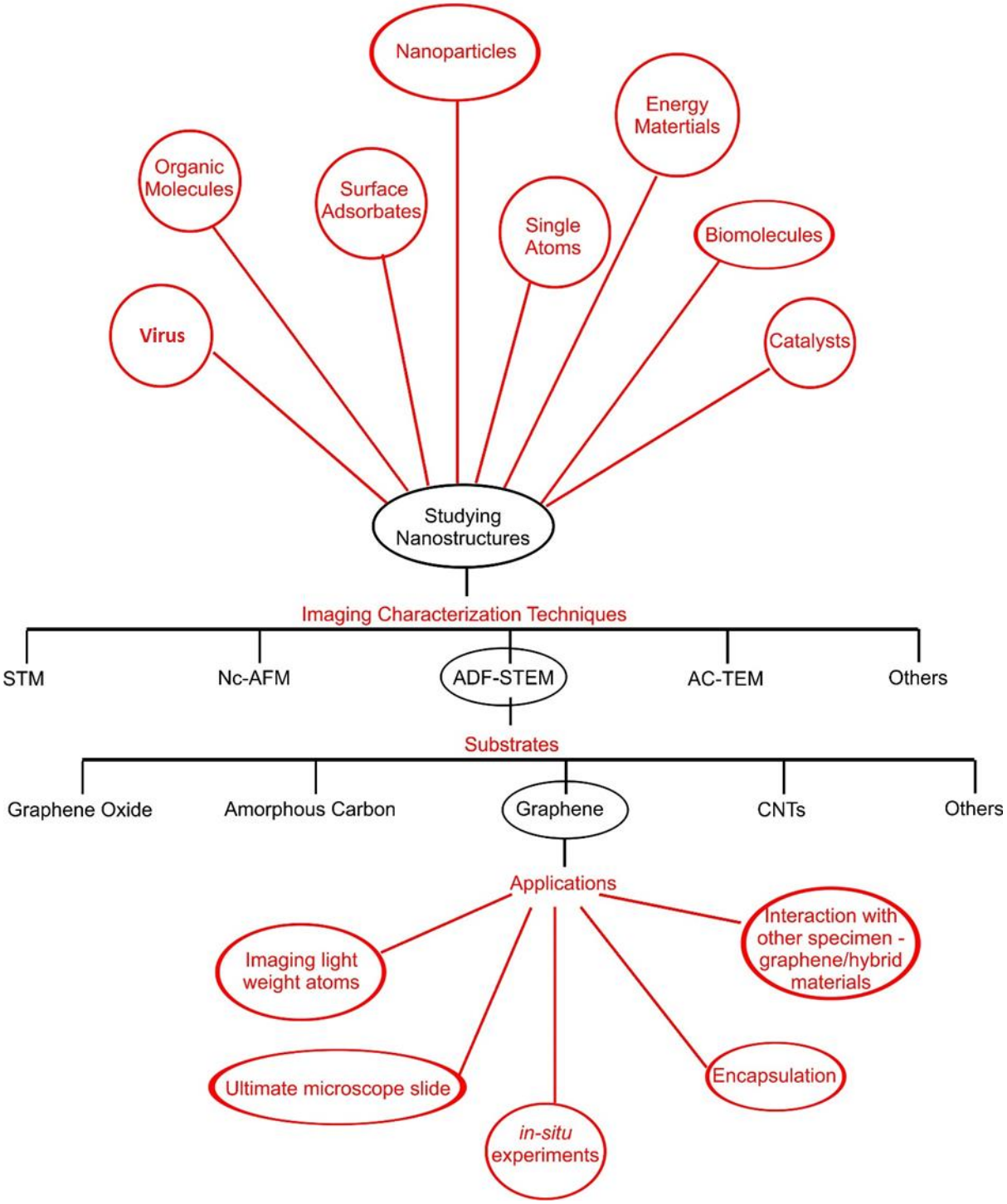

Figure 2.9. Schematic diagram of the study of nanostructures.

Chapter 3 Methodology

3.1 Introduction

The purpose of this chapter is to introduce the instruments, experimental setup and techniques used in this research project. The chapter covers the synthesis and transfer of different nanomaterials (fullerenes, graphene and PbI_2) and the various instruments used for their characterization. The last section covers the details and parameters used for electron microscopy and data processing.

3.2 Fullerenes: Synthesis, Extraction & Purification

This section describes the instruments and methods used for synthesizing and isolating different types of fullerenes.

3.2.1. Arc Discharge

Out of the limited ways to produce fullerenes, the large-scale production has only been carried out by Kratschmer-Huffman arc method(173), as shown in **Figure 3.1**. The arc-discharge machine used for synthesizing fullerenes was developed in Prof. Porfyrakis lab at the University of Oxford. Two electrodes inside the chamber act as anode and cathode and produce an electric arc in presence of high current and helium and lead to formation of carbon soot which contains different types of fullerenes, as well as carbon nanotubes. The arc chamber was first evacuated to low pressure since Oxygen is known to be detrimental to the formation

of fullerenes[28]. Subsequently, Helium was flushed into the chamber in order to remove the small traces of other air molecules present in the chamber. Helium also serves two more purposes. It facilitates collisions between carbon atoms for the formation of fullerene cages, and since it is small and inert, it does not take part in any reactions. One of the rods was doped with Lanthanum oxide (La_2O_3), which was used as the anode and another graphite rod with pure carbon was used as cathode. The dimensions of the rods used were 10 cm x 1 cm. Subsequently, the rods were aligned together in a close proximity to each other and then a DC current of around 200 – 250 A was applied, creating an electric arc between the electrodes and leading to very high temperatures at the arc point (as high as 3000-4000℃ in the presence of helium. As a result, the rods began to vaporize and different kinds of fullerenes (and other carbon materials) were deposited in the form of carbon soot on the inner walls of the arc chamber. The process was stopped after ~30 seconds since the continuous high temperature is a melting risk to the Teflon tube lining inside the chamber. The chamber is continuously cooled down with water flow and the arc process is repeated again after ~10-15 minutes. It takes almost 2 hours to burn one single 10 cm length La-doped graphite rod.

Doping concentration of the metals in the graphite rods is very important to get desired fullerenes. For instance, 0.8% (KM8) metal doping makes the monometallofullerene, such as $La@C_{82}$, but with 1.6% (KM16) doping of most synthetic metal would produce dimetallic fullerenes, such as $Y_2@C_{80}$. The focus of the research project is on monometallic fullerenes, hence, 0.8% La-doped graphite rods and 0.8% Y doped graphite rods were used for producing the $La@C_{82}$ and $Y@C_{82}$ metallofullerenes respectively. However, even though the method is known to produce scalable quantities of fullerenes, the overall yield of the endohedral metallofullerenes (EMFs) is still extremely low, at around 1% - 2% of all the fullerenes

[28] Oxygen is detrimental to the formation of fullerenes in the arc-discharge process because of its high reactivity.

synthesized in the process. One of the goals of this research project is to optimize the parameters in order to increase the yield of the EMFs in the carbon soot produces by arc – discharge, as discussed in more detail in **Chapter 4**.

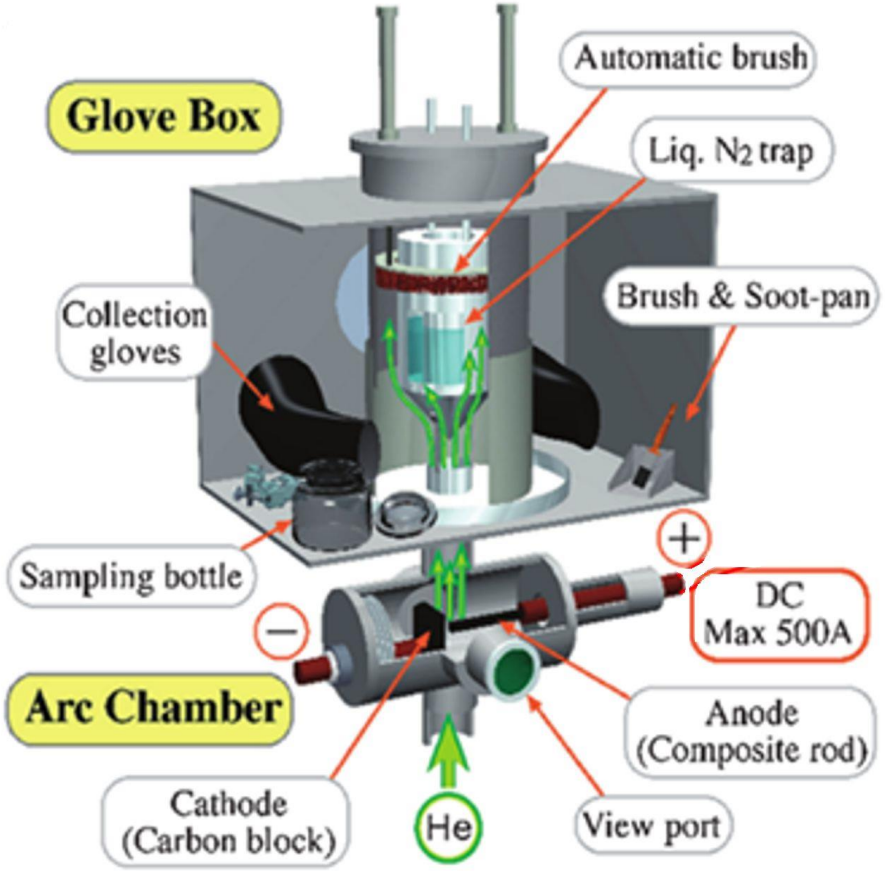

Figure 3.1 A schematic diagram of a typical arc-discharge apparatus used for synthesizing fullerenes. Figure reprinted with permission from: ref.(174), © 2007 The Japan Society of Applied Physics.

3.2.2. Extraction

The carbon soot obtained from the arc-discharge is very impure and contains amorphous carbons, carbon nanotubes, oxides, etc. along with different types of fullerenes. Therefore, it becomes necessary to extract the fullerenes and the EMFs. The most commonly used extraction method is soxhlet extraction process which has been schematically described in **Figure 3.2**. The carbon soot is placed in the extraction thimble inside the extraction chamber, which contains the extraction solvent of choice. The thimble is connected to the receiving flask and acts like a filter where the solvent flows through to the refluxing apparatus. There is a

siphon mechanism that is used as a control and empties the solvents from the thimble after a given amount of solvent. The receiving flask is set at a temperature that slowly evaporates the given solvent and the whole setup is left for about 24-48 hours (175,176) depending on the amount of soot. After the process, the boiler temperature is brought down to room temperature and the solvent left in the receiving flask contains all the fullerenes extracted from the soot. The solvents used for this project are toluene, DMF[29], o-DCB[30], aniline and o-xylene.

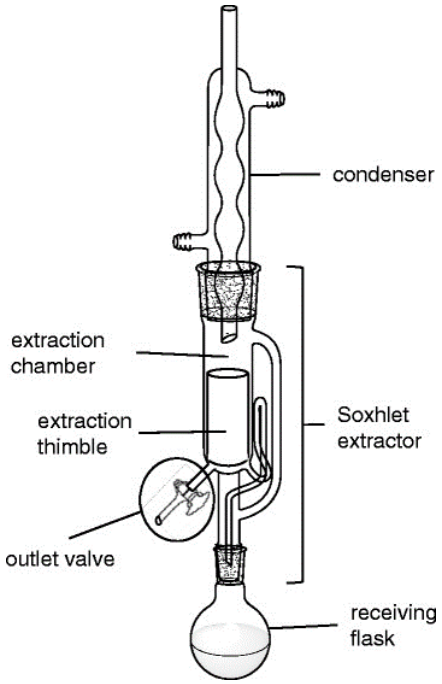

Figure 3.2. Schematic diagram of soxhlet extraction. Figure reprinted from: ref.(177), © 2017 Discoverfoodtech.

3.2.3. High Pressure Liquid Chromatography

High Pressure Liquid Chromatography (HPLC) is a powerful tool that has almost always been used for the separation and purification of the metallofullerenes from the dozens of other fullerenes that are contained in the carbon soot. The method is based on pumping mobile phase through a chromatography column, which is similar to conventional chromatography but with higher pressure. The key component for HPLC separation is using

[29] $(CH_3)_2NCH$, also known as Dimethylformamide.
[30] o-dichlorobenzene

the right column. In case of fullerene separation, HPLC separation exploits the fact that different kinds of fullerenes, dissolved in a certain mobile phase[31], have different degrees of interaction with the stationary phase in the column.(178) There are many different factors that affect the degree of interaction, such as polarity, difference in mass, etc.,(179) which in turn determine the retention time of a particular fullerene in the chromatography column. Therefore, when all the other parameters, such as flow rate, solvents, etc., are kept constant, then different fullerenes in the mobile phase elute and get separated at different known retention times. **Figure 3.3** shows the schematic diagram of our HPLC system. The HPLC system used for the work is based in Porfyrakis group at University of Oxford. It is called JAI LC-9103, used together with a Hitachi L-7150 pump. For all the experiments based on HPLC, COSMOSIL Buckyprep-m column (20x250 mm), manufactured by Nacalai tesque Inc., was used. The column consists of silica functionalized with aromatic organic group (phenothiazinyl) which serves as an excellent solid adsorbent material for different interactions with different types of fullerenes. Whilst passing through the column, a 312 nm wavelength UV detector is used to measure and record the intensity of the retention time of the fullerenes. The resulting data continually gets recorded in a data analysis software called Azur. All the HPLC process for this work has been carried out at room temperature.

Fullerenes are first dissolved in an organic solvent, which serves as the mobile phase. The solvent used for this project is toluene, unless other stated. The solvent is then inserted into the HPLC system manually, 2.5mL at a time, via a syringe and left to run through the chromatography column. A PTFE filter was used during injection to prevent solid particles from getting inside the HPLC system, and flow rate of 16mL/min was used to give a pressure of around 70-95bar. The retention peaks in the system show the interaction of different fullerenes within the chromatography column and are thus collected at the exit manually at

[31]Generally, an organic solvent is used as a mobile phase.

different times. The metallofullerene is obtained by eluting at the retention time of ~20min. In addition to separation, the amount (mass) of different types of fullerene going through the system can also be characterized by looking at their strong retention peaks and the area under each peak.

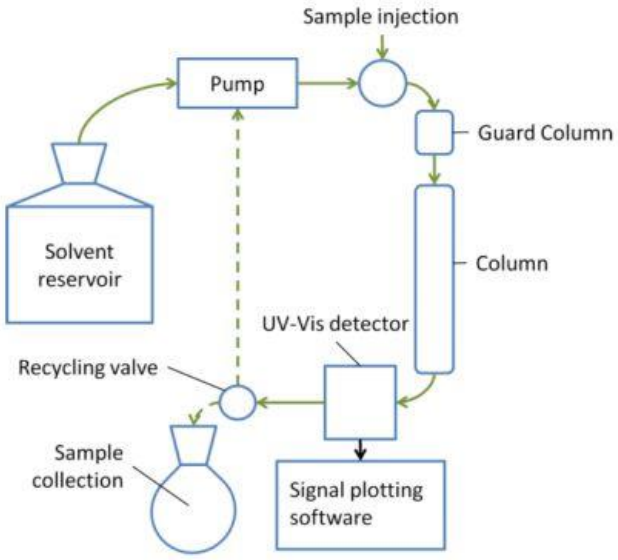

Figure 3.3. Schematic diagram of the an HPLC system. Figure reprinted with permission from: ref.(180) © 2013 Bodleian Libraries.

3.3 2D Materials synthesis & transfer techniques

3.3.1. CVD Graphene: Synthesis

Graphene was synthesized by chemical vapor deposition (CVD) on a copper substrate. A piece of copper foil was first sonicated in a diluted hydrochloric acid solution (HCl, 1 mol/L) to remove the oxides on the copper surface. The copper foil was then sonicated in DI water, acetone and isopropanol (IPA) for 5 min each to remove organic residues. To ensure uniformity of temperature during the whole growth process, the copper foil was positioned in the center of a furnace. 1% methane in argon (CH_4), 25% hydrogen in argon (H_2), and 100% argon (Ar) were used for graphene synthesis. Before the reaction started, the system was first purged with 1000 sccm Ar, 500 sccm H_2, and 100 sccm CH_4 for 30 min. The furnace was then heated to 1060 °C with a ramp rate of 50 °C/min accompanied by a flow of 500 sccm Ar and

100 sccm H_2. When the temperature reached 1060 °C, the copper was then annealed with the same flow rate for 1 hour. Following the annealing process, the synthesis was carried out at 1060 °C for 1 hr with a flow of 500 sccm Ar, 100 sccm H_2, and 5 sccm CH_4. After the synthesis, the furnace was removed from the sample, which allowed the sample to be fast cooled to room temperature.

3.3.2. CVD Graphene: Transfer for TEM sample preparation

In order to resolve single atoms on a graphene support, it should be exceptionally clean and thus, the transfer process has been optimized to yield impurity-free freestanding graphene on a TEM grid. Graphene grown by CVD was transferred onto the TEM grids (Cu TEM 400 mesh grid, SiN grids, DENS SiN *in-situ* heating holder), by the following process, to give suspended areas suitable for ADF-STEM imaging. Graphene was spincoated with PMMA, as PMMA acts like a support. Subsequently, the copper underneath graphene, was etched in ammonium persulfate (APS)[32] solution for 12hrs. After removing copper, graphene was transferred onto TEM grids with the help of the PMMA support. The graphene transferred onto the substrate was vacuum annealed at 150^{o}C for 3hrs. PMMA was then removed by keeping it in acetone at 45^{o}C for 12hrs. Graphene was then subsequently cleaned by Ar/H_2 and vacuum annealing to remove the possible impurities from the transfer process. The methodology has been described in the schematic in **Figure 3.4**.

[32] Ammonium Persulfate ($(NH_4)_2S_2O_8$)

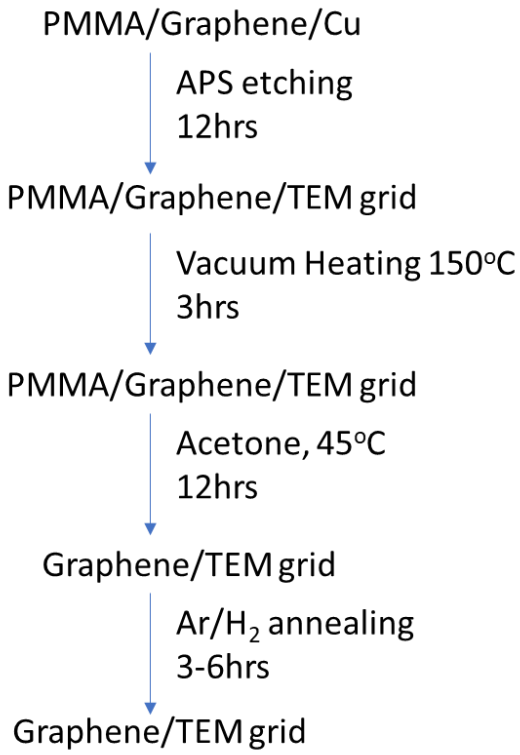

Figure 3.4. Schematic of the graphene transfer procedure.

3.3.3. PbI_2 Liquid Exfoliation & Transfer

PbI_2 powder from Sigma – Aldrich (99% purity) was added to solvents to form a solution of concentration 1 mg/ml (~ 0.2mM). The solution was sonicated in an unheated ultrasonic water bath (Ultrasonics effective output of 200W; Ultrasonics peak power of 600W; Ultrasonics operating frequency 30 - 40kHz) for a time-dependent study and it was made sure that all the lead iodide had exfoliated and dispersed in the solution. The dispersion was then left to stand for 24hrs to let the bulk particles to settle down at the bottom of the container. Then, the supernatant of the dispersion (from the top) was extracted with a pipette and used for preparing TEM samples. A few drops (10 - 20μL each) were taken from the supernatant of the dispersed solution (1mg/ml concentration of PbI_2 in the solvent) and drop-casted onto the TEM grid containing suspended graphene. The TEM holder was then baked in high vacuum at 60°C to remove all the solvents and other impurities from the surface. **Figure 3.5** is the schematic describing the standard procedure for carrying out synthesis of liquid exfoliated

PbI_2 with different solvents and fabricating graphene/PbI_2 interface on top of a TEM grid (or equivalent holding substrates).

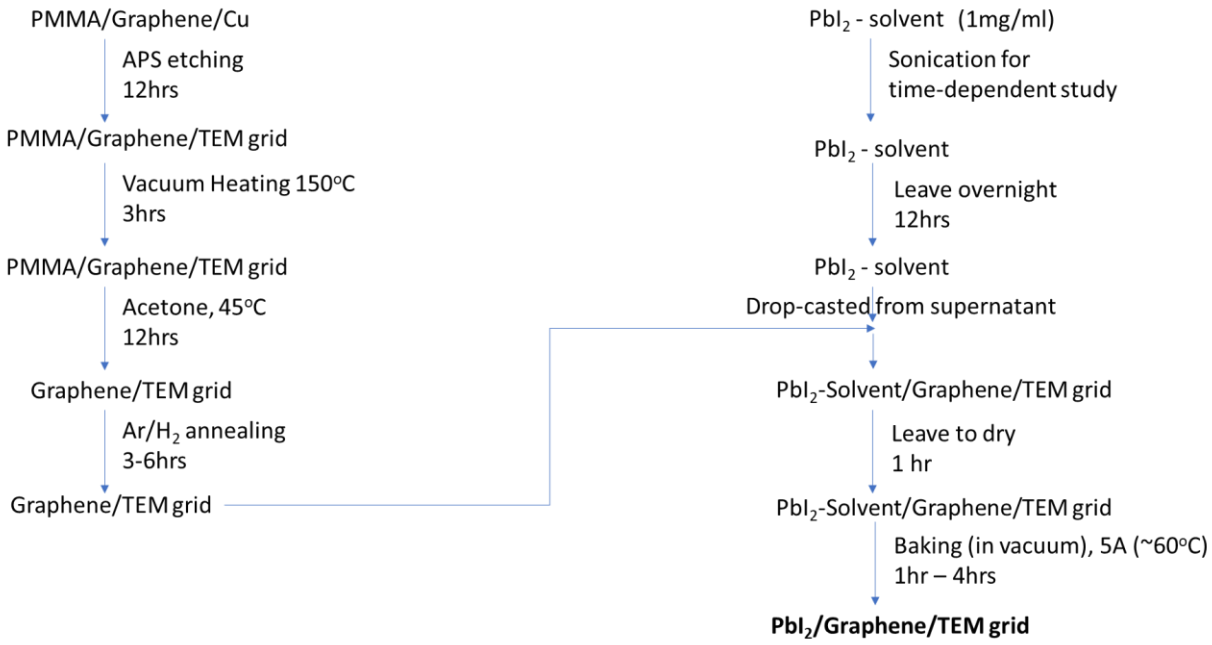

Figure 3.5. Schematic describing the standard procedure for carrying out synthesis of liquid-exfoliated PbI_2 with different solvents and fabricating graphene/PbI_2 interface on top of a TEM grid (or equivalent holding substrates).

3.4 Characterization

3.4.1. Matrix-Assisted Laser Desorption Ionization Mass Spectrometry

Mass spectrometry (MS) is one of the most popular and easy to use characterization technique for determining different types of fullerenes in a sample. The mass-to-charge ratio (m/z) of a charged particle can be measured through their different trajectories (time of flight) in a magnetic field. MS spectrometer measures such mass-to-charge ratio by applying the magnetic field. The comparison of the spectra with the known fullerene signal is then used to characterize the sample. There are different techniques which can be used to charge the fullerenes (or other sample materials), such as electron impact ionization (EI), electron spray ionization (ESI) and matrix-assisted laser desorption ionization (MALDI). For this project, MALDI-MS has been used to detect fullerenes, since it causes little fragmentation of the

material compared to the other two techniques as well as shows clear ion peaks in a higher weight detection range. Given the high molecular weight of fullerenes, MALDI-MS is one of the most popular methods to determine fullerenes. Bruker Microflex Spectrometer was the instrument based in Prof. Porfyrakis lab that was used to perform all the MALDI-MS experiments.

A matrix is used to form a solution with the material. The use of the matrix is necessary because it is acts as a shield to the fullerenes by absorbing most of the laser's power and reducing the fragmentation of the sample. The laser inside the MS vaporizes the sample resulting in a gaseous phase of negative and positive ions. This can be selectively picked up by the detector by selecting the right negative or position modes in the MS. It is possible to select both detection modes of either reflective or linear, and positive or negative. For the detection of fullerene samples, both positive and negative modes were used to ionize the sample, but the reflection mode was always used because then the ions can easily travel back and forth. In the actual experiment, dithranol or DTTB[33] was used as a matrix for the samples in this project, and the detection modes were specified for each experiment. 1µl of each sample-matrix mixture was dropcast onto the given metal plate and placed inside the instrument. After the sample was vacuumed to a pressure of at least 2.5×10^{-6} mbar, and the mode had been selected, the laser of the MS was turned on. The mode, laser power, number of laser shots, matrix and matrix:sample ratio was then tuned according to the noise level and the fragmentation seen in the spectra recorded in the MS. The recorded spectra was then compared to the predicted ion peaks in the online simulation program provided by Scientific Instrument Services Inc. to determine the types of fullerenes in the given sample.

[33] trans-2-[3-(4-tertbutylphenyl)-2-methyl-2-propenylidene] malononitrile

3.4.2. X-band continuous wave Electron Spin Resonance Spectroscopy – EPR/ESR

X-band (~9.5 GHz) cw-EPR spectroscopy is a powerful method to characterize the spin of a material by sweeping a magnetic field through the sample. The magnetic field causes the Zeeman effect, which leads to electron spin angular alignment with the magnetic field to be either parallel or antiparallel to the field. The split states have different energies and a certain magnetic field can lead to resonance of that energy difference with the given microwave frequency, and subsequently leads to electrons transitioning from one energy level to the other.(178) This transition between the energy levels (more populous lower energy level to less populous higher energy level) absorbs energy, resulting in an absorption spectra that can be recorded. In addition, the material can be characterized further by studying the resulting hyperfine couplings[34].

The technique can, thus be utilized to determine and characterize the unpaired spins in a metallofullerene, such as La@C_{82} or Y@C_{82}. Two instruments were used for EPR measurements in this study, namely Bruker EMX (based at the CAESR EPR facility in the Inorganic Chemistry Research Laboratory at University of Oxford) and Magnettech MiniScope MS200 (located in Prof. Porfyrakis lab, Dept. of Materials, University of Oxford). The samples were first checked in the Magnettech MiniScope MS200, which is located in our lab. It served as a convenient tool for quick check of the materials as well as for repetitive measurements. Accurate measurements and temperature dependent measurements were carried out at CAESR EPR facility, since that instrument has high spin sensitivity, as well as stable magnetic field.

To carry out the measurement, the metallofullerenes were first dissolved in either toluene or CS_2 and placed it inside an EPR tube. Subsequently, the tube is then de-oxygenated

[34] Hyperfine coupling occurs when spin states couple with the surrounding nuclei. That leads to additional lines in the EPR spectra of the material which can be recorded and studied in more details.

through the pump-freeze-thaw method, since oxygen is also paramagnetic and may override the signal measured from the sample. This degassing also allows for visually seeing the hyperfine couplings. After de-oxygenation, the tube is sealed, and placed inside a microwave cavity in the instrument. The cavity is then irradiated by a fixed-frequency microwave while sweeping the external magnetic field is being swept in a given region. The scanned frequencies and powers are chosen for what is typical for the type of the metallofullerene used and can be found in the literature.[35]

3.4.3. Ultraviolet-Visible (UV/Vis) Absorption Spectroscopy

UV/Vis spectroscopy is used to confirm the presence of a compound or material in a solution by comparing it with the reference solvent. For carrying out the spectroscopy, a solution of the sample and was loaded in a 1x1 cm cuvette and pure solvent in another cuvette of the same dimension was used as a reference for deducting the background signal, caused by the solvent in the solution. The two cuvettes were loaded between the light source and the detector and measured simultaneously. The wavelength of the irradiating source was used to sweep, from ultraviolet to near-infrared light (300 nm to 2000 nm), and the resulting wavelength dependent absorption features were recorded. The peaks and shapes of the absorption spectra could be then studied and used to confirm the presence of certain material in the solution. For this work, JASCO V-570 was utilized, which is in Prof. Porfyrakis lab at the University of Oxford.

3.4.4. Scanning Electron Microscopy

Scanning electron microscopy (SEM) is an important and easy to use characterization technique for studying the surface topography of a material. Secondary electrons (SEs) are generated on the surface of a material by the incident beam, thermionically emitted from an

[35] Scores of ESR studies have been conducted on endohedral fullerenes and their derivatives. Some of them have been summarized in the review papers listed here - (397,398)

electron gun, generating a contrast and thus an image. The electrons with different energies are collected – SEs, back scattered electrons (BSE) and X-rays. Because of the very thin nature of the 2D material, mostly SEs are collected to form the image contract of the surface of the material. For this project, Hitachi S-4300 field emission SEM was used to characterize the features of liquid-exfoliated lead iodide on SiO_2 substrate. The images generated by the instrument could be used for determining the domain size, shape, film continuity, solvent residue and exfoliation density on the substrate. During the actual experiment, the samples were placed on a sample stub and vacuumed inside the instrument. Accelerating voltage of 3kV was used for the experiment. The lower accelerating voltage lead to reduced electron charging and irradiation damage, as well as assisted in obtaining better clear surface topology.

3.4.5. Atomic Force Microscopy

Atomic Force Microscopy (AFM) is a type of scanning microscopy which can characterize different aspects of a 2D material, such as surface roughness, thickness, etc. The force between the sharp probe of a cantilever tip can and the sample causes deflection in the cantilever which can be detected and used to record a contrast. Especially for the study of 2D materials, AFM technique is considered to be a powerful method to study the surface roughness and the thickness of the sample. For this project, the tapping mode of AFM (AC-AFM) has been used to study the liquid-exfoliated lead iodide on SiO_2 substrate. The Asylum Research MFP-3D AFM in Prof. Bhaskaran's lab has been used in this project to conduct all the experiments and data was collected by Dr. Viktoryia Shautsova. The subsequent analysis of the images was carried out by the 'Gwyddion' software to study the profiles and height and thickness maps.

3.5 Electron Microscopy

3.5.1. Annular Dark Field Scanning Transmission Electron Microscopy

Annular dark-field scanning transmission electron microscopy (ADF-STEM) has emerged as one of the most popular techniques for carrying out electron microscopy on graphene(181) and other nanomaterials to investigate their structure, energetics and properties. ADF-STEM offers nonlinear contrast with atomic number[36] which makes it easy to identify even a single atomic substitution in a thin nanomaterial. Aside from graphene, the technique has also been used effectively to image numerous other nanomaterials such as hBN,(182) TMDs[37],(183) quantum dots,(184,185) as well as organic and biomolecules(186). Advances in STEM have facilitated use of aberration corrections to carry out imaging in real-space with high spatial and temporal resolution of sun-angstrom resolution even at low voltages, providing new insights into the dynamics of single atoms.(187) One of the biggest advantages of STEM is that it enables simultaneous elemental identification through atomic resolution EELS, owing to the condensed electron beam as small as 0.1nm. As discussed in **Section 2.3**, TEM can also act as a tool to manipulate structures of nanomaterials. That being said, it is a challenge to control the spatial and precise manipulation of atoms via TEM because of the complex interaction between the e-beam and the materials. However, STEM mode of imaging does make is feasible to use controlled electron beam irradiation which can potentially be used for single-atom manipulation.(188) This project has exploited the use of graphene substrate for studying various nanomaterials in the STEM mode.

3.5.2. ADF-STEM Experimental Parameters

Room temperature ADF-STEM imaging was performed using a JEOL ARM200F, equipped with CEOS corrector, located at the David Cockayne Centre for Electron

[36] Contrast approximately proportional to Z^2
[37] Transition Metal Dichalcogenides

Microscopy (DCCEM) within the Department of Materials at the University of Oxford. An acceleration voltage of 80 kV and 200kV was used for taking all the images, which have been stated in the results section. Imaging conditions used a 30 μm condenser lens (CL) aperture with a convergence semiangle of 22.5 mrad and a beam current of 35 pA. The acquisition angles for these images was 70–271 mrad. For lower acceleration voltage of 60kV, ADF-STEM imaging was carried out using an aberration-corrected JEOL ARM300CF STEM equipped with a JEOL ETA corrector, located in the electron Physical Sciences Imaging Centre (ePSIC) at Diamond Light Source. Dwell times of 5−20 μs and a pixel size of 0.006 nm px^{-1} were used for imaging. A CL aperture of 30 μm, convergence semi-angle of 31.5 mrad, beam current of 44 pA, and inner acquisition angle of 49.5−198 mrad.

Dose calculation

Images have been taken with 1024 x 1024 pixels, which gives the total number of pixels to be 1,048,576. With a dwell time of 20 microseconds, it therefore takes 20.8 seconds to capture one image. Probe current for all the experiments has been 35pA, which converts into 5.6 x 10^8 electrons per second. This gives 11.6 x 10^9 electrons per image. The low magnification images were taken at 1.2 Mx and have a field view of 35,000 nm^2. Therefore, that gives an estimated electron fluence of 3.3 x 10^5 electrons per nm^2. A high magnification image were taken at 3Mx and have a field view of 5,637 nm^2. Therefore, that gives an estimated electron fluence of 2.0 x 10^6 electrons per nm^2.

3.5.3. *In-situ* Heating

In-situ high-temperature imaging up to 900 °C was performed using a commercially available heating holder from DENS Solutions (SH30-4M-FS). Heating the sample was achieved by passing a current through a platinum resistive coil embedded in the TEM chip (DENS Solutions DENS-C-30). The resistance of the platinum coil was monitored in a four-point configuration, and the temperature was calculated using the Callendar-Van Dusen

equation (with calibration constants provided by the manufacturer). Slits were produced in the Si_3N_4 membranes using focused ion beam milling before transferring the graphene. Subsequently either the ARM 200F or ARM 300CF was used to carry out the *in-situ* heating and imaging. The majority of the data presented in this thesis has been recorded at room temperature, and in such cases the temperature is *not* stated in the caption to avoid repetition. In all cases where *in-situ* heating was used, this is stated in the relevant figure caption.

3.5.4. Image-processing and Simulations

Images were processed using the ImageJ software. Atomic models were constructed using Accelrys Discovery Studio Visualizer. Multislice image simulations were performed using JEMS with conditions that corresponding to the experimental conditions: chromatic aberration at 60 kV =0.89 mm; spherical aberration = 5µm; energy spread = 0.42eV; probe size =65pm and the convergence semi angle =31.5mrad. The anglular range for dark field imaging was between 49.5mrad to 198mrad. PbI_2 crystal structure was drawn using Crystal Maker Version 10.3.1.

Chapter 4 Metallofullerenes

This chapter gets into the details of fullerene synthesis, extraction, separation and characterization. Gd based metallofullerene ($Gd_3N@C_{80}$) molecules have been shown to be used to create single adatoms and nanoclusters on a graphene surface. An *in-situ* heating holder within an aberration corrected scanning transmission electron microscope is used to track the adhesion of endohedral metallofullerenes (MFs) to the surface of graphene, followed by Gd metal ejection and diffusion across the surface. ADF-STEM is used at both 60kV for *in-situ* heating work, and at 200kV for room temperature imaging. The higher accelerating voltage enables visualization of the Gd metal without the significant contrast from beam induced contamination at room temperature that occurs at lower voltages. The high atomic number of Gd enables easy identification in the presence of carbon atoms, surface carbon residue, and other lighter inorganic contaminants that are known to exist within graphene grown by chemical vapour deposition. Heating of the sample up to 900^{o}C is used to promote adatom migration and metal nanocluster formation, enabling direct imaging of the assembly of nanoclusters of Gd. It is also shown that hydrogen can be used to reduce the temperature of EMF fragmentation and metal ejection, enabling Gd nanocluster formation on graphene surfaces at temperatures as low as 300^{o}C. The process of EMF fragmentation and metal ejection is captured *in-situ* and reveals that after metal release, the C_{80} cage opens further and fuses with the surface monolayer carbon glass on graphene, creating a highly stable carbon layer for further Gd adatom adhesion. Small voids and defects (~1nm) in the surface carbon

glass act as trapping sites for Gd atoms, leading to atomic self-assembly of 2D monolayer Gd clusters. These results show that MFs can adhere to graphene surfaces at temperatures well above their bulk sublimation point, indicating that the surface bound MFs have strong adhesion to dangling bonds on graphene surfaces. The ability to create dispersed single Gd adatoms, and Gd nanoclusters on graphene may have an impact on spintronics and magnetism, where Gd shows unique properties. The work in this chapter was published in ACS Nano, 2018.

4.1 Introduction

4.1.1. Metallofullerenes

Discovery of fullerenes(189) sparked a great deal of curiosity and interest among the scientific community due to their unique closed cage-like structure that is composed solely from sp^2 hybridized carbon.(190,191) The robust nature of the carbon cage plays a very important role in isolating the atoms from the exterior environment while the electronic properties of the material can be tuned by the selection of the atoms inside. Many studies on individual EMFs have been carried out over the years, and it has become established that they exhibit novel structure, chemical and electronic properties which were completely different to those of their parent empty cages. La@C_{82} was the first discovered endohedral fullerene, where the symbol @ denotes the inclusion of a La atom inside C_{82} cage. Since then, fullerenes encapsulating metallic(192), carbide(193,194), nitride(195) and many methano-(196) and oxide-(197) clusters have been synthesized and isolated over the years. Among the endohedral fullerenes, the trimetallic nitride-containing cages of the type $M_3N@C_{2n}$ (where M = Sc, Gd; 2n = 68-96), shown in Figure 4.1 have been one of the most studied materials since their discovery in 1999(195) due to their high yields during synthesis.(198) This family of fullerenes has an especially high yield because of the charge transfer from the encaged cluster that results in a stable ion pair, which stabilizes the higher fullerene cages of various isomeric structures. In addition, the large HOMO-LUMO gaps gives further kinetic stability to the hybrid molecule.

Endohedral metallofullerenes containing rare earth metals carry additional negative charge on the fullerene cage because of the charge transfer which takes place from the metal atoms to the cage.(199) As a result, it alters the magnetic and optical properties of the fullerene molecule and also, the properties can be tuned by the particular selection of the metal atoms

inside the fullerene cage. In this study, I have chosen to study a few metallofullerenes for their varied properties and synthesized, characterized and look at their interactions with graphene.

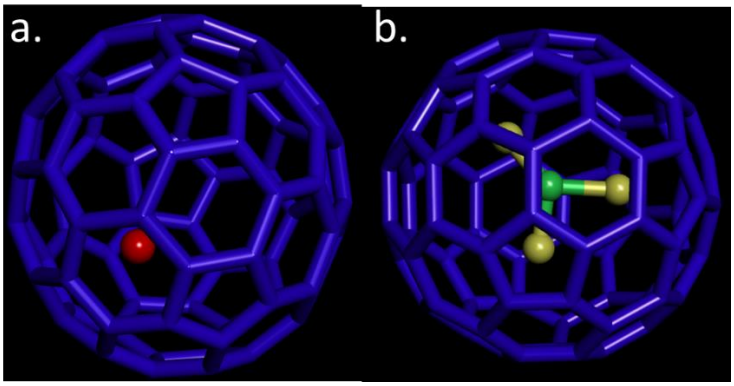

Figure 4.1. A representative figure of two endohedral metallofullerenes, a (a) monometallic in a C_{82} cage and (b) trimetallic nitride encapsulated in in a C_{80} fullerene cage. The red and the yellow balls correspond to the metal ion encapsulated in the carbon cage and the green to nitrogen.

4.1.2. Graphene Interface

In some cases, the presence of metal atoms on the surface of graphene causes catalytically promoted etching of the graphene, which leads to hole formation. Such effects are generally detrimental to the formation of well-ordered graphene-dopant systems. Studying the interactions between precursors, their reactive elements and graphene at the atomic scale is therefore important for the development of new 2D layered systems beyond graphene. One of the least damaging way of achieving molecular doping of graphene is by introducing organic and inorganic molecules to the graphene surface as carriers of the dopants, which can later self-assemble and decompose when heated. Similar approaches have been applied for many years to the interior of carbon nanotubes, where numerous materials were used to fill the inner void of single walled and multi-walled carbon nanotubes and the resulting chemical reactions investigated.(200–203) For graphene, few studies have been carried out on rare-earth magnetic particles and this field has yet to be fully explored for a diverse range of materials compared to those studied in nanotubes. An understanding of metal adsorption and interaction with graphene is, however, vital to the development of electronic devices based on this material.

4.1.3. Surface Dopant Introduction

There are many different approaches for introducing surface dopants to graphene, such as thermal evaporation,(204) chemical vapour deposition,(205,206) e-beam evaporation,(207) solution deposition of molecules/nanoparticles,(208–211) and the direct formation of material from deposited precursors. There have been a wide range of materials investigated as surface dopants and also as substitutional dopants in graphene, such as N, Si, P, B, Fe, Au (111,112,212–215) as substitutions, and Co, Pt, Ni, Au, Gd as surface adsorbates.(113,121,216,217) Importantly, doping can lead to changes in the conductivity, magnetism, transparency, and catalytic response.(218)

Many of these systems have been studied at atomic resolution using transmission electron microscopy (TEM)(219,220) and electron energy loss spectroscopy (EELS). High-angle Annular dark field scanning transmission electron microscopy (HAADF-STEM) can provide non-linear Z-dependent contrast that helps to discriminate the dopant from the C lattice with higher contrast than phase contrast TEM, however phase contrast TEM enables the dynamics to be observed at much faster time scales. Furthermore the bond lengths between substitutional dopants and C can be accurately measured from phase contrast TEM images, as has been demonstrated in measurements of elongated Si-C bonding at defects and edges of graphene.(221,222) Substitutional N dopants in graphene, typically only replace single C atoms, whereas larger atoms such as Si and Fe can form both single or double substitutions of C in the lattice.(223) EELS has been used to show different oxidation states for Fe atoms and extended plasmon resonances for Si atoms, as they transition between bonding to either 3 C atoms or 4 C atoms during electron beam induced transformations.(111,224) Larger atoms such as Au are generally found in sites larger than the C monovacancy. However, the formation of stable systems using surface doping of graphene is much more challenging due to the low migration barrier for diffusion of atoms on pristine graphene surfaces.

At room temperature, most atomic species have sufficient thermal energy to overcome the diffusion barrier and migrate freely across pristine graphene until they find either a defect, edge, or surface carbon glass layer (explained in **Section 4.3.3**, also see **Figure 4.15**). Prior work using *in-situ* heating within an aberration corrected TEM showed that Au nanocrystals form 2D monolayer and bilayer structures at high temperatures of 500-800^{o}C, and attach to defects and the edges of holes in graphene.(121) The observation of crystalline Au significantly above its predicted melting point indicated that surface interactions with graphene can lead to modified melting and evaporation behaviour. Recent work has shown that after Pt metals are deposited on graphene, via electrochemical deposition method, STEM analysis showed that 2D Pt monolayers could be found across pristine graphene regions (225). However, since the energy barrier for migration of atoms on graphene is low, the observation of 2D Pt layers on pristine graphene is likely due to the initial nucleation of Pt atoms from the binding of Pt atom clusters at the edge of surface carbon glass and then its subsequent lateral extension out into the pristine regions of graphene. This is also because the diffusion of Pt on graphene has a low energy barrier which cannot lead to Pt atomic localization in pristine graphene regions.

The deposition of most materials onto a graphene surface generally leads to them adhering to the surface carbon glass, which has sp^2 character but with heavy defect density of pentagons and heptagons, and also contains elements such as N and O.(226) In graphene grown by chemical vapour deposition (CVD), Si atoms are commonly found attached to this surface carbon glass. Recent work on understanding the interactions between Pt single atoms and MoS_2 monolayers also showed that Pt atoms only adhere to this surface carbon glass or to S vacancies in the MoS_2, with the diffusion across pristine MoS_2 having a low energy barrier.(227)

Herein, atomic scale interactions between Gd atoms and graphene has been investigated by the use of a Gd containing molecular precursor, in the form of high purity $Gd_3N@C_{80}$ for metal cargo release to achieve single Gd adatom dopants and clusters on the surface of graphene. Gd dopants show unique magnetic and spin properties that may yield interesting composite systems for spintronic applications. Theoretical calculations have shown that the Gd adatoms can significantly enhance the magnetic moment of graphene.(217,228) In addition, the sign and magnitude of magnetic anisotropy of such Gd-graphene hybrid was found to be based on the carrier accumulation.(229) The deposition of Gd onto graphene has been shown to result in n-type doping,(230) which is important as graphene is often p-type doped from interactions with substrates, water and surface residues.

4.2 Results & Discussions: Metallofullerenes

Obtaining high purity EMFs requires several independent steps, namely – Synthesis, Extraction and Purification. Synthesis is carried out by the use of the classic Kratschmer-Huffman apparatus where a typical standard direct current (D.C.) arc-discharge is used to form fullerenes, along with a lot of carbon soot (**Section 3.2.1**). Soxhlet extraction is the next step which involves a solvent to dissolve fullerenes and separate it from the rest of the carbon soot. The final step is purification that separates different kinds of fullerenes from each other. A lot of research has been done over the past few decades on optimization of the synthesis, isolation and purification of different kinds of EMFs. However, contradictory results have been reported over the years, especially regarding the pressure of helium in the arc-discharge chamber(231,232), use of different types of solvents for extraction of the EMFs(233) and the separation methods via HPLC and Lewis acids.(234,235) In this study, I have studied some of the parameters in order to optimize the synthesis, extraction and purification of EMFs and maximize their yield.

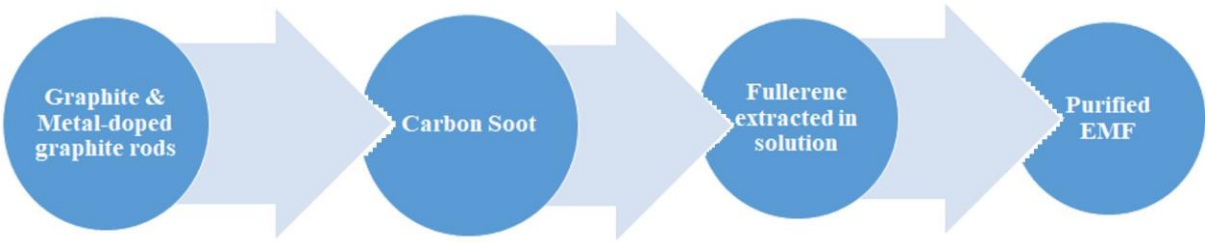

Figure 4.2. Schematic of fullerene synthesis, extraction, separation and purification.

4.2.1. Synthesis

Different kinds of parameters such as current, pressure, etc. have been studied and reported to affect the production of EMFs in high yield using the arc-discharge apparatus (see **Appendix A**). In this study, the D.C. power supply was kept constant at 200A. At the constant current, pressure in the chamber was changed for every arc discharge. It was found that the pressure of Helium in the chamber during the arc discharge plays a very important role in the formation of fullerenes in general and metallofullerenes in particular. Many articles over the years have reported the effect of different Helium pressure in the chamber(236–238) but show contradictory results when it comes to exact pressure range for operating the arc discharge. This discrepancy could arise because of the difference in the synthesis conditions and the machine set up which varies from one laboratory to another. Since the arc discharge in the laboratory is a home-made apparatus, it was upgraded and one of the aims was to continually improve the system (see **Appendix B**) whilst optimizing various parameters at the same time, such as, the current, the pressure of helium gas in the chamber and the optimum distance between the anode and cathode. **Figure 4.3** shows the mass spectrum of the materials produced from the arc-discharge process with the inset showing the presence of $La@C_{82}$.

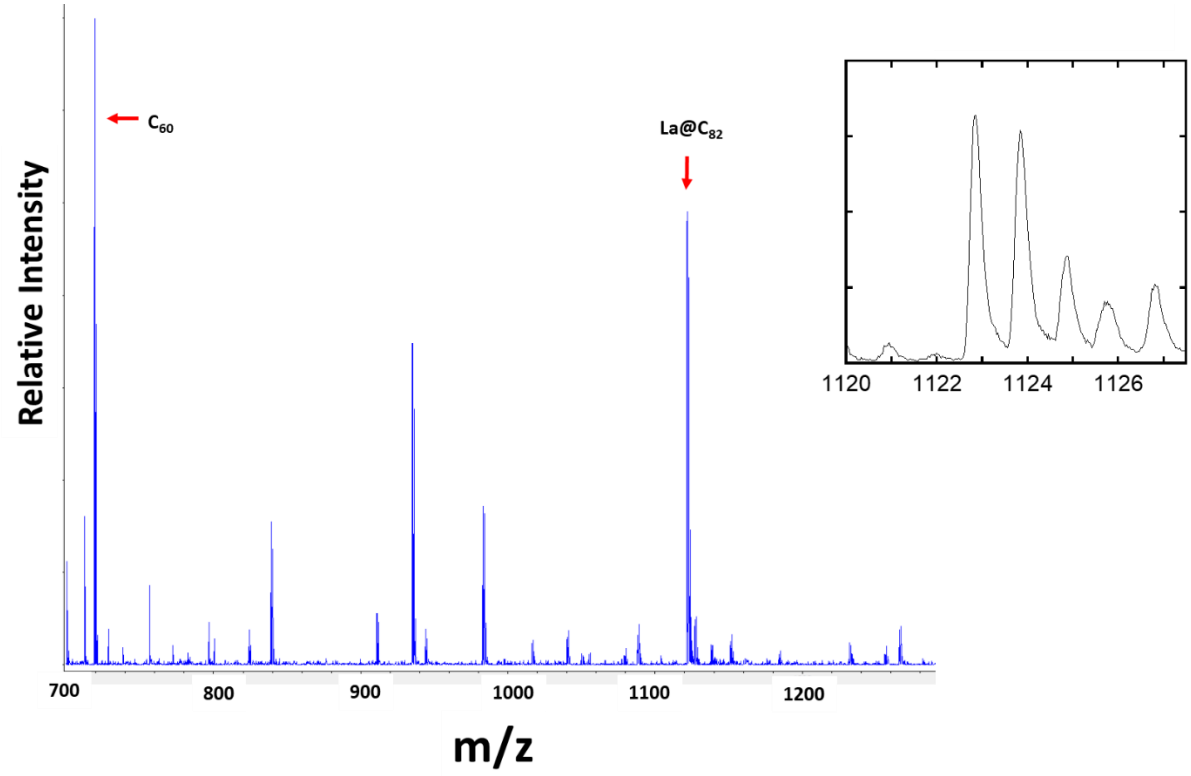

Figure 4.3. Mass spectrum of the soot produced from the arc-discharge. The inset in the black box shows the magnified mass spectrum of La@C_{82} showing the isotopic distribution of the material. Y-axis is counts, where the intensity is relative to C_{60}.

For studying the effect of pressure, very high and low He pressure was tested during the arc-discharge. The fullerenes were then extracted and purified (as explained in more details in **Section 4.2.2 and Section 4.2.3**) and HPLC was used to quantitatively determine the synthesis ratio of fullerenes. Almost no EMF was formed in the absence of helium whereas in very high He pressure range (more than 2 bar), extremely low yield of EMF of less than 0.01% was found in the overall fullerene mixture. The overall yield of the empty cage fullerenes like C_{60}, C_{70}, C_{76}, C_{82}, etc. were also found to be low (less than 1% of the total carbon soot). Increasing pressure decreases the C_{60} synthesis and hence, the ratio of La@C_{60}/C_{60} increases. Compared to 50mBar, the yield of C_{60} decreased by ~30 times at 250mBar. However, when the pressure of He went down to 60-100 mbar, the production yield of metallofullerenes increased to 1~2% of the overall fullerene produced. Moreover, the yield of the total fullerene in the carbon soot obtained after the arc discharge also increased by three times. In the

experiments carried out till now, the optimum Helium range seems to be ~250mbar for La@C_{82} synthesis.

Doping in the rods is also very important – 0.8% (KM8) metal doping makes the monometallofullerene. Otherwise (1.6%, (KM16) most synthetic metal would be dimetallic like Y2@C80. Hence, 0.8% La-doped graphite rods and 0.8% Y-doped graphite rods were used to synthesize La@C82 and Y@C82 repectively.

	P[1]	C_{60}[2]	C_{70}[2]	La@C_{82} + C_{90} + C_{92} + C_{94} + C_{96} + C_{98} [2]
1	80	81%	18%	~0.30%
2	120	75%	21%	~0.63%
3	**250**	**67%**	**25%**	**~0.87%**
4	500	65%	27%	~0.96%

1. P = He Pressure (in mBar) **2. % of all fullerene**

Table 4.1. Table showing the Helium pressure conditions in the arc discharge and relative fullerene yield, which has also been represented in the 2D graph in **Figure 4.4**.

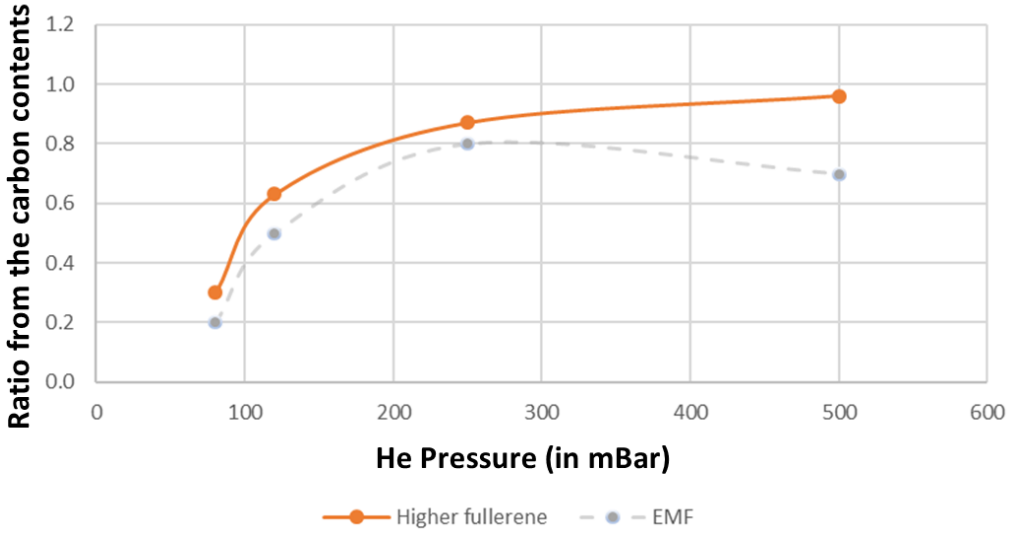

Figure 4.4. Graph showing the Helium pressure dependence of fullerene contents produced in the arc discharge.

4.2.2. Extraction

Most of the research in the past has been done on the use of a single solvent(233) but it has been shown that a single solvent may not be enough for the recovery of all the fullerenes.(239) Hence, in this study, two-step liquid extraction method was developed, where two different solvents were used consecutively to extract all the possible EMFs present in the soot in the most effective manner. Various solvents such as toluene, DMF, CS_2, o-xylene, pyridine, aniline, etc. have been reported in the past to extract fullerenes.(240) The combination of these two solvents were tried for different sets of fullerenes obtained from the same arc-discharge conditions, to optimize the 2-step extraction process. A flow diagram in **Figure 4.5.** summarizes all the different combinations of solvents used in the experiment.

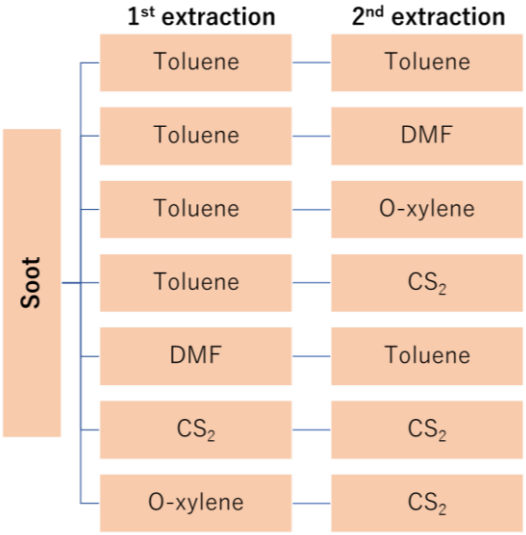

Figure 4.5. A flow diagram summarizing all the different combinations of solvents used in the experiment.

Out of all the combinations used, toluene was found to be the least efficient in extracting EMFs, especially La@C_{82} as well as La@C_{76}, although it extracts C_{60} and C_{70} very effectively. The same volume of toluene extracted 3 times less EMFs from the carbon soot compared to the other solvents used under the same synthesis conditions. One of the most efficient solvents to extract EMFs was DMF. It extracted more EMFs than CS_2, as can be seen

from the relative intensity of the mass spectrum of the extracted solution under the same conditions, shown in **Figure 4.6**. However, DMF is not a very viable solvent to use since it is extremely difficult to evaporate under low pressure due to its high boiling point.

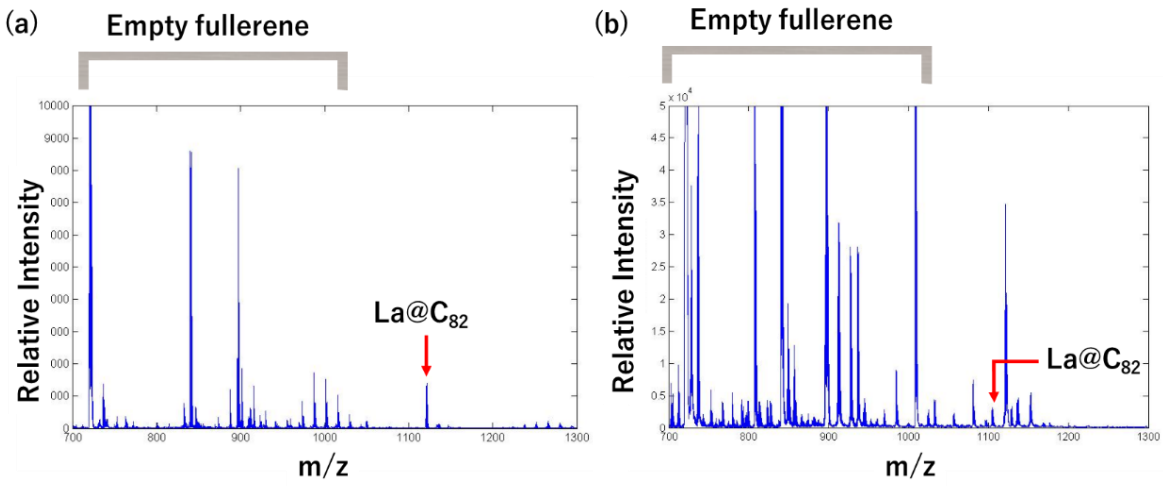

Figure 4.6. Mass spectrum after extraction from carbon soot using (a) DMF (b) CS_2. The higher mass peaks after $La@C_{82}$ in figure (b) correspond to either higher empty cage fullerenes, or other EMFs, such as $La_2@C_{80}$, $La@C_{84}$ etc. Y-axis in both the graphs is counts, where the intensity is relative to C_{60}.

Studying the mass spectrum and quantitatively analysing the HPLC data, it was found that CS_2 and o-xylene combinations were found to be the most effective for extraction of EMFs. O-xylene in particular, extracts more than 50 different types of fullerenes from the carbon soot. **Figure 4.7** shows the mass spectrometry results of extraction using o-xylene and toluene on equal amounts of carbon soot synthesized under the same conditions. It can be clearly seen in the mass spectrum that more fullerenes could be extracted via o-xylene than with toluene. The consecutive use of CS_2 and o-xylene led to extraction of about 50% more EMFs from the carbon soot than extraction with traditionally used toluene.

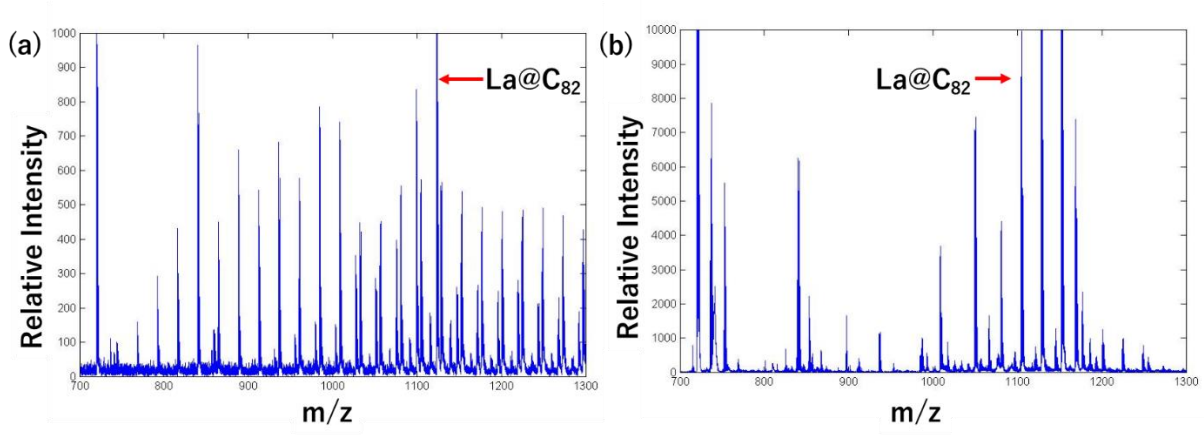

Figure 4.7. Extraction of fullerenes from the soot using (a) o-xylene (b) toluene. The y-axis is counts, relative to C_{60}. More fullerenes[38] could be extracted using the o-xylene as compared to toluene. The peaks on the mass spectrum beyond La@C_{82} correspond the higher empty cage fullerenes as well as other species of endohedral fullerenes, such as La@C_{84}.

4.2.3. Purification

The third step for purification is the isolation of one type of EMF from all the empty cages and all other EMFs. HPLC has been traditionally been used for the separation and purification process (as described in **Section 3.2.3**).(179) **Figure 4.8**a shows the typical HPLC profile for 2mL of fullerenes solution injected. Each of these sections were separated and collected in separate flasks and checked with mass spectrum to test their compositions after separation. The area under the peaks can be used to read the quantity of each material obtained. C_{60} is the main product of arc-discharge followed by C_{70}, and La@C_{82} constitutes the majority of the EMF obtained. The typical ratio of La@C_{82} to C_{60} in an optimum arc discharge condition, was found to be 15:85. **Figure 4.8**b is the magnified image of the La@C_{82} peak in the HPLC profile. The two peaks at 24 minutes represent the two different isomers - La@C_{82} (I) and La@C_{82} (II).[39] Thus the procedure was run twice to make sure that all the peaks were completely separated from each other and high purity EMFs could be obtained.

[38] More fullerenes in terms of greater number of species of fullerenes extracted as well as the quantity (mass) of fullerenes extracted.

[39] C_{82} fullerene has 9 distinct isomers of cages, but encapsulation of La in these cages is only favourable in three different cages with C_{2v}, C3v and Cs symmetry. Therefore, one isomer of La@C_{82} is found to be C_{2v} symmetry and the other one is found to have either C_{3v} or C_s symmetry.

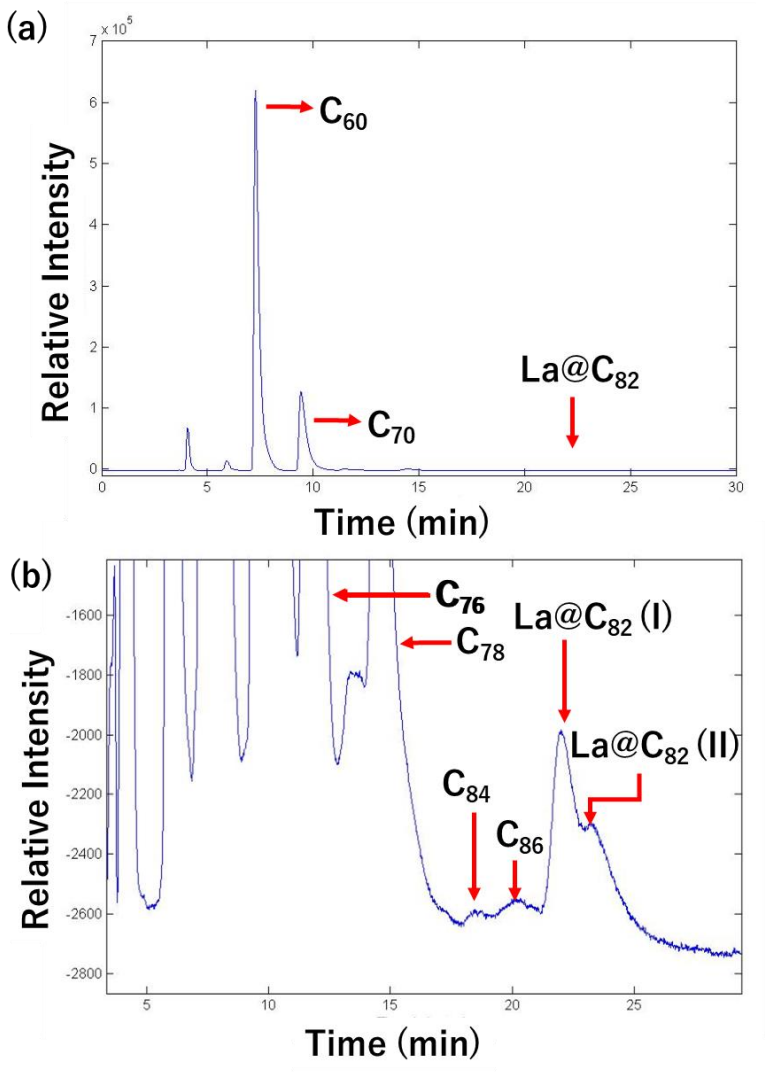

Figure 4.8. (a) Typical HPLC profile for separation of the fullerenes. (b) Zoom-in hplc profile of the first image which distinctly shows the two La@C_{82} isomers. Y-axis is relative intensity compared to C_{60}.

Similarly, other EMFs were also explored for potential use on graphene. Y@C_{82} was synthesized in our lab whereas Gd_3N@C_{80} was bought from Sigma-Aldrich. Both these materials were then also purified using the HPLC method. The purification was then tested by both mass spectrum and EPR in case of spin active EMFs. **Figure 4.9**a shows the typical HPLC profile of Y@C_{82} with all the indicated EMFs and empty cages in each peaks. Each peak obtained was then re-run to obtain purified material. In case of the spin active material Y@C_{82}, ESR was used to quantitatively measure the number of spins and thus, the concentration of the sample. **Figure 4.9**b shows the typical doublet hyperfine structure under vacuum at room

temperature.(241) The area under EPR was measured and compared with calibrated data to obtain the exact number of spins in the material. The number of spins can thus calculate the mass of the EMF present in the sample. The mass obtained from the ESR measurements was thus compared to the mass of sample calculated from the HPLC profile (area of the curve). Such comparison of the area obtained under the HPLC profile and the number of spins from ESR concluded that the sample was 96% pure.

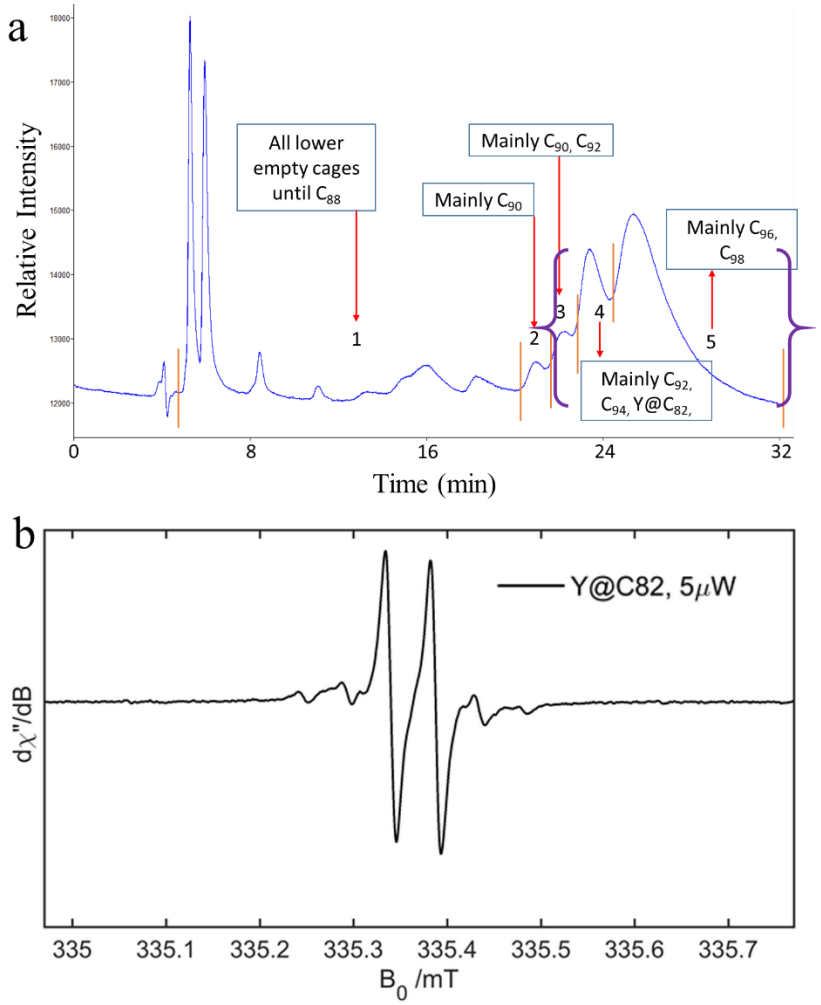

Figure 4.9. (a) HPLC profile of a typical Y-EMF showing the different sections of EMFs obtained after HPLC. Y-axis is relative intensity compared to C_{60}. (b) Typical ESR profile of Y@C_{82}.

Similarly, the $Gd_3N@C_{80}$ obtained from the company was also purified using HPLC. **Figure 4.10** shows the mass spectrum of the material after purification which only shows the $Gd_3N@C_{80}$ peaks with almost negligible presence of other fullerenes.

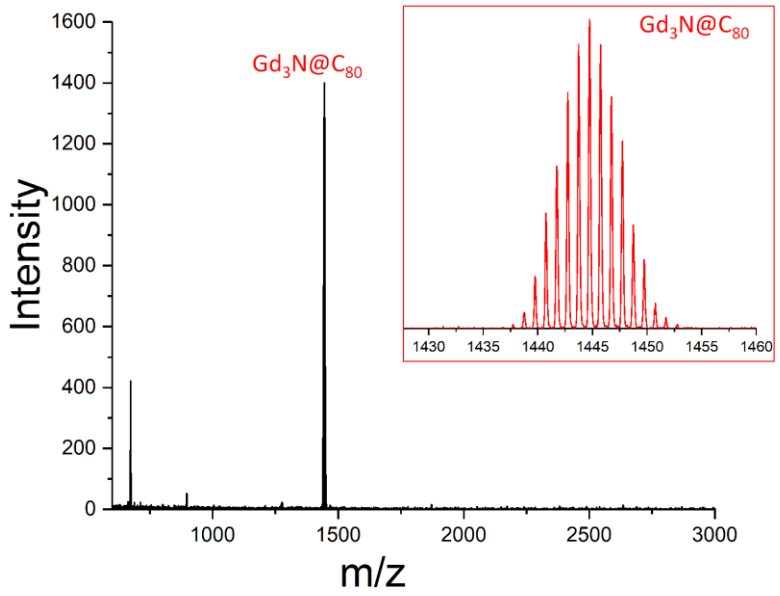

Figure 4.10. Mass spectroscopy of the $Gd_3N@C_{80}$ metallofullerenes showing the purity. Y-axis represents the counts in the mass spectrometry.

A typical HPLC process for 2mL of solution takes 30 minutes to separate and the amount of solution obtained from one arc-discharge experiment can vary from 1L – 2L, depending on the amount of carbon soot obtained. Therefore, even though the process is very effective to separate the different fullerene cages, it is extremely time-consuming. Hence other methods of separation of EMFs from the empty cages were also explored. One such method is Lewis acid separation process, an approach which has not been explored in details and only a handful of literature is available.(242,243) $TiCl_4$ was studied for the separation of EMFs but it was found that the method did not work as efficiently as claimed previously(235) and thus, the rest of the work was limited to the use of HPLC. The method and separation results have been discussed in details in **Appendix C**.

4.3 Results & Discussions: Graphene Interface

For studying fullerene interface, trimetallic endohedral fullerenes, $Gd_3N@C_{80}$ were selected. $La@C_{82}$ or $Y@C_{82}$ contains a single atom inside the fullerene cage, which makes it difficult to judge whether the translation or rotation motion is a result of the atoms moving or the fullerene cage itself. Thus, a Gd_3N cluster within a C_{80} cage offers the advantage over monometallo fullerene because it does not have completely free rotation at room temperature(244,245), and thus, the motion dynamics of the EMF could be studied on the graphene independently of the cluster inside. Moreover, Gd is a heavy metal resulting in a very bright contrast under ADF-STEM imaging and hence, although it is difficult to see the fullerene cage which is comprised of very light C-atoms, they could be easily identified by the presence of three Gd atom cluster. Thus $Gd_3N@C_{80}$ was the preferred EMF for the study of fullerene interface on graphene.

4.3.1. Synthesis

1mg/ml concentration of the solution of the EMF in Carbon Disulfide (CS_2) was used to drop cast on the graphene and the TEM holder was baked in vacuum at 60^oC to remove all the solvents from the surface. One sample was imaged as it was after vacuum baking and other one was H_2 annealed at 180^oC overnight.

Figure 4.11a-c shows a schematic illustration of EMF deposition onto graphene. Two types of TEM grids were used, one for ex-situ work (SiN with 2 micron holes), the other being SiN *in-situ* heating chips with FIB cut slits. Graphene grown by CVD was transferred onto the TEM grids to give suspended areas suitable for ADF-STEM imaging. The graphene samples were cleaned after transfer by annealing to remove excess PMMA resist residue. The details of the transfer process have been discussed in the Methodology **Section 3.3.2**. The MFs were drop cast onto the TEM chips from a CS_2 solution and allowed to dry. CS_2 is a good solvent for endohedral metallofullerenes (MFs) and also has a high volatility, leaving minimal surface

adsorbates on graphene. Some *ex-situ* samples were then annealed in argon/hydrogen gas after the EMF deposition at 180^{o}C to promote EMF-graphene chemical reactions. Initial attempts to image MFs on the surface of graphene using ADF-STEM at room temperature at 60kV were limited by excessive beam induced contamination. Therefore imaging at 200kV was used, as the dynamics of MFs could be studied within a short window of time before beam induced damage occurred and beam induced contamination was less limiting due to the lower contrast from light Z elements that are typical within the contamination. Figure 4.11d shows a low magnification optical image of the $Gd_3N@C_{80}$–graphene hybrid system on a SiN chip and Figure 4.11e shows a typical selected area electron diffraction pattern from the suspended graphene regions. **Figure 4.11**f shows a low magnification TEM image of graphene with surface bound MFs, with an energy dispersive x-ray (EDX) spectrum (**Figure 4.11**g) taken from the red boxed area, shown in **Figure 4.11**f. The EDX spectrum of the hybrid sample shows the presence of Gadolinium atoms together with silicon and copper peaks from the impurities from the SiN substrate and copper substrate used during typical CVD synthesis of graphene, respectively.

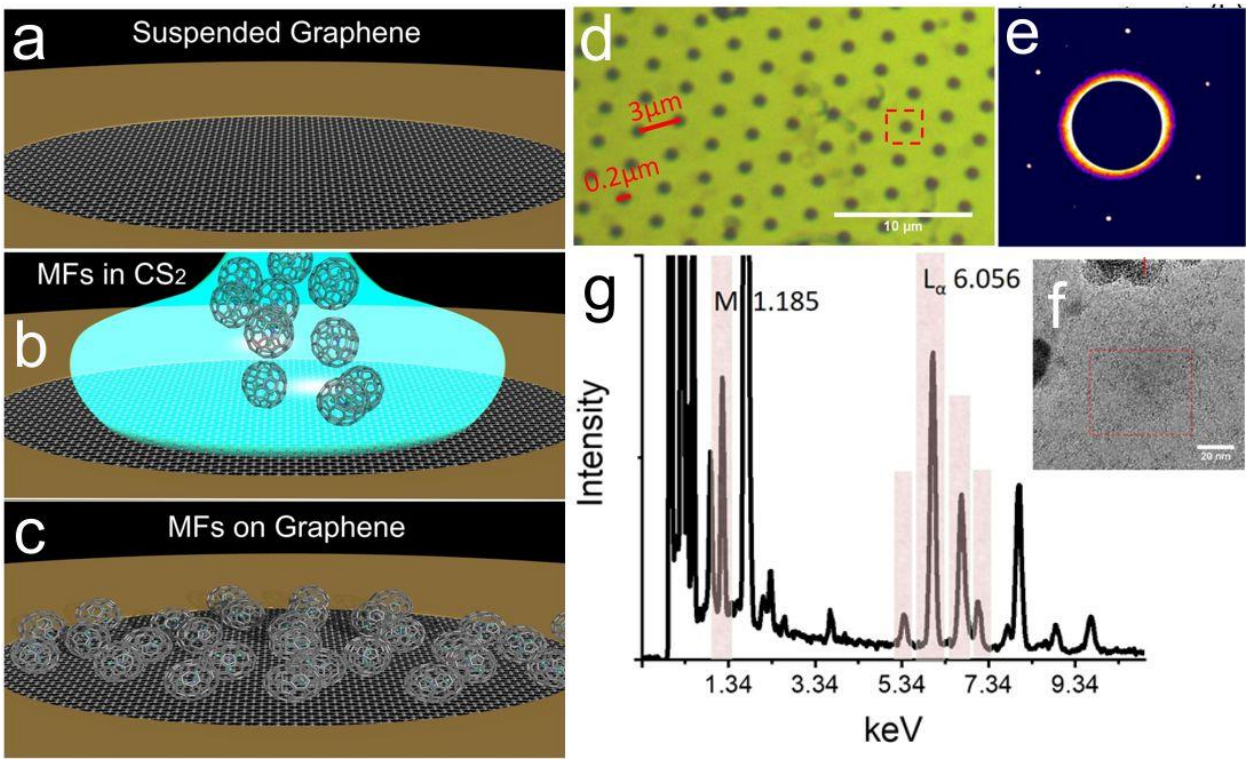

Figure 4.11. (a)-(c) Schematic illustration showing the deposition of MFs from solution onto the surface of graphene on a TEM grid. (d) Optical image showing the SiN TEM grid with graphene suspended across the holes. (e) Selected area electron diffraction pattern from an area of graphene suspended across the hole. (f) Low magnification TEM image of graphene with surface bound MFs indicating the region where EDX spectrum was recorded. (g) EDX spectrum from the red boxed region in (f) with Gd M and Lα peaks indicated and other L peaks highlighted in the image. The other peaks correspond to O K_a(0.52keV), Cr L_a(0.57keV), Cu L_a(0.92keV), Si K_a(1.73keV), Ca K_a(3.69keV), Cr K_a(5.4keV), Cu K_a(8.04keV), Au L_a(9.71keV) lines respectively. These elements are present in the sample because of the sample holder (made of copper/gold) and due to the exposure to water during the sample fabrication process, which contributes to Si, Ca, Cr.

Figure 4.12a shows an ADF-STEM image recorded using an accelerating voltage of 200kV of isolated $Gd_3N@C_{80}$ molecules dispersed on graphene, with metal trimer clusters clearly visible (**Figure 4.12**b). In general, the MFs were well dispersed across the graphene surface, mostly with sub-monolayer density, but some areas showed denser clusters of MFs, as expected from a drop-cast solution preparation. The projection of the three Gd atoms show variability, indicating they are randomly orientated across the surface. ADF-STEM image simulations were calculated using the multislice method,(246,247) from the atomic model shown in **Figure 4.12**c-d, for random orientations to show the effect on the relative Gd

locations (**Figure 4.12**e). The green box in **Figure 4.12**e shows the case when the orientation of the EMF is such that two Gd atoms overlap in projection, giving rise to only two spots, with one of increased intensity relative to the other. The yellow box in **Figure 4.12**e shows the case when the orientation leads to a linear projection of the three Gd atoms in the EMF with equal intensity. The red box in **Figure 4.12**e shows the case when the orientation of the Gd trimer is parallel to the graphene lattice giving rise to a symmetric triangular intensity pattern (**Figure 4.12**f). When noise was added to this image simulation, **Figure 4.12**g, it showed good qualitative agreement with the experimental ADF-STEM image (**Figure 4.12**h).

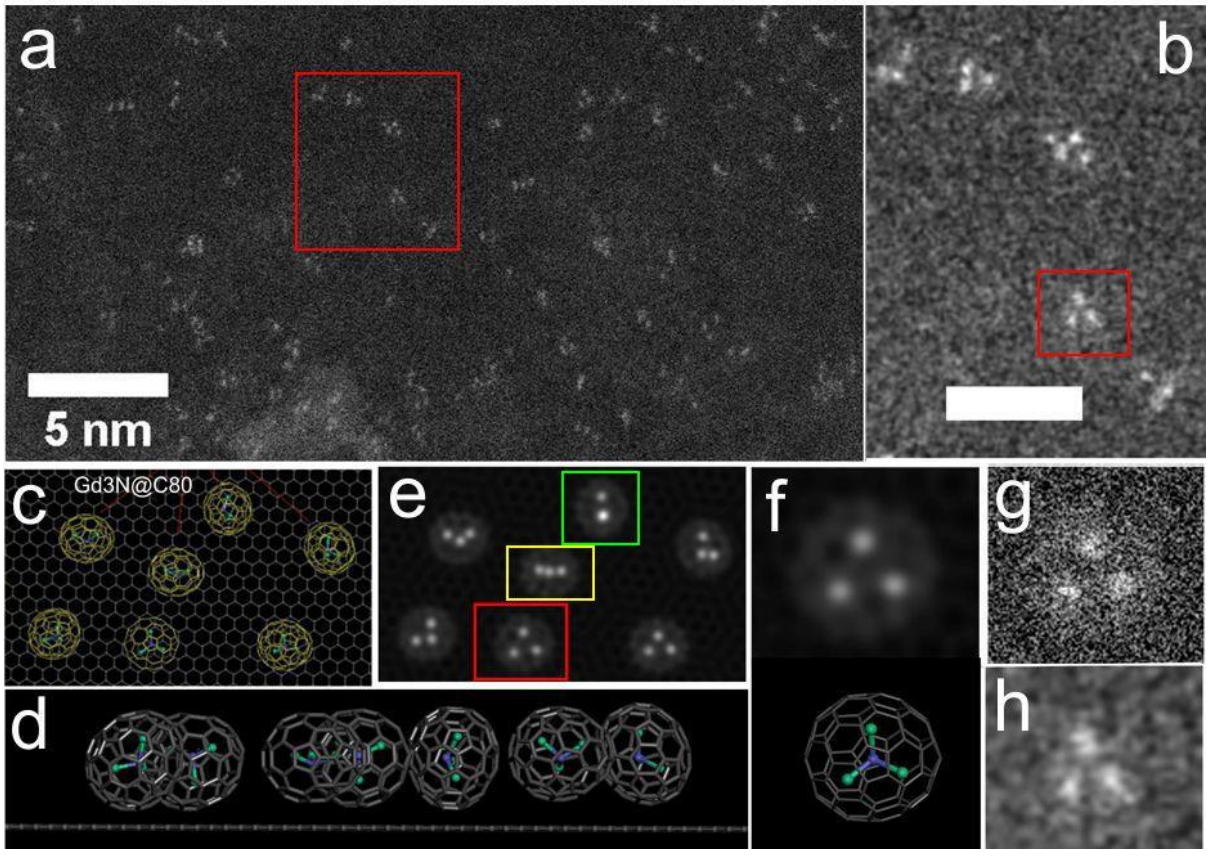

Figure 4.12. (a) Room temperature 200kV (dose: 5.6 x 10^8 e s^{-1}) ADF-STEM imaging of isolated $Gd_3N@C_{80}$ molecules on graphene. (b) Higher magnification image of the red boxed region in (a) showing several trimer contrast features from MFs. (c) Atomic model of $Gd_3N@C_{80}$ molecules on the surface of graphene (top view), and (d) side view. (e) Multislice ADF-STEM image simulation of the atomic model in (c) showing intensities from the Gd metal trimer atoms in various projected orientations. (f) Comparison of the image simulation from the red box area in (e) with the atomic model. (g) Noise added to the ADF-STEM simulated image in (f) compared to the experimental image shown in (h), taken from the red boxed region in (b).

4.3.2. Fullerene: Motion Dynamics

Time series of images (**Figure 4.13**a-e), revealed that the MFs showed both translational motion (green line in **Figure 4.13**a-e), as well as rotational dynamics, **Figure 4.13**f-y. **Figure 4.13**f-j shows a magnified view of the red boxed region indicated in **Figure 4.13**a. This region contains two adjacent MFs, with changes to the Gd trimer intensities from frame to frame (**Figure 4.13**f-j). Multi-slice image simulations, with added noise, shown in **Figure 4.13**k-o, are based on the atomic models shown in **Figure 4.13**p-t, and qualitatively match the experimental intensity profiles. **Figure 4.13**f-j, together with the image simulations shown in **Figure 4.13**k-o, show that the MFs are rotating and also moving apart. The orientation of the Gd trimer is indicated in **Figure 4.13**u-y, where the fullerene cages have been removed for visual clarity. Gd_3N is one of the largest rare earth nitride cluster which is known to have been encapsulated in a carbon cage. As per the previous literature in the field, Gd_3N cluster has been found to form a bond to the C_{80} cage which prevents the cluster=free rotations, and thus, it is known that the Gd_3N cluster within a C_{80} cage does not have free rotation at room temperature (244,245). Therefore, this indicates that it is most likely that the entire EMF molecule is rotating on the surface of graphene, rather than the Gd trimer rotating within a stationary EMF. In addition, prior reports of C_{60} within graphene sandwiches have also shown dynamic translational motion together with fullerenes on the surface of graphene that migrate (67). MFs trapped within peapods also exhibit rotation and translation motion of the entire molecule.

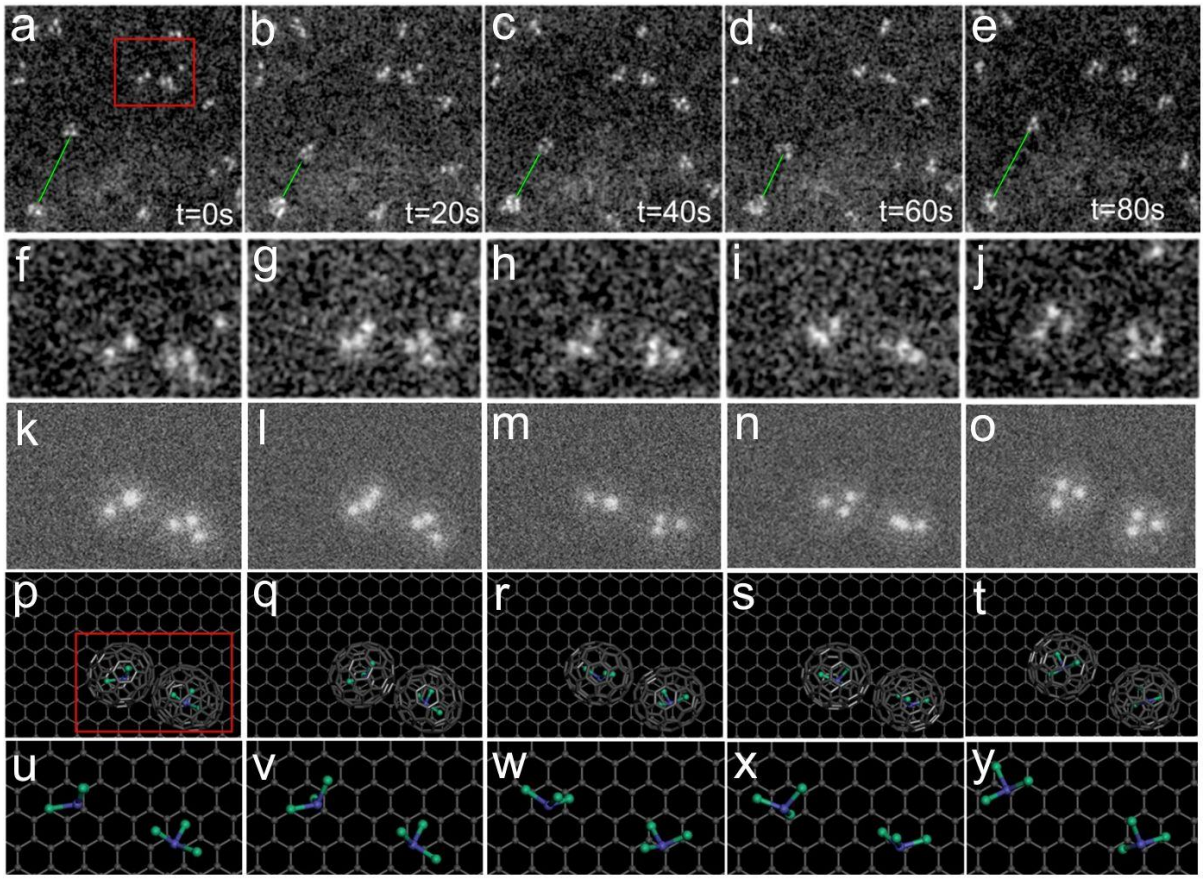

Figure 4.13. (a)-(e) Time series of ADF-STEM images recorded at 200kV (dose: 5.6 x 10^8 e s^{-1}), 20 s apart, showing trimer dynamics. The green line indicates translation migration of one EMF relative to another. Magnified views are shown in (f)-(j) from the red boxed region indicated in (a). (k)-(o) Multi-slice ADF STEM image simulations with added noise based on the atomic models shown in (p)-(t). (u)-(y). Enlargement of the red boxed area in (p), with the fullerene cage removed to reveal the relative orientations of the Gd trimer.

4.3.3. Fullerene Disintegration: *In-situ* heating & H_2 annealing

In-situ heating

To further explore the behavior of EMFs on graphene surface, *in-situ* heating was utilized to provide thermal energy to initiate chemical reactions. All the experiments from now on, have been conducted at 60keV to better understand the dynamics of this carbon nanomaterials with reduced beam damage. This also has the benefit that beam induced contamination is significantly reduced at higher temperatures. Our first set of observations were made at 300^{o}C, where several EMF molecules were observed isolated and immobilized on the graphene surface (**Figure 4.14**). **Figure 4.14**a shows a low magnification ADF-STEM

image of monolayer graphene on the *in-situ* heating TEM chip with deposited $Gd_3N@C_{80}$ at 300°C. The weak intensity visible is indicative of the surface coating of the EMFs on graphene before high temperature is reached. **Figure 4.14**b shows a higher magnification ADF-STEM image of the sample after heating to 500°C *in-situ*. Large sections of clean graphene are visible, along with a thin surface carbon layer and bright intensity from Gd atoms in both clusters and as isolated EMFs. The higher magnification ADF-STEM image in figure 4d clearly shows this, with yellow circles indicating immobilized $Gd_3N@C_{80}$ EMFs attached to the surface carbon layer. Some other impurity atoms are also present showing intensities that are higher than those from carbon but less than the heavy Gd; most likely these are Si atoms that are known to be contaminants in graphene samples grown in quartz tubes by CVD method[40]. The EMF circled in red within the red boxed region in **Figure 4.14**c is shown in more detail in **Figure 4.14**d-e. The Gd trimer is clearly visible in **Figure 4.14**d-e, along with diffuse intensity from the fullerene cage. The EMF is attached to the side of the surface carbon layer and sits on top of graphene. The power spectrum inset to **Figure 4.14**d shows the hexagonal reflections associated with monolayer graphene. The yellow box in **Figure 4.14**d shows an empty fullerene cage after Gd atoms have been released. The Gd-Gd spacing was measured from figure 4e, using line profiles, showing an average Gd-Gd distance of 0.34+/-0.02nm, which is in excellent agreement with the known Gd-Gd distance in $Gd_3N@C_{80}$.(244) Since the molecules have different orientation, the error in distance measurement comes from the degree of rotation. The line profile analysis in **Figure 4.14**f shows increased intensity at the edges of the EMF confirming the spherical nature of the object, rather than a flat disk which would have uniform contrast profile.

[40] The CVD reactor chamber used for the growth of graphene, is made of quartz-tube furnace, which is composed of fused quartz or fused silica, i.e. amorphous SiO_2. The phase transition of quartz, which happens during the CVD growth, leads to the contamination of graphene surface with Si or SiO_2 during the graphene growth process.(399) As shown in **Figure 4.11**, there is presence of Silicon in the samples, as analysed from the EDS spectrum.

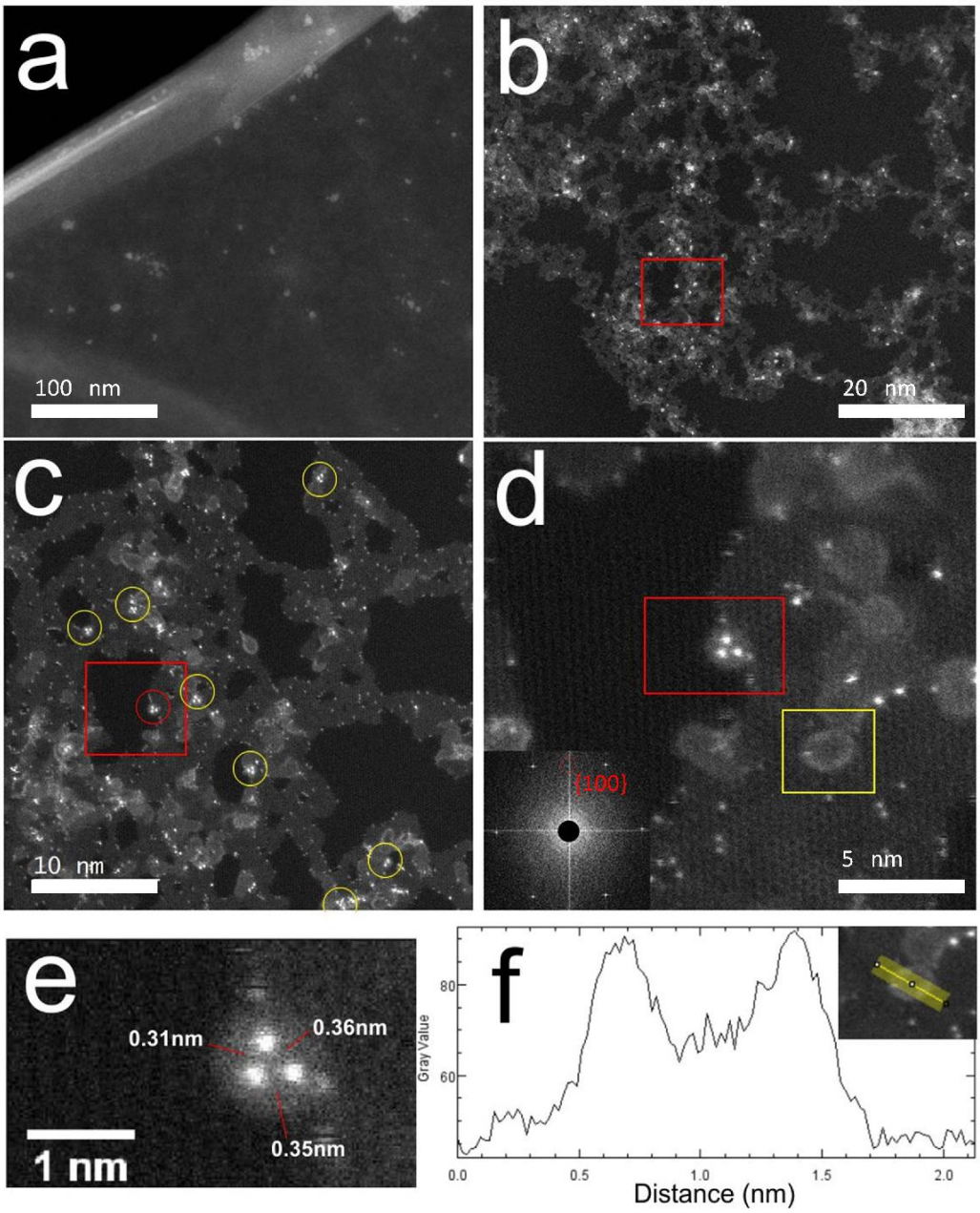

Figure 4.14. *In-situ* ADF-STEM images of $Gd_3N@C_{80}$ on graphene recorded at 60kV (dose: 5.6 x 10^8 e s^{-1}). (a) Low magnification ADF-STEM image of graphene suspended on an *in-situ* heating TEM grid with deposited EMFs. Temperature is 300ºC. (b) ADF-STEM image at 500ºC showing graphene with surface material. (c) ADF-STEM image from the red boxed area in (b) showing clean pristine patches of graphene along with a thin surface layer of carbon glass, with individual EMFs attached, indicated by the yellow circles. (d) ADF-STEM image from the red boxed region in (c) showing a single $Gd_3N@C_{80}$ attached to the edge of the surface carbon glass. Inset shows the power spectrum indicating that monolayer graphene supports this region. The red boxed area shows the single EMF and the yellow boxed area shows an empty fullerene cage attached to the surface. (e) ADF-STEM image from the red boxed area in (d) showing a single $Gd_3N@C_{80}$. Distances between Gd atoms are indicated. (f) Line profile taken across the empty fullerene cage, from the yellow boxed area in (d), showing increased intensity at the edge that is typical for fullerene cage. Inset shows the location of the line profile. *In-situ* temperatures are: (a) 300ºC, (b)-(f) 500ºC

Figure 4.15 shows a series of ADF-STEM images recorded at 500^{o}C that capture the metal cargo release onto the carbon glass and subsequent decomposition of the C_{82} cage, followed by its fusion with the surface monolayer carbon glass[41]. This process is driven *in-situ* by the combined result of heating and high energy electron beam induced effects. The transformation occurs sufficiently slowly to capture the fullerene cage opening. Multislice image simulations were used to help understand the expected intensities from the decomposing and fusing EMFs, **Figure 4.15**f-j, based on schematic atomic models shown in **Figure 4.15**k-o. After breaking the C_{82} cage, the pyramidal structure of the Gd_3N trimer(248) becomes energetically unstable, leading to the breaking of the Gd-N bonds and single Gd atoms diffusing across the carbon glass, **Figure 4.15**d,e or migrating across the edges (S.I. 1). The schematic atomic models in **Figure 4.15**p-r illustrate the process where $Gd_3N@C_{80}$ is first immobilized by attachment to the edge of the existing surface carbon layer on top of graphene (**Figure 4.15**p) followed by cage opening (**Figure 4.15**q). After Gd metal release the cage fuses with the surface carbon to enlarge its area (**Figure 4.15**r). This suggests that the surface carbon layer present in the sample also contains material from other fused fullerene cages to form this monolayer carbon glass, which is ideal for adhesion of Gd atoms due to its amorphous nature. Gd atoms are typically seen attached to either the edge of this surface layer, or to defective regions on the surface (**Figure 4.15**e). Gd is an unusual rare earth metal dopant in graphene which has been shown to produce n doping in the material with a doping efficiency of 0.7 electrons per Gd atom.(230) Moreover, it has been reported that the magnetic moments of the outer orbital of the atom (6s, 5p, 5d) has been shown to enhance after the atoms get adsorbed to the surface of graphene.(230) The facile way of introducing these Gd atoms to

[41] It was deduced that the 2D layer is indeed carbon glass instead of graphene because it consisted of 4, 5, 6-carbon rings fused together to form a 2D network instead of crystalline 6-carbon ring structures. A typical image of a carbon glass has been shown in **Figure 4.15**.

graphene, with the use of fullerene cages, can help carrying out these experiments easily, and can potentially lead to discovery of novel electron phenomenon which can change the electrical properties of graphene.

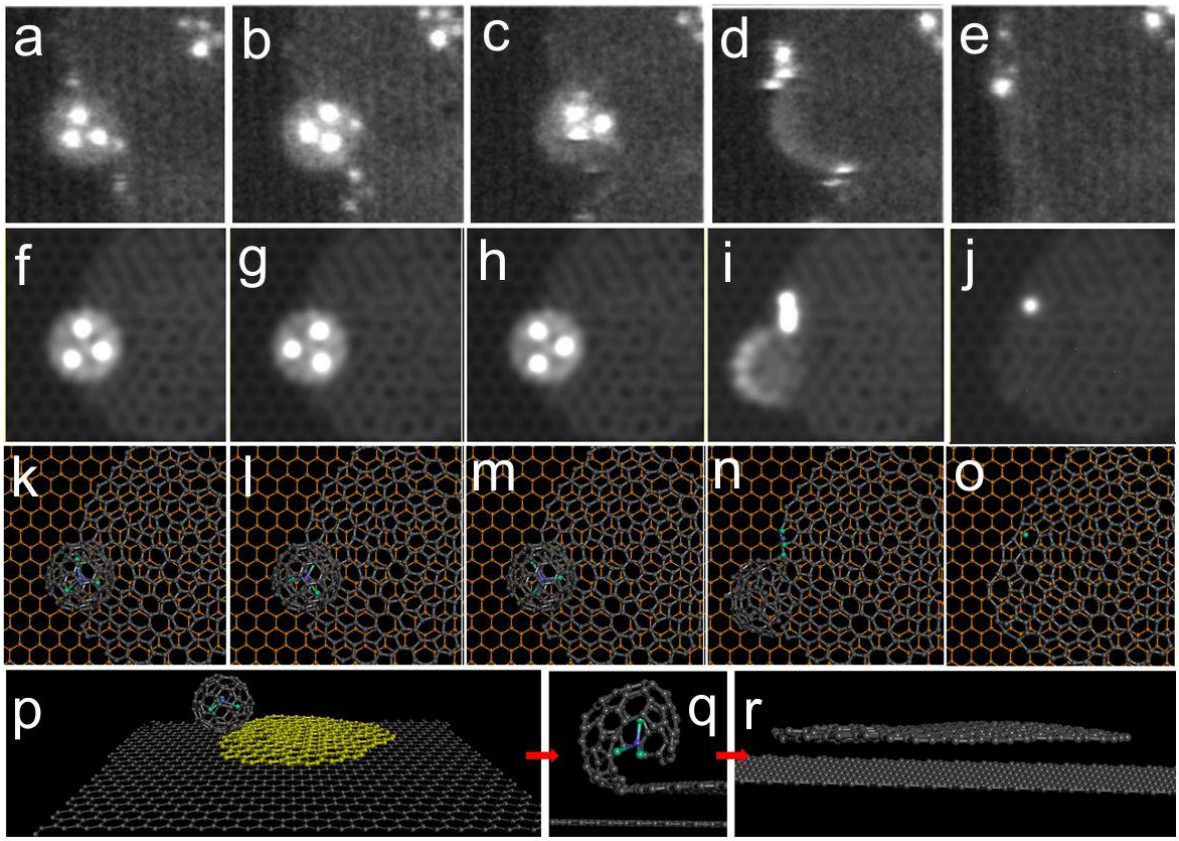

Figure 4.15. (a)-(e) Time series of ADF-STEM taken at 60kV (dose: 5.6 x 10^8 e s^{-1}) images showing an individual $Gd_3N@C_{80}$ attached to the side of surface carbon layer which fuses, with the release of Gd atoms. Temperature is 500°C; 60kV accelerating voltage. Time between images ~20s. (f)-(j) Multislice image simulations based on the atomic models in (k)-(o), schematically illustrating $Gd_3N@C_{80}$ fusion and Gd atomic release from the cage. (p) 3D schematic model showing a $Gd_3N@C_{80}$ attached to patch of surface carbon (yellow) on graphene. (q) Side view of a schematic atomic model showing cage rupturing and fusion to the surface carbon. (r) 3D schematic model showing how the cage fusion into the surface carbon layer causes the expansion of the surface region.

Similar phenomenon could be seen even when fullerenes were trapped within two graphene layers, forming a sandwich structure. **Figure 4.16** shows a typical example of a sandwich structure where the metallofullerenes are captured fusing into the surface carbon glass. CVD grown bilayer graphene has consistent stacking order and have same orientation.(249) The moire patterns in the images show that there is indeed two separate layers

of graphene transferred on the grid instead of bilayer graphene formed from CVD method. Similar to what was observed in an 'open sandwich', the C_{82} cage in the graphene sandwich also breaks and releases the Gd atoms onto the amorphous carbon surface. Because the Gd_3N is energetically unstable, after the cage opening, the Gd_3N loses its pyramidal structure and the Gd-N bonds break. The Gd atoms escapes, migrating across the edges of the amorphous carbon glass. The Gd atoms are readily visible under the ADF-STEM mode because of the heavy Gd atom but Nitrogen being a very light element, has very low contrast and hence is not visible in the images. The red box and the arrow in figure shows the fullerene atom attached to the edge of the amorphous carbon. The EEMF is intact and visible clearly in **Figure 4.16**a and slowly the cage opens up and leads to the residue carbon bonding to the glassy amorphous carbon on top of the graphene (**Figure 4.16**i). The red arrow in the figure shows the Gd atoms escaping from the cage and migrating on the surface. The images are taken at 700℃. This shows that the fullerene cage disintegration is a result of the temperature and it took a little higher temperature to break the material in a sandwich structure as compared to the open-sandwiches. The result can be explained by the thermal conductivity of graphene which is very high, and thus the presence of a protective layer required higher thermal energy to break these cages.(250,251)

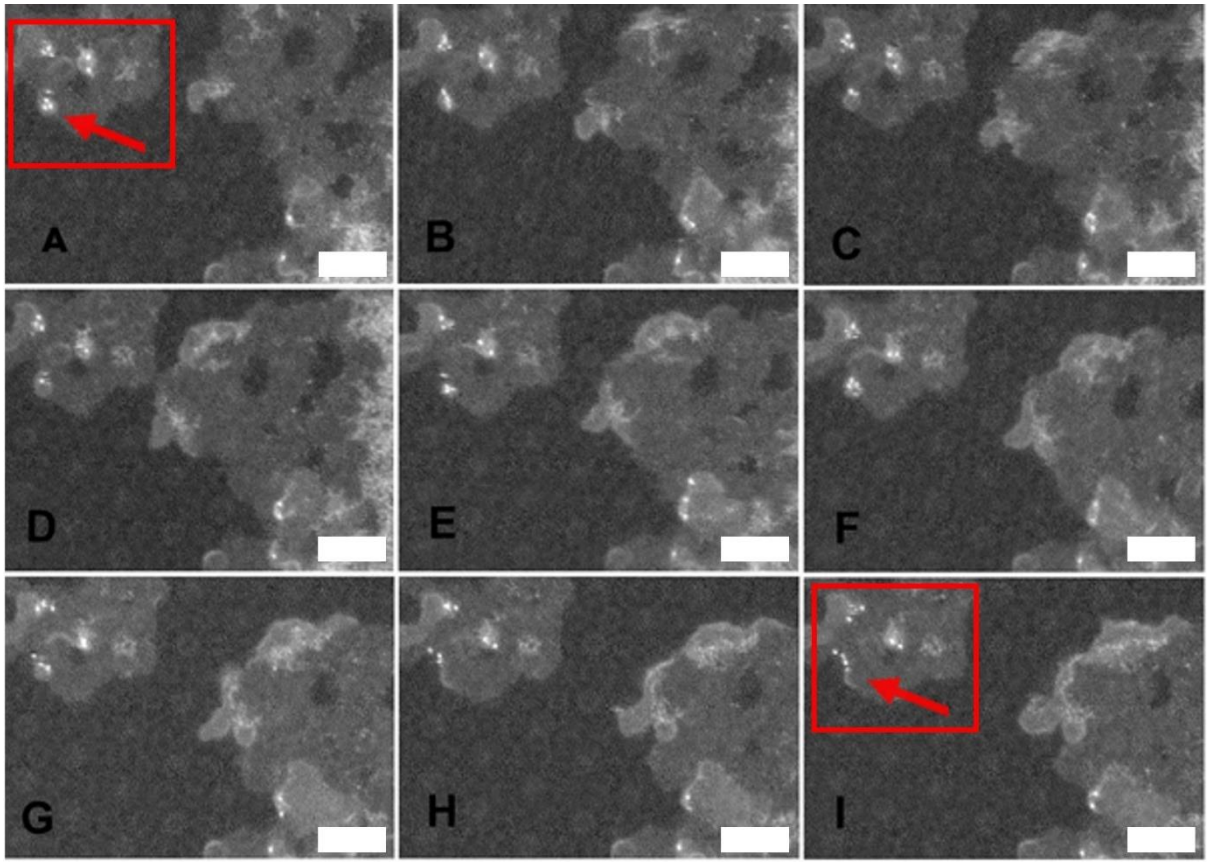

Figure 4.16. (a)-(i) Time series of ADF-STEM images taken at 60keV (dose: 5.6 x 10^8 e s^{-1}), showing the fusion of $Gd_3N@C_{80}$ with into the surface carbon glass on graphene and the release of Gd atoms. Time between frames is ~20s. The scale bars correspond to 5nm.

Hydrogen Annealing

The data from *in-situ* experiments shown in **Figure 4.14**, **Figure 4.15** and **Figure 4.16** were generally carried out at 500°C, above the sublimation point of the EMFs (~350°C under high vacuum conditions) and therefore only a small density of EMFs were found on the surface. In order to explore the activation of Gd atom release from EMFs onto graphene surfaces at lower temperatures below the sublimation temperature, hydrogen gas annealing was used at a temperature of 300°C. The aim of this was to enable a higher density of Gd decoration on the graphene surface. Talyzin *et. al.* studied C_{60}, showing that an increased hydrogenation period results in the fragmentation of the hydrogenated fullerenes following a CH_2 loss pathway.(252) It can be predicted that similar reaction should be active for higher

fullerene cages leading to cage opening and thus release of the Gd atoms onto the surface of graphene, as shown schematically in **Figure 4.17** below.

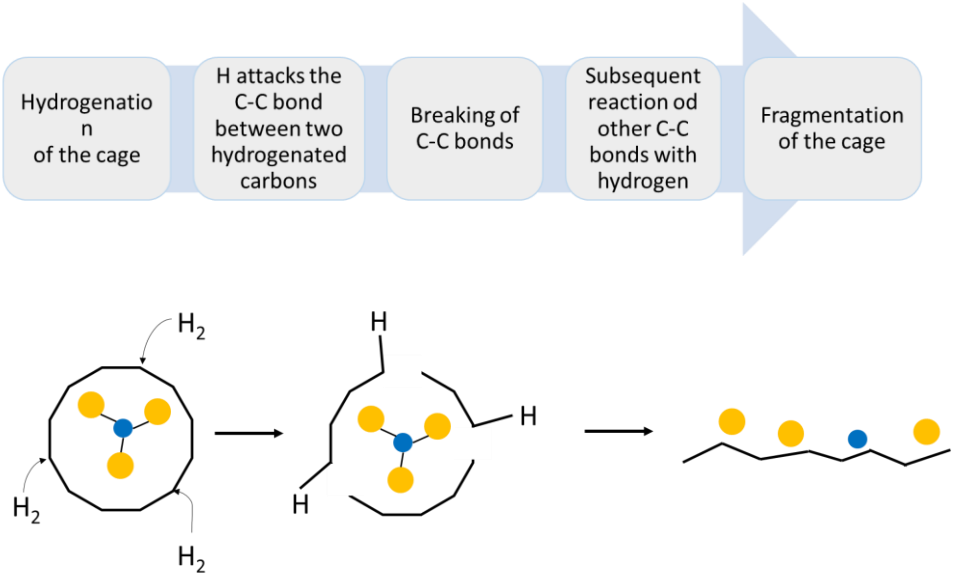

Figure 4.17. Flow chart as well as reaction schematic of proposed pathway for disintegration of higher fullerene cage in the presence of hydrogen.

Figure 4.18 shows ADF-STEM images of graphene: $Gd_3N@C_{80}$ samples on *in-situ* heating TEM chips that had been treated under hydrogen for 12 hrs. *In-situ* ADF-STEM imaging was carried out at 300^{o}C to prevent beam induced contamination. **Figure 4.18**a shows bright intensity features on the graphene region, distinctly different to the diffuse appearance seen in samples not treated with hydrogen annealing (**Figure 4.14**a). Higher magnification ADF-STEM images, **Figure 4.18**b-e, show that this area consists of Gd nanoclusters that formed on the surface, and that the surface of graphene is also covered with a carbon layer. In this area the Gd concentration appeared high and thus it contained some of the largest Gd clusters observed that were typically 2-4 nm wide and ranging from 1-3 atomic layers of Gd, as estimated from intensity profiles. **Figure 4.18e** shows a 2.5nm Gd nanocluster that is predominantly one atom thick, but with some secondary Gd atoms on top. The inset shows a colour version of the ADF-STEM image of the nanocluster showing two levels of intensity, one for single Gd atoms and the other where it is two Gd atoms thick. This is confirmed by

line profile analysis comparing the nanocluster to an isolated Gd atom (**Figure 4.18**f). No intact $Gd_3N@C_{80}$ EMFs were observed on the surface, due to their decomposition and furthermore most of the fullerene cages were fused within the surface carbon layer on graphene.

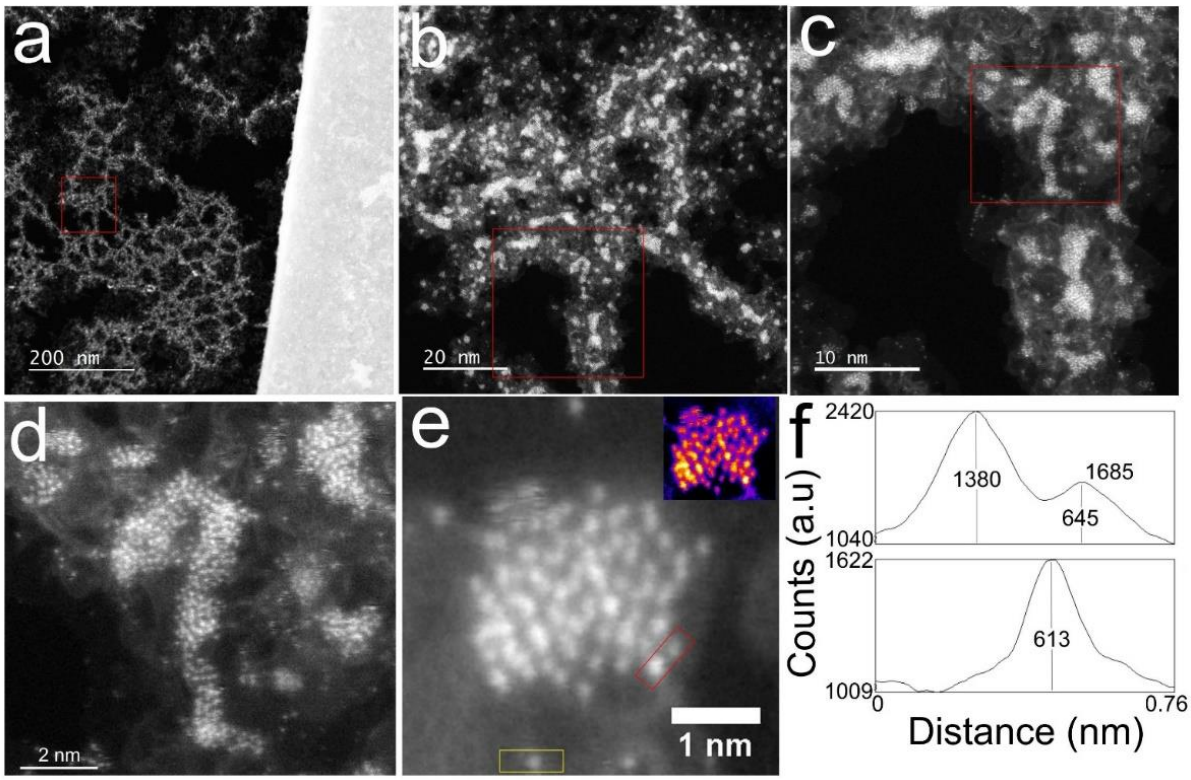

Figure 4.18. Low magnification ADF-STEM image of graphene:$Gd_3N@C_{80}$ after hydrogen annealing on an *in-situ* SiN TEM chip, taken at 60keV (dose: 5.6 x 10^8 e s^{-1}). The SiN area is on the right. The temperature is 300°C images were recorded at 60kV. (b) Higher magnification ADF-STEM image taken from the red box area in (a). (c) Higher magnification ADF-STEM image taken from the red box area in (b). (d) Higher magnification ADF-STEM image taken from the red box area in (c). (e) ADF-STEM image of a typical Gd nanocluster on the surface of graphene. The inset shows a colour version of the nanocluster to highlight the difference in intensity between single Gd atoms and regions with two Gd atoms in projection. A band pass filter with 100-1 pixel range was applied to the power spectrum to remove the long range intensity variations. (f) Line profiles taken from regions marked by the red box (top) and yellow box (bottom) in (f).

Apart from the high density area shown in **Figure 4.18**, the majority of the sample contained smaller 1-2nm Gd clusters (**Figure 4.19**), most likely from an area having initial lower $Gd_3N@C_{80}$ concentration before hydrogen annealing. **Figure 4.19**c shows small Gd clusters containing typically 10-20 Gd atoms, and **Figure 4.19d** shows a spherical fullerene-

like feature that is located within the surface carbon region on graphene. There are also regions of the sample that have even lower Gd concentration (**Figure 4.19**e), and have isolated Gd atoms and small dimers and few atom clusters.

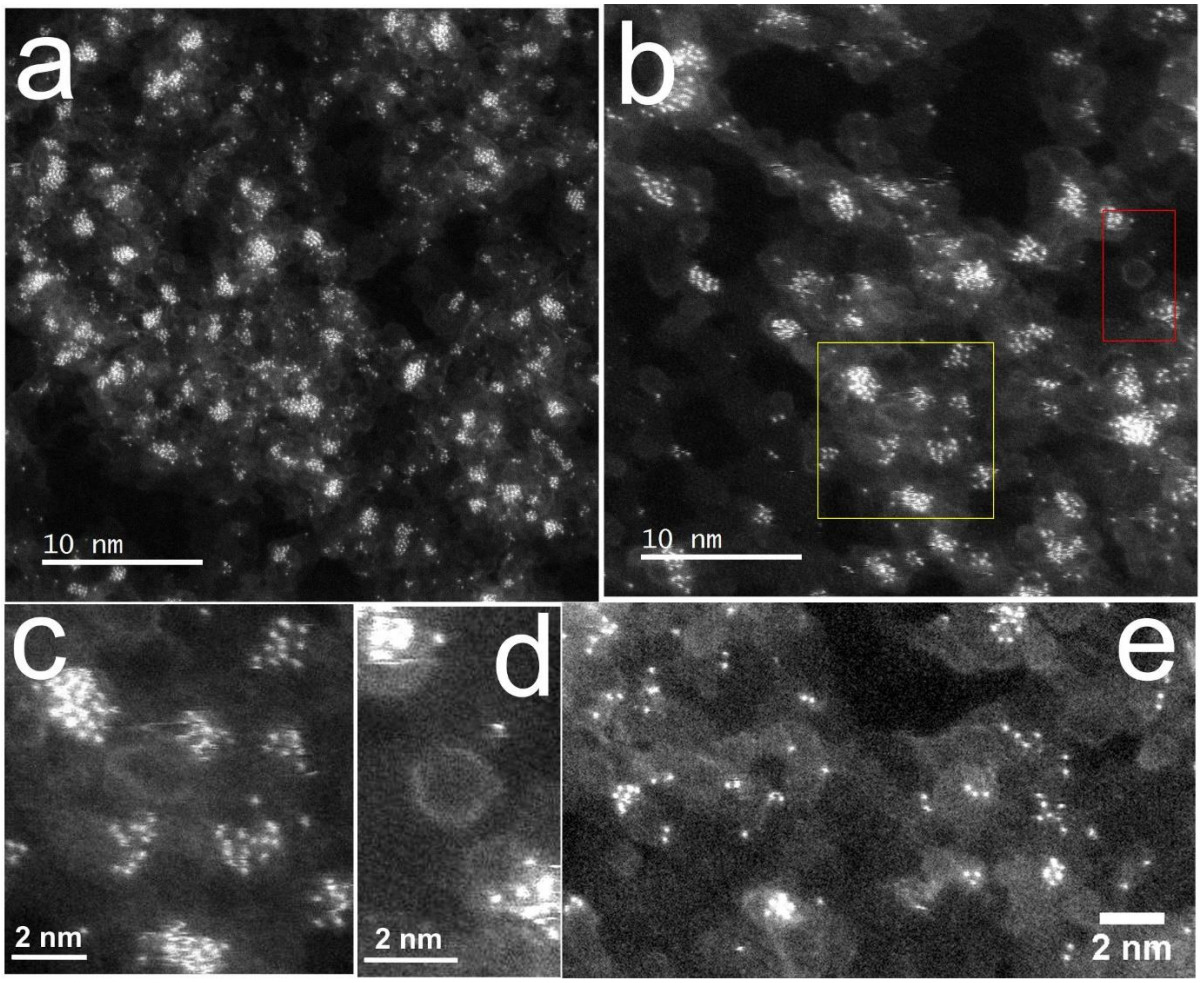

Figure 4.19. (a) ADF-STEM image of graphene:$Gd_3N@C_{80}$ after hydrogen annealing on an *in-situ* SiN TEM chip, taken at 60keV (dose: 5.6 x 10^8 e s^{-1}). The temperature is 300ºC and images were recorded at 60kV. Image taken from an area of lower Gd concentration. (b) ADF-STEM image taken at higher magnification showing 1-2nm Gd clusters on the surface of graphene, along with a visible surface carbon layer that has spherical intensity features. (c) Higher magnification of the region indicated with the yellow box in (b) showing small Gd clusters. (d) Higher magnification image taken from the red boxed region in (b) showing a fullerene-like feature in the carbon material on graphene. (e) ADF-STEM image from a low Gd concentration region showing many single Gd atom dispersions and small dimer and few atom clusters.

4.3.4. Atom Migration

In-situ dynamics of Gd atom migration is shown in **Figure 4.20**, from the region around the yellow box in **Figure 4.20**d. This area contains a thin monolayer of surface carbon

on graphene with three empty fullerenes attached to a small central region of a thicker carbon layer, the empty fullerenes indicated with yellow circles in **Figure 4.20**a, and six individual Gd atoms indicated with red circles and numbers in **Figure 4.20**a. The Gd atoms are clearly mobile, with the yellow spot in **Figure 4.20**b indicating the position jump. The green shaded area shows the underlying monolayer graphene. Gd atoms 1-3 remain localized throughout the sequence, whereas Gd atoms 4-6 are highly active and by **Figure 4.20**h, these have aggregated into a small cluster on the surface region, away from an edge site. The empty fullerene cage on the right in **Figure 4.20**a, hosting Gd atom 6, exhibits rotation between frame (a) and (b), which is shown at higher magnification in **Figure 4.20**i,j. The fullerene appears to have one part anchored to the edge of the central surface carbon material and rotates anti-clockwise. In many cases empty fullerene cages are also observed to migrate and move around the sample. Between **Figure 4.20**d and **Figure 4.20**e, the fullerene actually detaches and migrates to the right leaving a vacant area where the single Gd atom 6 is now bound to the surface carbon layer. The Gd atom 6 is most likely bonded within the carbon layer, immobilizing it and subsequently Gd atoms 4 and 5 migrate to join it, forming the trimer cluster, shown in detail in **Figure 4.20**k. The trimer cluster has Gd-Gd distances that are shorter than the Gd-Gd distances observed within the original $Gd_3N@C_{80}$, due to the presence of N in the trimer core of the EMF leading to larger bond distances,(244) **Figure 4.20**l.

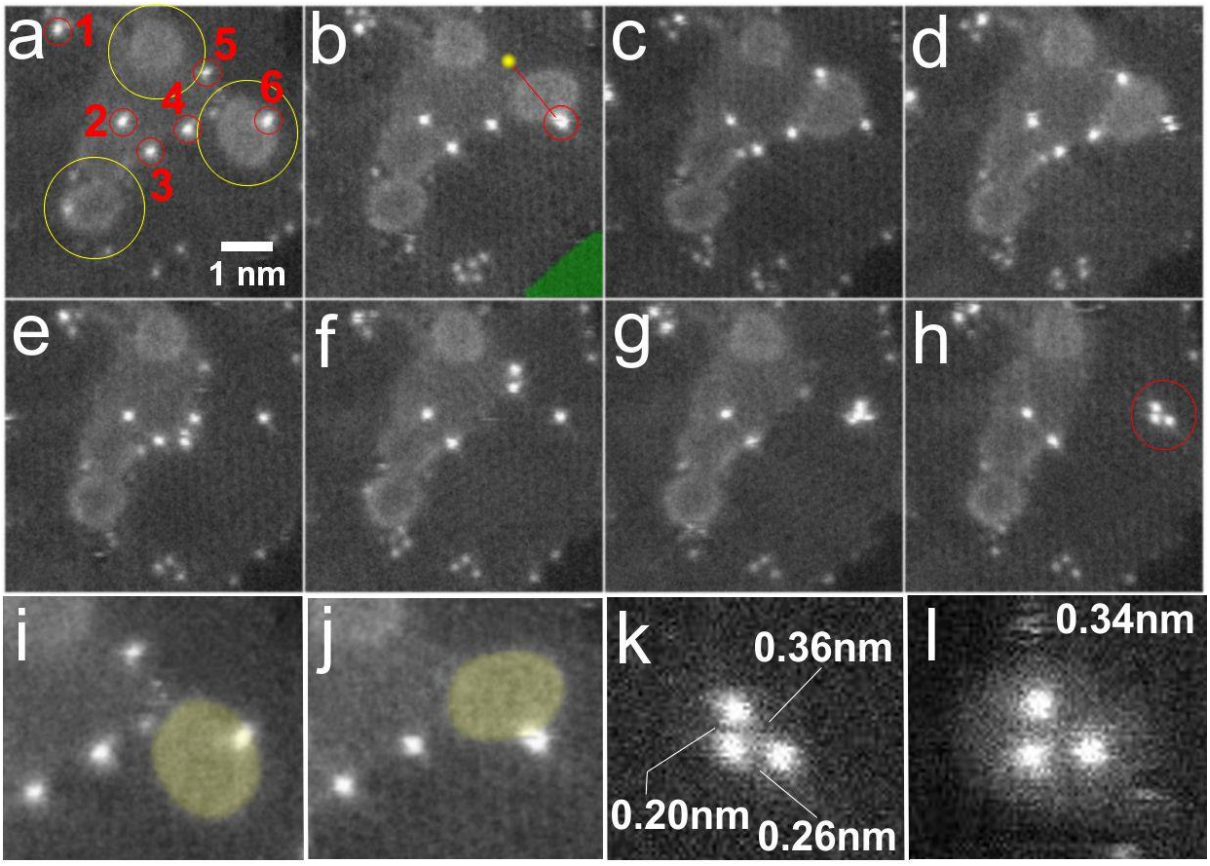

Figure 4.20. (a)-(h) Time series of *in-situ* ADF-STEM images recorded at 500^{o}C and 60kV accelerating voltage, (dose: 5.6 x 10^{8} e s^{-1}), showing migration of single Gd atoms (red circles and numbers in (a)) and movement of empty cages (yellow circle in (a)) on the surface carbon layer on graphene. The green area in (b) indicates a monolayer graphene region. The yellow spot and red line in (b) indicates the initial movement of a Gd atom from the prior frame. Time between frames is 20s. (i)-(j) Magnified views from (a) and (b) of the righthand fullerene cage. Yellow shading indicates the fullerene cage. (k) Magnified view of the Gd cluster indicated by the red circle in (h), with Gd-Gd distances determined from a line profile analysis. (l) ADF-STEM image of a $Gd_3N@C_{80}$ showing a Gd trimer for comparison with the Gd cluster in (k). Distance indicates the average Gd-Gd value.

Figure 4.21 shows another example of Gd atomic migration. **Figure 4.21a** – c, g-i; m-o is the time series of images (taken every 30 seconds) of the migration of Gd atom along the edge of amorphous carbon. **Figure 4.21**d-f; j-l; p-r correspond to **Figure 4.21**a – c; g-i; m-o respectively and highlights the Gd atoms and clusters. The green circle in the image sequence shows the binding of one Gd atom to the amorphous carbon dangling bond. It also shows that Gd atom does not etch away the graphene or the amorphous layer from the edges. The yellow circle shows the Gd clusters and other individual Gd atoms are shown in red cicles. The

clusters form (**Figure 4.21**i, l) as well as break (**Figure 4.21**n, q) while the Gd moves along the edges of the amorphous carbon to form a stable arrangement of gadolinium atoms in 2D space (**Figure 4.21**o,r).

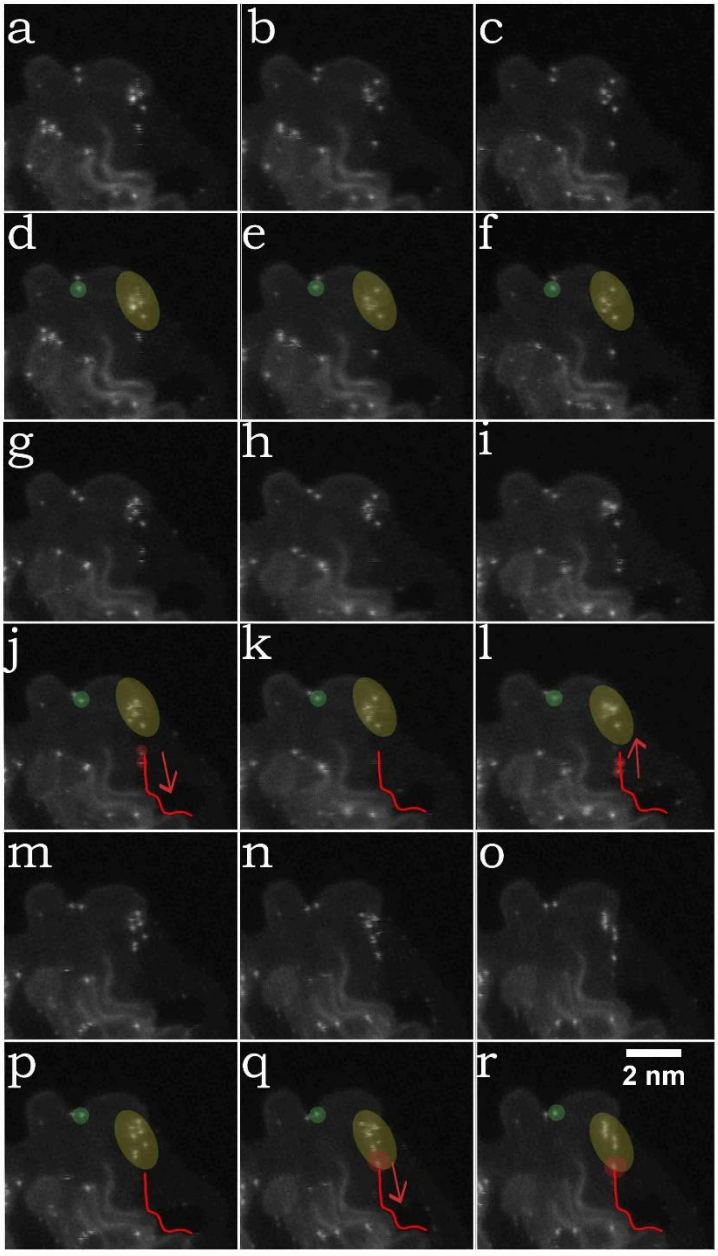

Figure 4.21. (a)-(c), (g)-(i), (m)-(o). Time series of ADF-STEM images showing Gd atom migration, taken at 60keV (dose: 5.6 x 10^8 e s^{-1}). Time between frames is 30s. (d)-(f), (j)-(l), (p)-(r) are the annotated version of the images above.

Another series of images showing migration of Gd atoms around amorphous carbon glass on graphene. The following sequence of images **Figure 4.22**(a-c) also show the migration of single Gd atoms on the amorphous carbon glass on graphene. **Figure 4.22**d-f are

the colour images. The first Gd atom in **Figure 4.22**a and **Figure 4.22**i gets trapped in the central region and remains fairly localized for the duration of imaging whereas the rest of the Gd atoms from a larger nanocluster join to form a cluster.

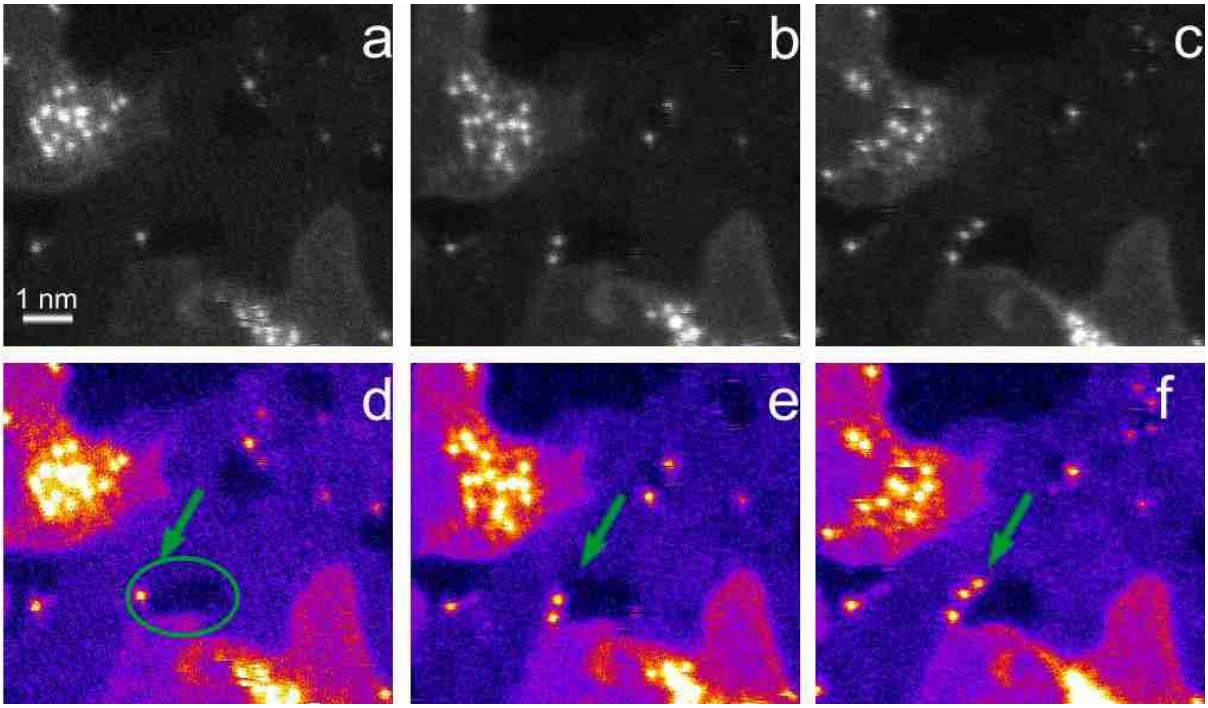

Figure 4.22. (a)-(c)Time series of ADF-STEM image taken at 60kV (dose: 5.6 x 10^8 e s^{-1}), taken at 500°C, showing Gd atom migration across surface carbon glass on graphene. (d)-(f) False color versions of (a)-(c). Time between images is ~30s.

To accelerate the Gd atom diffusion dynamics, temperature of the *in-situ* chip was increased to 900°C (**Figure 4.23**). During the *in-situ* heating process from 300°C to 900°C, increased migration rates of Gd atoms was observed, allowing the study of Gd atom dynamics and cluster formation. **Figure 4.23** shows a time series of ADF-STEM images of cluster formation from Gd atoms at 900°C. **Figure 4.23**a shows a hole (white circle), in the surface carbon that gets filled by mobile Gd atoms by **Figure 4.23**i. The Gd atoms are likely diffusing from the larger nanoclusters above and across the top of the surface carbon layer (**Figure 4.21** and **Figure 4.22**). Atomic model schematics of the Gd filling of the hole are shown in figure **Figure 4.23**k-m and figure **Figure 4.23**n and **Figure 4.23**o show the same region before and after filling with Gd atoms. **Figure 4.23**o shows that the small cluster is single atom thickness

as determined by the ADF-STEM intensity at each atomic position. The 2D lattice of Gd has a periodic arrangement of Gd atoms which are about 0.35 nm ± 0.2 nm apart. The distance within this 2D lattice is about 0.2nm larger than that of the known distance of Gd atoms in bulk hcp. The presence of more Gd atoms at one place, which is expected from the drop casting method, also led to the formation of a 3D crystal structure corresponding to a hexagonal close packed arrangement.

The size of the hole in the amorphous carbon in **Figure 4.23** is constant, which indicates that Gd atoms do not etch the graphene or the amorphous carbon at the edges, in contrast to previously published work (253). The increased mobility of Gd atoms at 900^{o}C indicates that this phenomenon happens due to the heating of the sample and is not driven by the electron beam. The Gd atoms only become temporarily localized on the amorphous carbon surface or along the edges and not on the pristine graphene surface, giving rise to step by step hopping and the absence of Gd atoms on pristine graphene regions, which agrees with previously published results (121). Pinning of Gd clusters to the edges of the amorphous surface carbon was also observed, even after a considerable amount of time (10 min of e-beam exposure) which may indicate that the Gd atoms bonded to the lattice become embedded in the graphene as dopants.

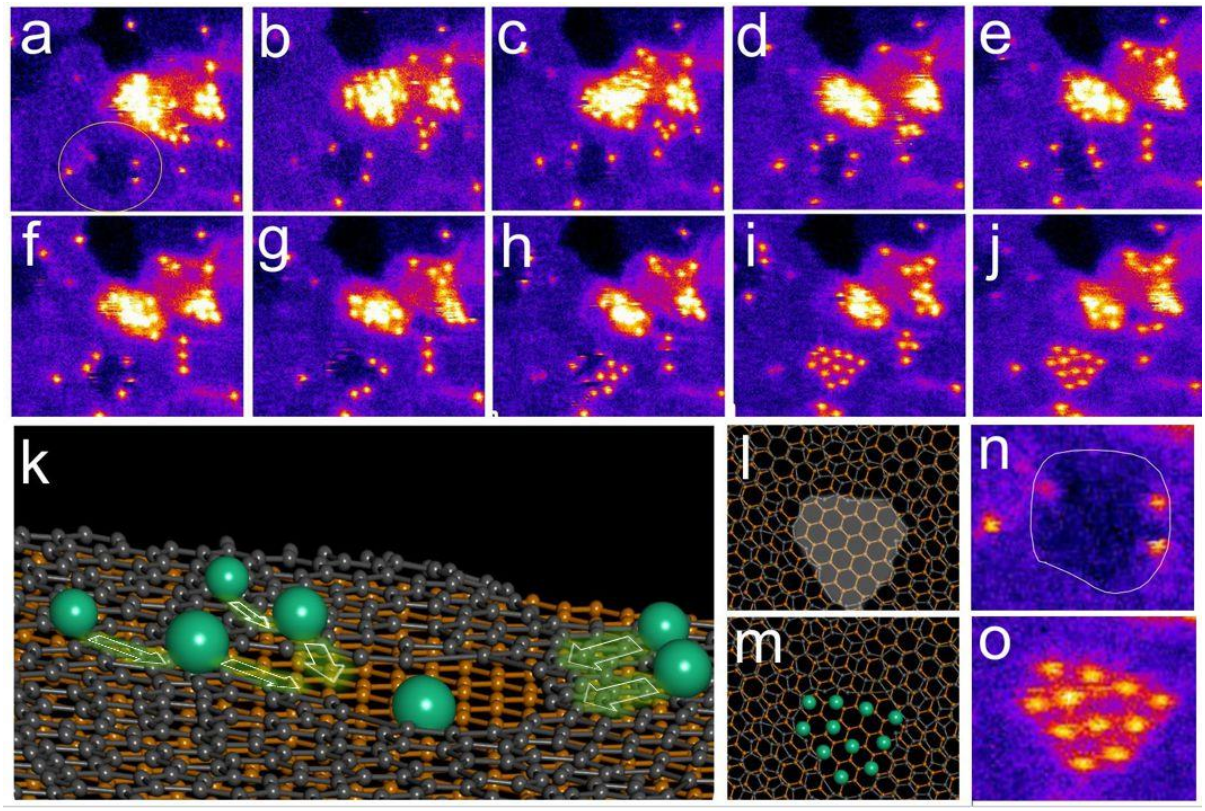

Figure 4.23. (a)-(j) Time series of ADF-STEM images recorded at 900°C at an accelerating voltage of 60kV (dose: 5.6 x 10^8 e s^{-1}), of Gd atoms migrating across the surface of graphene. Colour is used to increase the contrast from Gd atoms. The circle in (a) indicates a void in the surface carbon layer that acts as a sink to trap mobile Gd atoms. Time between frames is ~20s. (k) Schematic atomic model illustrating the migration of Gd atoms into the hole present in the monolayer surface carbon layer that resides on the graphene. (l) Schematic atomic model showing a hole (white shaded area) in top view and (m) after filling with Gd atoms (green). (n) ADF-STEM image of the region indicated by the circle in (a) of the hole and (o) the same area from (j) with Gd filling.

Edge mediated diffusion of Gd atoms also occurs as shown in detail in **Figure 4.24**, where sequential ADF-STEM images were taken from the same hydrogen annealed graphene: $Gd_3N@C_{80}$ sample examined in **Figure 4.19**, **Figure 4.20, Figure 4.21, Figure 4.22, Figure 4.23**, again measured *in-situ* at 900°C. Annotated images are displayed below each respective ADF-STEM image in **Figure 4.24**, showing the Gd atoms as yellow spots, the graphene monolayer in orange, the monolayer surface carbon as green and the secondary surface carbon layer as cyan. White lines are marked on **Figure 4.24**e to indicate the edge regions. Red circles in **Figure 4.24**e show Gd atoms that remain localized during the imaging. The white arrows

are used to indicate the general migration direction of atoms in the frame. In **Figure 4.24**g, one Gd atom has diffused across the surface carbon layer to be trapped in the central region and remains fairly localized during the subsequent imaging. However, the Gd atoms indicated in **Figure 4.24**e were generally mobile and end up migrating on the step edge between the graphene and the monolayer surface carbon during the image sequence (**Figure 4.24**i-l). One by one, Gd atoms migrate around the edge region confirming that the edge mediates a diffusion pathway.

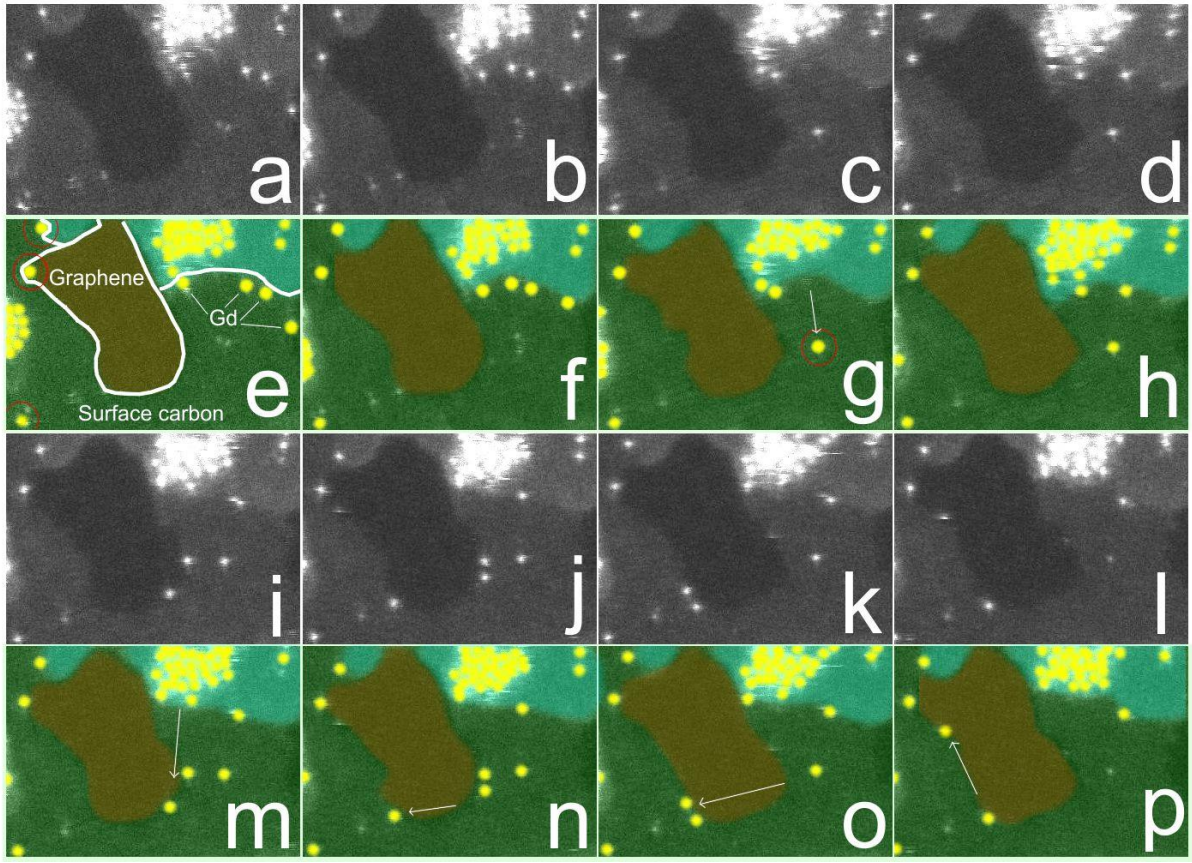

Figure 4.24. (a)-(d),(i)-(l) Time series of ADF-STEM images, taken at 60keV (dose: 5.6 x 10^8 e s^{-1}), taken from a hydrogen annealed graphene:$Gd_3N@C_{80}$ sample with *in-situ* heating at 900°C showing diffusion of Gd atoms around the edge of the surface carbon regions on graphene. Time between frames is 20s. (e)-(h),(m)-(p). Annotated images from the ADF-STEM images are shown above each, with Gd atoms in yellow, graphene in orange, the green area showing monolayer surface carbon and cyan showing bilayer surface carbon. White arrows indicate the general direction of atom migration. All images were recorded at 60kV.

Finally the time-dependent cluster-cluster interactions was studied, at the sub-10 atom level (**Figure 4.25**), in the same samples as in **Figure 4.23** and **Figure 4.24** (Hydrogen

annealed and *in-situ* at 900°C). The Gd clusters in **Figure 4.25** reside on top of the surface carbon layer and yellow circles are used to indicate two small Gd clusters of 5 atoms and one larger of ~17 Gd atoms in **Figure 4.25**a. The larger cluster then splits into three smaller ones in **Figure 4.25**b, reassembles back into a larger linear cluster (**Figure 4.25**c), before splitting up again into three smaller clusters as shown in **Figure 4.25**d. The two smaller clusters from **Figure 4.25**a remain fairly constant in size and structure during this process. The small clusters of ~5 Gd atoms typically have Gd-Gd distances of 0.35nm[42], similar to those in **Figure 4.23**o and adopt similar in-plane arrangements. From **Figure 4.25**d-f, the three small clusters that came from the fragmentation of the larger cluster in figure 11c, remain separated before recombining as shown in **Figure 4.25**g, and remain in this configuration in **Figure 4.25**h. These time series of images show that small Gd clusters of ~5 atoms are relatively stable and rapidly fragment from bigger clusters on the surface carbon layer at high temperatures of 900°C, and do not aggregate into larger nanoclusters. Although the cluster fragmentation is slower at lower temperature, they still show energetically more stable states in 2D space instead of 3D clusters. The surface carbon layer is known to be highly defective and is thus likely to offer multiple binding sites to stabilize the Gd atoms and reduce their migration.

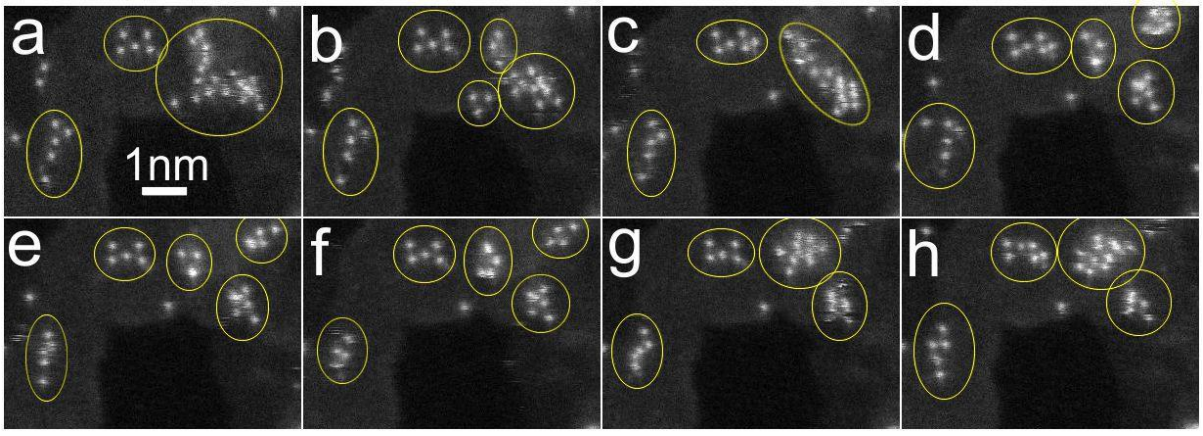

Figure 4.25. (a)-(h) Time series of ADF-STEM images taken from a hydrogen annealed graphene:$Gd_3N@C_{80}$ sample with *in-situ* heating to 900°C, taken at 60keV (dose: 5.6 x 10^8 e s^{-1}). Time between images is 20s. Yellow ovals indicate clusters.

[42] The distance is close to the Gd metal crystal structures which form hcp structure with a=0.362 nm.

4.4 Conclusion

The results described reveal how single rare earth metal atom dopants can be delivered to the surface region of 2D materials, with good dispersion and stability up to temperatures reaching 900^{o}C in vacuum using a molecular precursor deposited from solution. An *in-situ* heating holder is used to heat the EMF-graphene film stepwise to 900^{o}C, with atomic resolution tracking of the structural transformation pathways using STEM. This was carried out by using FIB to cut slits into a SiN heating chip and transferring graphene suspended across the slit. *Ex-situ* experiments are performed using hydrogen to achieve EMF cage rupture at low temperatures and subsequent Gd atom decoration across monolayer graphene surfaces.(252) The molecular precursor was in the form of an endohedral metallofullerene. ADF-STEM images revealed the atomic level structure and dynamics of Gd atoms during their temperature dependent transformation. Longer time-lapse studies and higher temperature studies have been carried out using ADF-STEM at 60kV to avoid damage of the graphene.(254,255) The surface carbon layer on graphene played an important role to first provide anchor sites for EMFs to bind before they sublime from the graphene surface. It's shown that fullerene cage first attaches to the surface carbon before opening up and releasing the Gd atoms. The surface carbon then provides the framework for Gd diffusion across the top and also around its edges, enabling Gd atoms to assemble into small clusters. Gd clusters of 5 atoms were stable at temperatures up to 900^{o}C, and migrating Gd atoms were found to assembly in voids within the surface carbon and form 2D monolayer crystals with a closed-packed structure. Hydrogen annealing at low temperatures has been demonstrated to be an effective way to achieve high Gd loading onto graphene surfaces. Prolonged exposure of hydrogen to the $Gd_3N@C_{80}$ – graphene system enables fragmentation of the cages without exposing the sample to very high temperatures. Empty fullerene-like cages were found

attached to the surface carbon region at various temperatures, which eventually fused into the surface carbon layer to expand its area. These results provide a pathway to realizing a wide range of rare earth dopants on graphene surfaces. Furthermore, a degree of control on dopant levels and structures can be achieved via a combination of in situ heating and hydrogen annealing. This can be important for several applications of graphene, including spintronics and catalysis, especially taking into account the dozens of different types of endohedral metallofullerenes that are available from work over the past couple of decades, and can contain encapsulated single-, double- or tri - rare earth heavy metals. Gadolinium based molecules still remain one of the most important contrast agents for magnetic resonance (MRI) imaging. In this case, our method can potentially be used for drug delivery where graphene can act as a host to introduce the Gd atoms. The opening of EMFs causes cargo release of dopant adatoms on the graphene surface without chemically etching of the underlying graphene or damaging the sample itself, providing an excellent way to create doped graphene monolayers.

4.5 Contributing Statement

$Y@C_{82}$ was synthesized using arc discharge by former students of Prof. Porfyrakis. $Gd_3N@C_{80}$ (97% purity) was purchased from Sigma Aldrich. Graphene was synthesized by Dr. Yuewen Sheng.

Chapter 5 2D Lead Iodide

Lead Iodide (PbI_2) is a large band gap 2D layered material that has potential for 2D semiconductor applications. However, atomic level imaging of PbI_2 monolayer crystal structure and its fundamental defects has been limited due to challenges in obtaining suitable quality thin crystals. Here, liquid-exfoliation has been used to produce monodisperse 2D monolayer PbI_2 nanodisks (30-40nm in diameter and >99% monolayer purity) and deposit them onto suspended graphene supports that have high electron beam transparency to enable atomic resolution annular dark field scanning transmission electron microscopy of PbI_2. The 1-H structure of PbI_2 has been reported for the first time which is the result of commensuration with the graphene underneath. The epitaxial alignment of the material on graphene has been studied in details and it is shown how PbI_2 has a preferential alignment on graphene. In the later half of the chapter, the defects, atomic migration and edge structure of PbI_2 have been discussed and studied on graphene surface. The results of the chapter have been published in Nature Communications, 2020.

5.1 Introduction

Two-dimensional (2D) materials attract interest because of their unique chemical and physical properties, facilitating the study of novel physics, e.g. trions, valley polarization, etc.(256–258) Although graphene exhibits an exceptionally high carrier mobility (>10^6 cm^2 V^{-1} s^{-1} at 2K), its zero band gap poses difficulties for many semiconductor applications.(259) Monolayer transition metal dichalcogenides (TMDs), such as MoS_2, can have direct band gaps of ~1.8eV, but do not exhibit very high charge carrier mobility.(260–262) For Mo- and W-based TMDs, such as $MoSe_2$, WS_2, WSe_2, etc., the band gaps fall within the range of 1.0eV - 2.0eV, which is the red to near IR regions.(263,264) In addition, blue, green, and ultraviolet light emitting diodes are also needed in optoelectronics, for full colour displays and cameras. Currently there are not many experimental studies of 2D materials that can satisfy the demands for the green to UV spectral regions and more research is needed to expand this area.

5.1.1. PbI_2

PbI_2 is a layered direct band gap semiconductor with band gap of 2.4 eV in its bulk form, whereas its 2D monolayer has an indirect bandgap of about 2.5 eV, with possibilities to tune the band gap between 1-3eV.(265–268) PbI_2 is frequently used to fabricate organic-inorganic halide perovskite solar cells,(269,270) and as a high-energy photon detector material for gamma-rays and X-rays.(271–273) PbI_2 has a wide variety of I-Pb-I stacking and this gives rise to more than a dozen polymorphs.(274) However, the thickness of each single layer (0.7 nm) and the distance between each lead and iodide atoms (0.32 nm) is independent of the polytypes.(274) The 2H structure is the most commonly found polytype of 3D PbI_2, where each plane of Pb and I atoms are shifted with respect to each other and form overlapping hexagons, and each Pb atom is surrounded by 6 other I atoms, forming a near octahedral unit of $[PBI_6]^{4-}$, with space lattice dimension of a = 0.459 nm and c = 0.679 nm.

Layered PbI_2 has been shown to be excellent candidate for use in optoelectronic applications, photodetectors and photon detection.(275–278) Ultrathin PbI_2 is an interesting system for studying quantum-confinement effects because the exciton-phonon couplings are dependent on the degree of localization of electronic charge.(279,280) Cabana *et. al.* fabricated PbI_2 interfaces with carbon nanotubes and studied the change in the density of states (DOS) of the system.(281) Zhou *et. al.* studied the graphene/PbI_2 van der Waals interface and predicted 1.5eV increase in the visible light absorption capability of the heterostructure as compared to pure 2D PbI_2.(265) Recent work on few-layer shows PbI_2 as a promising candidate for application in the field of ultrafast saturable absorbers.(282) However, research into the atomic structure of monolayer PbI_2 has been limited to date because of the challenges in obtaining high quality monolayer crystals and preparing suitable samples for transmission electron microscopy studies. Further work is needed to reveal the structure and dynamics of edges, point defects, vacancy clusters and nanopores in PbI_2 monolayer and its interaction with other 2D crystals such as graphene.

5.1.2. Liquid-Exfoliation

Liquid-phase exfoliation is one of the simplest methodologies for producing 2D materials on a large scale.(283–285) Some of the advantages of liquid exfoliation is that it doesn't require high growth temperature, has shorter growth time and does not need special atmospheric or vacuum conditions to carry out the procedure. There are different approaches for carrying out liquid exfoliation; here, the scope of this work is limited to sonication-assisted exfoliation. However, there are thousands of solvents available and it is very important to choose appropriate solvents for carrying out exfoliation of a particular 2-D material. **Figure 5.1** shows a schematic description of sonication-assisted exfoliation. In the past decades, various research has been carried out to find suitable solvents based on their interactions with the 2D material to produce suspended 2D monolayer crystals. Surface tension, the Hilderbrand

solubility parameter, the Hansen solubility parameter, surface tension components etc. have been the widely used parameters to screen appropriate solvents.(286–290) Using these parameters, the commonly used solvents were screened and used to isolate PbI_2 monolayer flakes from a starting bulk PbI_2 powder.

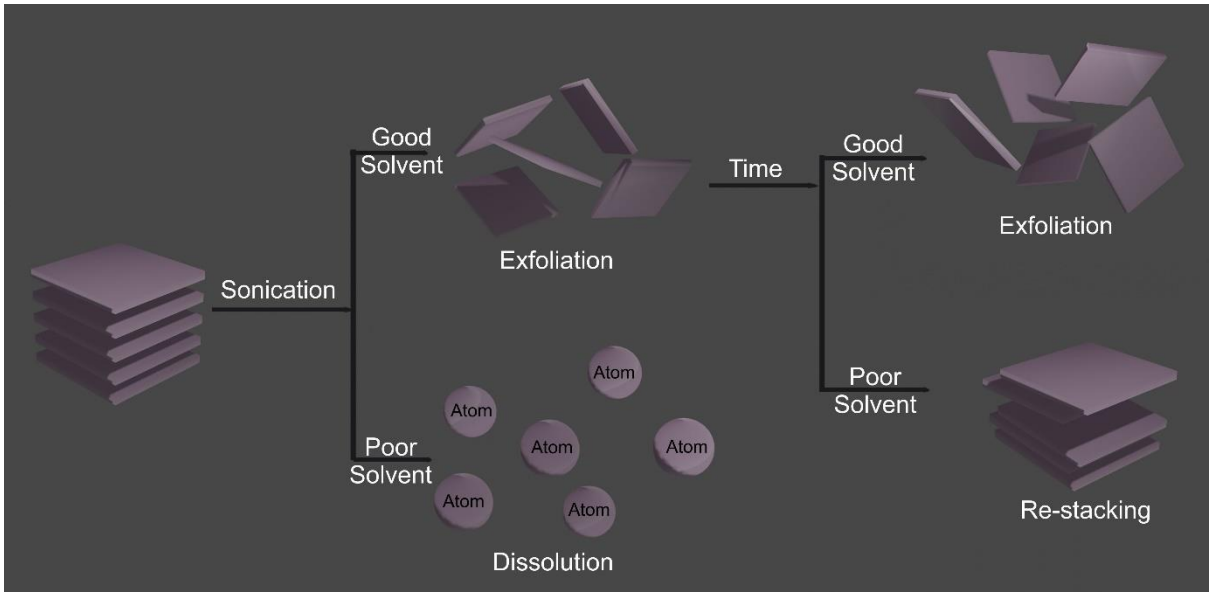

Figure 5.1. Schematic description of sonication-assisted liquid exfoliation.

5.1.3. Graphene Interface

High-angle annular dark field scanning transmission electron microscopy (HAADF-STEM) was used for studying the PbI_2 atomic structure, by depositing it from solution onto a suspended graphene support and allowing it to dry.(291–293) The high electron transparency of graphene, provides excellent contrast from the Pb and I atoms in ADF-STEM. Therefore it facilitates the study of the fundamental atomic structure, point vacancies, vacancy clusters, vacancy dynamics, edge terminations and edge etching. In addition, as discussed in depths in **Chapter 2**, the role of graphene support in influencing the epitaxial alignment and morphology of PbI_2 is also studied and reported.

5.2 Results & Discussions

5.2.1. Liquid – exfoliation

Solvent selection

I explored a variety of commonly used lab solvents that were easily available. The solvents studied and the parameters used to screen them have been listed in **Appendix D**. The results on the relationship between the different solvent parameters and successful liquid exfoliation of PbI_2 have been described briefly below:

a. Solvents that dissolve PbI_2 - PbI_2 is a unique exception to all the metal halide compounds that show CdI_2 structure, in that it has the largest metal-halide bond length.(294) This is due to the fact that lead and iodide have a small difference in their electronegativity values[43] and thus, as a result, the bonds are not as ionic as that of the other compounds which also show CdI_2 crystal structure, such as MgI_2, $FeBr_2$, etc. as shown in **Figure 5.2a**. However, it is sufficiently ionic to dissolve into polar solvents.(295,296) I found that polar solvents, especially the nitrogen containing compounds such as Aniline, DMF, etc. were good at dissolving PbI_2. As shown **Figure 5.2b**, NMP, DMF and THF were easily able to dissolve PbI_2, imparting a colour to the solution, whereas, PbI_2 sticks to the sides of the container in toluene and completely precipitates in case of benzonitrile. If PbI_2 is deposited on graphene from such solutions, it either results in formation of atoms on the surface or they re-crystallize to form multilayer PbI_2, as shown in red and blue boxed regions respectively in **Figure 5.2c-d**. **Figure 5.2**e shows the re-crystallization occurring from a saturated solution of water at 100°C (ϵ_{water} = 55 at 100°C)[44]. We do not want PbI_2 to dissolve into the solvents for the exfoliation purposes and hence, we were easily able to screen the rest of the solvents based on these results.

[43] Electronegativity of Pb = 1.8 and I = 2.7.

[44] ϵ is known as the dielectric constant, also known as the relative permittivity of a material. It is the ratio of the permittivity of a material, relative to vacuum permittivity.

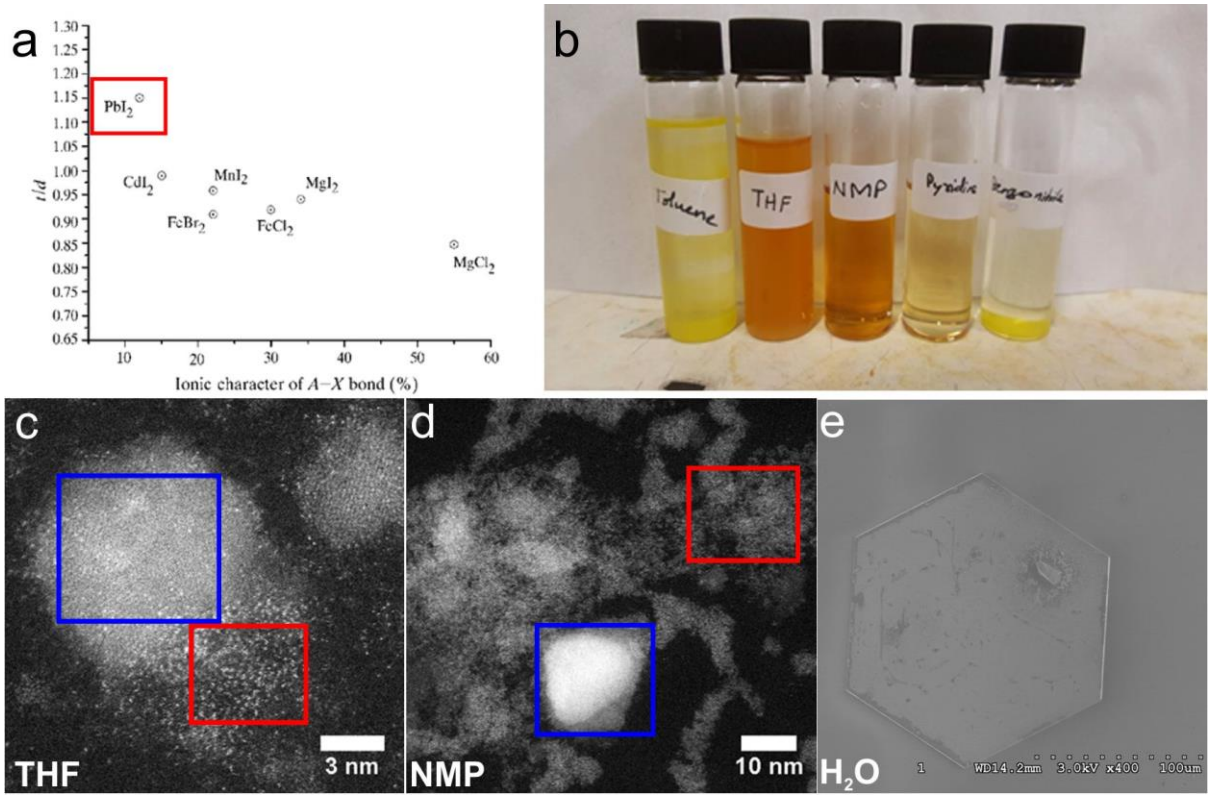

Figure 5.2. (a) Plot of the layer thickness/interlayer gap ratio (t/d) versus ionic character (ionicity) of the A–X bond [Reproduced from (294)]. (b) Picture of solutions of PbI2 in various solvents after soication. From the right – Benzonitrile, Pyridine, NMP, THF, Toluene. (c-e) ADF-STEM image of PbI_2 after being dropcasted from (c) THF, (d) NMP and (e) H_2O solutions. The red and blue boxed regions in the figure shows the atomic disintegration of the material and re-crystallization to form multi-layer thick PbI_2 respectively.

b. <u>Dipole and Dielectric constants</u> - The solubility of PbI_2 in water strongly depends on the temperature in the range between 20 °C and 100 °C, with PbI_2 being more soluble in hot water (4.1g l^{-1} at 100 °C) than in cold water (0.8g l^{-1} at 20 °C).(297) However, this is to note that the dielectric constant of water changes considerably over temperature, i.e. it goes from $\epsilon = 80$ at room temperature to $\epsilon = 55$ at 100ºC. Noting that PbI_2 is only slightly polar, and also dissolves in other solvents (DMF, DMSO, etc.) that have dielectric constants in the same range, I could deduce that solvents with high dipole moment/dielectric constants do not dissolve it either (**Figure 5.3e-f**). Thus, I screened and eliminated the solvents if they had very high dielectric constants and dipole moment.

c. Polarity – I found that solvents with very low dipole moment, for example CS_2 (μ = 0.06D), n-hexane (μ = 0.00D), Toluene (μ = 0.36D) did not work very well with PbI_2 either, and were completely unable to exfoliate it, as shown in **Figure 5.3a-c**. Moreover, even water at room temperature (ϵ_{water} = 80 at 80^oC) is also unable to exfoliate the PbI_2. As discussed previously, although PbI_2 is not a highly polar compound it still shows some ionic properties, which can explain why both these solvents of very high and very low polarity were unable to interact and thus exfoliate the material. **Figure 5.3e-f** schematically describes the relationship between these solvent parameters and PbI_2 exfoliation.

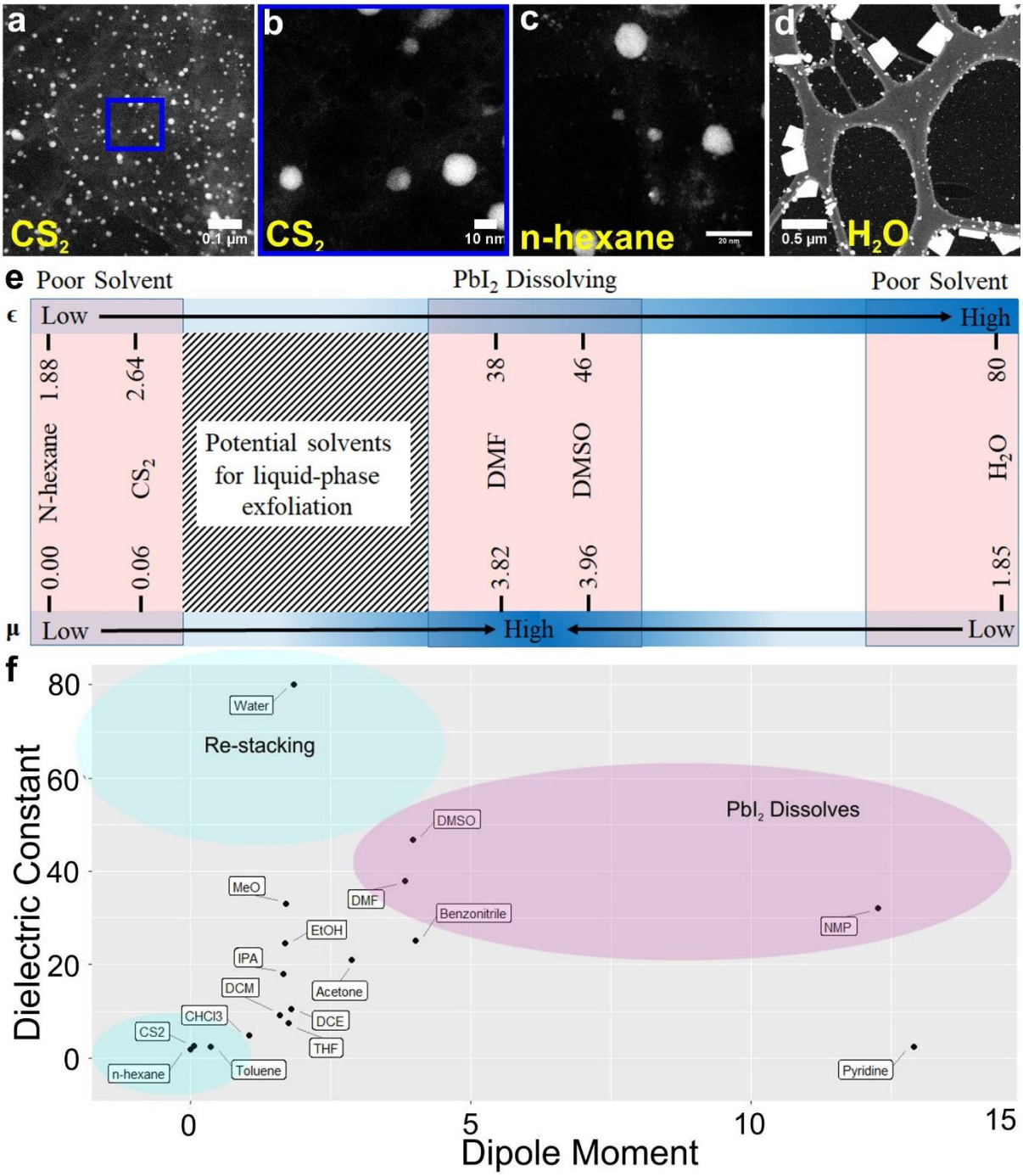

Figure 5.3. (a-d) ADF-STEM images taken at 200kV (dose: 5.6 x 10^8 e s^{-1}), of solution processed PbI_2 in (a-b) CS_2 (c) n-hexane (d) H_2O. (b) is the high resolution of the region boxed in blue in figure a. The high white contrast shows the multi-layer thick PbI_2 crystals on the graphene surface. (e-f) Schematic and graphical representation respectively, showing the relationship between dielectric constant (ϵ) [45] and dipole moment (µ)[46] with the solubility and exfoliation of PbI_2 in different solvents. The pink area in the graph refers to where PbI_2 gets

[45] Note that in Figure 5.3e, water is shown to have high dipole moment, but corresponds to low dielectric constant.

[46] Dielectric constants of the materials have been taken from the data available in various literature. It is the is based on measuring the capacitance of dielectric probe in solvent at room temperature.

dissolved in the solution whereas the blue regions show where PbI_2 re-stacks after leaving it overnight post sonication.

d. Solvent residue: Almost all the solvents with boiling point more than 100°C left behind solvent residue after drop-casting on a substrate or graphene, as shown in **Figure 5.4**.

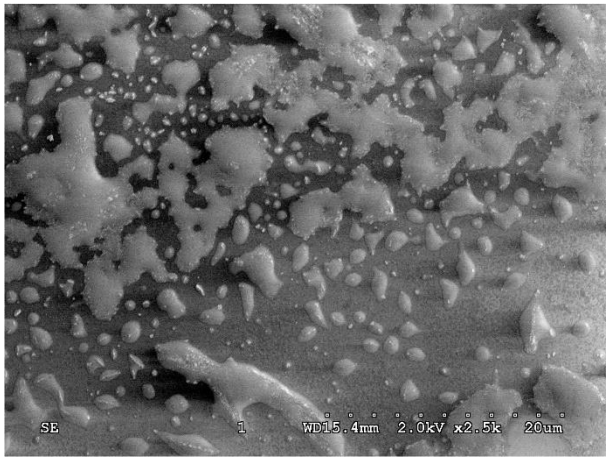

Figure 5.4. SEM image of the solvent residues on PbI_2/graphene substrate after dropcasting from a solution of Pyridine.

e. Hydrogen bonding - Previous results on the liquid-phase exfoliation for other 2D materials have shown that the most efficient solvents have H-bonding components so as to maximize the dispersability of the material in the solution, which is in agreement with the Hansen solubility parameter theory.(298,299) And thus, we selected solvents that show some sort of hydrogen bonding.

f. Gutmann donor number - Recent research on Lewis basicity of solvents, also quantified by Gutmann's donor number - D_n, has shown that solvents that solubilize the precursor (PbI_2) at a total concentration of 1M, have higher D_n values of more than 25.(300) Therefore, solvents with Gutmann donor number less than 25 were taken into consideration.

Chloroform

Based on these basic criteria, we explored several different solvents and found that chloroform serves as an excellent medium to exfoliate PbI_2. $CHCl_3$ has dipole moment (μ = 1.04) and dielectric constant ($\epsilon_{T=20^oC}$ = 4.8) in the right lower range, low donor number (D_n =

4) as well as has the ability to form hydrogen bonds.(301–303) In addition, $CHCl_3$ has a very low boiling point of 61^oC which facilitates quick and easy removal after solution dropcasting onto substrates. We also performed different kinds of basic characterizations on the PbI_2/Chloroform solvent and dropcast PbI_2/graphene samples. **Figure 5.5**a shows the time dependent UV-Vis absorption spectroscopy on a diluted $PbI_2/CHCl_3$ solution, showing the characteristic PbI_2 peaks. It shows that the material still stays dispersed in the solution even after a day. **Figure 5.5**b shows a typical SEM image of PbI_2 on graphene on top of SiO_2 substrate. The weak contrast shows the thin layered PbI_2 of about 20-100nm in size without any trace of solvent residue on the surface. **Figure 5.5**c shows the dynamic light scattering (DLS) result of a dilute $PbI_2/CHCl_3$ solution after leaving the solution overnight. The size distribution showed that the flakes were about 100-125nm in size and dispersed well in the solution, which agrees with the results from UV-Vis absorption spectroscopy and SEM. We also attempted AFM measurements of the PbI_2/graphene samples for further characterization, as shown in **Figure 5.5**d. AFM results show the average RMS roughness of 7.13 nm, where clean graphene shows RMS roughness of 1.54 nm. The results also showed 100nm average size (**Figure 5.5**e) which agrees with the results from other characterization techniques. However, the average height distribution via AFM measurements showed an average >100nm thickness instead of monolayer thickness. I believe that these results are not reliable because of the particles on the surface of the SiO_2 or graphene as the available instrument could not be used for high resolution imaging and the target sample area was very big, which could have induced some imaging artefact. It has been discussed in more details in the following sections.

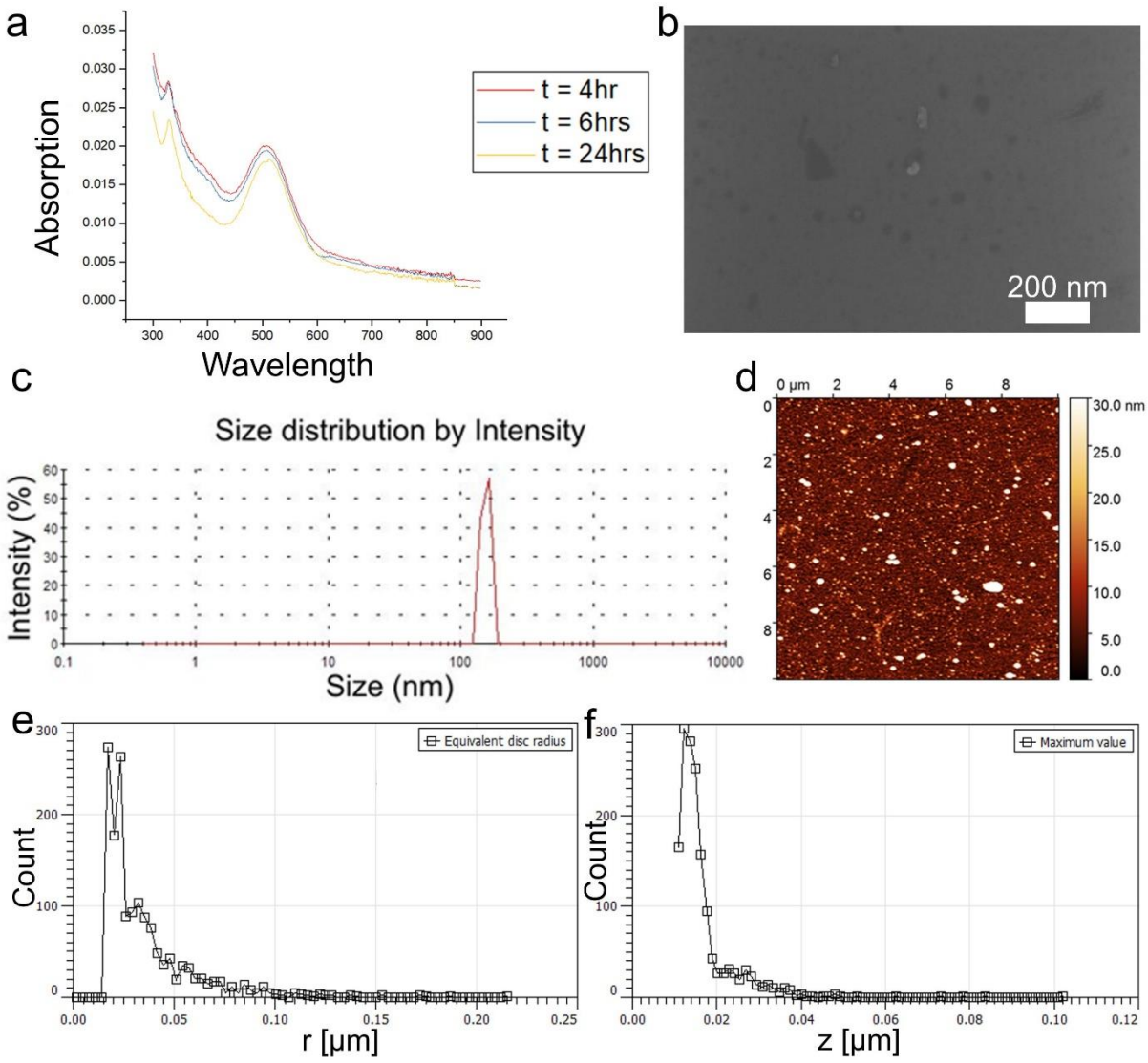

Figure 5.5. (a) Time dependent UV-Vis absorption spectroscopy on PbI_2 dispersed in $ChCl_3$ solution (b) SEM of PbI_2 on graphene. (c) Size distribution by Inensity of a PbI_2 solution. (d) AFM image of the drop casted exfoliated PbI_2 on SiO2 substrate. (e-f) AFM measurements of the PbI_2/graphene samples showing the size distribution and height distribution respectively.

After getting the initial data on the samples, I performed a detailed study on processing conditions and their results with HAADF-STEM imaging. **Figure 5.6** shows the schematic diagram of the liquid exfoliation experimental procedure. **Figure 5.6**(**b-d**) shows the HAADF-STEM images of the monolayer PbI_2 suspended on monolayer graphene on a TEM grid at various magnifications. The length and width of ~300 flakes was measured (**Figure 5.6e,f**), giving ~42 nm and 28 nm respectively with bigger flakes ranging to more than 160 nm in size.

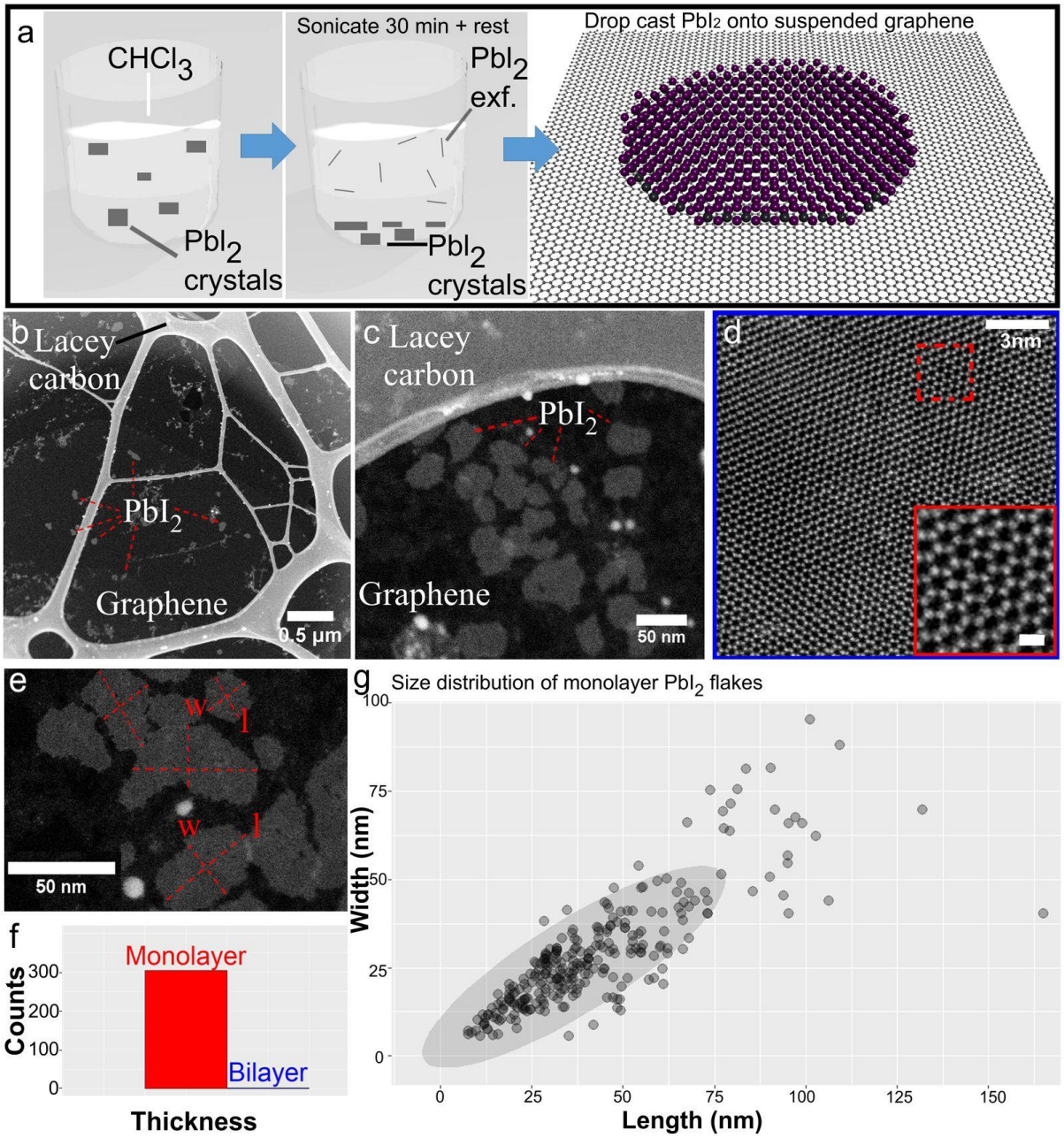

Figure 5.6. (a) Schematic of the LPE synthesis of monolayer PbI_2 flakes and deposition on to suspended graphene. (b-c) ADF-STEM image of monolayer PbI_2 flakes at different magnifications. (d) Atomic resolution ADF-STEM image of a monolayer PbI_2 flake. The inset in the figure shows an atomic resolution image of the structure. The scale bar is 0.5nm. (e) Typical method for measuring the length(l) and width(w) of the monolayer flake. (f) Histogram showing the thickness distribution of PbI_2 flakes. (g) Plot of the size distribution for more than 300 monolayer flakes. Overlapping sizes of different flakes show darker color for their marker dots. The oval represents the highest congregation of flake sizes in the overall sample distribution. Images taken at 200kV (dose: 5.6 x 10^8 e s^{-1}); electron fluence of 3.3 x 10^5 e nm^{-2} for figures b,c,e; electron fluence of 2 x 10^6 e nm^{-2} for figures d.

The sonication time is important for controlling the exfoliation of PbI_2. Less sonication leaves multilayer PbI_2 dispersed in the solution whereas longer sonication time renders very small flakes or completely destroys the sheets, as seen from **Figure 5.7**. Moreover, the dispersed solution was found to be stable for a considerable number of days. Even after a week of the sonication process, we could still observe monolayer flakes dispersed in the solution (**Figure 5.7**).

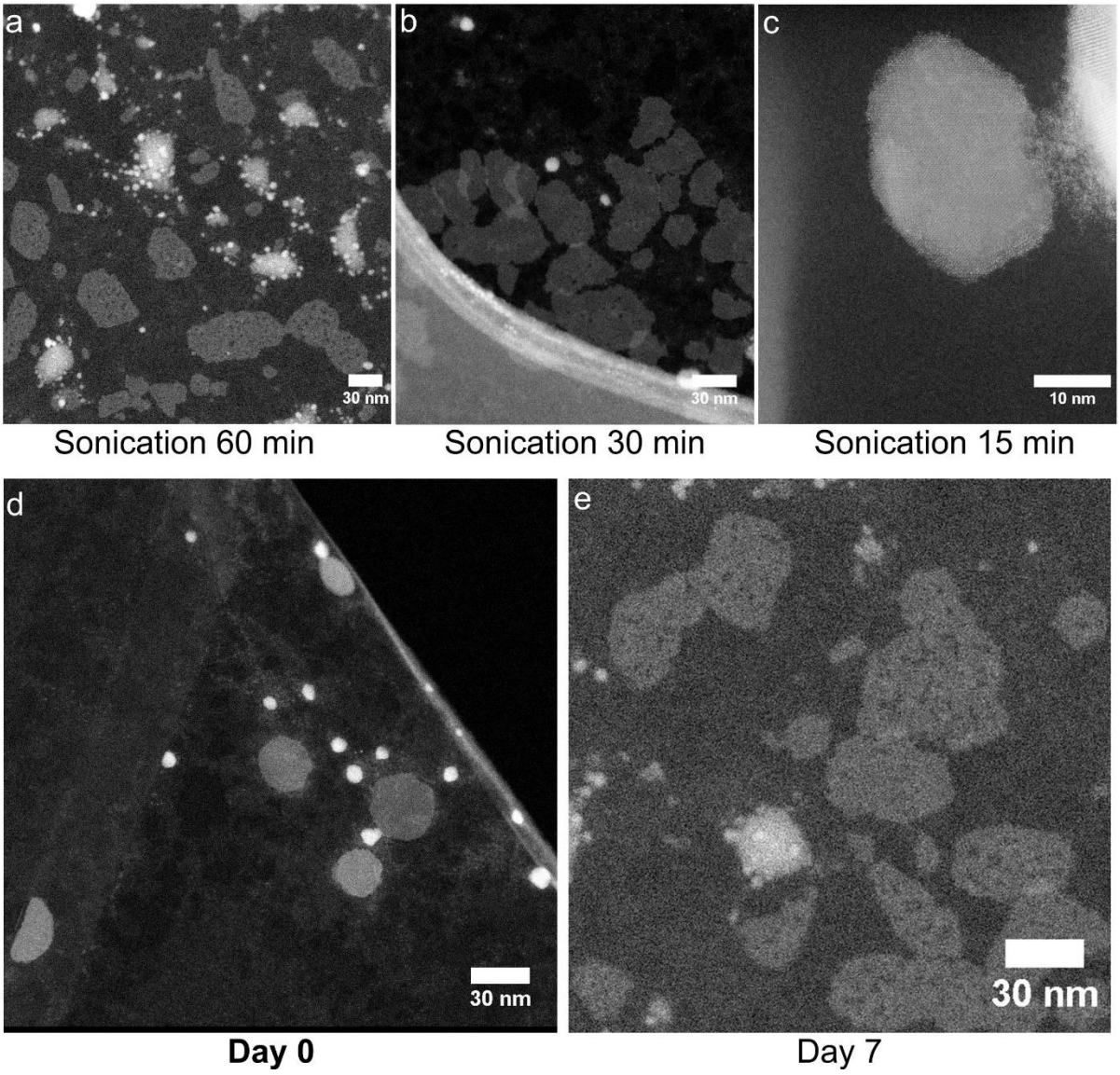

Figure 5.7. ADF-STEM image taken at 200kV (dose: 5.6 x 10^8 e s^{-1}) of PbI_2 suspended on graphene. The exfoliation was carried out via sonication after (a) 60 minutes (b) 30 minutes (c) 15 minutes. ADF-STEM images of 30-minute sonicated samples on (d) day 0 (e) day 7.

Small high contrast nanoparticles are residue from the graphene support and are not from the PbI_2 sample.[47]

The supernatant used for dropcasting also plays a role, and only the solution from the top has been used as shown in **Figure 5.8**. The thicker PbI_2 settled at the bottom of the container, as shown in **Figure 5.8**a. The thickness of PbI_2 at the bottom and top is not the same. The flakes at the bottom were comparable to the thickness of the flakes that were found at the top of an inadequately sonicated solution (as shown above in **Figure 5.7**).

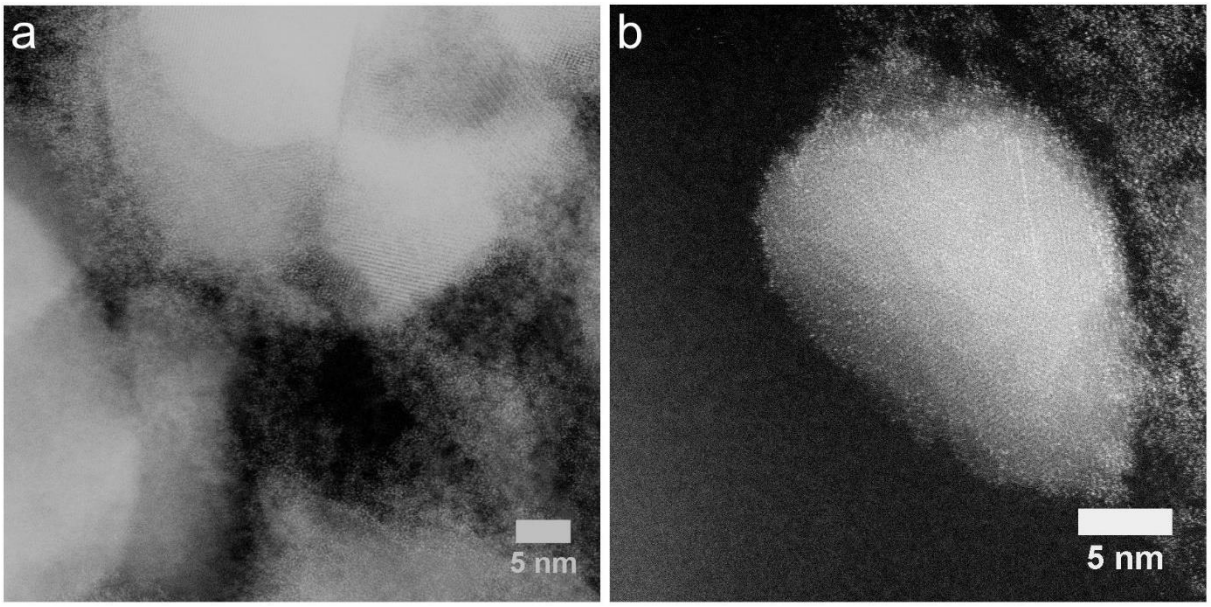

Figure 5.8. ADF-STEM image of PbI_2 taken at 2000kV (dose: 5.6 x 10^8 e s^{-1})suspended on graphene. The exfoliation was carried out via sonication after (a) 30 minutes and the solution was taken from the bottom of the container. (b) 15 minutes and the solution was taken from the top of the container.

Our results show successful exfoliation of mostly monolayer flakes of the PbI_2 from its bulk counterpart. Out of more than 300 flakes studied in this experiment, we only found 2 flakes with bilayer structure (**Figure 5.9**), whereas all others were monolayers. **Figure 5.9**

[47] Unfortunately, because of the presence of large chunks of materials, next to the desired place of interest, it was difficult to obtain a low-magnification image. The lower magnification of image, similar to that of **Figure 5.7a-**b resulted in over-saturation of the desired place of interest because of the presence of large clusters of heavy atoms nearby, thus making it difficult to analyse the sample of interest.

shows ADF-STEM images of two flakes of PbI_2 suspended on graphene. **Figure 5.9b** and **Figure 5.9c** are the magnified images of the monolayer flake in **Figure 5.9**a in the blue box. **Figures Figure 5.9d** and **Figure 5.9e** are the magnified images of the bilayer flake in **Figure 5.9a**, in the red box. The intensity difference in ADF-STEM images of the monolayer and bilayer regions can be seen clearly in **Figure 5.9a**. **Figure 5.9f** shows the line profile of the bilayer flake at one of the edges which has some monolayer region. The intensity of the bilayer region, as expected, is twice as high as that of the monolayer region. Moreover, as it can be seen in **Figure 5.9c**, there is presence of vacancies in the monolayer region. This is another proof that there is no layer underneath and thus, it should be monolayer region and not AA stacked multilayer.

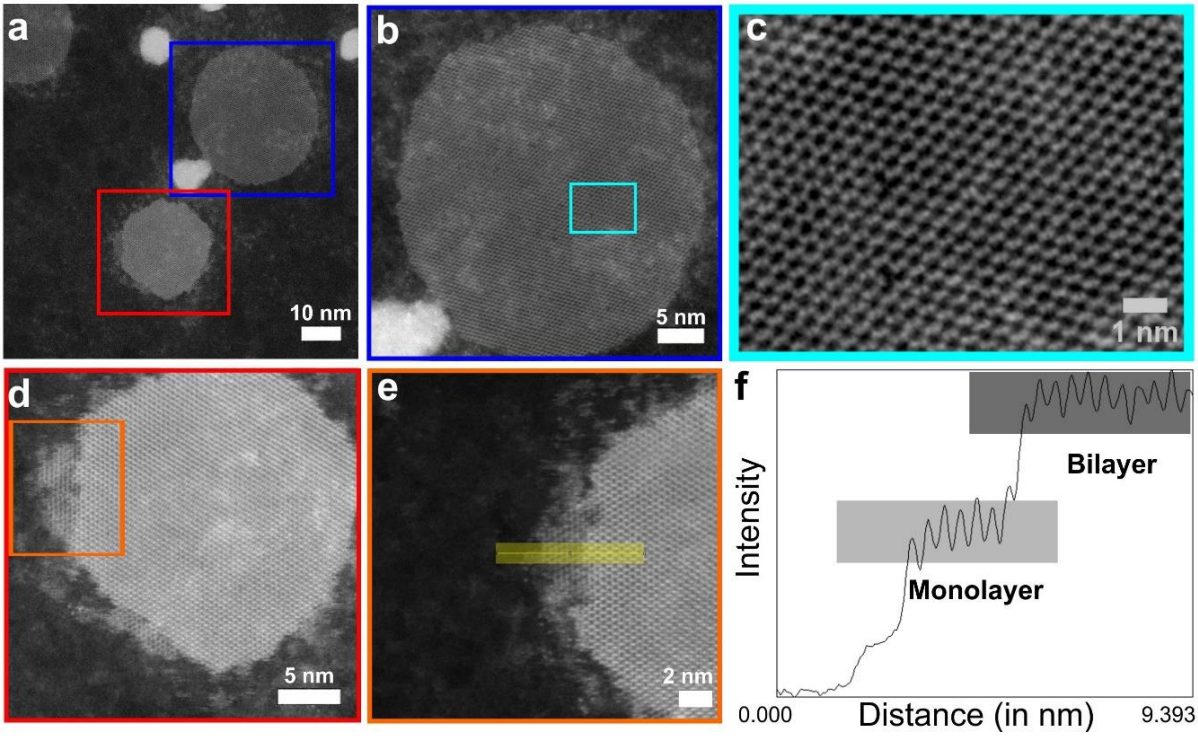

Figure 5.9. (a) Low-magnification ADF-STEM image taken at 200kV (dose: 5.6 x 10^8 e s^{-1}) of monolayer and bilayer regions. (b) High magnification image of monolayer region marked in blue box in figure (a). (c) Higher magnification image of monolayer region marked in cyan colored box in figure (b). (d) High magnification image of bilayer region marked in red box in figure (a). (e) Higher magnification image of monolayer and bilayer region in the flake marked in orange colored box in figure (d). (f) Line profile of the region marked with yellow color in figure (e) showing the increase in intensity, confirming the presence of bilayer.

The nanoparticles that are observed come from the graphene underneath and not from PbI_2 itself (**Figure 5.10**)[48]. The small high contrast nanoparticles come from graphene sample and are not from the PbI_2. **Figure 5.10** below shows the graphene samples without any dropcasted PbI_2, suspended on the lacey carbon TEM grid.

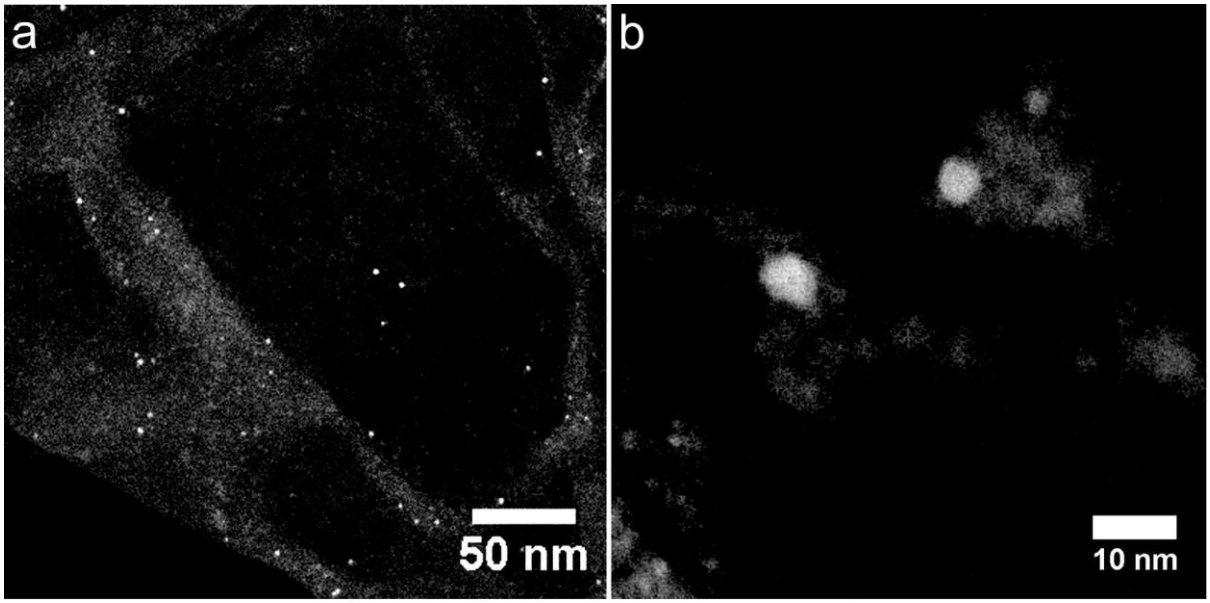

Figure 5.10. (a) Low magnification and (b) High resolution ADF-STEM images of residue nanoparticles on graphene. Images taken at 200keV (dose: 5.6 x 10^8 e s^{-1}).

5.2.2. 1-H structural phase

The bulk crystal structure of PbI_2 has a CdI_2 structural type with lead and iodide layers stacked together in ABC instead of ABA stacking. However, in the monolayer form there are two structural phases, namely – 1H-phase and 1T-phase. PbI_2 has similar structures to the TMDs (MoS_2 and WS_2) where the metal (Pb) atomic plane is in the middle and the two iodide atomic layers at the top and the bottom. A monolayer from a 2H PbI_2 bulk crystal structure (**Figure 5.11a**) of PbI_2 typically has a 1T-phase (**Figure 5.11b**), where the two iodide atoms do not share the same z-axis and are located in an octahedral co-ordination. Whereas the 1H-

[48] These particles were small enough in number to not have enough count to detect in the EDS. However, some of them were similar to what is obtained for CVD graphene after carrying out the transfer process. Some of the impurities were of Ca, Cr, Si and Cu, which have been seen in my other samples after transfer and processing, as also explained in **Figure 4.11g**.

phase of monolayer PbI_2 (**Figure 5.11e-f**) has two iodide atomic layers on top of each other in a trigonal-prismatic coordination, as shown in **Figure 5.11e** and **Figure 5.11f** respectively. The position of the Pb and I atoms can be determined by their contrast in ADF-STEM images. Pb has Z = 82, I has Z = 53 and 2I has Z = 106, which means that the 2I positions will have higher contrast than the single Pb. The line profiles (**Figure 5.11d**, **Figure 5.11h**) of the multislice image simulations for 1T and 1H PbI_2 monolayers give the distance across 1 -> 2 and 3->4 in figures **Figure 5.11c** and **Figure 5.11g** respectively for comparison to our experimental data, **Figure 5.11(i-k).** The experimental Pb-Pb distance of 1.027 nm and the inter-atomic Pb-2I distances are in excellent agreement with the simulated distances of the 1H structural type, **Figure 5.11h**.

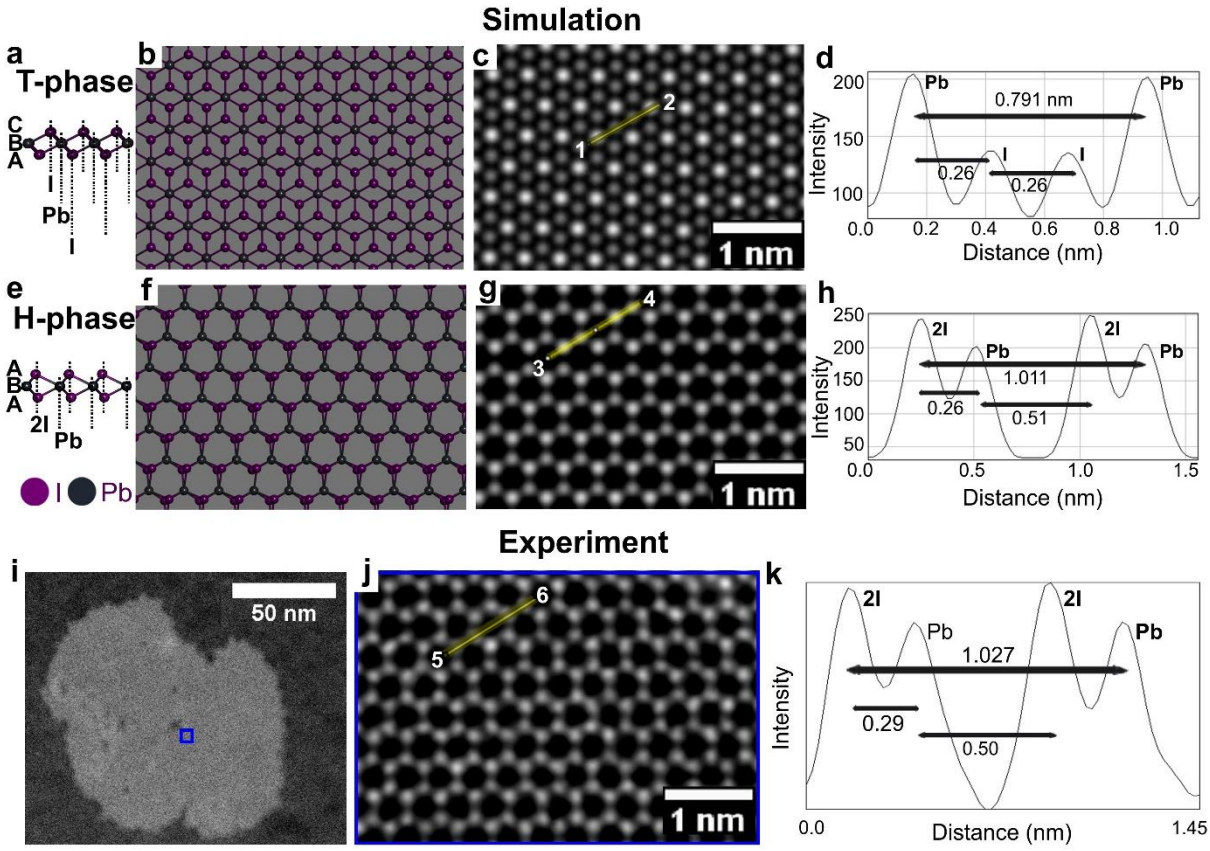

Figure 5.11. (a) Side view of the 1T atomic structure of PbI_2. (b) Top view of the 1T atomic model of single layer PbI_2. (c) Multislice ADF-STEM image simulation of the 1T atomic model in (b). (d) Line profile of the lead and iodide intensities marked with yellow line in the atomic model in (c), along the direction 1-2. (e) Side-view of 1H monolayer atomic crystal structure of PbI_2. (f) Top view of the 1H atomic model of single layer PbI_2. (g) Multislice ADF-STEM image simulation of the 1H atomic model shown in (f). (h) Line profile of the

lead and iodide intensities marked with yellow line in the atomic model in (g), along the direction 3-4. (i) Low-magnification ADF-STEM image of a monolayer PbI_2 flake suspended on graphene. (j) Higher magnification of the region indicated by the blue box in (i) showing the 1H atomic structure. (k) Line profile taken from region marked by the yellow box in (j) which corresponds to same position with the region marked in simulation (g), along the direction 5-6. Images taken at 60kV (dose: 5.6 x 10^8 e s^{-1}).

To further validate the case of monolayer 1H structure, we bombarded the nanodisks with electron beam. **Figure 5.12** shows one of the typical flakes of PbI_2 produced by liquid exfoliation. At t=0, the monolayer is as shown in **Figure 5.12a**. However, upon extended exposure from the electron beam at the dose of 5.6 x 10^8 e s^{-1}, after 2 minutes, there is hole opening up as well as edges damaged. The hole opening can be clearly seen in **Figure 5.12b**, highlighted with red arrow. This indicates that the area in the red box in **Figure 5.12a** is indeed a monolayer instead of AA' stacked 1H structural phase of lead iodide that looks identical to the monolayer 1H lead iodide. The images are taken at room temperature. Previous studies have reported that the initial defect or hole formation occurs layer-wise instead. (293,304) Since, the hole formation revealed no further layers underneath, it is conclusive to say that this is a monolayer structure instead of AA' stacked bilayer 1H structure.

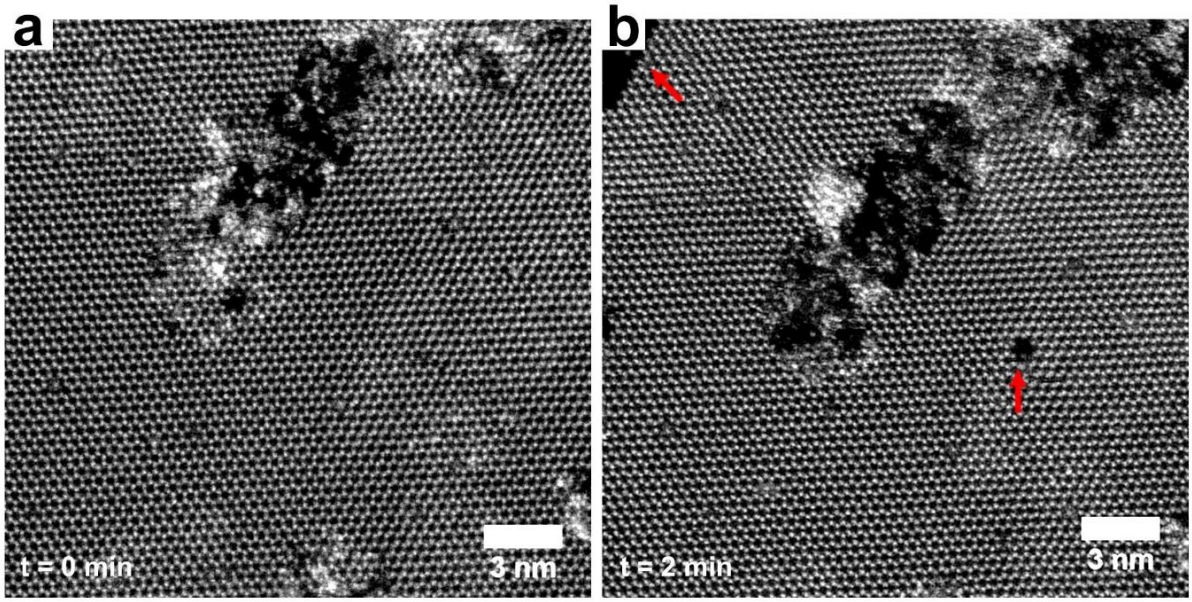

Figure 5.12. (a) ADF STEM image of monlayer lead iodide region, taken at 60kV (dose: 5.6 x 10^8 e s^{-1}) at t=0. (c) At t=2min, hole opening up in the monolayer region of figure a. The red arrows indicate the regions where the defects form.

The 1T phase is expected to be more stable than the H-phase with total energy 165meV per unit cell lower,(305) unlike the other 2D materials such as MoS_2, where the 1H phase is generally known to be more stable than the 1T phase.(306) However, all PbI_2 flakes suspended on graphene, from hundreds of nanometers in size (**Figure 5.13a**) to as small as 3nm (**Figure 5.13b**), showed 1H phase, attributed to epitaxial interactions with the underlying graphene support.

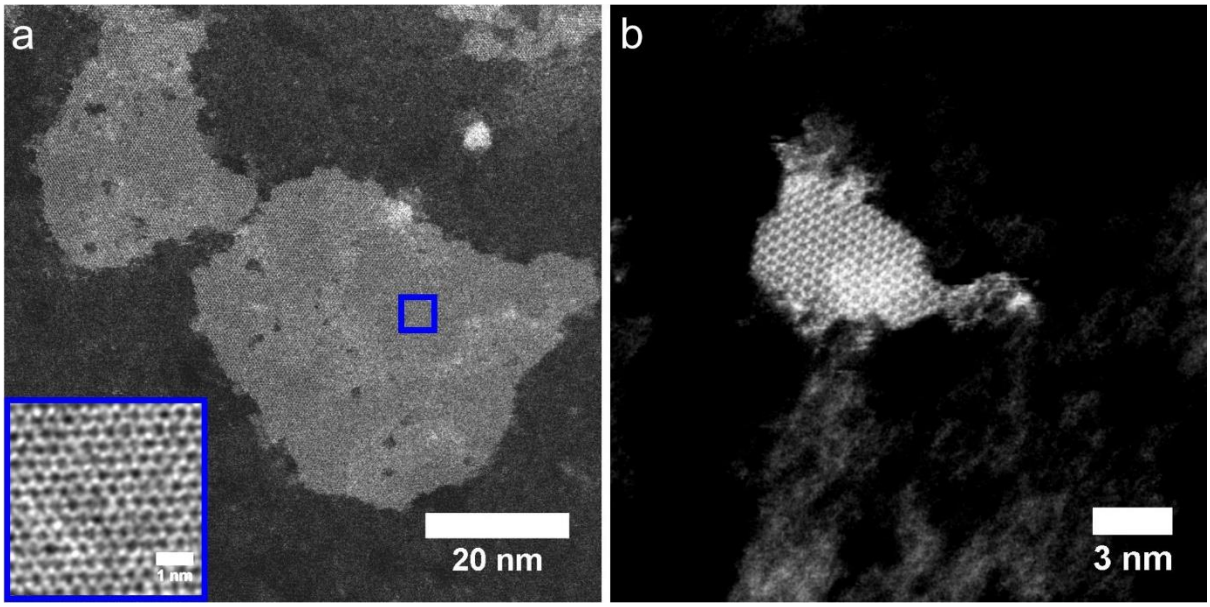

Figure 5.13. ADF-STEM image taken at 60kV (dose: 5.6 x 10^8 e s^{-1})of (a) large (b) small PbI_2 suspended on graphene.

Graphene lattice plays a role in influencing the orientation of PbI_2 lattice after it has been drop-casted on top. The CVD grown graphene is known to have grain boundaries and different orientations on the substrate on which it is grown.[50,51] Hence, different regions of interest showed different PbI_2 orientation but all the PbI_2 crystals in one particular area (1-5 µm) had the same orientation. **Figure 5.14** shows two different regions on the same sample. Both of them had different orientations because of different graphene domains. However, the flakes in the same region had the same lattice orientation (**Figure 5.14**a-c and **Figure 5.14**d-f).

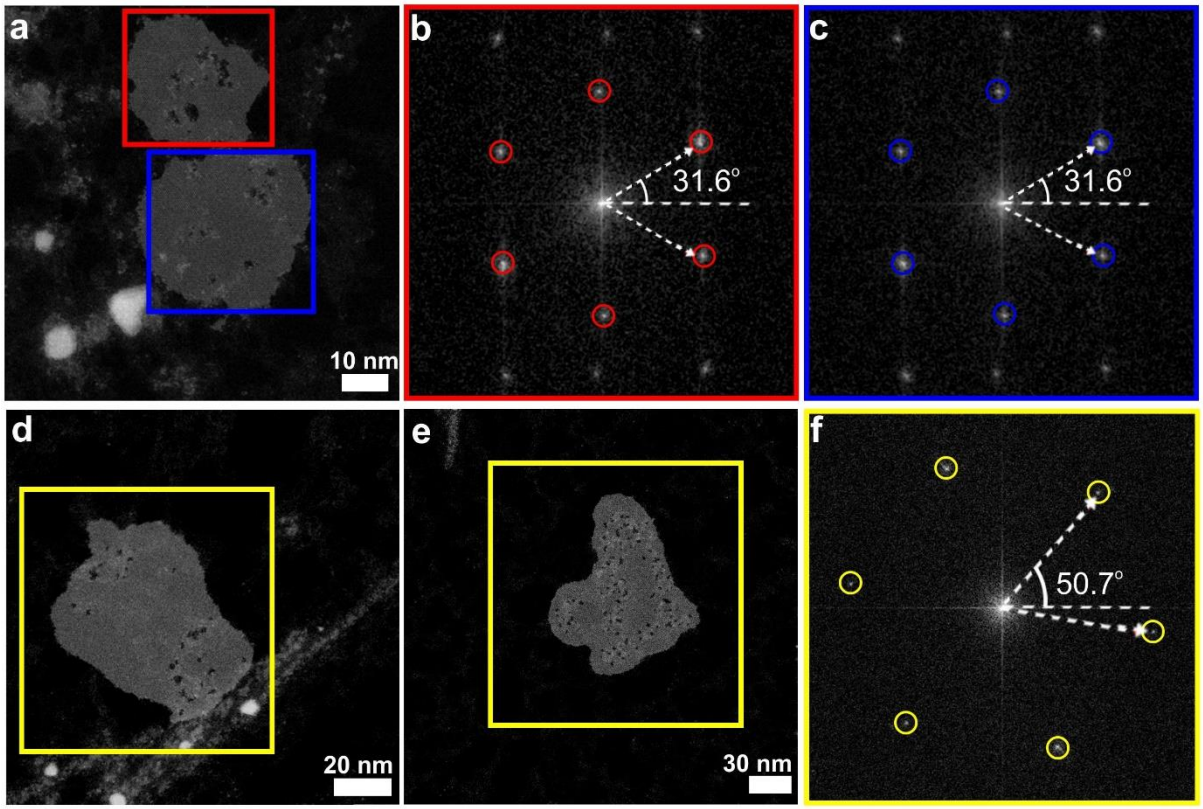

Figure 5.14. (a) ADF-STEM images taken at 60kV (dose: 5.6 x 10^8 e s^{-1}) of two PbI_2 flakes in the same area of interest. (b) FFT of the flake in the red boxed region in figure a. (c) FFT of the flake in the blue boxed region in figure a. (d-e) ADF-STEM images of two monolayer crystals of PbI_2 in the same region of interest, close to each other (< 200 nm). (f) FFT of the flakes in the yellow boxed regions of figure d and e showed the same orientation and pattern.

Another example of PbI_2 in **Figure 5.15** shows the same lattice orientation on top of graphene. All the nanodisks were imaged from the same region of the TEM grids, and hence, all of them orient with similar direction, as it can be seen by their FFT (as shown in the insets of the **Figure 5.15a-f**).

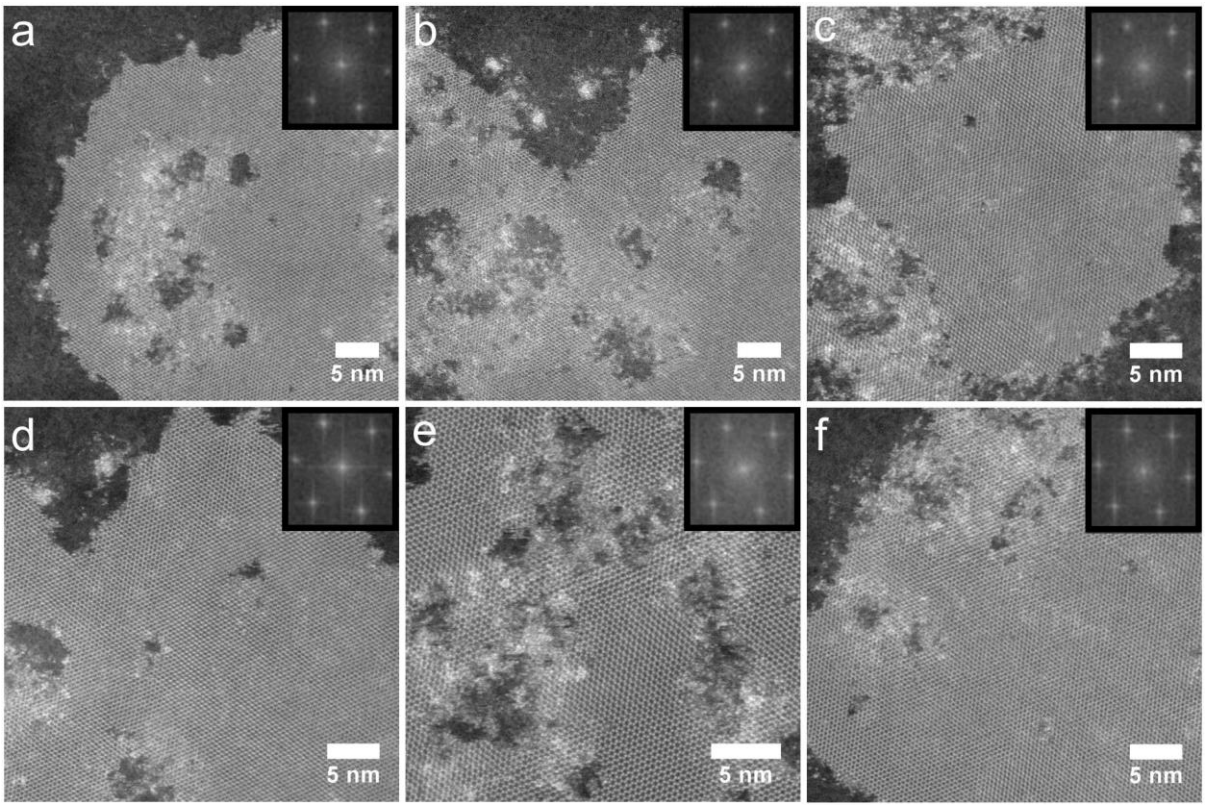

Figure 5.15. (a-f) ADF-STEM images taken at 200kV (dose: 5.6 x 10^8 e s^{-1}) of PbI_2 flakes in the same area of interest. The insets show the FFT of the flake. All the FFTs showed the same orientation and pattern.

To confirm the case of PbI_2-graphene interactions, we deposited PbI_2 flakes directly on top of lacey carbon TEM grids without graphene, and observed PbI_2 flakes with 1T structure instead, as shown in the **Figure 5.16**. The intensity and the structure of the monolayer flakes are not as good as that of the flakes suspended on graphene because graphene is a very clean substrate whereas lacey carbon has impurities on top. Intensity of the lead and iodine atoms as well as the inter-column spacing between Pb-Pb, as shown in **Figure 5.16d** agrees with that of the simulation of 1T phase, discussed and shown in **Figure 5.11**.

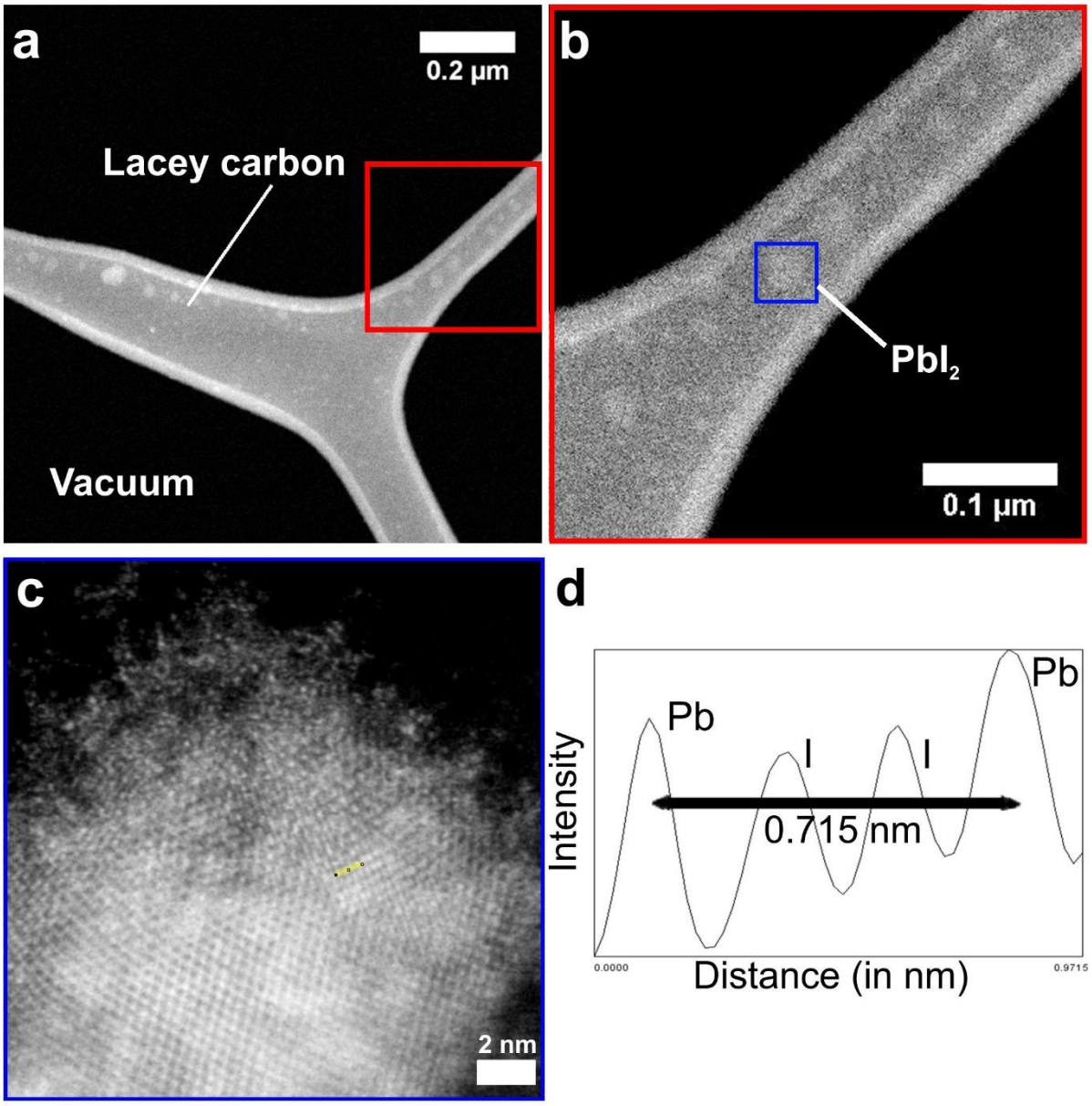

Figure 5.16. (a) Low magnification ADF-STEM image taken at 200kV (dose: 5.6 x 10^8 e s^{-1}) of PbI_2 flakes deposited on top of lacey carbon via the liquid phase exfoliation method. The small white contrasts on the lacey carbon are the PbI_2 flakes. (b) Higher magnification of the region drawn with a red box in (a). (c) Higher magnification of the monolayer region drawn with a blue box in (b). (d) Line profile of the region marked with yellow in (c).

We also carried a time-dependent study and concluded that the spatial variations in the PbI_2 lattice occurred during the early stages after deposition on graphene, eventually completely transforming to well-defined 1H phase over time (**Figure 5.17**). We carried out ADF-STEM imaging of PbI_2 flakes within 20 minutes after being dropcasted on graphene. We observed mechanical shift in the structure while it transforming into 1H phase. **Figure 5.17a**

shows the mixed structural phases in PbI_2 right after dropcasting. The structures other than 1H have been indicated with the X sign. **Figure 5.17c** is the high resolution image of the area boxed in red color in **Figure 5.17a**. An example of line profile from one of the X structural regions is shown in **Figure 5.17e**. The X phase cannot be slightly warped 1H structural phase, because the next day, none of those X phases were observed and only plane 1H phase could be observed. The interatomic distance is very different to what has been observed for 1T or 1H phases and also differs in different regions, indicating that the material is going some transformations. And after a day, it was observed that all the flakes on graphene showed 1H structural phase with same orientations in a given area. **Figure 5.17b** shows the uniform 1H structural phase in PbI_2 after a day in air at room temperature. **Figure 5.17d** is the high resolution image of such flake. An example of line profile from any region is shown in **Figure 5.17f**. The interatomic distance confirms that it is indeed the 1H phase.

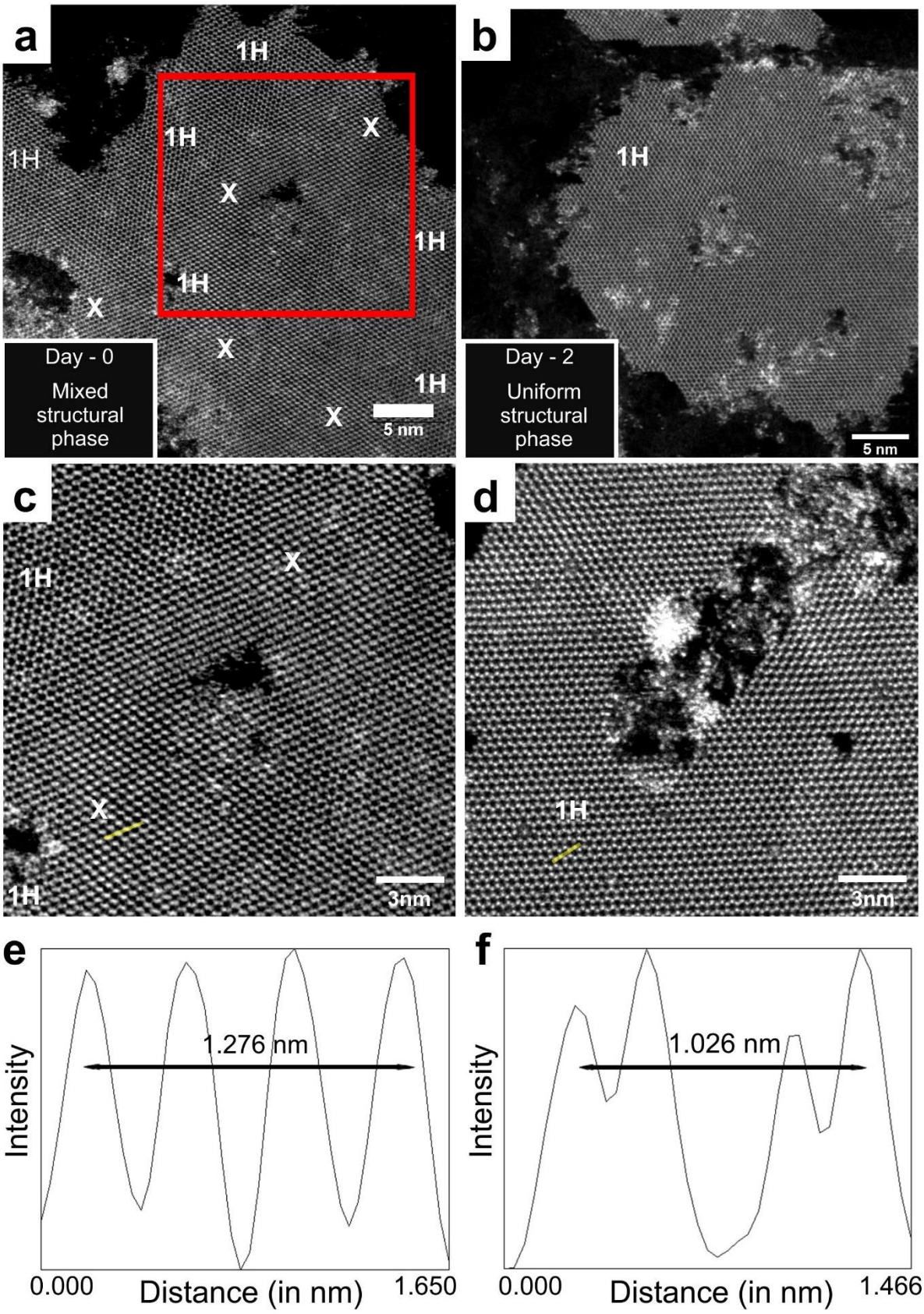

Figure 5.17. (a) ADF-STEM image taken at 200kV (dose: 5.6 x 10^8 e s^{-1}) of mixed structural phases in PbI_2 right after dropcasting. The structures other than 1H have been indicated with the X sign. Figure S6 (b) shows the uniform 1H structural phase in PbI_2 after a day. (c) High

resolution image of the area boxed in red color in figure a. (d) High resolution image of uniform 1H structural phase. (e) Line profile from one of the X structural regions is shown in yellow annotation in figure c. (f) Line profile from yellow annotated region in figure d confirming that it is indeed the 1H phase.

To understand why PbI_2 adopts 1H structure with concomitant alignment to the armchair direction of graphene, we examine the Moire patterns formed between the two crystals (**Figure 5.18a-d**). The different lattice spacings of 1T and 1H PbI_2, result in various degrees of epitaxial commensuration with the underlying graphene lattice. The smaller the difference in the relative lattice spacings between the two crystals, the larger the van der Waals interaction is likely to be. The best lattice match occurs when the PbI_2 adopts 1H phase and is aligned to the arm-chair direction, which agrees with our experimental findings.

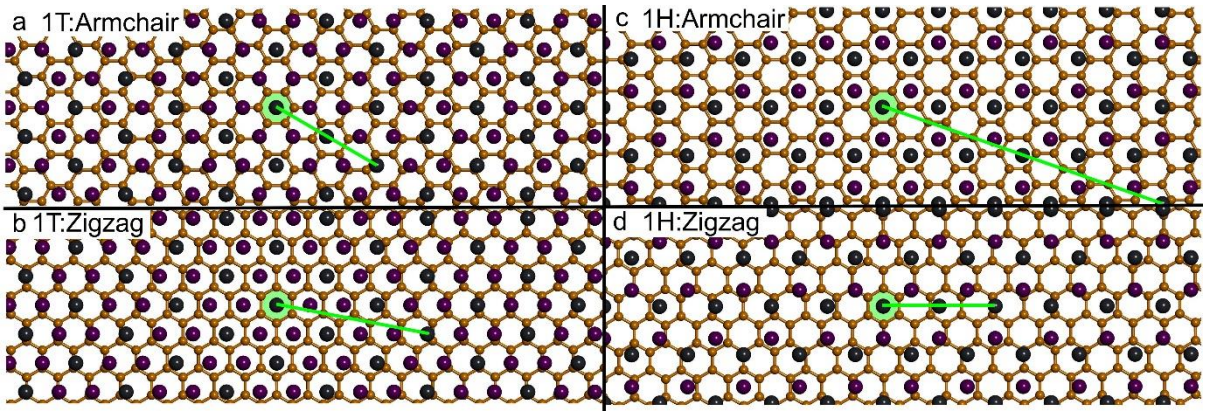

Figure 5.18. Atomic images of (a) PbI_2 (1T) aligned to graphene armchair, (b) PbI_2 (1T) aligned to graphene zigzag, (c) PbI_2 (1H) aligned to graphene armchair, (d) PbI_2 (1H) aligned to graphene zigzag. Green shading indicates the position of Pb located in center of graphene hexagon. Green line indicates the minimum distance where Pb atom overlaps a C-C bond in graphene, indicating loss of commensuration.

Interestingly, we also found that the crystal orientation of PbI_2 on graphene had preferred orientation of PbI_2 zigzag aligned to graphene armchair direction, with only a small fraction showing the zigzag to zigzag alignments. **Figure 5.19a** and **Figure 5.19f** show the ADF-STEM images and their FFTs of the two different types of orientations of PbI_2 on graphene. **Figure 5.19k-r** shows the atomic models of PbI_2 on graphene for the two aligned

directions and the multislice image simulation, along with the FFT results matching the experimental data. To understand why PbI_2 adopts 1H structure with concomitant alignment in these particular directions of graphene, density functional theory (DFT) calculations were employed to study the structural and energetic stability of the different alignments. A short-range relaxed atomic model of PbI_2 on graphene was used, as shown in **Figure 5.19s**, and rotated it every 5 degrees (**Figure 5.19s**) to find the most energetically stable heterostructure (**Figure 5.19t**). This shows that different rotation angles of PbI_2 on graphene have very different energetic stability and only the 'magic angle' is the energetically stable conformer at the room temperature. This also confirms our results to how the graphene influences the stability of the PbI_2 and leads to these energetically favourable structure which are also observed in the experimental results. The details of the DFT models have been described in **Appendix E**.

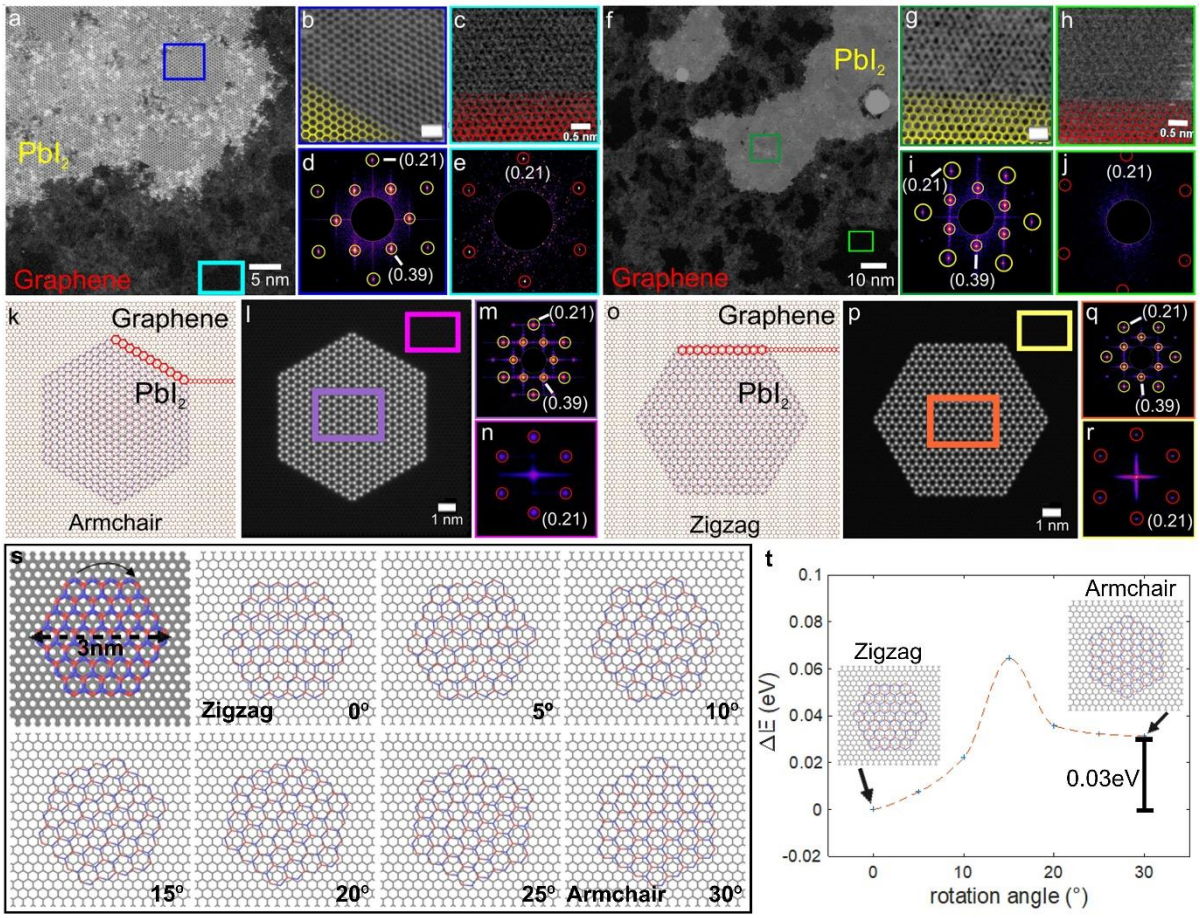

Figure 5.19. (a) ADF-STEM images taken at 60kV (dose: 5.6 x 10^8 e s^{-1}) of PbI_2 flake suspended on graphene. (b) High resolution image of PbI_2 crystal annotated in the dark blue box in panel a. Scale bar corresponds to 1 nm. (c) High resolution image of graphene taken from the cyan box region indicated in panel a. (d) FFT of PbI_2 from the region indicated in panel b. (c) FFT of graphene from the region indicated in panel c. (f) ADF-STEM images of PbI_2 flake suspended on graphene. (g) High resolution image of PbI_2 crystal indicated by the dark green box in panel f. Scale bar corresponds to 1 nm. (h) High resolution image of graphene from the light green box in panel f. (i) FFT of PbI_2 from the region indicated in panel g. (h) FFT of graphene from the region indicated in panel f. (k) Atomic model of PbI_2 (1H) on graphene in the armchair direction. (l) Multislice image simulations based on the atomic model in figure k. (m) FFT of PbI_2 from the region indicated by the purple box in panel l. (n) FFT of graphene from the region indicated by the pink box in panel l. (o) Atomic model of PbI_2 (1H) on graphene in the armchair direction. (p) Multislice image simulations based on the atomic model in figure k. (q) FFT of PbI_2 from the region indicated by the orange box in panel p. (r) FFT of graphene from the region indicated by the yellow box in panel p. (s)-(v) Atomic models showing PbI_2 relative to graphene for (s) DFT-relaxed atomic model of PbI_2 on graphene, rotated every 5 degrees (t) Energy profile of various orientation angles of the PbI_2 flake on graphene.

5.2.3. Structural defects

Next I examined the edge terminations of PbI_2, because edges of 2D materials can influence the electrical, chemical and catalytic properties due to the different bonding (angles,

bond distances, etc.) between atoms.(307–310) **Figure5.20a** shows the typical edges of two different monolayer PbI_2 flakes, just after being deposited on the graphene. The edges are rough and do not appear to be highly faceted to a specific crystal lattice direction. After electron beam irradiation, **Figure5.20b**, the edges are etched to form sharp zig-zag faceted terminations, **Figure5.20c**. The zig-zag edges have iodide atoms protruding out on one side and lead atoms on the adjacent edge of the same flake, **Figure5.20d,e**. Metal and chalcogenide terminated zigzag edges have been routinely observed for as grown monolayer TMDs, such as MoS_2.(311,312) However, when the edges of PbI_2 are etched to form sharp zig-zag faceted terminations after electron beam irradiation, it maintains alignment with graphene, i.e. the etching takes place in zigzag-PbI_2 and armchair graphene direction. **Figure 5.20a** shows the low magnification image of PbI_2 flake on top of graphene at t=0s. **Figure 5.20b-c** show the red and blue boxed regions of figure **Figure5.20**a respectively. From these figures, we can see that initially the zigzag PbI_2 was aligned in the armchair graphene direction. **Figure 5.20b-c** show the time lapse series of ADF-STEM images recorded after 30 seconds of electron beam exposure. The yellow lines marked in **Figure 5.20e** show the edge etching directions. **Figure 5.20f** is the atomic model of the PbI_2/graphene with same lattice orientation as of figure a. As it can be seen, the FFT of the atomic model is shown in the inset of **Figure 5.20f** as the PbI_2/graphene nanodisk imaged at t=0s in **Figure 5.20a**. Comparing that with the atomic model of PbI_2/graphene in **Figure 5.20f,** we can see that the termination of the edges in **Figure 5.20d-e** still conform to the same directionality, i.e. zigzag PbI_2-armchair graphene.

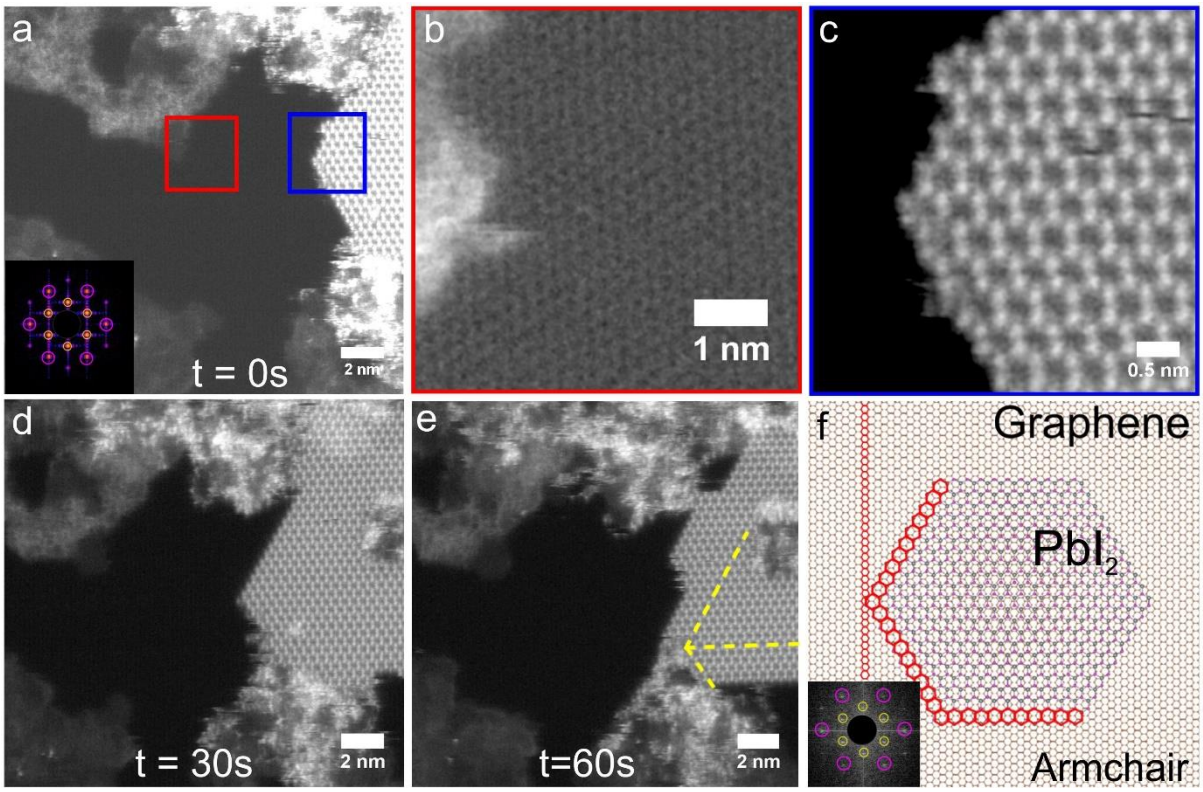

Figure 5.20. (a) ADF-STEM image taken at 60kV (dose: 5.6 x 10^8 e s^{-1}) of PbI2 flake on top of graphene at t=0s. (b) Higher magnification of the region indicated by the red box in (a) showing the graphene resolution. (c) Higher magnification of the region indicated by the blue box in (a) showing the PbI_2 orientation. (d-e) Time lapse ADF-STEM image of the edge at t = 0 seconds and t = 30 seconds of electron beam exposure. The yellow arrow indicates the ejection of the electrons from the edges due to the damage from the electron beam, leading to 'un-zipping' of the chain, maintaining the zig-zag edge of the flakes. (f) Atomic model of the PbI2/graphene with same lattice orientation as of figure (a). The Inset shows the FFT of the atomic model.

Edge etching occurred by atomic loss under the electron beam as shown in **Figure 5.21h-i**. Moreover, the edges also showed atomic attachment to restructure, **Figure 5.21j-l**. **Figure 5.22** shows the time lapse ADF-STEM image for the relative alignment frames for the region of PbI_2 shown in **Figure 5.21j-l**. **Figure 5.22a-c** shows the relative alignment of the picture frame based on the presence of the stable defect shown in red and blue boxes (higher resolution images shown in the **Figure 5.22d-f** and also on the accumulated atomic clusters shown by the orange and yellow arrowheads. The following figures show the relative alignment of the time frames of the captured images shown in **Figure 5.21j-l**. After 30s of electron beam exposure, the atoms at the edge are sputtered out, by unzipping such that the

atoms are removed one by one from the edge in a continuous line, in the same way that a zip is opened. Meanwhile, the outer most atoms to retain its uniform zig-zag termination (**Figure 5.21i**).[56] Prolonged exposure to the electron beam eventually leads to edge roughening. DFT and ab-initio molecular dynamics simulations have shown the edge reconstructions effect the electrical and magnetic properties of the material.(313)

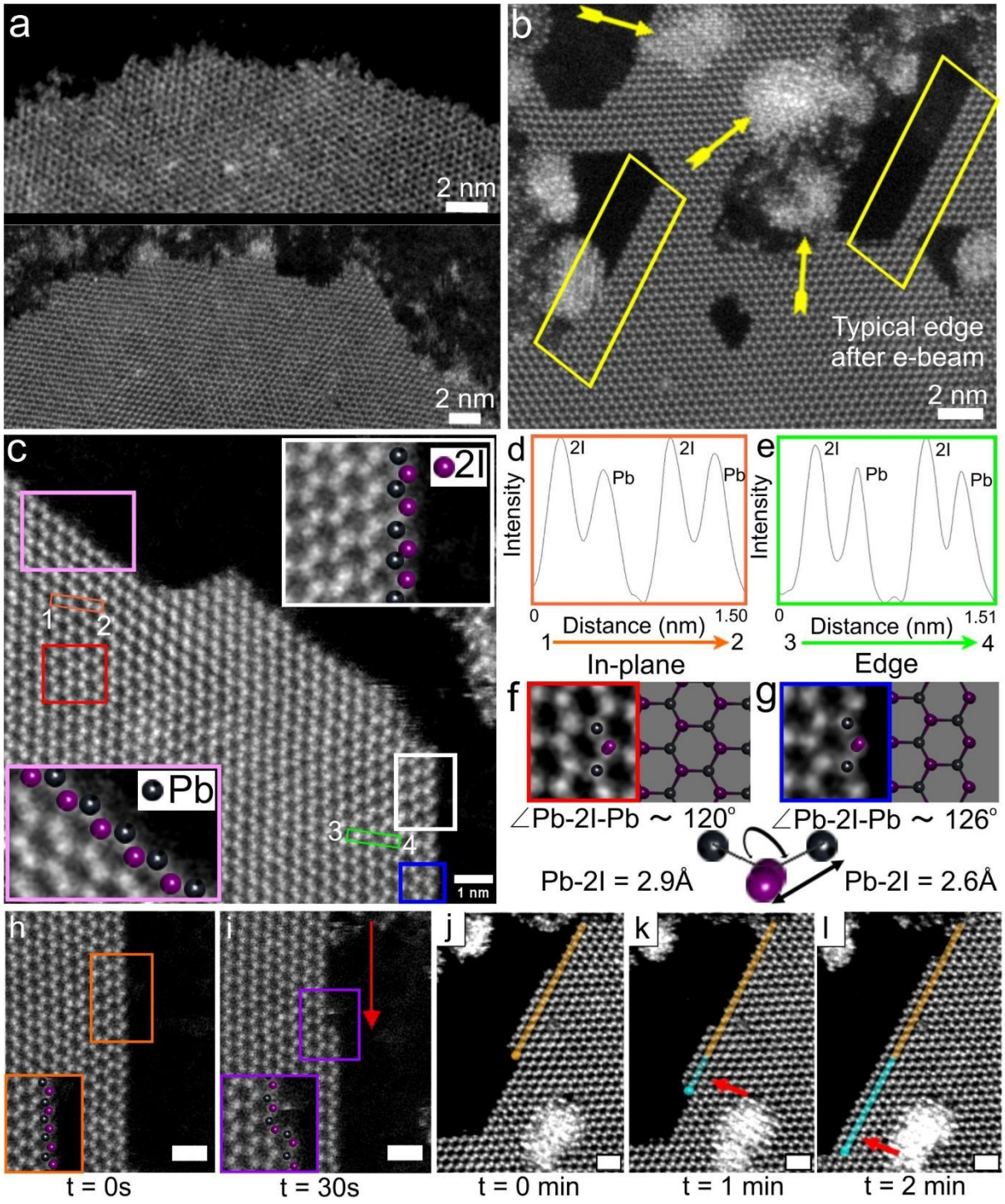

Figure 5.21. ADF-STEM image taken at 60kV (dose: 5.6 x 10^8 e s^{-1}; electron fluence of 2 x 10^6 e nm^{-2}) of (a) typical intrinsic edges of two different monolayer PbI_2 flakes just after deposition on the graphene and (b) sharp zig-zag faceted edges of the monolayer PbI_2 flake after electron beam irradiation. The arrows show the clustering of the atoms after having been sputtered out of the edges. The yellow boxes show the faceted zig-ag edge formation from the intrinsic edges after the damage from electron beam. (c) ADF-STEM images showing I- and Pb- terminated zigzag termination. The two insets in the image shown with white and pink boxes show the high resolution of the areas with same color annotation that have I- and Pb-terminated edges. The line profile of the regions marked in orange and green boxes confirms the position of the lead and iodide in the honeycomb structure. (d-e) The line profile of the

orange and green boxes shown in (c) in the direction of 1-2 and 3-4. (f) High resolution ADF-STEM image of the area shown under red box in figure c. (g) High resolution ADF-STEM image of the area shown under blue box in figure c. (h-i) Time lapse ADF-STEM image of the edge at t = 0 seconds and t = 30 seconds of electron beam exposure. The red arrow indicates the ejection of the atoms from the edges due to the damage from the electron beam, leading to 'un-zipping' of the chain, maintaining the zig-zag edge of the flakes. (j-l) Time lapse series of ADF-STEM images recorded after 1 minute of electron beam exposure. The yellow annotations show the edge terminated bonds at the edge at t = 0 seconds which starts reconstructing in (k), annotated with blue. After 2 minutes, figure l, the edge was fully reconstructed, as shown with growing blue annotated region. The scale bars in h-l correspond to 1 nm.

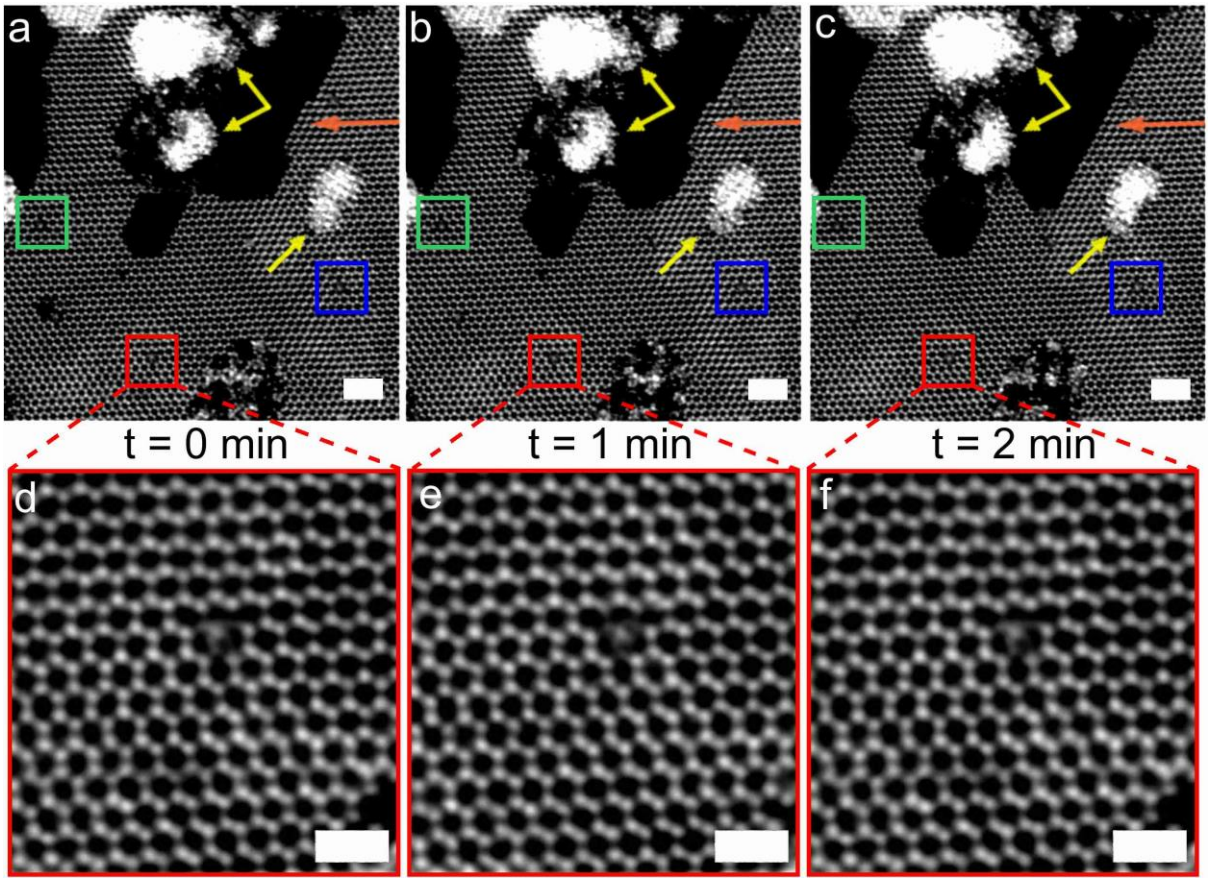

Figure 5.22. (a-c) ADF – STEM time lapse image taken at 60kV (dose: 5.6 x 10^8 e s^{-1}) of a section of PbI_2 taken after every 1 minute of electron beam irradiation. The red and blue boxes show the stable defect and yellow and orange arrowhead are used to point the accumulated atomic clusters which have been used for relative alignment of the frames. (d-f) Higher resolution images of the stable defect boxed in red in figures (a-c) respectively.

ADF-STEM of the central lattice region of the PbI_2 monolayers revealed point defects across the region as shown in **Figure 5.23**. Single point vacancies were observed for both the lead and iodide sub-lattice sites in PbI_2, as shown in **Figure 5.23b-c**, and identified using line

profiles shown in **Figure 5.24**. The interpretation and assignment of the experimental images to their simulated configurations, in **Figure 5.23b-c**, were made on the line profile of the defects after normalizing their intensities. As it can be seen, the line profiles of the corresponding images, in the following **Figure 5.24 a-b**, show clear Lead and Iodide vacancies in blue and red respectively. Several different types of multiple atom point vacancies are identified, ranging from 2 atoms (**Figure 5.23d,e**) to the 7 atom defect clusters (**Figure 5.23k**).

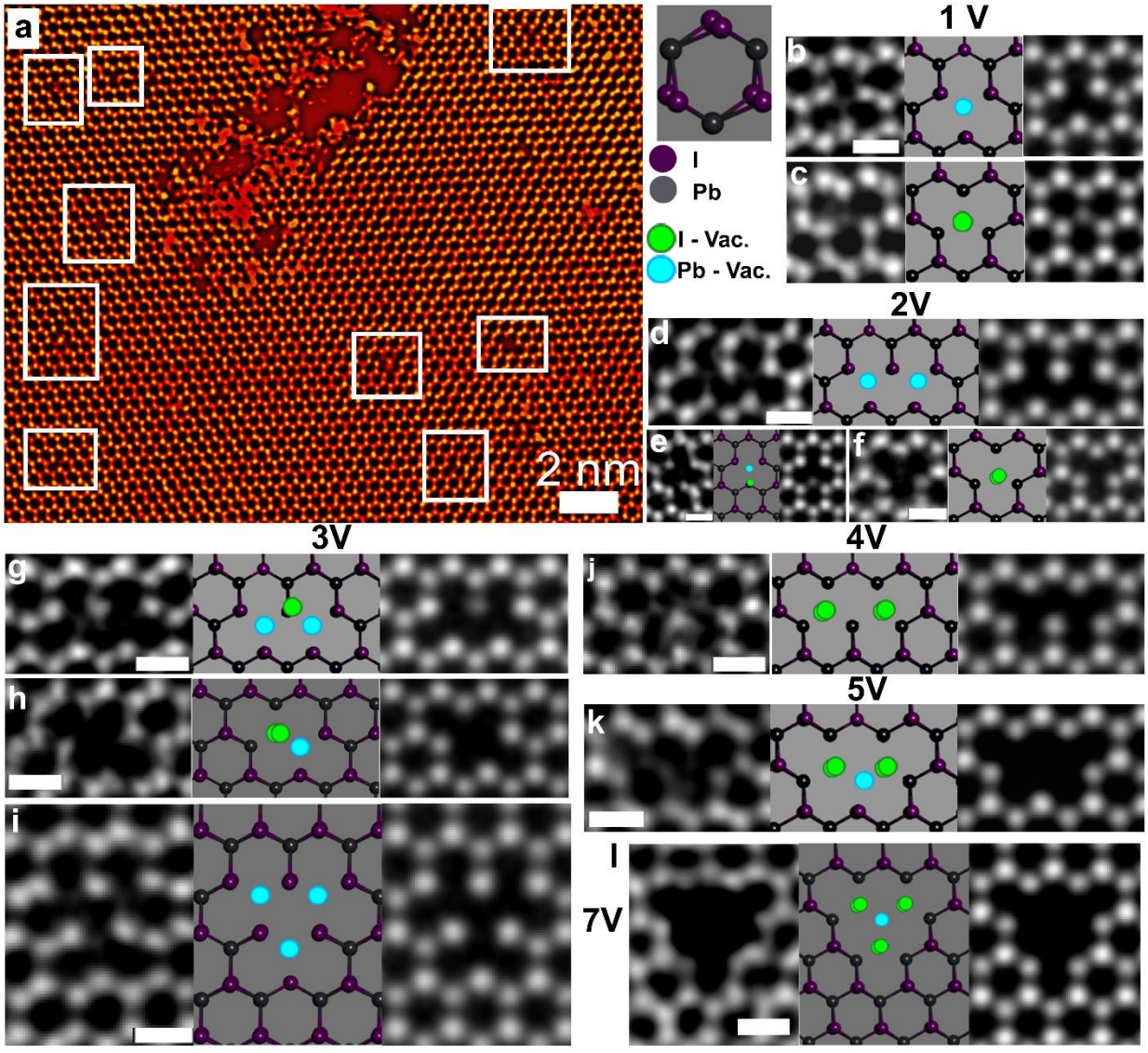

Figure 5.23. (a) Low magnification ADF-STEM image taken at 60kV (dose: 5.6 x 10^8 e s^{-1}) of monolayer PbI_2 region after electron beam exposure. The purple and grey spheres correspond to lead and iodide in the structure. The green and blue spheres correspond to the iodide and lead vacancies in the system. ADF-STEM images and their corresponding 1H – PbI_2 structured atomic model as well as multislice simulations have been shown for (b) point defect with a missing lead atom, (c) point-defect with a missing iodide atom, (d) double-point

defect with 2 – Iodide atoms missing, (e) double – point defect where two lead atoms from adjacent crystal cells are lost, (f) double – point defect with one lead and one iodide atoms missing. It can be observed that the single iodide has lower intensity than that of lead or 2-Iodides, (g) 3 vacancies formed out of two lead and one iodide loss. It can be observed that the remaining single iodide in the middle has lower intensity than that of lead or 2-Iodides, (h) 3-vacancy formed by the absence of three lead atoms from adjacent crystal cells, (i) another 3-vacancy formed by 2 iodide and 1 lead loss, (j) four vacancy defect formed by loss of 2-I from adjacent honeycomb structures, (k) 5 vacancies formed because of loss of 4 iodide atoms and a lead atom in a row, (l) bigger triangular defect formed because of the loss of one lead and 6 iodide atoms from the center. The scale bar in all the images indicate 0.5 nm.

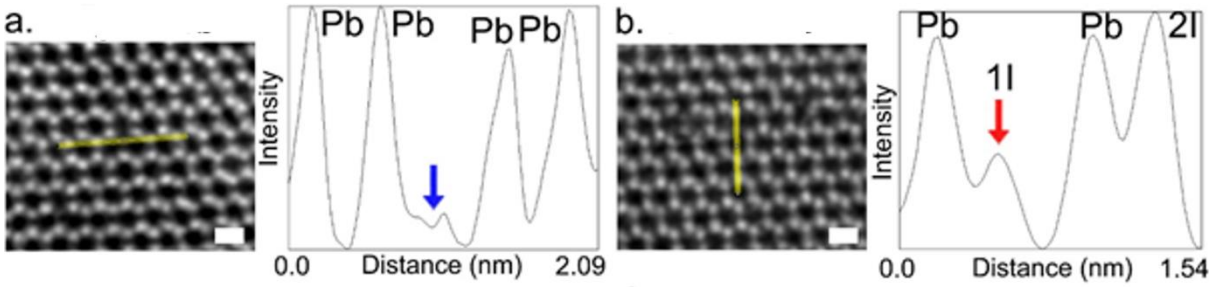

Figure 5.24. ADF-STEM image taken at 60kV (dose: 5.6 x 10^8 e s^{-1}) of lead iodide defects. The blue and red arrows correspond to lead and iodide vacancies respectively. (a) 1 Lead vacancy, as can be seen from corresponding line profile. (b) 1 Iodide vacancy, as can be seen from the corresponding line profile.

The energy[49] to remove a single iodide or lead atom from the lattice into the vacuum was calculated by DFT. A 10×10×1 supercell is used for calculating the sputtering energy. The sputtering energy is defined by the energy difference between the crystalline structure and the one with a vacancy, for instance, the I sputtering energy is $\Delta E_I = E_{crystal} - (E_{V_I} + E_I)$. The energy tolerance is set to 0.0001 for all energy calculations. The following **Figure 5.25** shows (a) Pristine supercell, (b) supercell with one I vacancy, and (c) supercell with one Pb vacancy. The energy differences, as calculated are:

$$\Delta E_I = E_{crystal} - \left(E_{V_I} + E_I\right) = (-837.01) - (-840.16) = 3.15\ eV$$

$$\Delta E_{Pb} = E_{crystal} - \left(E_{V_{Pb}} + E_{Pb}\right) = (-833.80) - (-840.16) = 6.36\ eV$$

[49] The energy discussed here is the enthalpy needed to remove the atoms from the surface. It is important to calculate the energy barrier of such removal. However, current DFT calculations are limited to calculation of the enthalpy and it is extremely difficult to calculate or predict the energy barrier of the removal of atoms from the surface.

he maximum amount of energy (E) transferred by an incident electron (@80keV) to a single Iodide or Lead atom is calculated to be 1.38eV and 0.85eV respectively. This energy transfer from the incident electron to the specimen atoms is much lower than the required sputtering energy calculated by DFT. Hence, we can deduce that the mechanism of damage in this system is more complicated than purely knock-on damage from atomic sputtering, and likely involves radiolysis. This is not surprising, since PbI_2 is a large bad-gap semiconductor and therefore prone to ionization effects from the electron beam, even on graphene.

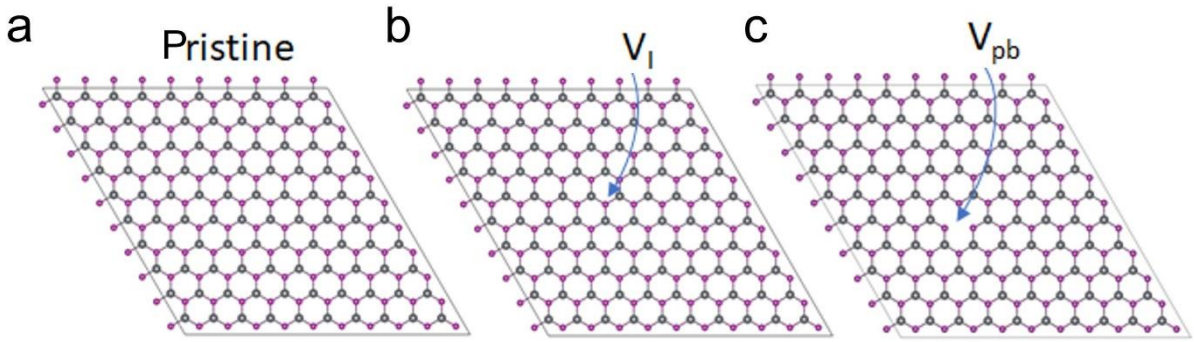

Figure 5.25. Atomic model of the PbI_2 (a) pristine supercell (b) one I vacancy supercell (c) one Pb vacancy.

Moreover, we observed that vacancies did not assemble into linear structures, as in TMDs, but instead aggregated to form clusters. The following **Figure 5.26** shows the effect of the accumulation of the atoms after electron beam exposure. Iodine atoms are relatively lighter than Pb atoms and hence, the likelihood of them getting displaced from the lattice is higher. The contrast of the single atoms imaged are of similar magnitude to that of Lead within the PbI_2 lattice. The atoms aggregate to form amorphous clusters, as shown with red arrows in **Figure 5.26a** or get dispersed on the surface of graphene as shown in **Figure 5.26b**.

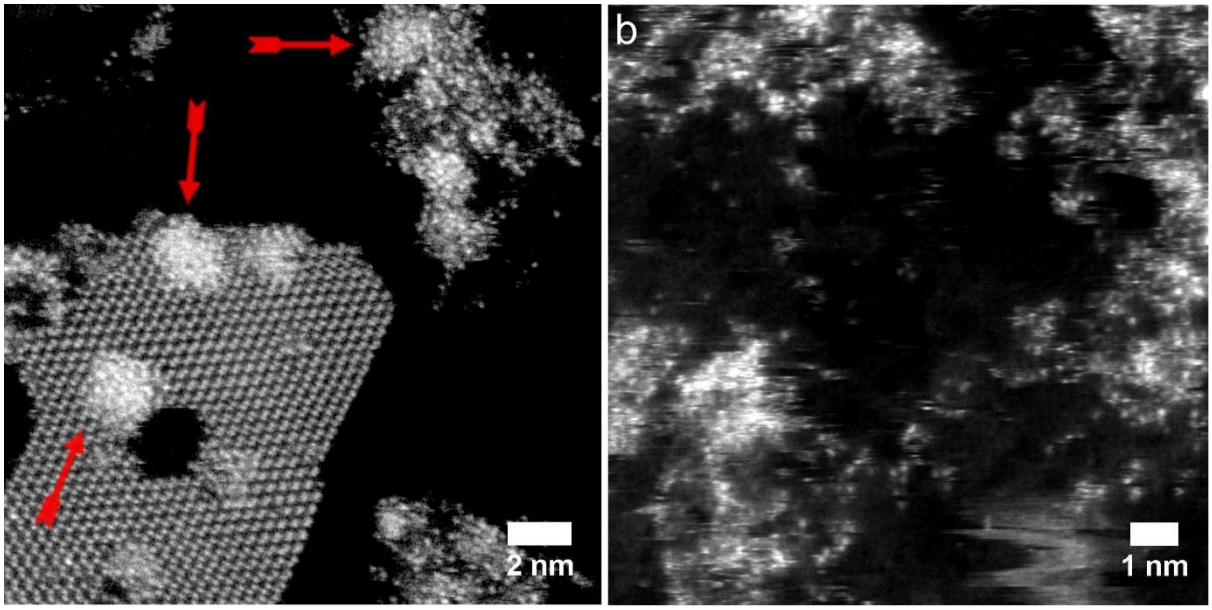

Figure 5.26. ADF-STEM image of lead atoms taken at 60kV (dose: 5.6 x 10^8 e s^{-1}), forming (a) clusters (b) dispersion on the graphene.

On multiple occasions it was also observed that where the defect (**Figure 5.27**) had one Pb atom in the center and five iodide atoms surrounding it, which was stable even under prolonged electron beam irradiation (**Figure 5.27a-d**). **Figure 5.27f-g** and **Figure 5.27i-j** show the proposed atomic model and the simulation of the two different configurations of this defect, **Figure 5.27e** and **Figure 5.27**h respectively. Since a single iodine atom is much lighter (Z = 53) than the single Pb atom (Z = 82), it has lower contrast in ADF-STEM. The line profiles in **Figure 5.27** confirm the presence of iodide atoms close to the lead atom in the center, causing the iodide peaks to be only partially resolved and forming a tail either side of the lead atom. **Figure 5.27x** shows the structure of the system where Pb is coordinated with 5 other Iodine atoms with interatomic distance varying from 1.4 Å - 2.3 Å. 3D PbI_2 is known for having more than 20% defect in the crystal.(274) Therefore, it is interesting to see formation of new types of defects in the 2D form pf PbI_2 as well – the nature and type of which has not been determined yet and can prove to be interesting to study in further studies. Here, formation of a stable 4-membered ring was observed around the lead atoms (**Figure 5.27f**, **Figure 5.27i**), where the lighter iodide atoms substitute the heavier lead atoms (**Figure 5.27f**).

Similar stable 4-membered ring configuration have also been reported for monolayer MoS_2 structures.(314)

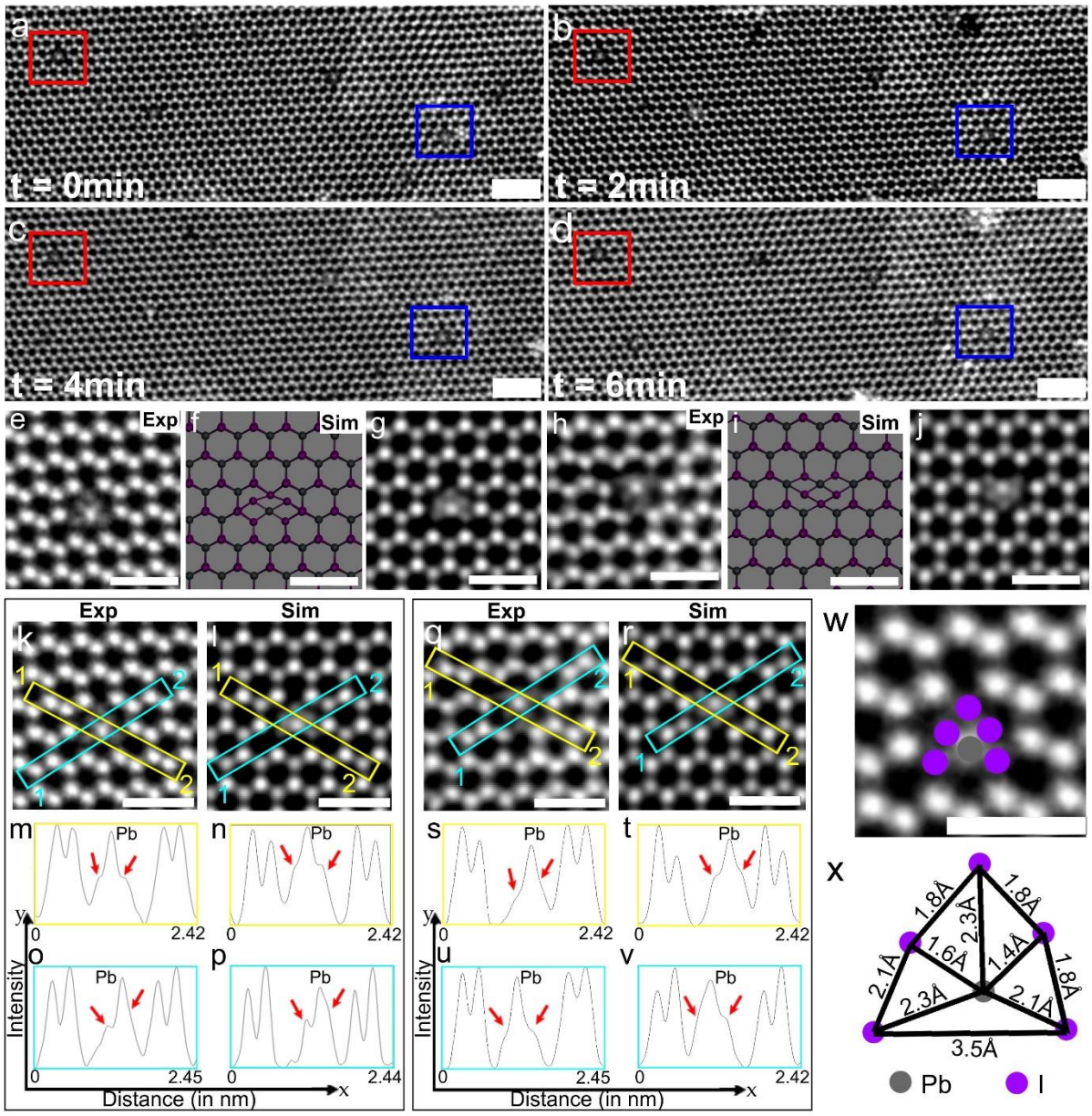

Figure 5.27. (a-d) Time lapse ADF-STEM images taken at 60kV (dose: 5.6 x 10^8 e s^{-1}), after every 2 minutes. The red and blue boxes show the two different orientations of the substitutional defect which is rather stable under the electron beam exposure. (e) ADF-STEM image of a defect with lead in the center and surrounded by 5 other iodide atoms. (f) Atomic model which shows the atomic model of the corresponding experimental result. (g) Multislice image simulations based on the atomic model in (f), schematically illustrating the lower intensity of the single iodide atoms surrounding the lead, which agrees with the experimental data in (e). (m-n) Line profile taken across the lead and iodide atoms across the yellow annotated regions in the experimental data (k) and multislice simulated image in (l). The red arrow shows unresolved iodide peaks around the lead. (o-p) Line profile taken across the lead and iodide atoms across the blue annotated region in (k) and (l) respectively. The red arrow

shows unresolved iodide peaks around the lead. (j) (h) ADF-STEM image of the opposite orientated substitutional defect. (i) Atomic model which shows the atomic model of the corresponding experimental result. (j) Multislice image simulations based on the atomic model in (i), schematically illustrating the lower intensity of the single iodide atoms surrounding the lead, which agrees with the experimental data in (h). (s-t) Line profile taken across the lead and iodide atoms across the yellow annotated regions in the experimental data (q) and multislice simulated image in (r). The red arrow shows unresolved iodide peaks around the lead. (u-v) Line profile taken across the lead and iodide atoms across the blue annotated region in (q) and (r) respectively. The red arrow shows unresolved iodide peaks around the lead. (w) Annotated image of (e). (x) Distance between the different atoms shown in the annotated region in (w). Scale bar figure (a-d) correspond to 2 nm whereas in the rest of the images correspond to 1 nm.

During electron beam irradiation the vacancies migrated through the lattice and reconstructed. DFT calculations were performed for vacancy migration. 10×10 supercells and 4×4 k-point grids are employed, and a criterion of 0.03 eV/ Å is set for the force convergence. For V_I migration, two pathways are considered (**Figure 5.28**): in plane and out-of-plane directions, and only in-plane V_{Pb} migration is considered. The starting and end points for NEB search are prepared by removing the corresponding atoms from the relaxed pristine structure, and then further relaxed. The 6 intermediate images are interpolated by the Vasp TST toolkit. The converged energy paths are the fitted by cubic spline functions. It was found that the energy barrier for migration of lead atom, the in-plane migration of the iodide atom and the out-of-plane migration of iodide atom which corresponded to 0.32eV, 0.22eV and 0.07eV respectively (**Figure 5.28**). The vacancy of migration of the atoms on the surface is considerably lower than the energy imparted from the electron beam (1.38eV and 0.85eV for Iodide and lead atoms respectively @80kV) and thus explains the quick migration of the vacancies and defects in the system. **Figure 5.29** is an example of a double iodide vacancy (**Figure 5.29b**) and its migration (**Figure 5.29c**) before subsequently healing to render the original structure in **Figure 5.29a** (**Figure 5.29d**). Defect healing occurred in point defects and also with in multiple atom vacancies, such as **Figure 5.29e-g** where a large defect with 7 atoms missing (1 Pb and 6 I) is healed.

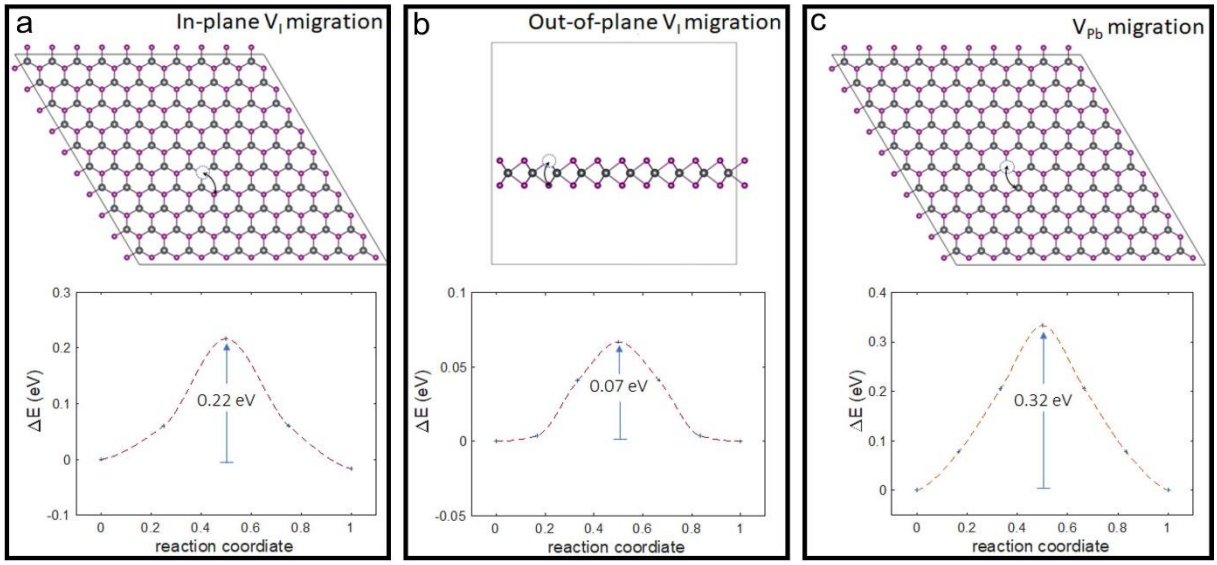

Figure 5.28. Atomic structure and energy profile for vacancy migration of (a) Iodide atom in-plane (b) Iodide atom out-of-plane and (c) Lead atom.

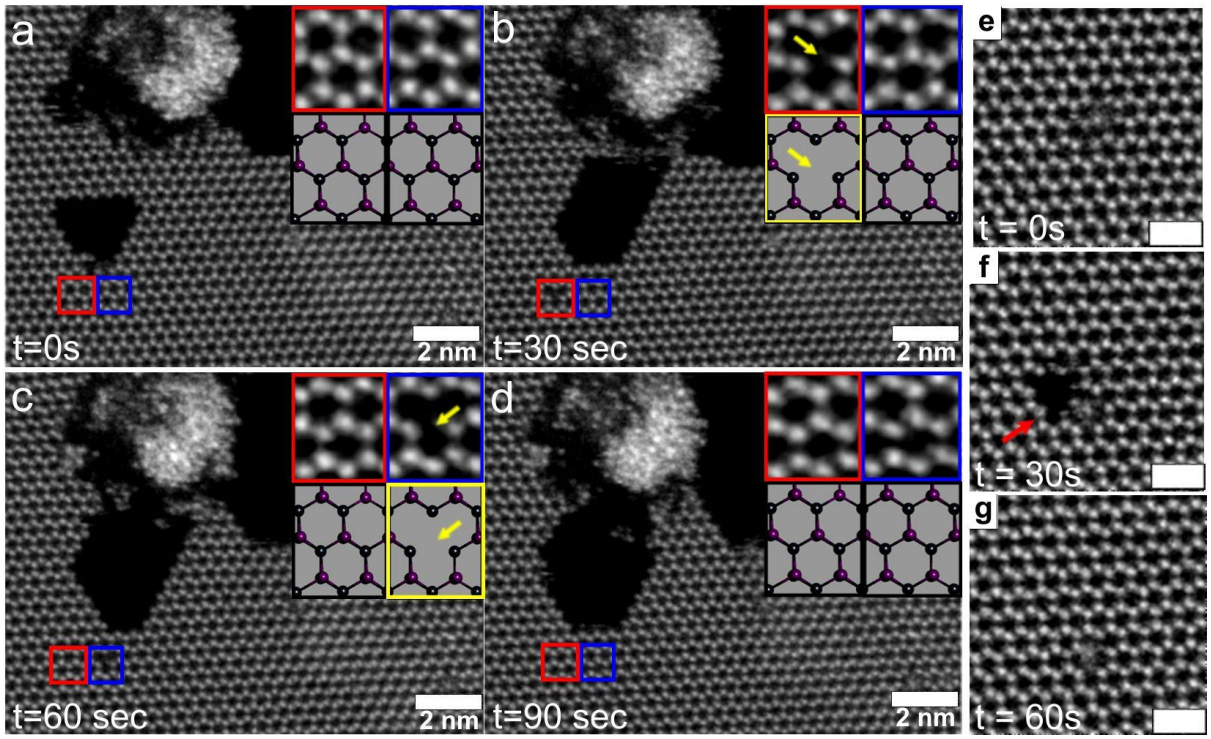

Figure 5.29. (a-d) Time series of ADF-STEM images taken at 60kV (dose: 5.6 x 10^8 e s^{-1}) recorded after every 30 seconds, of point defect formation, migration and then reconstruction. The inset under red and blue boxes in the images are high-magnification images of the defects that have been marked with smaller red and blue box respectively in the same image. The inset figures in black and yellow boxes below the high-magnification insets are the corresponding atomic models. The yellow boxes and arrows in (b) and (c) highlights the formation of a point vacancy and its migration in the inset above, before finally reconstructing in (d). (e-g) Time series of ADF-STEM images recorded at an accelerating voltage of 80 kV after every 30 seconds of electron beam exposure. The red arrow in figure (f) shows the formation of 7

vacancy defect, but it gets quickly reconstructed in image (g) after another 30 seconds of exposure. The scale bar in e-g correspond to 1 nm.

Further electron beam exposure caused the vacancies to grow larger and form nanopores in monolayer PbI_2 crystals.(315,316) The nanopores undergo geometric reconstructions by atomic loss, **Figure 5.30**a-p, but also sometimes gain atoms, **Figure 5.30**o-p. Diffusing Pb and I atoms add to the edge sites of the nanopores to enable reconstruction. The nanopores in general adopt zigzag edge terminations and have triangular or hexagonal shape. In several cases, atoms migrate from one side of the nanopore to another side to change the nanopore shape. **Figure 5.30**q-u shows a case where a large triangular nanopore is formed by electron beam irradiation, and is then back-filled by its nearby atoms. Between **Figure 5.30**s-p, the top left section of the triangular nanopore has contracted by atoms filling it in from the nearby edge region. The red arrows indicate the possibility of migration of the atoms from one position to the other. The electron beam damages the material and forms the nanopore but at the same time, fast migration of atoms and the self-healing process in the material in real time is also observed. However, prolonged exposure to the electron beam ultimately leads excessive sputtering of atoms than the self-healing itself leafing to a bigger nanopore formation. Similarly, in **Figure 5.30**q-t, the self-healing is not perfect, but the nanopore is no longer present and vacancies have been eliminated by the migration to the edge.

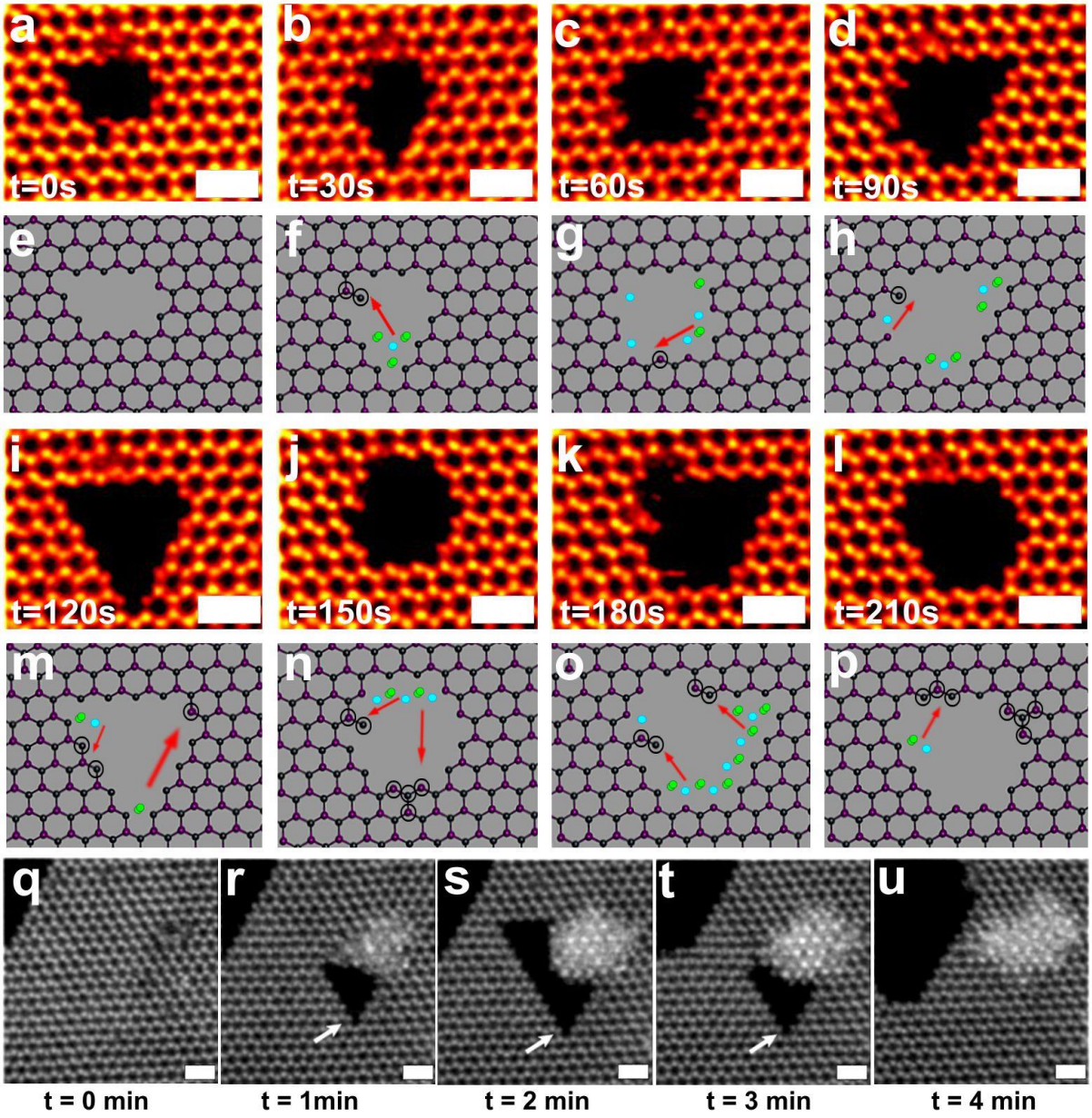

Figure 5.30. (a-p) Time series of ADF-STEM images taken at 60kV (dose: 5.6 x 10^8 e s^{-1}), and their corresponding atomic models. Holes can be seen to change its shape in monolayer PbI_2 flake. The blue atoms correspond the lead defect region and the green corresponds to the iodide defect region. The black circles around the atoms in the atomic models correspond to the new atomic bond in the structure as compared from the previous frame. (q-u) Time series of ADF-STEM images recorded after every 1 minute of electron beam exposure. The defect starts forming after 1 minute, in image (r) and more atoms are ejected to form a bigger defect in (s). Then the atoms at the edge starts ejecting out in (t) and reconstruction of the flake starts occurring leading to again defect-free surface in (u).The scale bar in all images corresponds to 1 nm.

Migration of entire nanopores, as a single entity, up to 4 nm on the same monolayer flake was also observed. **Figure 5.31**(a-i) is set of time lapsed images, taken every 30 seconds,

of hole formation and reconstruction as well as migration on the same monolayer flake upon beam exposure. The yellow boxes in **Figure 5.31** (g-i) show the accumulation of the atoms at the edge and surface region next to the nanopore. The quick variation in the position and size of these holes clearly show how mobile the lead and iodide atoms are on the surface and continuously try to form new structures.

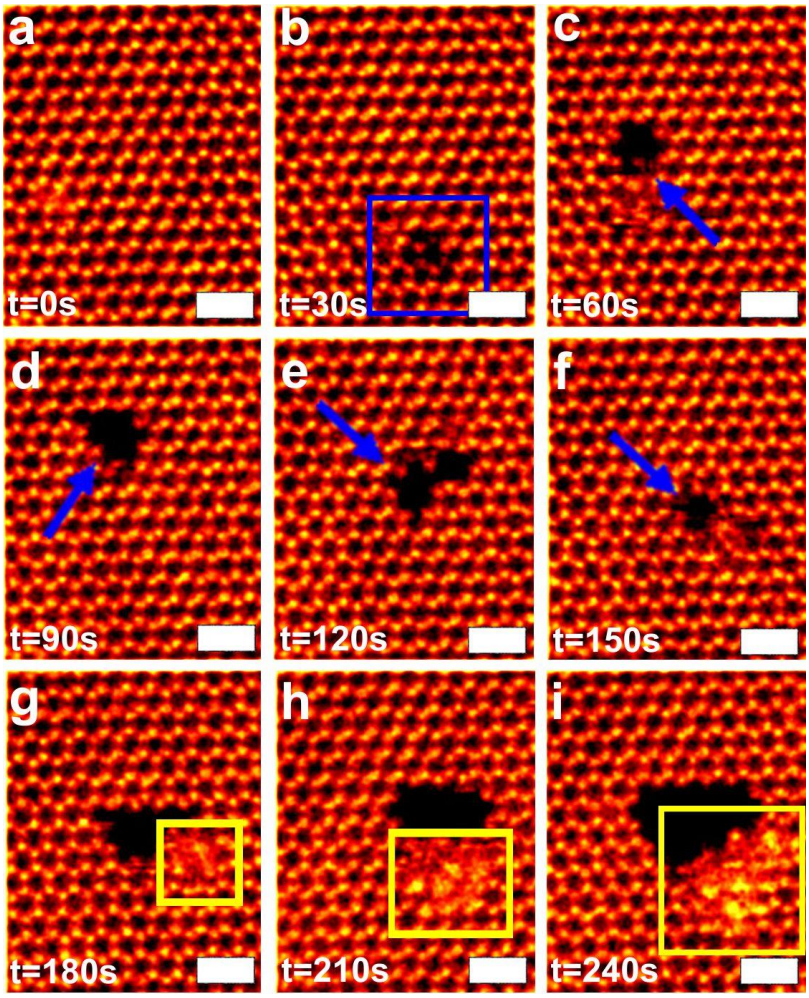

Figure 5.31. (a-i) Time series of ADF-STEM images taken at 60kV (dose: 5.6 x 10^8 e s^{-1}) recorded of nanopores changing form as well as migrating large distances within single monolayer PbI_2 flake. The scale bar corresponds to 1 nm.

5.3 Conclusion

Strong epitaxial alignment of PbI_2 monolayers with the underlying graphene lattice occurs, PbI_2 zig-zag matching graphene arm-chair direction, leading to a phase shift from the 1T to 1H structure to increase the level of commensuration in the two lattice spacings (PbI_2

and graphene). The fundamental point vacancy structures in PbI_2 monolayers are directly imaged, showing rapid vacancy migration to the edges and self-healing. The relative lattice spacing of PbI_2 and graphene results in preferential alignment of the PbI_2 zigzag direction to the arm-chair direction of graphene to maximize the commensuration of the two lattices. Zig-zag edges are observed to dominate the PbI_2 nanodisks and sequential atom-by-atom edge etching is imaged. Nanopores are produced by electron beam irradiation of the PbI_2 nanodisks and undergo migration as an intact entity throughout the lattice. These results provide a detailed insight into the atomic structure and defects in monolayer PbI_2, and the impact of the strong van der Waals interaction with graphene, which has importance for future applications in opto-electronics. Integrating monolayer PbI_2 with other 2D materials provides a huge scope for new applications and the ability to manipulate its atomic monolayer structure provides a unique opportunity to tune its properties. Studying the influence of the substrate on the structure of PbI_2 would hopefully make it easier to understand the complicated polytypes and stacking arrangement in PbI_2. ADF-STEM imaging of the PbI_2 monolayers revealed highly mobile point vacancies and their growth into nanopores, which exhibited reconstructions and self-healing. Studying these vacancies in the 2D material is important for the foundation knowledge of the semiconducting properties for future work.

5.4 Contribution Statement

Dr. Jamie Warner helped with the study and analysis of the ADF-STEM data. Dr. Viktoryia Shautsova helped with taking the AFM images of the samples. Dr. Yuewen Sheng provided CVD-grown graphene for this study. Dr. Taishan Zhu carried out the DFT calculations.

Chapter 6 Phase transformation of 2D $PdSe_2$

Phase change occurs in materials when the stoichiometry of the chemical compound is modified leading to a different crystal structure. Bulk materials have been studied thoroughly for their phase change behavior. However, 2D materials are not quite as well understood in terms of their phase transformation. Work in this area is of particular importance as it can provide a way to control and modify the properties of the material. However, controllable transformation between the semiconducting and metallic phases of transition metal chalcogenides has been, so far, technologically challenging. Here, we demonstrate that controlled laser irradiation can be used to directly ablate Palladium diselenide ($PdSe_2$) thin films using high power, or trigger the local transformation of $PdSe_2$ into a metallic phase $PdSe_{2-x}$ using lower laser power. Such transformations are possible due to the low decomposition temperature of $PdSe_2$ compared to other 2D transition metal dichalcogenides. Presence of graphene underneath has interesting effect on the amount of transformed sample. ADF-STEM is used to reveal the laser-induced Se-deficient phases of $PdSe_2$ material. These findings contribute to the development of nanoscale devices with homojunctions and scalable methods to achieve structural transformations in 2D materials. The results of this chapter have been published in ACS Nano, 2019.

6.1 Introduction

6.1.1. $PdSe_2$

$PdSe_2$ is a particularly interesting 2D material as it is a less explored, group-10 transition metal dichalcogenide, that shows gradual transition in its electronic properties from semiconductor in monolayer to semimetal in the bulk material.(317,318) Moreover, its tunable band gap in the range of 0.3–1.5 eV is highly desirable for electronic and optoelectronic applications. As a phase change material, $PdSe_2$ is attracting a lot of attention as it has an interesting atomic structure on top of its unique electronic properties. It has a unique anisotropic structure with the metal atoms and intralayer chalcogen atom bonding resulting in an unusual 4-fold coordination. This results in a strong interlayer interaction, giving rise to interesting phase engineering results such as superconductivity, interlayer fusion, etc.(319–327) Hence the Se vacancy can lead to large distortions and thus formation of different structural phases leading to completely new electronic properties. It has already been shown that polymorphic phases of this material can be obtained by weakening the Se-Se intralayer bonds under high pressure, leading to new phases such as layered monoclinic phase,(319) layered 1T phase(320) and pyrite-type phase.(321) Moreover, recent studies have shown that Se vacancies can convert the layered semiconducting $PdSe_2$ phase into metallic phases such as $Pd_{17}Se_{15}$(322) and Pd_2Se_3.(323,324) Furthermore, both elemental depletion of selenium or palladium in binary compounds can result in formation of new material phases with different compositions and new properties.(325–327) These phase transitioned materials can have abrupt change in physical properties, offering great potential for future applications in electronic and optoelectronic device applications.(328) For instance, Zuluaga et al. demonstrated that lateral junction between a $PdSe_2$ bilayer and a Pd_2Se_3 monolayer results in formation of a 1D channel with smaller band gap.(324) Similarly, seamless Ohmic contacts have been formed for field effect transistors from $Pd_{17}Se_{15}/PdSe_2$ junction(322) and

ferroelastic transitions predicted with the breaking of Pd-Se bond.(329) Hence, facilitating controlled local phase transitions in $PdSe_2$ offers a vast arena of opportunities to modify the structure and also create high quality heterophase structures with new properties.

6.1.2. Laser-driven Phase-Transformation Technique

Although phase transformations and crystal structure change have been studied thoroughly for bulk materials, it's still not well established for 2D materials.(330,331) Phase modifications have been enduced in 2D materials using a variety of processing methods, such as plasma treatment,(322) electron or ion beam irradiation(323,324) chemical reactions,(332–334) strain engineering,(335) and laser exposure.(336,337) Chemical medication or ion beam irradiation offers little control over the area and magnitude of effect on the material. In addition, producing phase engineered 2D material with atomic layer precision and geometrical pattern, using other methods, is still a practical challenge. Therefore, the laser-driven phase patterning is of particular importance because it offers relatively higher controllability and precision in patterning the nanoscale features with more reliability, scalability and lower cost.(338,339) The phase transition in a region occurs when it is exposed to laser irradiation and thus it also does not require predefined pattern designs. By tuning in the laser power and laser exposure time, we can control the phase transition of the 2D material both spatially and extent of transformation. This technique has been studied and used for both graphene and TMD materials to not only pattern the thin layers but also reduce them locally. In graphene, local material ablation can be carried out using pulsed lasers(340,341) and graphene oxide can be reduced locally to facilitate the junction formation.(342–344) In case of TMD materials, for instance MoS_2, laser-induced thinning has been shown to have enabled the formation of single-layers from previously multilayers materials.(345) $MoTe_2$ has been demonstrated to form homojunction Ohmic contacts when exposed to laser-induced phase patterning.(336)

Here we have employed the laser-driven phase transformation technique to locally modify and transform the $PdSe_2$ to Se-deficient phase.

6.1.3. Underlying Graphene Support

Laser annealing is known to causes local thermal heating. Since both the laser heating and substrate cooling can have an effect on the phase transition of the material, the end result can change depending on the type of substrate being used.(339) It is known that graphene has high intrinsic thermal conductivity exceeding 3000 W/mK near room temperature for large graphene flakes.(346–348) Moreover, it has been previously shown that liquid-phase-exfoliated graphene can act like a filler material in phase change materials and can potentially have use in thermal management of high-power-density battery parks.(349) Here we prepare the graphene-$PdSe_2$ heterostructure and study the effects of laser annealing on the material. Graphene not only provides support to $PdSe_2$ to carry out ADF-STEM imaging but also effects the local phase transformation acting as a substrate.

6.2 Results & Discussion

6.2.1. $PdSe_2$ Structure & Simulation

$PdSe_2$ is one of the materials of the class of noble transition metal chalcogenides, such as $PtSe_2$ etc. The monolayer has a unique pentagonal bonded crystal structure (**Figure 6.1**a) which has not been reported for any other TMD materials before. As shown in the top view, side-view and its multislice image simulation in **Figure 6.1**(a-b) respectively, the entire monolayer region consists of the pentagonal rings where the vertices form a slightly asymmetrical boat confirmation, similar to the puckered structure of 2D monolayer black phosphorene (BP).(350) Each Pd atom shows unusual tetra-coordination, binding to four Se atoms in the same layer, as seen from the top view (**Figure 6.1**a) and two neighbouring Se atoms can form Se-Se covalent bond, as it can be seen in the side-view (**Figure 6.1**b). The few

layered $PdSe_2$ is interesting because odd and even layered multilayer flakes appear differently in ADF image, as it was confirmed from the multislice image simulation. **Figure 6.1**(d-e) and **Figure 6.1**.(g-h) show the atomic model of odd and even number of layers in a few layer PdSe2 respectively and **Figure 6.1**f and **Figure 6.1**i are the corresponding simulated images.

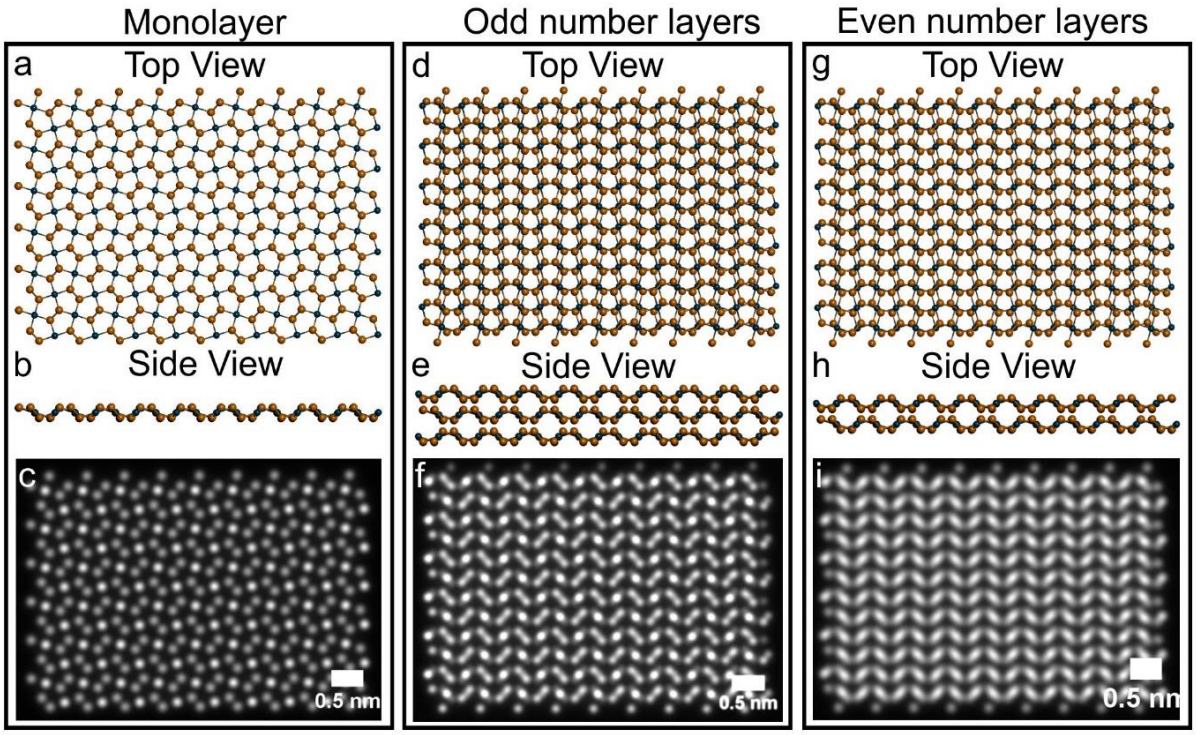

Figure 6.1. Crystallographic structural atomic models of monolayer and few-layer $PdSe_2$ and their corresponding side view and multislice simulated images. Blue corresponds to Pd atom whereas the orange corresponds to Se atom. (a-c) Top view, side view and multislice simulation of of the monolayer $PdSe_2$ respectively. (d-f) Top view, side view and multislice simulation of a few odd number layered $PdSe_2$ respectively. (g-i) Top view, side view and multislice simulation of a few even number layered $PdSe_2$ respectively.

6.2.2. Sample Preparation

CVD grown $PdSe_2$ of the size 2cm x 2cm was purchased from 2D Semiconductors. The commercial grade $PdSe_2$ was found to be a few layers in thickness instead of one. In a typical experiment, the commercial multilayer $PdSe_2$ film on a sapphire substrate was etched using Potassium Hydroxide (KOH) solution. The substrate was cut into small pieces of the size of 5mm x 5mm and spin coated with PMMA to provide support. $PdSe_2$ was then transferred onto a substrate of interest. For this experiment, we transferred it to holey Si_3N_4 TEM grid, with and

without a graphene supporting layer, as shown as ① and ② respectively in the schematic below (**Figure 6.2**).

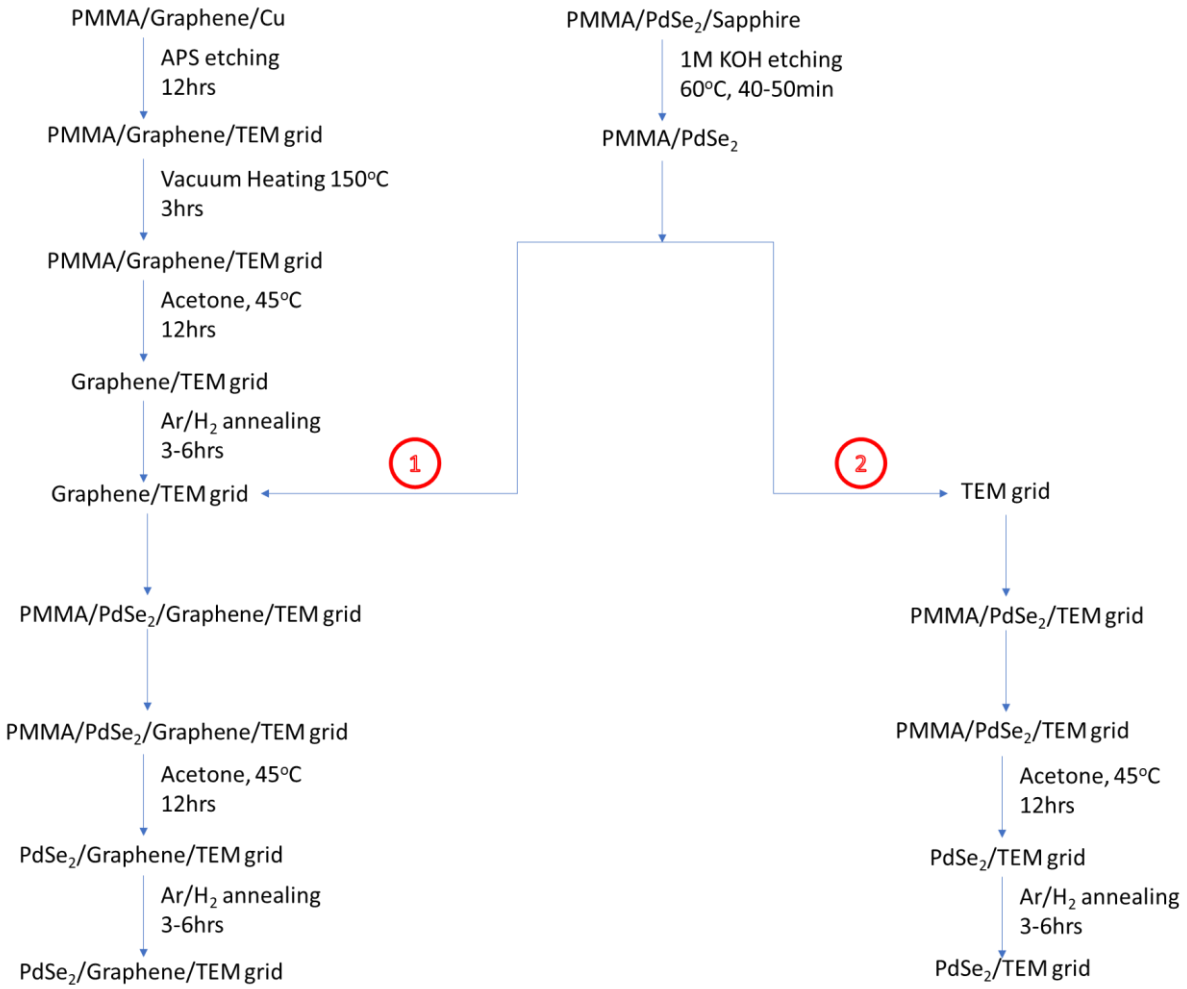

Figure 6.2. Schematic diagram describing the developed procedure for carrying out the $PdSe_2$ transfer on ① graphene and ② directly on a TEM grid.

Typical images of $PdSe_2$, after the transfer process, is shown in **Figure 6.3**. Here the $PdSe_2$ is suspended across the holey Si_3N_4 TEM grid, without any graphene support underneath. **Figure 6.3**(a-d) shows the $PdSe_2$ film suspended across the hole in various magnifications. Comparing with the **Figure 6.1**(f,i), we can see that the multilayer $PdSe_2$ in the sample has even number of layers (**Figure 6.3**d). Energy Dispersive X-Ray spectroscopy (EDX) of the few-layer $PdSe_2$ flakes (**Figure 6.3**e) shows PdL_α, SeK_α and SeL_α at 2.83keV, 11.20keV and 1.37keV respectively. These are the characteristic peaks of Pd and Se, which confirm that the material was successfully transferred to the TEM grid using the KOH transfer

method. After the transfer, we used Laser modification a LabRam Aramis Raman Spectrometer with a 532 nm laser excitation and ×100 objective lens which had a laser spot size of ~500 nm to carry out phase modification. We then used ADF-STEM to study the structural modifications in the material which were exposed to laser.

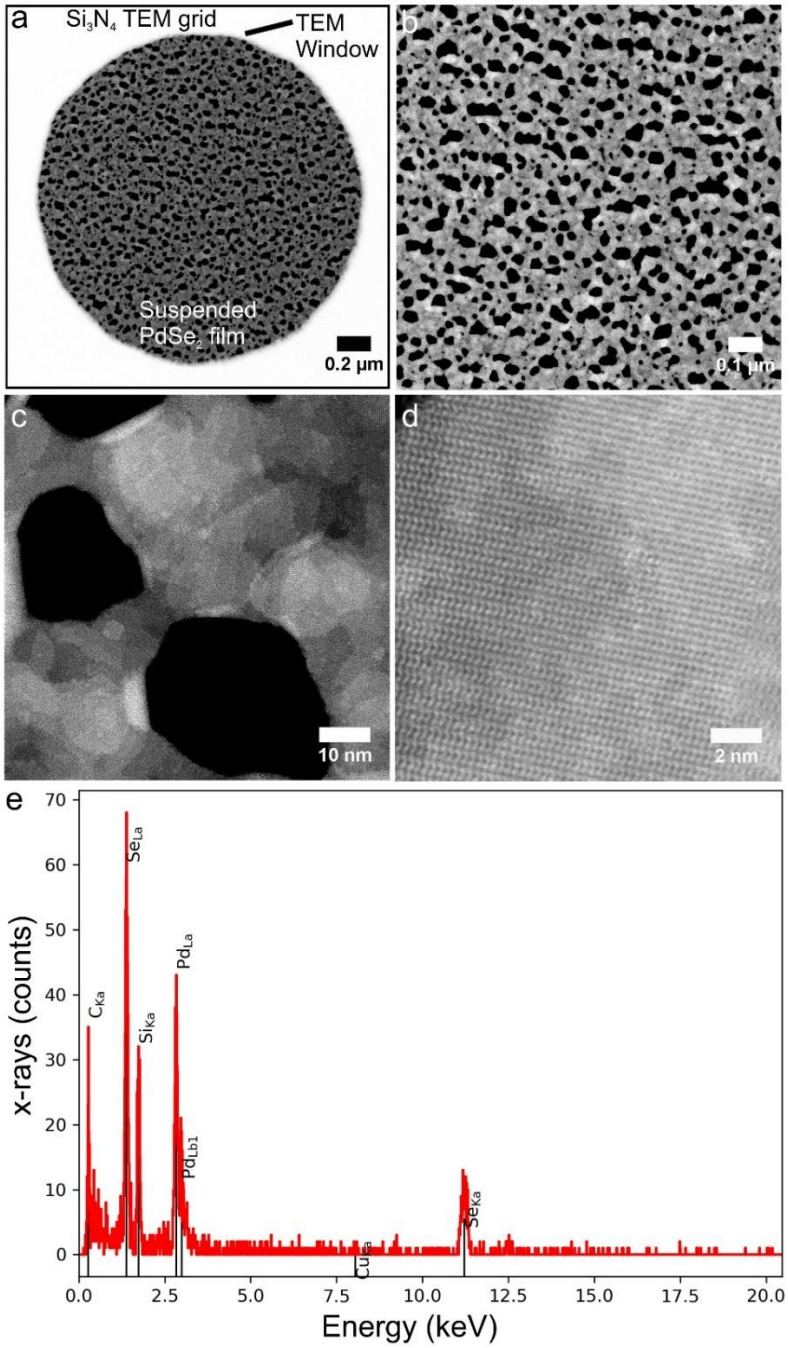

Figure 6.3. $PdSe_2$ on holey Si_3N_4 TEM grid post transfer process. Low magnification ADF-STEM taken at 200kV (dose: 5.6 x 10^8 e s^{-1}) of a typical holey region. (b) Magnified ADF-STEM image of the material suspended across the hole. (c) Magnified ADF-STEM image of typical $PdSe_2$ (d) Atomic resolution ADF-STEM image of the material showing even-layered

multilayer flakes. (e) EDX of the material shown in (c), where the y-axis is the x-ray counts whereas the x-axis is the Energy in keV.

6.2.3. Laser Annealing & Role of Graphene

Initial experiment was carried out by using laser exposure of 7.8mW. **Figure 6.4** shows the more detailed ADF-STEM study of the laser irradiated $PdSe_2$ suspended on graphene. **Figure 6.4**a shows the edge of the laser induced hole in the region boxed in red. **Figure 6.4**b is the magnified region from the edge area annotated in **Figure 6.4**a. The white dashed line shows the boundary between two visibly separate phases: original $PdSe_2$ region (left) and Se-deficient $PdSe_{2-x}$ region (right) in the sample. **Figure 6.4**c shows one of the edge regions with three separate boxed regions for the three different kinds of phases. **Figure 6.4**d is the magnified image of the area annotated in yellow in **Figure 6.4**c. As seen, the multilayer $PdSe_2$ is unchanged and retains the same phase from before laser transformation (**Figure 6.3**d). **Figure 6.4**e is the magnified image of the area annotated in blue in **Figure 6.4**c. The material has clearly transformed into another crystalline form showing sharp facetted structure. These modified phase structures have been studied in more details in the next section. **Figure 6.4**f is the magnified image of the area annotated in green in **Figure 6.4**c. This is the material phase at the very edge of the hole showing only Pd NPs, which has been discussed in more details in the next section.

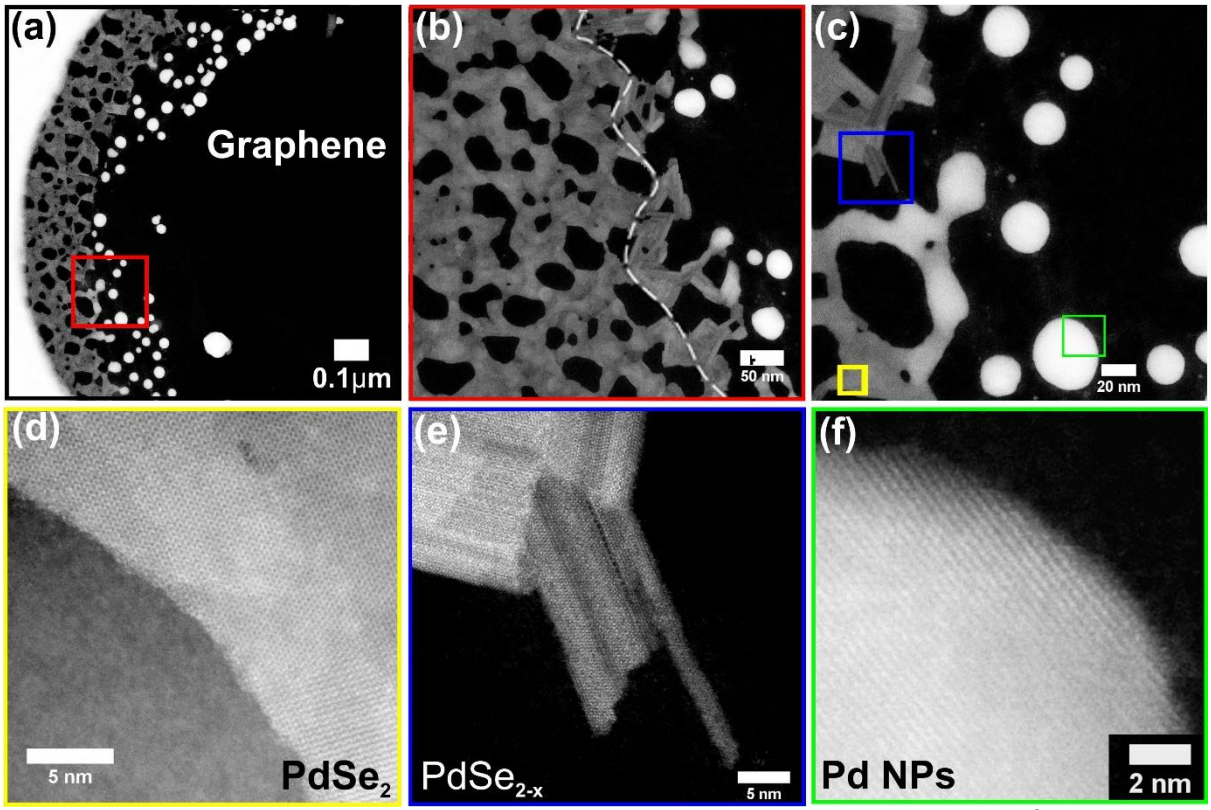

Figure 6.4. (a) Low magnification ADF-STEM taken at 200kV (dose: 5.6 x 10^8 e s^{-1}) of the sample on graphene after laser exposure (7.8 mW). (b) Magnified ADF-STEM image of the material annotated in the red box in (a), where the white line shows the demarcation between two different phases of the material. (c) Edge region with three separate boxed regions for the three different kinds of phases. (d) High resolution ADF-STEM image of the region annotated in the yellow box in (c) showing the original $PdSe_2$ (e) High resolution ADF-STEM image of the region annotated in the blue box in (c) showing Se-deficient phase. (f) High resolution ADF-STEM image of the material annotated in green box in (c) showing the Pd nanoparticles formed after complete ejection of Se atoms.

Subsequently, laser dependent study was conducted on the $PdSe_2$ film suspended both with and without graphene. **Figure 6.5** shows the result of laser modification at different powers. It was seen that $PdSe_2$ demonstrated strong sensitivity to laser exposure. High laser power resulted in local material degradation and formation of Pd nanoparticles (NPs), whilst lower laser power was demonstrated to be able to use it to controllably modify the $PdSe_2$ phase into Se-deficient $PdSe_{2-x}$ phase. The confocal Raman microscope system was used to perform the laser annealing with minimum exposure time of 1s. $PdSe_2$ samples, both supported and un-supported by graphene film, were exposed to a range of laser power from 60µW to 7.8mW. As seen in **Figure 6.5**(a-b), for both the samples, the laser exposure resulted in local material

degradation leading to hole formation that expanded significantly with increasing laser power. Similar to the initially observed results in **Figure 6.4**, a closer inspection of all different kinds of samples revealed four distinct regions within the film after laser exposure (**Figure 6.5**(c-d)), namely: hole region with fully damaged $PdSe_2$ as well as graphene film (red coloured area in **Figure 6.5**d), Pd Nanoparticles (NPs) regions (yellow coloured area **Figure 6.5**d), phase changed Se-deficient $PdSe_{2-x}$ transformed region (green coloured area in **Figure 6.5**d) and unmodified $PdSe_2$ region (blue coloured area in **Figure 6.5**d). However, it was observed that by varying the laser power, the degree of material damage changed substantially between the $PdSe_2$ samples which were supported by graphene and which were not. For instance, the laser damage, i.e. the hole, could be easily induced at 60 μW laser power, into $PdSe_2$ film suspended across vacuum, whereas no damage was seen for $PdSe_2$ suspended on graphene film, as shown in **Figure 6.5**(a-b). The samples containing underlying graphene had to be exposed to at least 600μW laser power to be able to carry any laser assisted phase modification. This demonstrates that the film without the underlying graphene support showed 10 times lower laser power threshold (60μW) for damage and also larger size of the formed holes for any given laser power (**Figure 6.5**e). This result is consistent with thermal energy transfer to underlying graphene layer which results in lower local temperatures within $PdSe_2$ film.(250,251)

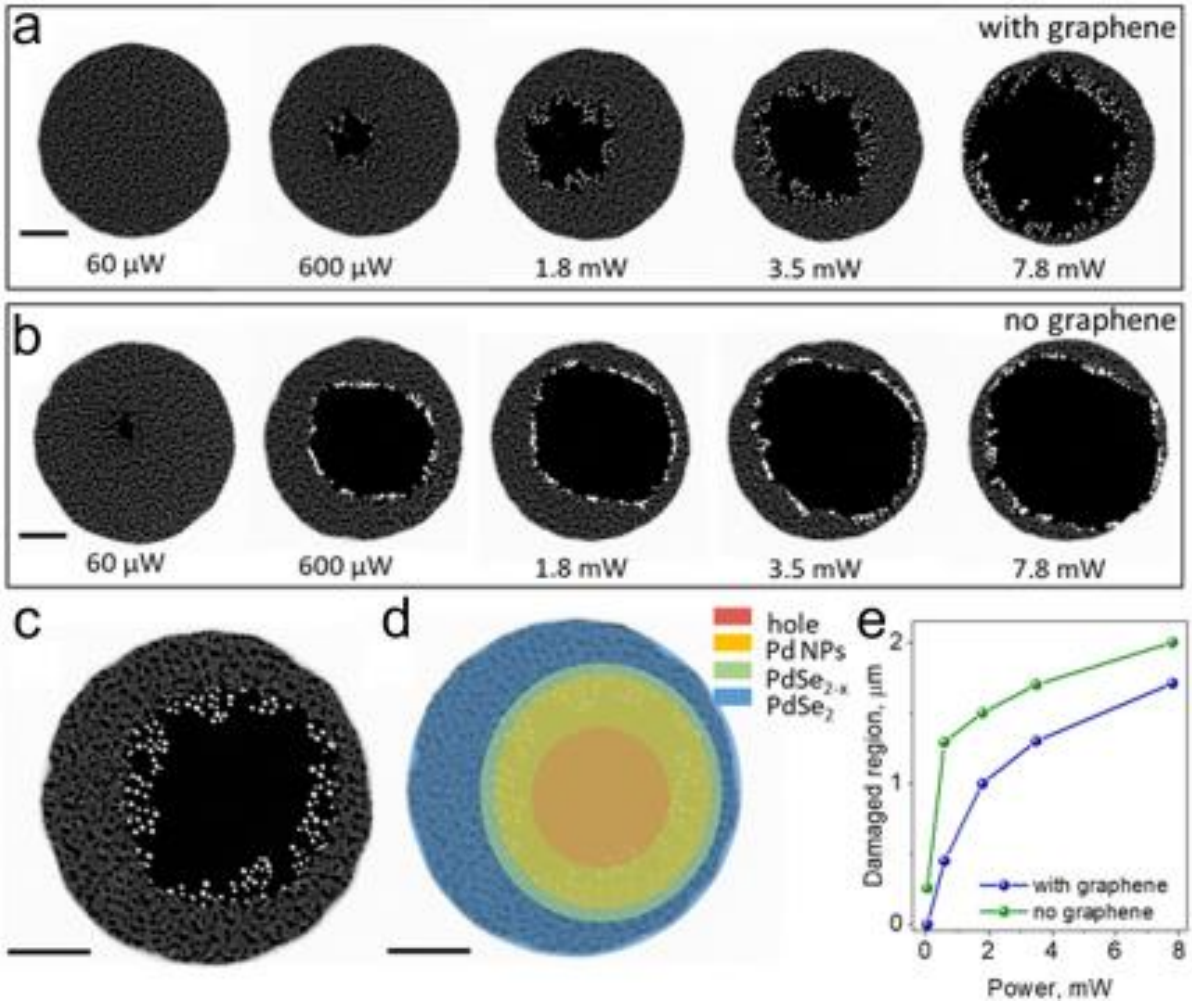

Figure 6.5. Laser induced modifications of $PdSe_2$. (a-b) Laser induced film damage with various laser power for the samples with/without underlying graphene support. Scale bar is 500 nm. (c) TEM image of the laser annealed sample. There are four distinct regions present in the sample: graphene and $PdSe_2$ film annihilation resulting in hole formation, $PdSe_2$ destruction resulting Pd NPs formation, phase modified Se-deficient $PdSe_{2-x}$ region and unaffected original $PdSe_2$ area. Different regions are schematically presented in (d). Scale bar is 500 nm. (e) Dependence of the hole size on the laser power.

The schematic of the laser annealing experiment is presented in **Figure 6.6**, where the laser is positioned in the centre of TEM window. The laser is emitted from the confocal Raman microscope system to perform the annealing. The observed material modifications can be explained by the following mechanism. Laser exposure introduces local heating in the material that facilitates removal of lighter Se atoms from the top layer, while the Se atoms in the middle regions are rearranged forming $PdSe_{2-x}$ structure. Similar process has been recently reported for controlled thermal annealing of few layer $PdSe_2$ which resulted in the formation of $PdSe_{2-}$

$_x$ striated phase with 1D sub-nm etched channels in Pd_2Se_3 bilayers, as discussed in our recent work.(351) In general, this process can be said to originate from extraordinary interlayer interaction between the $PdSe_2$ layers as well as because of the low decomposition temperature of $PdSe_2$ and a variety of stable phases compared to other 2D TMDs. The layer binding energy of 190meV/atom(352) for $PdSe_2$ is much higher compared to the other typical 2D materials. For instance, graphene and hBN show the layer binding energy of only about ~32 meV/atom(353) and 52 meV/atom(354) respectively. This can be explained by presence of only weak van der Waals interaction between the layers of graphene and other TMDs even in the presence of defects. Moreover, it has been observed that during the heating processe, the chalcogen vacancies are typically activated in the TMDs resulting in the formation of line defects which subsequently lead to the formation of 2-dimensional holes.(315,355,356) However, in $PdSe_2$, the Se vacancies reduce the distance between layers, leading to the melding of two layers into one and thus forming a new phase.(323) Zuluaga et al. have demonstrated that the electron beam irradiation can be used to facilitate the emission of Se atoms resulting in the transformation of bilayer $PdSe_2$ into a monolayer Pd_2Se_3 phase.(324) The local nature of e-beam induced modification of the $PdSe_2$ material facilitates fabrication of two-dimensional $PdSe_2$-Pd_2Se_3 junctions. However, this conversion process is expensive and extremely time consuming due to small size of the electron beam significantly limiting the application of this technique. Laser irradiation is, however, cheaper and delivers the same control and results for phase transformation of $PdSe_2$ where high laser power causes ablation removes material while lower power causes Se deficiency and phase changes.

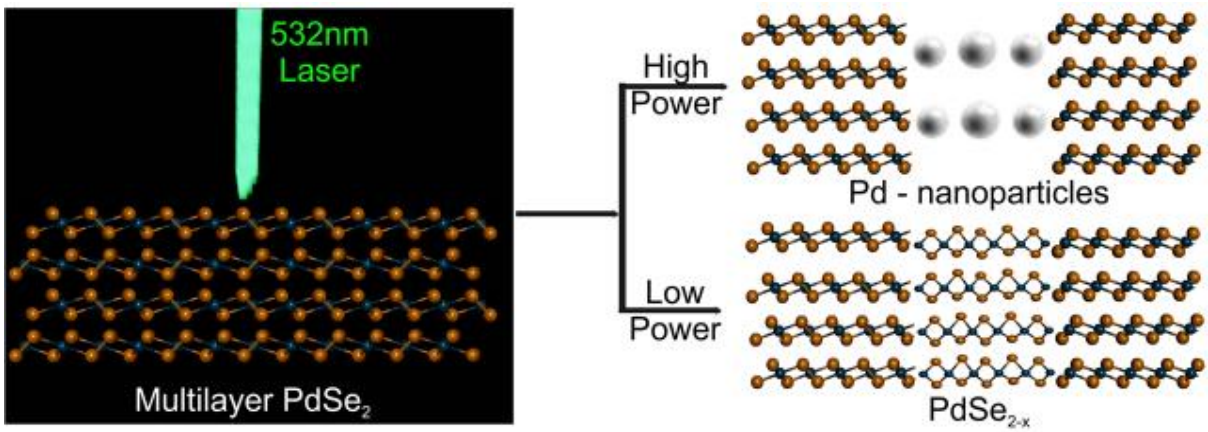

Figure 6.6. (a) Schematic representation of the $PdSe_2$ material transformation under laser exposure.

6.2.4. $PdSe_2$ and $PdSe_{2-x}$

Figure 6.7 shows the atomic resolution ADF-STEM images of $PdSe_2$ in the region where it stays intact after the laser exposure, and its comparison with the atomic simulated model of a few layered $PdSe_2$ which was previously discussed in **Section 6.2.1**. **Figure 6.7**a shows the atomic resolution image of pristine few layered $PdSe_2$ that is far from the laser induced hole, and its FFT is shown in **Figure 6.7**b. The corresponding fast Fourier transform (FFT) patterns show the rectangular structure which is distinct from the hexagonal structure of other TMD materials.(357,358) Both the atomic resolution image (**Figure 6.7**a) as well as its FFT (**Figure 6.7**b) show excellent agreement to the $PdSe_2$ atomic model's multislice simulation (**Figure 6.7**c) and it's FFT (**Figure 6.7**d) respectively. Each flake has an identical lattice structure with similar diffraction patterns, confirming that $PdSe_2$ still consists of a few even number layers and that the crystallinity of the flake away from the laser exposure remains intact.

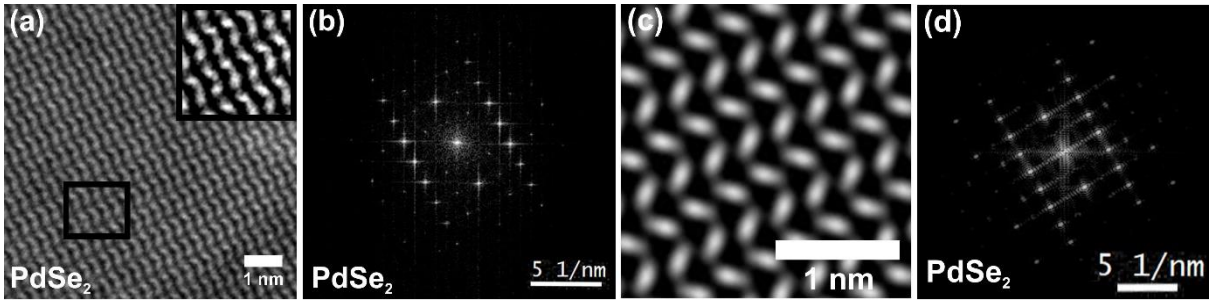

Figure 6.7. (a) High resolution image of the initial material, which clearly shows the $PdSe_2$ structure. The inset is the atomic resolution image of the boxed region. (b) Fast Fourier transform (FFT) of (a). (c) Multislice ADF-STEM image simulation of the atomic model of $PdSe_2$. (d) FFT of the simulation in (c). ADF-STEM images taken at 200kV (dose: 5.6 x 10^8 e s^{-1}).

Figure 6.8 shows the study of the Pd NPs at the outermost region, next to the hole created by the laser. **Figure 6.8**(a-c) shows the atomic model of Face Centred Cubic (FCC) crystal structure of Pd atoms, its multislice image simulation, and the typical FFT respectively. **Figure 6.8**d shows the actual atomic resolution ADF-STEM image of the Pd NPs found at the edges of the hole (as discussed in **Section 6.2.3**). The crystal spacing in the FFT of the NPs (**Figure 6.8**d) is in excellent agreement with that of the FFT of the the simulation (**Figure 6.8**c), enforcing our previous hypothesis of almost-complete removal of Se from this region after the laser annealing process.

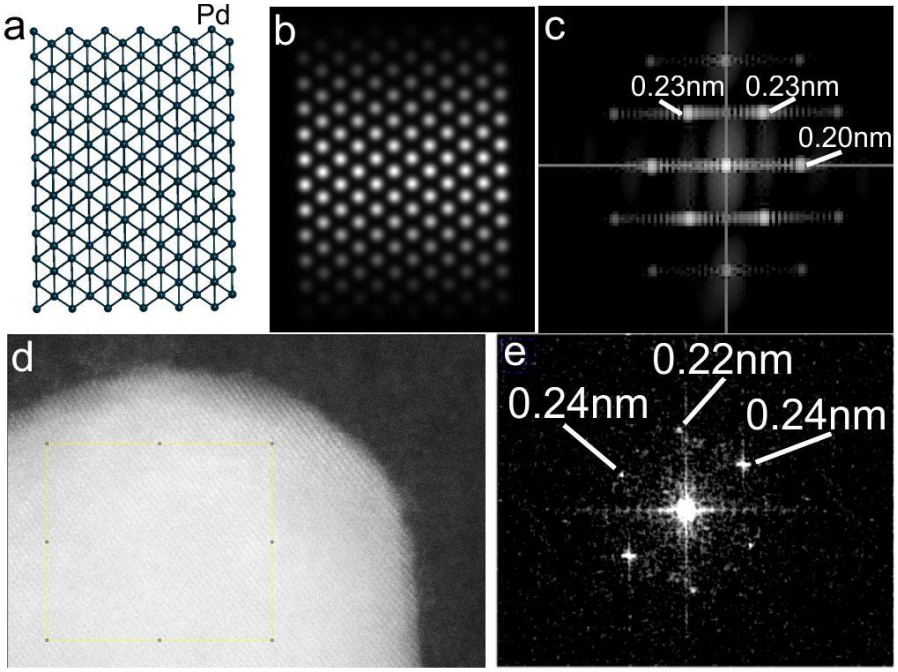

Figure 6.8. (a) Atomic model of the Pd crystal. (b) STEM image simulation of the atomic model presented in (a). (c) FFT of the simulation in (b) showing crystal spacing. (d) ADF-STEM image of the Pd nanoparticle and corresponding FFT (e) with crystal spacing indicated. We attribute the minor differences in crystal spacing to scan drift observed during imaging. ADF-STEM images taken at 200kV (dose: 5.6 x 10^8 e s^{-1}).

Figure 6.9 shows the selenium deficient $PdSe_{2-x}$ region that is found between the Pd NPs and the pristine few layer $PdSe_2$. The crystal structure of $PdSe_{2-x}$ phase presented in **Figure 6.9**a is highly defective and does not have a determinable unit cell due to the nanoscale distribution of Pd-Se bonding, but it is not amorphous, as can be seen from its FFT in **Figure 6.9**b. Images of the sharp interface between the $PdSe_2$:$PdSe_{2-x}$ are shown in **Figure 6.9**(c-d) where the red dotted line represents the interface where the phase changes from $PdSe_2$ on the left to the $PdSe_{2-x}$ on the right, as shown in **Figure 6.9**(d-e). **Figure 6.9**(f-g) show the typical FFT of the two different phases on either side. **Figure 6.9**(h-i) predicts the two atomic model structures of the possible conversions of $PdSe_2$ to the Se-deficient structural phase where Pd loses one of two of its tetra-coordination bonds with Se leading to di- or tri-coordination geometry with the remaining Se atoms.

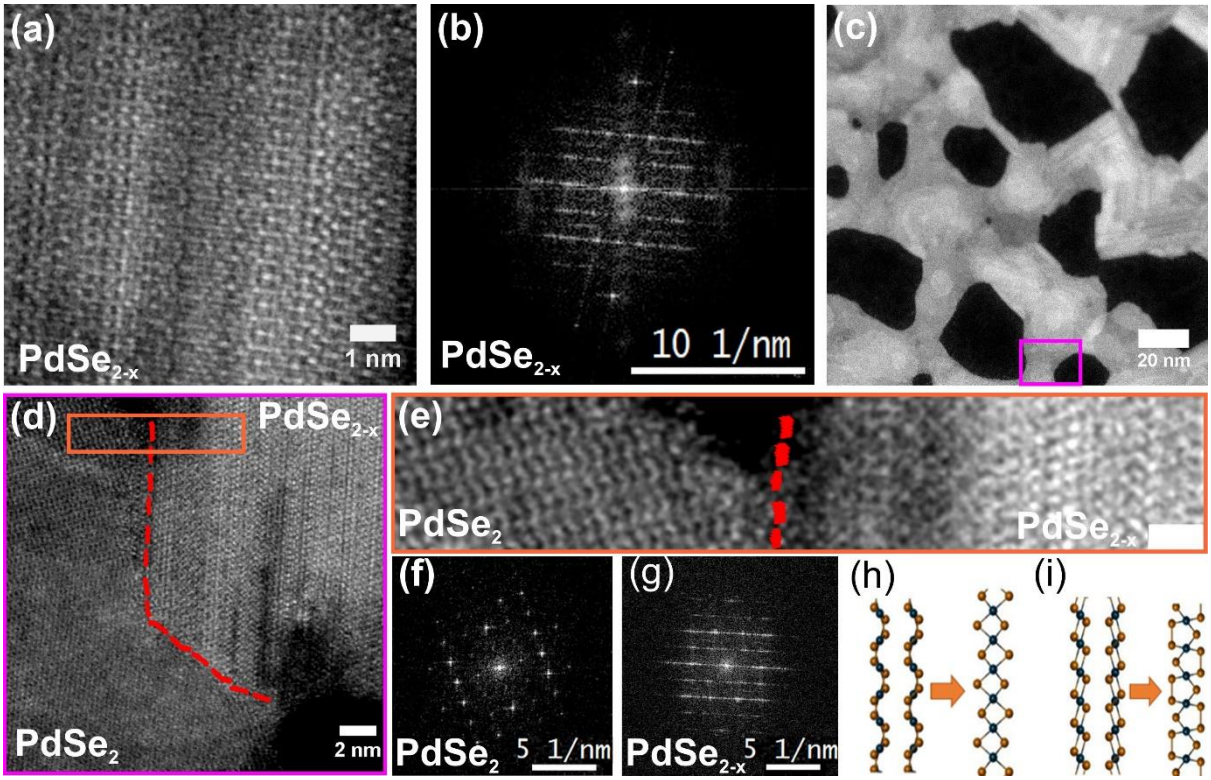

Figure 6.9. (a) The high resolution ADF-STEM images taken at 200kV (dose: 5.6 x 10^8 e s^{-1}), which clearly shows the transitioned $PdSe_{2-x}$ structure. (b) FFT of the (a). (c) Low magnification ADF-STEM image of the region transitioning from $PdSe_2$ to $PdSe_{2-x}$. (d) Magnified image of the transition material annotated in the pink box in figure (c). The red line shows the grain boundary. (e) Atomic resolution of image annotated in orange box in (d). The left side shows the $PdSe_2$ structure whereas the right side shows the Se-deficient $PdSe_{2-x}$ structure. (f-g) FFT of $PdSe_2$ and $PdSe_{2-x}$ respectively, taken from the material in figure r. (h-i) Atomic model structures of possible conversions of the material from $PdSe_2$ to Se-deficient material.

To study the phase transformations in more details, various laser exposure conditions for $PdSe_2$ phase transformation was also studied. The laser exposure conditions were also changed such as it resulted in large area exposure. In contrast to 100x objective used in all the previous study, 10x objective was utilized which gave a 5 µm laser spot and thus, a much larger coverage of area. Although the laser power for exposure was between 23.3µW to 4.9mW, the use of 10x objective resulted in laser density being strongly reduced whilst at the same time resulting in exposure of a larger area of the material above the laser power for the phase transformation threshold. It was observed that for the lower laser powers, below 3mW, there was no phase transformation observed and PdSe2 remained intact as shown in **Figure**

6.7. However, above the laser power of 3mW, Se-deficient phases could be observed. One of the observed interesting selenium deficient phases corresponded to $Pd_{17}Se_{15}$ as shown in **Figure 6.10**. **Figure 6.10**(a-c) shows the ADF-STEM image of $Pd_{17}Se_{15}$ under different magnifications. **Figure 6.10**(d-e) shows the atomic model of this phase whereas **Figure 6.10**f is the corresponding multislice image simulation. It is difficult to exactly point out the intensity peaks in the image simulation (**Figure 6.10**(g-i)), since $Pd_{17}Se_{15}$ has a rather complicated crystal structure with many layers of Pd and Se in a crystal cell. However, comparing the image simulation (**Figure 6.10**(g-i)) to the actual experimental data (**Figure 6.10**(j-l)), it is evident that the two agree with each other in terms of the crystalline structure and the bonding distances. Interestingly, $Pd_{17}Se_{15}$ crystalline phase has previously been reported to have formed when $PdSe_2$ was treated with Ar plasma.(322) This observation indicates the potential similarities in the mechanism of the material phase transformation that is driven by the defects induced during the material treatment process as discussed previously in **Section 6.2.3**.

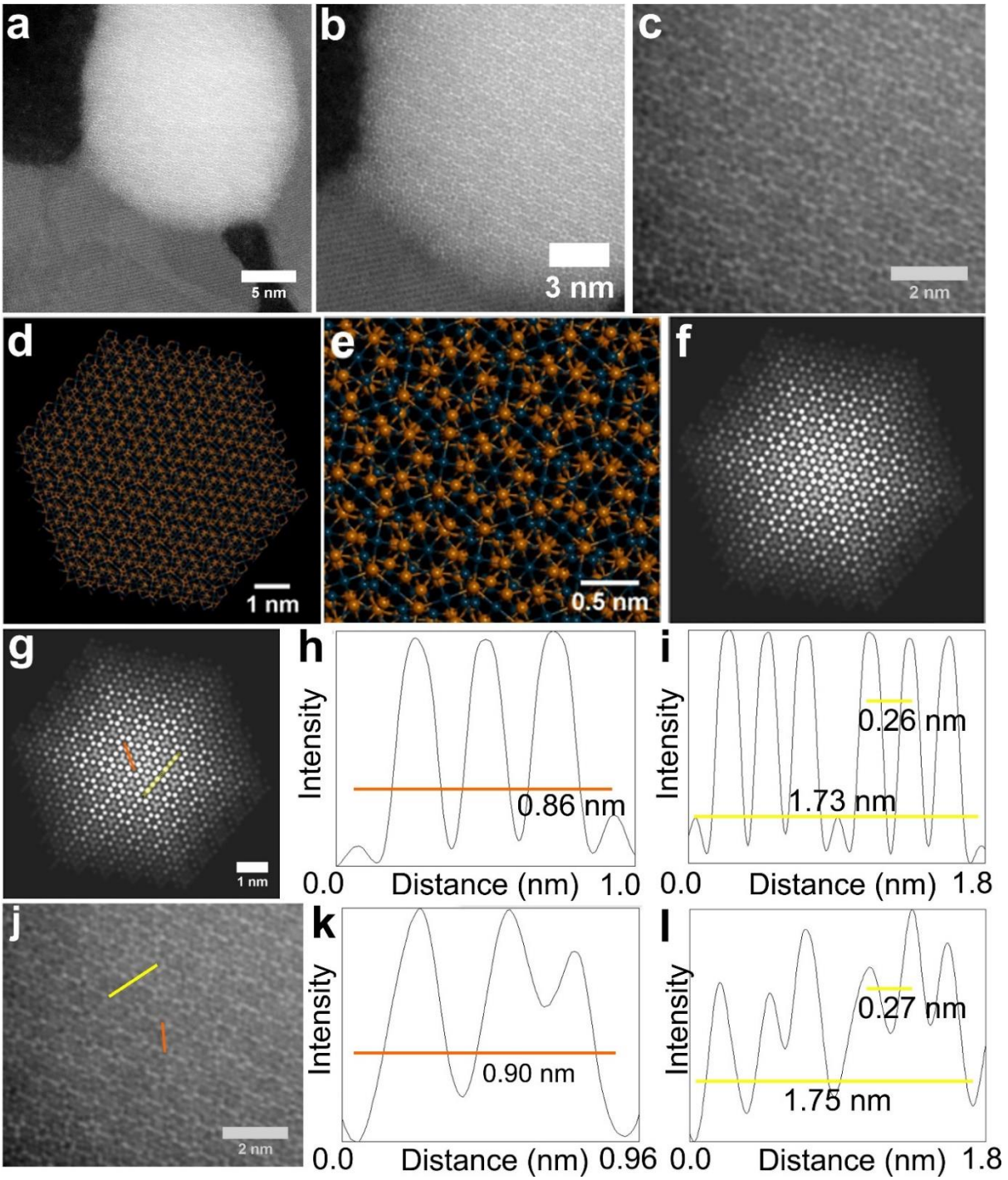

Figure 6.10. STEM characterization of crystal structure of laser-induced $Pd_{17}Se_{15}$ phase. Images taken at 200kV (dose: 5.6 x 10^8 e s^{-1}) (a) Low magnification ADF-STEM of the material after laser exposure with 3 mW power and 5 µm laser spot. (b-c) Magnified ADF-STEM image of the laser-modified material. (d) Atomic model of the $Pd_{17}Se_{15}$ phase. (e) Magnified atomic model of the $Pd_{17}Se_{15}$ phase. (f) STEM image simulation of the atomic model presented in (d). (h-i) Line profiles orange and yellow respectively, in the multislice simulation in (g). (k-l) Line profiles of the positions shown in orange and yellow lines respectively, in the actual STEM image simulation in (j), showing excellent agreement with line profiles of the simulations in (h-i).

Subsequently, a collaborative work was carried out to fabricate and characterization devices based on laser induced transformed $PdSe_{2-x}$[50]. We published results that showed the laser-patterned devices demonstrating a laser-induced metallic phase $PdSe_{2-x}$.(359) which was found to be stable as well as showed increased conductivity by a factor of 20 compared to the usual $PdSe_2$.(359) The results of the study are out of scope of the current thesis, but it shows that this method can contribute massively to the development of nanoscale devices containing homojuntions. It also provides avenues to develop scalable methodology to these phase transformations in 2D materials.

6.3 Conclusion

Accessible heterophase homojunction in atomically thin 2D layers is of great importance for next generation nanoelectronics and optoelectronics applications. Crystal structural phase in a 2D material can be selectively modified using various techniques. However, the other techniques either provide little spatial control or the conversion process is expensive and extremely time consuming. Since the laser irradiation can produce similar selenium deficient modifications to the material, as well as total ablation, this technique has been used to drive phase change in $PdSe_2$ with high controllability and precision. In this work we report laser-driven phase change in $PdSe_2$ to Se-deficient phase. Laser irradiation results in material transition to the palladium-rich phase $PdSe_{2-x}$ followed by formation of Pd nanoparticles as confirmed by atomic resolution scanning transmission electron microscopy (STEM). Using STEM imaging, we identified that the formation of the Se vacancy is a most

[50] Unfortunately, apart from Se deficiency in PdSe2 material, it was not possible to quantify exact deficiency or the Pd:Se ratio in the compound, due to lack of resources. However, the electrical measurements did prove the change in electronic properties in the material after the phase change, i.e. it changed from semiconducting PdSe2 to metallic PdSe2-x phase. The results were published in our recent paper by Shautsova *et. al.* (359).

likely origin of the phase transition. With selective laser power conditions, we modified $PdSe_2$ to different forms of structural phases.

6.4 Contribution statement

CVD grown $PdSe_2$ was purchased from 2D Semiconductors. The $PdSe_2$ transfer to TEM grid was carried out by myself but some of them were also prepared by Dr. Viktoryia Shautsova. The confocal Raman microscope system used to perform the laser annealing at 100x objective was carried out by Dr. Viktoryia Shautsova but the laser annealing using the 10x objective was carried out by myself. Linlin Hou and Qianyang Zhang carried out the CVD growth of graphene on the copper substrate.

Chapter 7 Conclusion & Future Outlook

In this DPhil project, I have investigated the synthesis conditions, properties and morphology of low-dimensional materials, with the use of graphene under TEM. Novel characteristics of 0D and 2D materials could be observed. Here is the summary of the main results and discussion of the prospects for the future research.

7.1 Thesis Summary

In Chapter 4, La@C_{82} and Y@C_{82} was synthesized, extracted, purified and characterized by different methodologies. The optimum pressure of Helium required for the synthesis of La@C_{82} was investigated and the material was subsequently separated to yield high purity EMFs. $Gd_3N@C_{80}$ was then used to study the effect of e-beam on fullerenes and to also look at the interface of EMFs on graphene. Room temperature and *in-situ* heating showed the translation and rotational dynamics of fullerenes under the presence of e-beam. EMF also acted like a molecular precursor to introduce metal atoms on top of graphene. The results described reveal how single rare earth metal atom dopants can be delivered using a molecular precursor deposited from solution to the surface region of 2D materials, with good dispersion and stability, which forms 2D monolayer crystal structures, up to temperatures reaching 900^{o}C in vacuum. The opening of MFs causes cargo release of dopant adatoms on the graphene surface was observed to occur without chemically etching of the underlying

graphene or damaging the sample itself. The results demonstrate an excellent way to create doped graphene monolayers.

In Chapter 5, >99% efficient liquid-exfoliation process for obtaining monolayer PbI_2 was designed and its structure on graphene was presented. It was demonstrated that PbI_2 monolayers have strong epitaxial alignment with the underlying graphene lattice, leading to a phase shift from the 1T to 1H structure. It was shown that the relative lattice spacing of PbI_2 and graphene results in preferential alignment of the PbI_2 zigzag direction to the arm-chair direction of graphene to maximize the commensuration of the two lattices. It was also observed that zig-zag edges are observed to dominate the PbI_2 nanodisks and sequential atom-by-atom edge etching was imaged. The fundamental point vacancy structures in PbI_2 monolayers were also directly imaged, showing rapid vacancy migration to the edges and self-healing. Similarly, nanopores that were produced by electron beam irradiation of the PbI_2 nanodisks, were shown to undergo migration as an intact entity throughout the lattice. The results provided insights into the previously unknown 1H crystal structure of PbI_2 and the effect of van der Waals interactions with graphene.

Chapter 6 demonstrated the laser-driven phase change in $PdSe_2$ to Se-deficient phase. Laser irradiation resulted in material transition to the palladium-rich phase $PdSe_{2-x}$ followed by formation of Pd nanoparticles as confirmed by atomic resolution STEM. Here, it was also demonstrated that controlled laser irradiation can be used to directly ablate Palladium diselenide ($PdSe_2$) thin films using high power or trigger the local transformation of $PdSe_2$ into a metallic phase $PdSe_{2-x}$ using lower laser power. Using STEM imaging, it was identified that the formation of the Se vacancy is a most likely origin of the phase transition. With selective laser power conditions, $PdSe_2$ was modified to different forms of structural phases. Such transformations are possible due to the low decomposition temperature of $PdSe_2$ compared to other 2D transition metal dichalcogenides. The presence of graphene had an interesting effect

on the laser induced transformation and it was shown that in the presence of graphene, the laser induced change was much lower than when there was no graphene.

7.2 Future Outlook

My DPhil work has shown graphene as a versatile substrate for studying other nanomaterials under STEM. Moreover, the facile and preparation of large area suspended graphene on TEM grids, makes it easy to handle in the lab and reproduce the experiments. However, as discussed in detail in Chapter 4, the amorphous carbon layer or the carbon glass has a major impact on enabling the study of nanoparticles on top of graphene. Graphene itself is known to have small energy barrier for migration of nanomaterials and it is the amorphous carbon, impurities and defects in graphene that makes it possible to study other materials on its surface. With the advent of new materials and techniques, it is a possibility that in the coming decade, we are able to obtain pristine graphene without any impurities or defects. However, this can have a possible downside for studying materials on its surface since they would not be stable and migrate to the edges. The role of impurities on graphene should be kept in mind whilst using this material as a substrate for microscopy. Another important point to keep in mind is that graphene has a big influence on the structure and phase transformation of the material that is being studied on its surface, as shown in Chapter 5 and Chapter 6 respectively. Therefore, it is of immense importance to decouple the role of graphene from the observed results so as to understand the intrinsic behaviour of the material that is being studied. In the next decade, I believe that we will be better able to understand the electronic and structural influence of graphene on different materials, especially in the presence of electron beam and use the information to understand the intrinsic properties of other materials, as well as make novel hybrid materials with graphene.

My PhD work can develop along three different directions. First is to obtain a degree of control on dopant levels and structures on graphene (or other 2D materials), which can be achieved via a combination of *in situ* heating under TEM or hydrogen annealing. This can be important for several applications of graphene, including spintronics and catalysis, especially taking into account the dozens of different types of endohedral metallofullerenes, that are available from work over the past couple of decades, and can contain encapsulated single-, double- or tri - rare earth heavy metals. It also provides a pathway for realizing a wide range of rare earth dopants on graphene surfaces. Gadolinium based molecules still remain one of the most important contrast agents for magnetic resonance (MRI) imaging. In this case, our method can potentially be used for drug delivery and imagine where graphene can act as a host to introduce the Gd atoms.

The second direction is studying and characterizing the electrical properties of monolayer PbI_2, and the impact of its strong van der Waals interaction with graphene, which has importance for future applications in opto-electronics. Integrating monolayer PbI_2 with other 2D materials also provides a huge scope for new applications and the ability to manipulate its atomic monolayer structure and a unique opportunity to tune its properties. Studying the influence of the substrate on the structure of PbI_2 would hopefully make it easier to understand the complicated polytypes and stacking arrangement in PbI_2. ADF-STEM imaging of the PbI_2 monolayers revealed highly mobile point vacancies and their growth into nanopores, which exhibited reconstructions and self-healing. Studying these vacancies in the 2D materials is important for the foundation knowledge of the semiconducting properties for future work.

The third direction is to explore the phase change materials and their properties in further details. Accessible heterophase homojunction in atomically thin 2D layers is of great importance for next generation nanoelectronics and optoelectronics applications. Crystal

structural phase in a 2D material can be selectively modified using various techniques. Since the laser irradiation can produce similar selenium deficient modifications to the material, as well as total ablation, this technique was used to drive phase change in $PdSe_2$ with high controllability and precision. One of the important areas of future work can include the study of the exact chemical pathway during laser transformation, i.e. whether the exposure to laser causes oxidation or vaporization of the Se atoms. Detailed study in this direction can be conducted via the use of glove box where laser annealing can be carried out in the presence of Argon instead of Oxygen. Work in this area is of particular importance as it can not only provide a way to control and modify the properties of the material, but also provide a controllable transformation between the semiconducting and metallic phases of transition metal chalcogenides which has been, so far, technologically challenging. Presence of graphene underneath has interesting effect on the amount of transformed sample and further work in this area can further offer opportunities to spatially control the structural modification of 2D materials. These findings contribute to the development of nanoscale devices with homojunctions and scalable methods to achieve structural transformations in 2D materials.

Appendix A

Supporting Information for Chapter 4: Fullerene Synthesis

A metal oxide/graphite composite is used as the anode whereas graphite is used as the cathode and both of them are arced in the D.C. mode in the presence of an inert gas (usually Helium). Despite three decades of extensive research and various proposed pathways, a well-established formation mechanism for the synthesis of fullerenes and endohedral metallofullerenes (denoted as EMFs) is missing. Their ambiguous reaction pathways, alongside the violent conditions involving plasma formation, arc, and chemical ionization that are required for the synthesis is a major drawback in the field of these unique carbon nanostructures. Furthermore, there are various other drawbacks that hinder the scaled-up synthesis and consequently the applications of endohedral metallofullerenes. The overall yield of the arc discharge synthesis of EMFs is low, with the ratio of EMF to empty cage typically around 1%).(360) As a result, a mixture of empty cage and endohedral fullerenes is typically produced, thus limiting the applications of the existing chromatographic methodologies for their fast and efficient separation.

The yield of the EMF has been observed to be highly dependent on the pressure of He gas, the arc-current, arc-gap and the composition of anodes among other factors.(361,362) The Liu(363) and Bandow(364) groups have argued that other parameters such as the presence of catalysts (Cu, Fe, etc.), back-burning of anodes and

in-situ activation during arc-discharge also have an effect on the EMF yield. However, the latter two parameters would not increase the yield by a huge fraction because they do not modify the arc-conditions drastically or change/influence the synthesis chemistry, e.g. lower the activation energy of the formation of the endohedral metallofullerenes. However, in order to maximize the efficiency of the method, a balance between the time spent during the synthesis and the increase in yield needs to be established. Predominant aspects of overcoming the above challenge are anode composition, ionization potential, catalysts, and helium pressure in synthesis, which have been discussed in details below.

A.1. Anode Composition

Metal-oxide (e.g. La_2O_3, Y_2O_3, etc) mixed with graphite has generally been used as the anode material during the arc-discharge process. However, there has been no general consensus on the ratio of metal/carbon used in the metal. Inakuma et. al. also showed that the abundance of different types of EMF present in the soot depends heavily on the metal/carbon mixing ratio in the composite rods.(361,362) The M/C ratio has varied widely over the years, also depending on the metals that are incorporated inside the graphite, broadly summarized in Table B.1. Furthermore, it has also been found that anodes made out of metal-carbide rods actually produce EMFs in a bigger yield than metal-oxide rods, which has been experimentally proved by several authors.(363,364) Using La as the example metal, the authors showed that the presence of LaC_2 in supersaturated carbon vapour plays an important role in generating the metallofullerenes. But this conclusion is in contrast with the work published later by Lian et al.(238) who studied Ni-La alloy anode rod for the preparation of lanthanum-containing metallofullerenes ($La@C_{82}$ (I), $La@C_{82}$ (II), and $La_2@C_{80}$). It was found

that $LaNi_2$ is a much better dopant than conventional La_2O_3 in the anode rod and the ratio of La:C is very important for increasing the yield. The absence of oxygen in the $LaNi_2$ dopant can partly be the reason for such observation as well as Nickel can said to have a catalytic effect in the formation of fullerenes. They also found out that the use of $LaNi_2$ instead of La_2O_3 enhanced the amount of raw soot produced from arc discharge. The authors attributed the results to reduction in the amount of formation of cathode deposits and debris. The optimum conditions increased the yield of La-EMF by almost 30% compared to conventional substrates. Comparing the existing literature in this field, summarized in the Table 1, it seems rather hard to deduce which single metal/carbon ratio in the anode would produce the best yields for different types metallofullerenes. It surely is a huge determinant of the yield of a particular type of EMF but more research, both experimental and theoretical, needs to be undertaken in this direction to test different combinations of metals for anode and also to explore the chemistry behind it.

A.2. Ionization Potential

The ionization potential (I.P) of the EMFs have been known to play a very important role in EMF extraction and chemical reactivity, but it only recently came to light that the first ionization potential of the metal itself plays an important role in EMF synthesis. Ross et al.(365) deduced that I.P. of the metal atom does not only influence the efficiency of the synthesis but may partly determine the metallofullerene formation. Their group noted that when graphite anode rods were impregnated with Y/La atoms and with Sc/Y atomic composition in equal ratio, there was a greater abundance of La- and Y-containing metallofullerenes than Y or Sc, respectfully. The results suggested that metals with lower I.P. (La<Y<Sc) tend to react more efficiently, i.e., the growth reaction of metal ions and fullerene precursor species play important role in the arc

discharge process. This is consistent with other experimental studies which show that lanthanides are easier to encapsulate inside a fullerene cage compared to other alkali earth metals or transition metals.(366) Comparing the yields of the synthesis of Pt-EMF(367,368), Fe-EMFs(369) and Sc-EMFs(370) ($Pt_{I.P.}$ =8.96 > $Fe_{I.P.}$ = 7.90 > $Sc_{I.P.}$ = 6.56), Pt-EMFs have the lowest yield whereas the Sc-EMFs have the highest yield even though the covalent radii of the metals are not very different (Pt = 1.17A; Fe = 1.3 A; Sc = 1.44A). Since the overall yield of EMFs is generally low and their synthesis is a very time-consuming process, it is important that the choice of the metal atom, that can potentially form EMFs, is based on their ionization potential and chemical nature of bonding with the carbon clusters.

A.3. Effect of Catalyst

The catalytic growth of carbon nanomaterials has long been known from the synthesis of carbon nanotubes(371) and more recently, graphene.(15) However, the use of catalysts for the synthesis of fullerenes was not developed until 2008, when Stevenson et. al. (197) doped the graphite rods with copper nitrate in a modified arc chamber. They observed that the presence of metallic copper increased the overall yield of endohedral fullerenes. However, it still remains unclear if it also facilitates the formation of endohedral mono-metallofullerenes and if the ratio of metallofullerenes to other empty cages in the carbon soot is, in fact, higher than previously reported. Other groups have noted that using transition metal alloys (i.e. Ni) in the anode composition(238), increases the yield of the EMFs. But again, results published in the literature make it difficult to judge whether the transition metal plays an active role as a catalyst or it just reduces the detrimental effects that the oxygen has when using metal oxide composite rods during the arc discharge. We deduce that catalysts have not been studied in depth largely because it is difficult to produce homogeneous composite anode

rods containing different catalysts so that they can be actually used systematically during the arc operation. The development of new methods for efficient dispersion of catalytic particles inside the electrodes during their fabrication could help solve these problems. Studying the effect of metal clusters or metal alloys as additives in the arc discharge, could be worthwhile not only for increasing the yield of EMFs, but also for elucidating the formation pathways for fullerenes and carbon nanotubes in the arc reactor chamber.

A.4. Effect of Helium Pressure

The presence of helium in the arc-discharge chamber is well known to be necessary for the formation of endohedral fullerenes.(372) It is still not clear what the exact science behind it is but it is believed that He, being a small and inert species, facilitates collisions between carbon atoms without taking part in reactions. Therefore, it enhances the possibility of carbon-carbon bond formation. There is also a general consensus that varying the pressure of helium leads to different yields of the EMFs. Literature survey (**Table A.1**) in the field of using lower pressure of Helium (50-100mBar) has been the standard arc-discharge parameter until recently, when researchers have started using high He pressures (up to 500-700mBar) for EMF synthesis. In 2017, Qian et. al.(373) published the first theoretical study on how the self-assembly of fullerene during the arc-discharge process is influenced by the presence of helium. They also proposed how the concentration of helium can change the distribution of different fullerene formation in the arc, which is consistent with the experimental results published in 2016 by Churilov et al.(232) The authors experimented with a range of helium pressures (30kPa-150kPa) and their effect on the formation of different types of Y-EMFs and concluded that 120kPa results in the maximum yield for the EMF $Y@C_{82}$. However, they did not consider higher pressures

nor tested whether the results were consistent for synthesizing other EMFs or if they varied depending on the entrapped metals. The exact reaction pathways behind the formation of EMFs is still under investigation.

Table A.1. Summary of the parameters used over the years to synthesize different types of EMFs.

Year	**Anode**	**Fullerene**	**He Pressure (mBar)**	**Current**	**Extraction Solvent**	**R[51]**
1992	Sc_2O_3	Sc-EMF	66.6	---	Toluene & Pyridine & CS_2[52]	(374)
1992	La_2O_3	La-EMF	266.6	---	Toluene	(375)
1992	Sc_2O_3	Sc-EMF	266.6	---	Toluene	(376)
1993	Sc_2O_3 M/C = 2.3/100 atomic ratio	Sc- EMF	66	220 A	CS_2	(362)
1993	8 wt% La_2O_3	$La@C_{82}$	133.3	2.3 A/mm^2	Toluene	(364)
1994	Sc_2O_3 M/C = 1:10	Sc-EMF	66 – 133	500A	CS_2	(361)
1995	Gd_2O_3 (1-2% atomic %)	Gd-EMF	60	250 A	TCB[53]	(377)
1995	La_2O_3 (La/C = 2:100)	$La@C_{2n}$	133	200 A	Toluene	(363)

[51] Citation
[52] Carbon Disulfide
[53] 1,2,4-Trichlorobenzene

1995	-	$Y@C_{82}$	66	500 A	Toluene	(378)
1996	Tm/C = 1:50	$Tm@C_{82}$	200	175A	Toluene	(379)
1996	CeO_2	$Ce@C_{82}$	66	---	DMF[54]	(380)
1996	Pr_6O_{11} (Pr/C = 1:100)	$Pr@C_{82}$, $Pr_2@C_{80}$	66		DMF	(381)
1998	---	$Sc@C_{82}$	66	300 – 400A	Toluene	(370)
1999	Sc_2O_3 Sc/C = 2.8/100	$Sc_3@C_{82}$	66	500 A	CS_2	(192)
1999	Sc_2O_3 Sc/C = 1/185 (3wt%)	$Sc_3N@C_{80}$	400 (1.3-3.6 mBar N_2)		CS_2	(195)
2002	Tm/C composite rod	$Tm@C_{82}$	240	600A	TCB	(382)
2002	M/C = 1/100 (M= La,Y)	$La@C_{2n}$[55], $Y@C_{2n}$	160	90A	o-xylene+ DMF/DMA [56] / DMSO[57]	(383)
2002	---	$Gd@C_{82}$	960	50A	DMF	(384)
2003	Gd_2O_3	$Gd@C_{60}$	133	--	Dichloro-benzene	(385)
2004	MNi_2	All EMF	960	50A	DMF (~6-7 %)	(386)

[54] N,N-Dimethylformamide
[55] $68 \geq 2n \geq 96$
[56] Dimethylacetamide
[57] Dimethyl sulfoxide

					CS_2 (~1.5%) Pyridine (~1.5%) Aniline (~1%)[58]	
2005	CeO_2 (Ce/C = 2/100)	$Ce_2@C_{80}$	666	70A	TEA[59] /acetone	(387)
2006	Sc_2O_3 Sc/C = 2/100	Sc- EMF	66	150 A, 40V	TCB	(388)
2010	Gd_2O_3	$Gd@C_{82}$	200	90A	DMF liq.-liq. extraction	(389)
2014	Gd_2O_3	$Gd@C_{82}$	506	110-120A	o-xylene & DMF	(390)

In recent years, the Kratschmer-Huffman arc design has also been modified mechanically in several ways to make it more environmental friendly. For instance, the use of de-mineralized coal electrodes, minimizing the use of current, using direct current instead of high AC current, etc.(391) Recently, Kyesmen et al(392), showed scaled up production yield of fullerenes by employing such methods and including resistive heating of one of the electrodes along its length. Such green methodologies should be explored more for future research purposes and industrial scale production of fullerenes to ensure environment friendly approach towards using nanomaterials.

[58] Extraction yield by weight percent of (Tb, Y, La, Gd)-EMF to soot
[59] Triethylamine

Appendix B

Supporting Information of Chapter 4: Arc-Discharge

The arc machine is based on the Kratschmer – Huffman method of synthesizing fullerenes, as explained in the **Section 3.2.1**. Two electrodes inside the chamber act as anode and cathode and produce an electric arc in presence of high current and helium and lead to formation of carbon soot which contains different types of fullerenes and carbon nanotubes. The arc discharge system was upgraded, as shown in **Figure B.1,** so as to increase the efficiency of the EMF synthesis process.

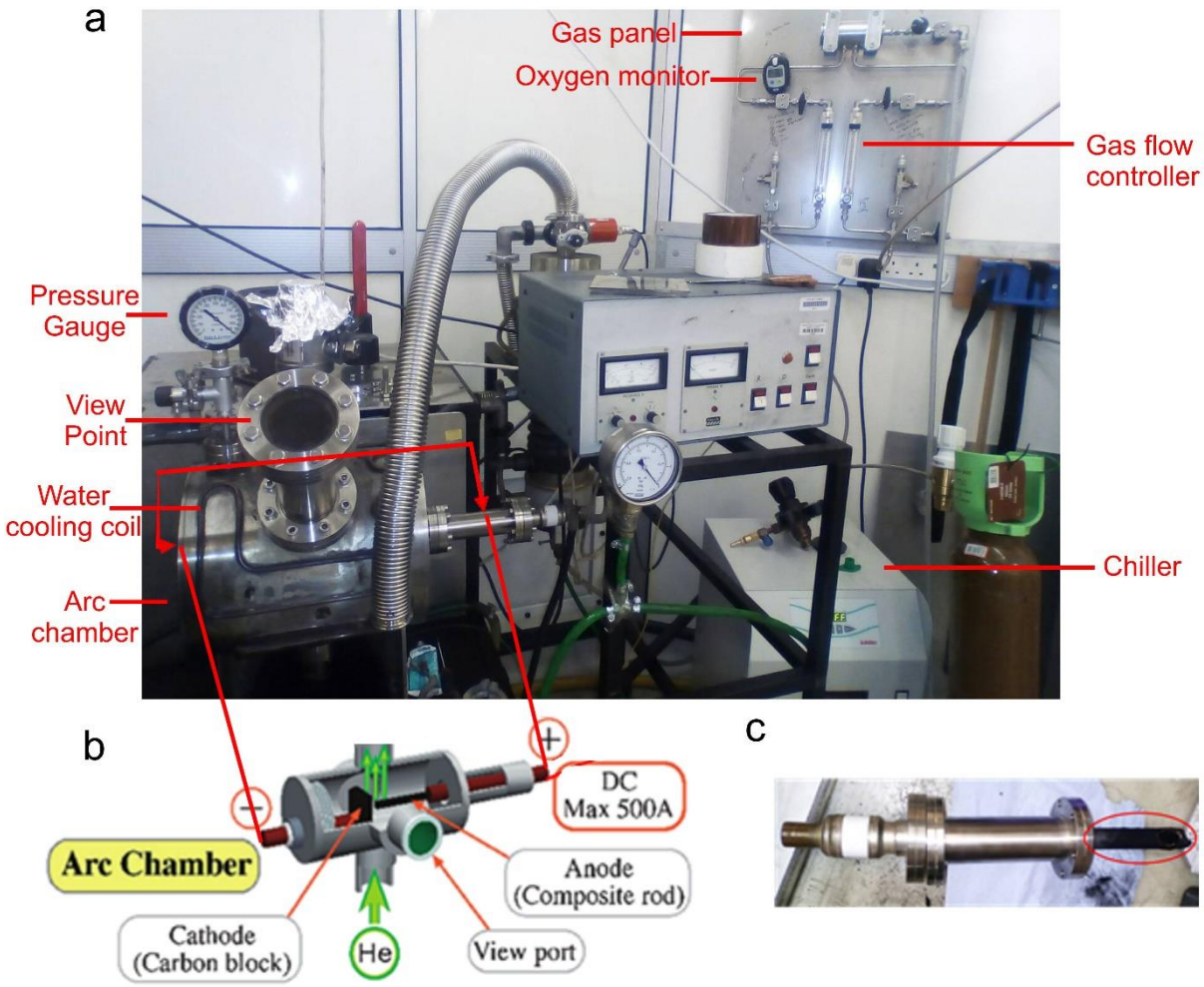

Figure B.7.1. (a) An image of an actual arc-discharge apparatus from our lab at the University of Oxford. (b) A schematic diagram of a typical arc-discharge apparatus used for synthesizing fullerenes [Reproduced from (174)]. (c) Image of a metal oxide/graphite composite rod used during an arc discharge process.

i. Installation of gas panel – A gas panel was installed and connected to the arc-chamber (**Figure B.1**) to monitor and control the pressure of the gas going to the arc-discharge system. The gas panel has two different inlets to allow two different types of gases to be used during the arc-discharge. One inlet was connected to Helium source whereas the other one was used to connect to Nitrogen source.

ii. Pressure gauge – The arc-discharge chamber was modified to also fit a pressure gauge (**Figure B.1)** to the chamber to accurately measure the pressure inside – before, during and after the arc-discharge.

iii. Cooling coil – During the arc-discharge process, the arc point can go up as high as 3000-4000℃ in the presence of helium. Hence, to cool the system, a new and powerful chiller was installed (**Figure B.1)**. A retrofitted coil was then welded on the surface of the arc discharge chamber as shown in the figure above, to cool down the system continuously.

iv. Mechanical feed-through – The Metal-doped graphite rods used were of the dimension 10cm x 1cm. It takes about 2hrs to arc and vaporize one rod and produce about 5g of carbon soot. Changing the rods after every cycle of arc-discharge required pumping down the vacuum and then mechanically remove it and install a new one and then pump down the vacuum again. Hence, a mechanical feed through system was installed which could hold 6 rods at a time, as shown in **Figure B.2**. The mechanical feed through could be rotated, so that multiple rods could be burnt consecutively, without opening the chamber after burning arc-discharge.

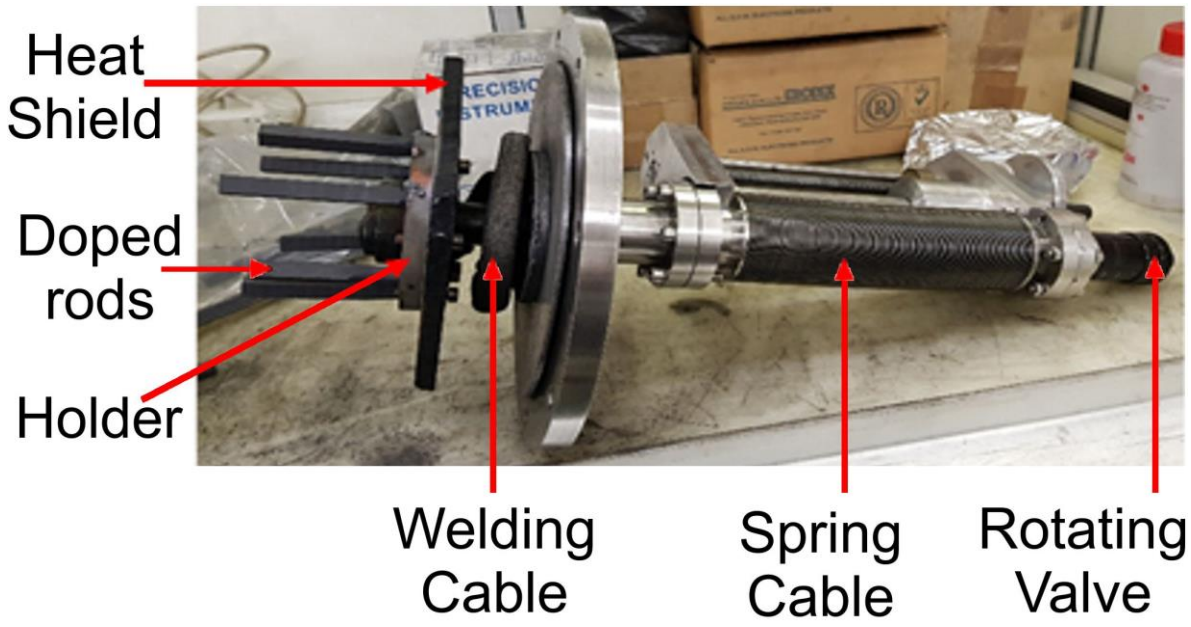

Figure B.2. Mechanical feed-through system (detachable).

Appendix C

Supporting Information of Chapter 4: Lewis-Acid

HPLC is known to be a very effective process and is very effective to separate the different fullerene cages, it is known to be extremely time-consuming. Hence, I also explored other methods of separation of EMFs from the empty cages. One such method is Lewis acid separation process, the field which has not been explored properly yet and only a handful of literature is available.(234,235,242,243) Lewis acid separation of metallofullerenes from the empty cage fullerenes has not been explored extensively in the past. Stevenson et al.(242) and Akiyama et al.(235) have previously reported a few Lewis acids to be successful in separating endohedral fullerenes from empty fullerene cages. I have modified the method and tried to use it on our EMFs.

C.1. Introduction

Out of all the Lewis acids, I decided to use $TiCl_4$ which has a tendency to form complexes primarily with $La@C_{82}$ because of the latter's oxidation potential. Also, I used this Lewis acid for practical reasons such as the physical state of $TiCl_4$ which is liquid, at room temperature and pressure, making it easier to handle and use in the crude extract solution. A lewis-acid forms a complex with the endohedral fullerene, owing to the difference in the redox potential of the EMF and the empty cages, and thus, separates out when filtering the solution. The reaction of Lewis-acid and EMF was carried out in almost inert (Ar) atmosphere and the reaction time was 5-10 min. The whole process of separation has been shown in the diagram

in the **Figure C..** The process was tried on two different EMFs, namely, La@C_{82} and Y@C_{82}. The results have been outlined below in following section.

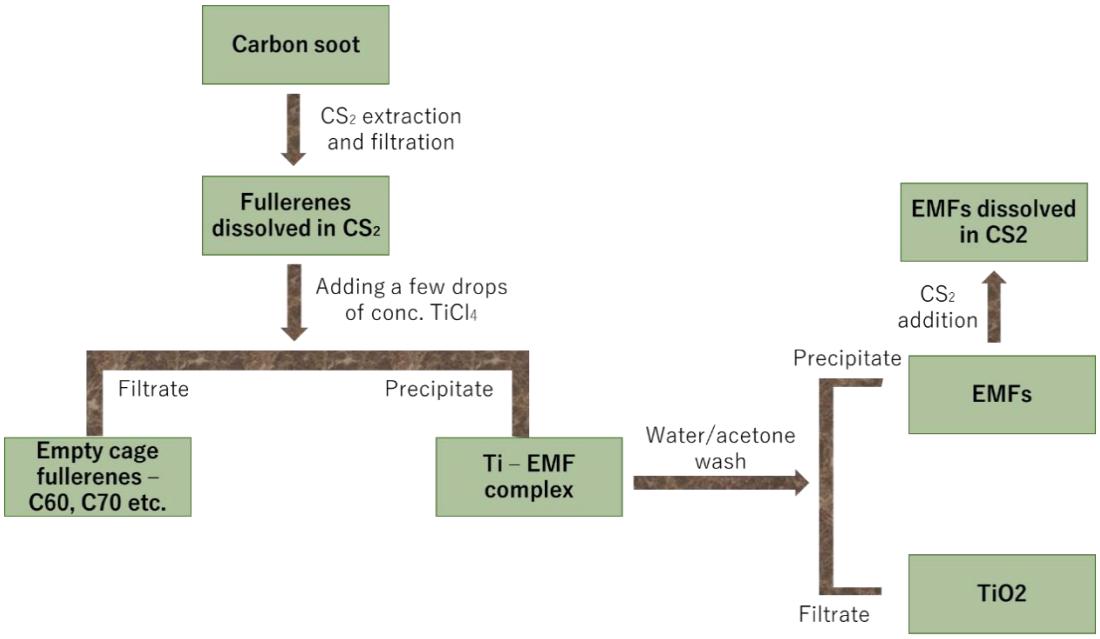

Figure C.1. Schematic diagram of the Lewis acid separation method of EMF from the empty fullerenes.

C.2. Results & Discussions

Results were taken from La@C_{82} and Y@C_{82}. La@C82 was separated from a crude soot extract and the mass spectrometry of before and after the lewis acid separation was compared. Whereas 98% pure Y@C_{82} was used to determine the efficiency of the before and after EPR measruements, since it has only ½ spin which is easier to calculate and interpret.

C.2.1. La@C_{82}

The process does separate primarily the EMFs, i.e. La-based fullerenes from the lower cage fullerenes, as shown in the comparative mass spectrum in **Figure C.2.** As it can be seen, the sharpest peak in the figure is of La@C_{82} as compared to the mass spectrum of La@C_{82} in the main text, where the EMF intensity is rather very low. We can still see the peaks of for empty fullerene like C_{60}, C_{70} etc. and other higher molecular mass fullerenes like C_{90}, C_{120} etc which could have resulted because of the excessive amount of the acid used and should be separated in one step HPLC process.

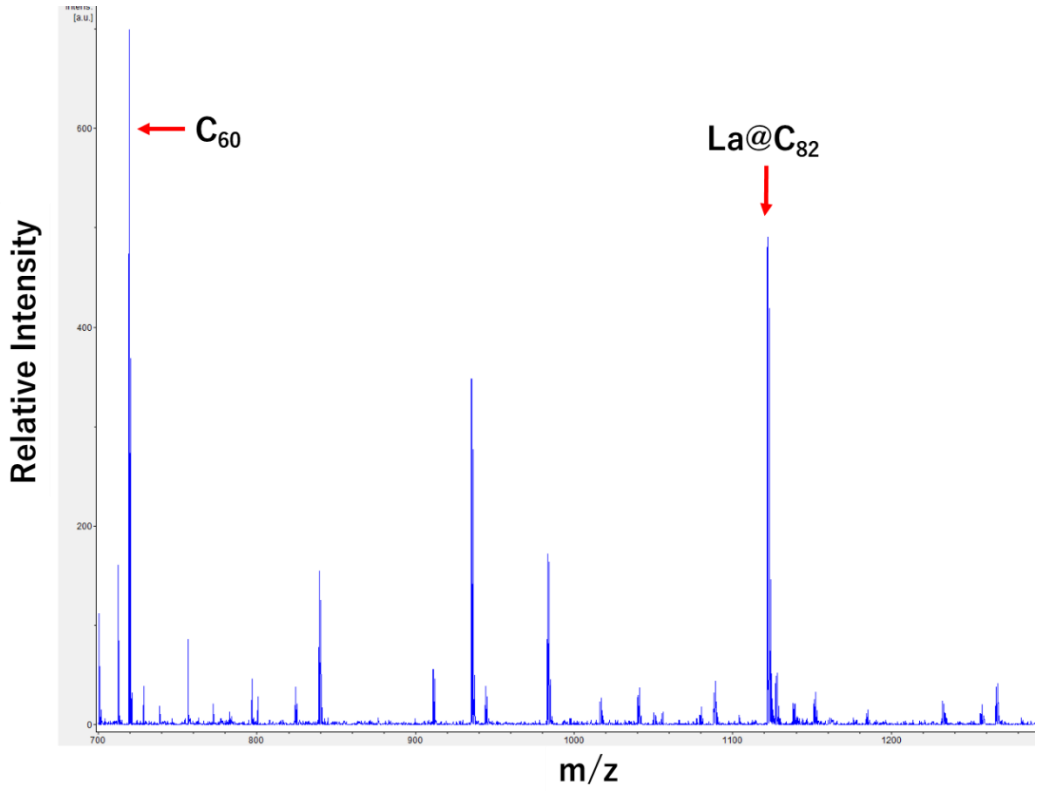

Figure C.2. Mass spectroscopy after Lewis acid separation method. The EMF peak can be seen to be as strong in intensity as that of the C_{60} peak.

C.2.2. Y@C_{82}

To determine the efficiency of the method quantitatively, Y@C_{82} was used and EPR was employed. As Y@C_{82} only has ½ spin, the calculation of the efficiency of separation is easier and also more accurate. Y@C_{82} is mixed with C60 in the ratio of 1:9, mimicking the crude extract, assuming 10% EMF yield.

Hence, quantitatively:

Y@C_{82} = 5 x 10^{-9} moles

C_{60} = 45 x 10^{-9} moles

Concentration of the solution measured by EPR = 10^{-5} M

However, after Lewis-acid separation, the intensity of the colour of the EMF was visibly lower than before, as shown in **Figure C.1.** Moreover, as shown in **Figure C.2**, the spin signal is 3.42 times weaker. Considering that the sample volume is also almost 10 times

less, the total spin loss rate was c.a. 30 times. Moreover, the efficiency definitely doesn't look like more than 99% as claimed in the paper. The 99% yield, as claimed in the paper, could never be achieved. This is the first ever reported EPR results on Lewis acid separation. Radioactivity was used as a measurement technique to determine the yield of the metallofullerenes before and after. However, we believe that the EPR gives more concrete results since it is based on the spins of the EMFs.

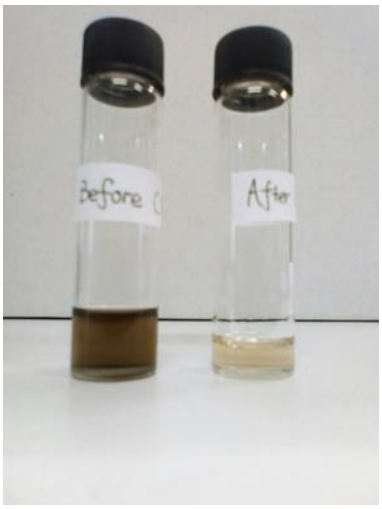

Figure C.1. Colour of the solution before and after Lewis-acid separation

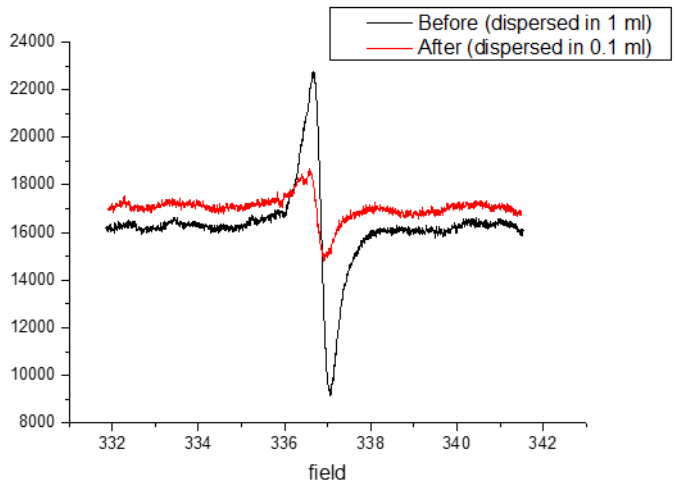

Figure C.2. EPR signals from $Y@C_{82}$ as measured before (black) and after (red) Lewis-acid separation.

C.3. Conclusions

Although the lewis acid method works much faster (in 10 min compared to weeks of HPLC), it is not very efficient at separating EMFs. More work needs to be done in this area to be able to speed up the purification and separation process of the EMFs.

Appendix D

Supporting Information of Chapter 5: Solvent properties

Solvents	S[60]	B.P.[61]	H.B.[62]	μ[63]	ϵ[64]	Hansen Solubility Parameters[65]				δ[66]
						δ_T	δ_D	δ_P	δ_H	
Acetone 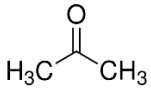	-	56.5	-	2.88	21	19.9	15.5	10.4	7.0	10.0
Benzonitrile 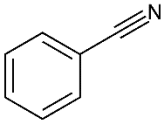	-	191.1	-	4.01	25.2	19.9	17.4	9.0	3.3	8.4
Carbon disulfide (CS_2) S=C=S	-	46	-	0.06	2.64	20.5	20.5	0.0	0.6	9.92

[60] Solubility of PbI2 in these solvents.
[61] Boiling Point
[62] Hydrogen bonding
[63] Dipole Moment
[64] The symbol refers to Dielectric constant. Dielectric constants of the materials have been taken from the data available in various literature. It is the is based on measuring the capacitance of dielectric probe in solvent at room temperature.
[65] Hansen solubility parameter for solvents at 25° in $(J/cm3)^{1/2}$. Hansen parameters divide the total Hildebrand value into three parts: a dispersion force component, a hydrogen bonding component, end a polar component. $\partial_t^{2=}\partial_d^{2+}\partial_p^{2+}\partial_h^2$ where ∂_t^2 = Total Hildebrand parameter; ∂_d^2 = dispersion component; ∂_p^2 = polar component; ∂_h^2 = hydrogen bonding component.
[66] δ= Hildeband solubility parameter, in $(cal^{1/2}\ cm^{-3/2})$. The physical constant used to describe the relationship between the physical properties of the solvent and its effectiveness in dissolving specific solutes. The thermodynamic term is the cohesive energy density, introduced by Scatcharf and later incorporated by Hilderbrand into solubility parameter concept. The cohesive energy density, sometimes referred as the internal pressure, is the isothermal internal energy of the vaporization of the liquid to the ideal gas state decided by the volume of the liquid. In simplest terms, the cohesive energy density (c) is a measure of the energy required to overcome all of the intermolecular forces holding a liquid together. So, it can be expected that materials with similar cohesive energy density values would be miscible and this is, in fact, what happens. $c = (\Delta H_v - RT)/V_m$;$\delta = \sqrt{c}$

Solvents	S[60]	B.P.[61]	H.B.[62]	μ[63]	ϵ[64]	Hansen Solubility Parameters[65]				δ[66]
						δ_T	δ_D	δ_P	δ_H	
Chloroform ($CHCl_3$) 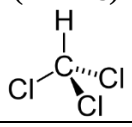	-	61	✓[67]	1.04	4.81	19.0	17.8	3.1	5.7	9.49
1,2-dichloroethane (DCE) 	-	84	-	1.80	10.5	20.8	19.0	7.4	4.1	9.78
Dichloromethane (DCM) 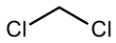	-	40	-	1.60	9.1	20.2	18.2	6.3	6.1	9.88
N,N-dimethylformamide (DMF) 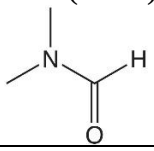	✓	153	-	3.82	38	24.9	17.4	13.7	11.3	12.1
Dimethyl sulfoxide (DMSO) 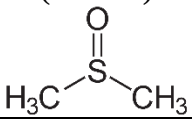	✓	189	-	3.96	46.7	26.7	18.4	16.4	10.2	12.0
Ethanol (EtOH) 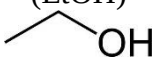	-	79	✓	1.69	24.5	26.5	15.8	8.8	19.4	12.7
n-hexane 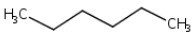	-	69	-	0.00	1.88	14.9	14.9	0.0	0.0	7.24
Isopropanol (IPA) 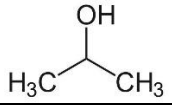	-	82	✓	1.66	18	23.6	15.8	6.1	16.4	11.5
Methanol (MeOH)	-	65	✓	1.70	33	29.6	15.1	12.3	22.3	14.5

[67] Chloroform is non-polar solvent, however, weaker hydrogen bonds are known for hydrogen atoms bound to elements such as sulfur (S) or chlorine (Cl).

Solvents	S[60]	B.P.[61]	H.B.[62]	μ[63]	ϵ[64]	Hansen Solubility Parameters[65]				δ[66]
						δ_T	δ_D	δ_P	δ_H	
N-Methyl-2-pyrrolidone (NMP) 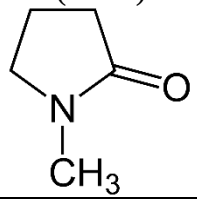	✓	204	-	12.2	32.2	23.0	18.0	12.3	7.2	11.3
Pyridine 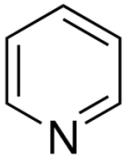	✓	115.2	-	12.9	2.37	21.8	19.0	8.8	5.9	10.6
Tetrahydrofuran (THF) 	-	66	-	1.75	7.5	19.4	16.8	5.7	8.0	9.4
Toluene 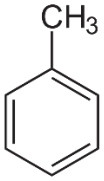	-	111	-	0.36	2.38	18.2	18.0	1.4	2.0	8.91
Water 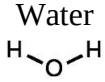	Par-tly	100	✓	1.85	80	47.8	15.6	16.0	42.3	23.5

Appendix E

Supporting Information of Chapter 5: DFT

Density Functional Theory Calculations for PbI_2

The structural, energetic and defect-migration calculations in this work are based on density functional theory (DFT) implemented in the Vienna Ab-initio Simulation Package (VASP).(393,394) A 10×10×1 supercell is used for calculating the sputtering energy and defect migration barriers, and two more different systems are designed to probe the short-range angle dependence of stacking energy: a hexagonal PbI_2 flake (side length 4 PbI_2 unit cells, 1.8 nm) on continuous graphene substrate. The systems are varied with different angles between PbI_2 and graphene (i.e., armchair to zigzag stacking order). The elements are represented by projector-augmented wave (PAW) potentials(395) with 500 eV energy cutoff and the 4 ($6s^2 6p^2$) valence electrons for Pb, 7 ($5s^2 5p^5$) for I and 4 ($2s^2 2p^2$) for C are treated explicitly.(400) Initial relaxation and energetics are calculated *via* the generalized gradient approximation, Perdew−Burke−Ernzerhof (PBE), augmented by DFT-D3 method with Becke-Jonson damping for the interlayer dispersive interaction.(401,402) The first Brillouin zone is sampled by the tetrahedron method on a 4 × 4 × 1 *k*-mesh for the 10×10×1 supercell, and only Gamma point for the angle-dependence studies. All structures are relaxed until the force on each atom is less than 0.01 meV/Å. The sputtering energy is defined by the energy difference between the crystalline structure and the one with a vacancy, for instance, the I sputtering energy is $\Delta E_I = E_{crystal} - (E_{V_I} + E_I)$. The energy tolerance is set to 0.0001 for all energy calculations. The minimum energy paths for defect migration are determined by the nudged

elastic band (NEB) method.(403,404) 10×10 supercells and 4×4 k-point grids are employed, and a criterion of 0.03 eV/ Å is set for the force convergence. For V_I migration, two pathways are considered: in plane and out-of-plane directions, and only in-plane V_{Pb} migration is considered. The starting and end points for NEB search are prepared by removing the corresponding atoms from the relaxed pristine structure, and then further relaxed. The 6 intermediate images are interpolated by the Vasp TST toolkit. The converged energy paths are the fitted by cubic spline functions.

References

1. L. Gross *et al.*, Organic structure determination using atomic-resolution scanning probe microscopy. *Nat. Chem.* **2,** 821–825 (2010).

2. A. Riss *et al.*, Imaging single-molecule reaction intermediates stabilized by surface dissipation and entropy. *Nat. Chem.* **8,** 678–683 (2016).

3. H. Zhou *et al.*, Direct Visualization of Surface-Assisted Two-Dimensional Diyne Polycyclotrimerization. *J. Am. Chem. Soc.* **136,** 5567–5570 (2014).

4. M. Di Giovannantonio *et al.*, Insight into Organometallic Intermediate and Its Evolution to Covalent Bonding in Surface-Confined Ullmann Polymerization. *ACS Nano* **7,** 8190–8198 (2013).

5. Q. Sun *et al.*, On-Surface Formation of One-Dimensional Polyphenylene through Bergman Cyclization. *J. Am. Chem. Soc.* **135,** 8448–8451 (2013).

6. J. Björk, Y.-Q. Zhang, F. Klappenberger, J. V. Barth, S. Stafström, Unraveling the Mechanism of the Covalent Coupling Between Terminal Alkynes on a Noble Metal. *J. Phys. Chem. C* **118,** 3181–3187 (2014).

7. L. Gross *et al.*, Atomic Force Microscopy for Molecular Structure Elucidation. *Angew. Chemie Int. Ed.* **57,** 3888–3908 (2018).

8. E. I. Altman, M. Z. Baykara, U. D. Schwarz, Noncontact Atomic Force Microscopy: An Emerging Tool for Fundamental Catalysis Research. *Acc. Chem. Res.* **48,** 2640–2648 (2015).

9. A. Bachmatiuk *et al.*, Low Voltage Transmission Electron Microscopy of Graphene. *Small* **11,** 515–542 (2015).

10. A. I. Kirkland, S. L. Chang, J. L. Hutchison, in *Springer Handb. Microsc.* (Springer Handbooks. Springer, Cham, 2019).

11. C. B. Murray, D. J. Norris, M. G. Bawendi, Synthesis and characterization of nearly monodisperse CdE (E = sulfur, selenium, tellurium) semiconductor nanocrystallites. *J. Am. Chem. Soc.* **115,** 8706–8715 (2002).

12. S. J. Rosenthal, J. McBride, S. J. Pennycook, L. C. Feldman, Synthesis, surface studies, composition and structural characterization of CdSe, core/shell and biologically active nanocrystals. *Surf. Sci. Rep.* **62,** 111–157 (2007).

13. Z. Adam Peng, X. Peng, Mechanisms of the Shape Evolution of CdSe Nanocrystals. *J. Am. Chem. Soc.* **123,** 1389–1395 (2001).

14. A. K. Geim, K. S. Novoselov, The rise of graphene. *Nat. Mater.* **6,** 183–191 (2007).

15. K. S. K. S. Novoselov *et al.*, Electric field effect in atomically thin carbon films. *Science (80-.).* **306,** 666–669 (2004).

16. M. Coroș, F. Pogăcean, L. Măgerușan, C. Socaci, S. Pruneanu, A brief overview on synthesis and applications of graphene and graphene-based nanomaterials. *Front. Mater. Sci.* **13,** 23–32 (2019).

17. R. S. Pantelic *et al.*, Graphene: Substrate preparation and introduction. *J. Struct. Biol.* **174,** 234–238 (2011).

18. R. R. Nair *et al.*, Graphene as a transparent conductive support for studying biological molecules by transmission electron microscopy. *Appl. Phys. Lett.* **97,** 153102 (2010).

19. F. Schäffel, M. Wilson, J. H. Warner, Motion of Light Adatoms and Molecules on the Surface of Few-Layer Graphene. *ACS Nano* **5,** 9428–9441 (2011).

20. J. H. Warner, Z. Liu, K. He, A. W. Robertson, K. Suenaga, Sensitivity of Graphene Edge States to Surface Adatom Interactions. *Nano Lett.* **13,** 4820–4826 (2013).

21. C. Lee, X. Wei, J. W. Kysar, J. Hone, Measurement of the Elastic Properties and Intrinsic Strength of Monolayer Graphene. *Science* **321,** 385–388 (2008).

22. X. Wang *et al.*, Large-Scale Synthesis of Few-Layered Graphene using CVD. *Chem. Vap. Depos.* **15,** 53–56 (2009).

23. K. V. Zakharchenko, M. I. Katsnelson, A. Fasolino, Finite Temperature Lattice Properties of Graphene beyond the Quasiharmonic Approximation. *Phys. Rev. Lett.* **102,** 046808 (2009).

24. J.-H. Chen *et al.*, Charged-impurity scattering in graphene. *Nat. Phys.* **4,** 377–381 (2008).

25. J. Robertson, Amorphous carbon. *Adv. Phys.* **35,** 317–374 (1986).

26. K. Ziegler, Robust Transport Properties in Graphene. *Phys. Rev. Lett.* **97,** 266802 (2006).

27. C. Herbig, T. Michely, Graphene: the ultimately thin sputtering shield. *2D Mater.* **3,** 025032 (2016).

28. S. T. Skowron, S. L. Roberts, A. N. Khlobystov, E. Besley, The effects of encapsulation on damage to molecules by electron radiation. *Micron* **120,** 96–103 (2019).

29. Z. Lee *et al.*, Direct Imaging of Soft−Hard Interfaces Enabled by Graphene. *Nano Lett.* **9,** 3365–3369 (2009).

30. C. Gómez-Navarro *et al.*, Electronic Transport Properties of Individual Chemically Reduced Graphene Oxide Sheets. *Nano Lett.* **7,** 3499–3503 (2007).

31. A. Reina *et al.*, Large Area, Few-Layer Graphene Films on Arbitrary Substrates by Chemical Vapor Deposition. *Nano Lett.* **9,** 30–35 (2008).

32. J. Zhao, J. Zhu, Electron microscopy and in situ testing of mechanical deformation of carbon nanotubes. *Micron* **42,** 663–679 (2011).

33. S. Reich, C. Thomsen, J. Maultzsch, *Carbon Nanotubes: Basic Concepts and Physical*

Properties. (Wiley-VCH: Weinheim, Germany, 2004).

34. Z. Liu, K. Yanagi, K. Suenaga, H. Kataura, S. Iijima, Imaging the dynamic behaviour of individual retinal chromophores confined inside carbon nanotubes. *Nat. Nanotechnol.* **2,** 422–425 (2007).

35. A. N. Khlobystov, D. A. Britz, G. A. D. Briggs, Molecules in Carbon Nanotubes. *Acc. Chem. Res.* **38,** 901–909 (2005).

36. D. A. Britz, A. N. Khlobystov, Noncovalent interactions of molecules with single walled carbon nanotubes. *Chem. Soc. Rev.* **35,** 637–659 (2006).

37. J. Zhao, J.-Q. Huang, F. Wei, J. Zhu, Mass Transportation Mechanism in Electric-Biased Carbon Nanotubes. *Nano Lett.* **10,** 4309–4315 (2010).

38. C. Jin, H. Lan, K. Suenaga, L. Peng, S. Iijima, Metal Atom Catalyzed Enlargement of Fullerenes. *Phys. Rev. Lett.* **101,** 176102 (2008).

39. K. Harano *et al.*, Conformational Analysis of Single Perfluoroalkyl Chains by Single-Molecule Real-Time Transmission Electron Microscopic Imaging. *J. Am. Chem. Soc.* **136,** 466–473 (2013).

40. A. N. Khlobystov, Carbon Nanotubes: From Nano Test Tube to Nano-Reactor. *ACS Nano* **5,** 9306–9312 (2011).

41. S. T. Skowron *et al.*, Chemical Reactions of Molecules Promoted and Simultaneously Imaged by the Electron Beam in Transmission Electron Microscopy. *Acc. Chem. Res.* **50,** 1797–1807 (2017).

42. S. A. Miners, G. A. Rance, A. N. Khlobystov, Chemical reactions confined within carbon nanotubes. *Chem. Soc. Rev.* **45,** 4727–4746 (2016).

43. T. W. Chamberlain *et al.*, Stop-Frame Filming and Discovery of Reactions at the Single-Molecule Level by Transmission Electron Microscopy. *ACS Nano* **11,** 2509–2520 (2017).

44. A. N. Khlobystov, D. A. Britz, A. Ardavan, G. A. D. Briggs, Observation of Ordered Phases of Fullerenes in Carbon Nanotubes. *Phys. Rev. Lett.* **92,** 245507 (2004).

45. D. A. Britz, A. N. Khlobystov, K. Porfyrakis, A. Ardavan, G. A. D. Briggs, Chemical reactions inside single-walled carbon nano test-tubes. *Chem. Commun.* 37–39 (2005). doi:10.1039/B414247K

46. A. Chuvilin *et al.*, Self-assembly of a sulphur-terminated graphene nanoribbon within a single-walled carbon nanotube. *Nat. Mater.* **10,** 687–692 (2011).

47. J. R. McBride *et al.*, Few-Layer Graphene as a Support Film for Transmission Electron Microscopy Imaging of Nanoparticles. *ACS Appl. Mater. & Interfaces* **1,** 2886–2892 (2009).

48. R. S. Pantelic, J. C. Meyer, U. Kaiser, H. Stahlberg, The application of graphene as a sample support in transmission electron microscopy. *Solid State Commun.* **152,** 1375–1382 (2012).

49. J. C. Meyer, C. O. Girit, M. F. Crommie, A. Zettl, Imaging and dynamics of light atoms and molecules on graphene. *Nature* **454,** 319–322 (2008).

50. K. Kim *et al.*, High-temperature stability of suspended single-layer graphene. *Phys. status solidi – Rapid Res. Lett.* **4,** 302–304 (2010).

51. Y. Kabiri *et al.*, Distortion of DNA Origami on Graphene Imaged with Advanced TEM Techniques. *Small* **13,** 1700876 (2017).

52. M. Rummeli *et al.*, In Situ Room Temperature Electron-Beam Driven Graphene Growth from Hydrocarbon Contamination in a Transmission Electron Microscope. *Materials (Basel).* **11,** 896 (2018).

53. M. Terrones, Visualizing fullerene chemistry. *Nat. Chem.* **2,** 82–83 (2010).

54. S. B. Chikkannanavar, D. E. Luzzi, S. Paulson, A. T. Johnson, Synthesis of Peapods Using Substrate-Grown SWNTs and DWNTs: An Enabling Step Toward Peapod Devices. *Nano Lett.* **5,** 151–155 (2005).

55. D. Obergfell *et al.*, Transport and TEM on dysprosium metallofullerene peapods. *Phys. Status Solidi Basic Res.* **243,** 3430–3434 (2006).

56. B. Verberck, K. H. Michel, A. V. Nikolaev, The C_{60} Molecules in $(C_{60})_N$@SWCNT Peapods: Crystal Field, Intermolecular Interactions and Dynamics. *Fullerenes, Nanotub. Carbon Nanostructures* **14,** 171–178 (2006).

57. S. Berber, Y.-K. Kwon, D. Tománek, Microscopic Formation Mechanism of Nanotube Peapods. *Phys. Rev. Lett.* **88,** 185502 (2002).

58. C. Meyer, C. Spudat, L. Houben, C. M. Schneider, Defects induced on chemical vapour deposition carbon nanotubes during peapod synthesis on substrates. *Nanotechnology* **20,** 065603 (2009).

59. K. Urita, Y. Sato, K. Suenaga, Electron-Induced Puncturing of Endohedral Metallofullerenes. *Fullerenes, Nanotub. Carbon Nanostructures* **14,** 261–267 (2006).

60. X. Ye *et al.*, Single-particle mapping of nonequilibrium nanocrystal transformations. *Science* **354,** 874–877 (2016).

61. J. M. Yuk *et al.*, High-Resolution EM of Colloidal Nanocrystal Growth Using Graphene Liquid Cells. *Science* 61–65 (2012).

62. G. Algara-Siller, S. Kurasch, M. Sedighi, O. Lehtinen, U. Kaiser, The pristine atomic structure of MoS $_2$ monolayer protected from electron radiation damage by graphene. *Appl. Phys. Lett.* **103,** 203107 (2013).

63. R. Zan *et al.*, Control of Radiation Damage in MoS2 by Graphene Encapsulation. *ACS Nano* **7,** 10167–10174 (2013).

64. K. Kurotobi, Y. Murata, A Single Molecule of Water Encapsulated in Fullerene C60. *Science* **333,** 613–616 (2011).

65. J. Choe *et al.*, Direct imaging of rotating molecules anchored on graphene. *Nanoscale* **8,** 13174–13180 (2016).

66. J. Choe *et al.*, Direct imaging of structural disordering and heterogeneous dynamics of fullerene molecular liquid. *Nat. Commun.* **10,** 4395 (2019).

67. R. Mirzayev *et al.*, Buckyball sandwiches. *Sci. Adv.* **3,** e1700176 (2017).

68. T. Xu, Y. Shen, K. Yin, L. Sun, Precisely monitoring and tailoring 2D nanostructures at

the atomic scale. *APL Mater.* **7,** 050901 (2019).

69. P. Solís-Fernández, M. Bissett, H. Ago, Synthesis. structure and applications of graphene-based 2D heterostructures. *Chem. Soc. Rev.* **46,** 4572–4613 (2017).

70. J. R. Fryer, C. H. McConnell, F. Zemlin, D. L. Dorset, Effect of temperature on radiation damage to aromatic organic molecules. *Ultramicroscopy* **40,** 163–169 (1992).

71. T. Lehnert, O. Lehtinen, G. Algara–Siller, U. Kaiser, Electron radiation damage mechanisms in 2D $MoSe_2$. *Appl. Phys. Lett.* **110,** 033106 (2017).

72. S.-Y. Kim *et al.*, Substantial improvements of long-term stability in encapsulation-free WS_2 using highly interacting graphene substrate. *2D Mater.* **4,** 011007 (2016).

73. R. Zan *et al.*, Imaging Two Dimensional Materials and their Heterostructures. *J. Phys. Conf. Ser.* **902,** 012028 (2017).

74. M. J. Mohn, R. Hambach, P. Wachsmuth, C. Giorgetti, U. Kaiser, Dielectric properties of graphene/MoS_2 heterostructures from *ab initio* calculations and electron energy-loss experiments. *Phys. Rev. B* **97,** 235410 (2018).

75. T. Van Khai *et al.*, Synthesis and Optical Properties of MoS_2/Graphene Nanocomposite. *J. Electron. Mater.* **49,** 969–979 (2020).

76. Y. Lee *et al.*, Fabrication and Imaging of Monolayer Phosphorene with Preferred Edge Configurations via Graphene-Assisted Layer-by-Layer Thinning. *Nano Lett.* **20,** 559–566 (2019).

77. B. C. Bayer *et al.*, Atomic-Scale in Situ Observations of Crystallization and Restructuring Processes in Two-Dimensional MoS_2 Films. *ACS Nano* **12,** 8758–8769 (2018).

78. D. B. Williams, C. B. Carter, *Transmission Electron Microscopy*. (Springer: Berlin, 2009).

79. J. R. Mcintosh, in *Methods Cell Biol. Vol. 79* (Academic Press: Boston, MA, 2007).

80. T. L. Daulton, B. J. Little, K. Lowe, J. Jones-Meehan, In Situ Environmental Cell–Transmission Electron Microscopy Study of Microbial Reduction of Chromium(VI) Using Electron Energy Loss Spectroscopy. *Microsc. Microanal.* **7,** 470–485 (2001).

81. A. H. Castro Neto, F. Guinea, N. M. R. Peres, K. S. Novoselov, A. K. Geim, The electronic properties of graphene. *Rev. Mod. Phys.* **81,** 109–162 (2009).

82. N. R. Wilson *et al.*, Graphene Oxide: Structural Analysis and Application as a Highly Transparent Support for Electron Microscopy. *ACS Nano* **3,** 2547–2556 (2009).

83. A. A. Balandin *et al.*, Superior Thermal Conductivity of Single-Layer Graphene. *Nano Lett.* **8,** 902–907 (2008).

84. N. Mohanty, M. Fahrenholtz, A. Nagaraja, D. Boyle, V. Berry, Impermeable Graphenic Encasement of Bacteria. *Nano Lett.* **11,** 1270–1275 (2011).

85. A. Cerf, T. Alava, R. A. Barton, H. G. Craighead, Transfer-Printing of Single DNA Molecule Arrays on Graphene for High-Resolution Electron Imaging and Analysis. *Nano Lett.* **11,** 4232–4238 (2011).

86. T. Ogawa *et al.*, Graphene-supporting films and low-voltage STEM in SEM toward

imaging nanobio materials without staining: Observation of insulin amyloid fibrils. *Micron* **96,** 65–71 (2017).

87. H. Cho *et al.*, The Use of Graphene and Its Derivatives for Liquid-Phase Transmission Electron Microscopy of Radiation-Sensitive Specimens. *Nano Lett.* **17,** 414–420 (2016).

88. K. S. Munir, C. Wen, Y. Li, Carbon Nanotubes and Graphene as Nanoreinforcements in Metallic Biomaterials: a Review. *Adv. Biosyst.* **3,** 1800212 (2019).

89. Y. Kabiri *et al.*, Distortion of DNA Origami on Graphene Imaged with Advanced TEM Techniques. *Small* **13,** 1700876 (2017).

90. R. S. Pantelic, J. Won Suk, Y. Hao, R. S. Ruoff, H. Stahlberg, Oxidative Doping Renders Graphene Hydrophilic, Facilitating Its Use As a Support in Biological TEM. *Nano Lett.* **11,** 4319–4323 (2011).

91. B. E. Janicek *et al.*, Quantitative Imaging of Organic Ligand Density on Anisotropic Inorganic Nanocrystals. *Nano Lett.* **19,** 6308–6314 (2019).

92. X. Ke *et al.*, Dynamic Motion of Ru-Polyoxometalate Ions (POMs) on Functionalized Few-Layer Graphene. *Small* **9,** 3922–3927 (2013).

93. N. Vats *et al.*, Electron microscopy of polyoxometalate ions on graphene by electrospray ion beam deposition. *Nanoscale* **10,** 4952–4961 (2018).

94. A. D. Dukes, J. R. McBride, S. J. Rosenthal, Synthesis of Magic-Sized CdSe and CdTe Nanocrystals with Diisooctylphosphinic Acid. *Chem. Mater.* **22,** 6402–6408 (2010).

95. A. Markevich *et al.*, Electron beam controlled covalent attachment of small organic molecules to graphene. *Nanoscale* **8,** 2711–2719 (2016).

96. M. A. Gerkman, S. Sinha, J. H. Warner, G. G. D. Han, Direct Imaging of Photoswitching Molecular Conformations Using Individual Metal Atom Markers. *ACS Nano* **13,** 87–96 (2019).

97. J. Kyung Lee *et al.*, Metal Atom Markers for Imaging Epitaxial Molecular Self-Assembly on Graphene by Scanning Transmission Electron Microscopy. *ACS Nano* **13,** 7252–7260 (2019).

98. M. H. Rummeli *et al.*, New Frontiers in Electron Beam–Driven Chemistry in and around Graphene. *Adv. Mater.* **31,** 1800715 (2019).

99. B. Westenfelder *et al.*, Transformations of Carbon Adsorbates on Graphene Substrates under Extreme Heat. *Nano Lett.* **11,** 5123–5127 (2011).

100. M.-T. Nguyen, P. Nam Phong, Accelerating Dynamics of H on Graphene by Coadsorbates. *J. Phys. Chem. A* **121,** 5520–5523 (2017).

101. M.-T. Nguyen, P. N. Phong, Atomic Transport at Charged Graphene: Why Hydrogen and Oxygen Are So Different. *ChemistrySelect* **2,** 2797–2802 (2017).

102. G. Hong *et al.*, Recent progress in organic molecule/graphene interfaces. *Nano Today* **8,** 388–402 (2013).

103. J. M. MacLeod, F. Rosei, Molecular Self-Assembly on Graphene. *Small* **10,** 1038–1049 (2014).

104. F. Börrnert *et al.*, Amorphous Carbon under 80 kV Electron Irradiation: A Means to

Make or Break Graphene. *Adv. Mater.* **24,** 5630–5635 (2012).

105. K. Yin *et al.*, Unsupported single-atom-thick copper oxide monolayers. *2D Mater.* **4,** 011001 (2016).

106. K. Kim, E. J. G. Santos, T. H. Lee, Y. Nishi, Z. Bao, Epitaxially Grown Strained Pentacene Thin Film on Graphene Membrane. *Small* **11,** 2037–2043 (2015).

107. Z. P. L. Laker *et al.*, Monolayer-to-thin-film transition in supramolecular assemblies: the role of topological protection. *Nanoscale* **9,** 11959–11968 (2017).

108. A. W. Robertson *et al.*, PbTe Nanocrystal Arrays on Graphene and the Structural Influence of Capping Ligands. *Chem. Mater.* **26,** 1567–1575 (2014).

109. R. Zan, U. Bangert, Q. Ramasse, K. S. Novoselov, Interaction of Metals with Suspended Graphene Observed by Transmission Electron Microscopy. *J. Phys. Chem. Lett.* **3,** 953–958 (2012).

110. B. Westenfelder *et al.*, Bottom-up formation of robust gold carbide. *Sci. Rep.* **5,** 8891 (2015).

111. A. W. Robertson *et al.*, Dynamics of single Fe atoms in graphene vacancies. *Nano Lett.* **13,** 1468–1475 (2013).

112. Z. He *et al.*, Atomic structure and dynamics of metal dopant pairs in graphene. *Nano Lett.* **14,** 3766–3772 (2014).

113. Y. Gan, L. Sun, F. Banhart, One- and Two-Dimensional Diffusion of Metal Atoms in Graphene. *Small* **4,** 587–591 (2008).

114. C. Gong *et al.*, Interactions of Pb and Te atoms with graphene. *Dalt. Trans.* **43,** 7442–7448 (2014).

115. R. Zan, U. Bangert, Q. Ramasse, K. S. Novoselov, Evolution of Gold Nanostructures on Graphene. *Small* **7,** 2868–2872 (2011).

116. J. H. Warner, M. H. Rümmeli, A. Bachmatiuk, M. Wilson, B. Büchner, Examining Co-Based Nanocrystals on Graphene Using Low-Voltage Aberration-Corrected Transmission Electron Microscopy. *ACS Nano* **4,** 470–476 (2009).

117. M. G. Panthani *et al.*, Graphene-Supported High-Resolution TEM and STEM Imaging of Silicon Nanocrystals and their Capping Ligands. *J. Phys. Chem. C* **116,** 22463–22468 (2012).

118. S. Godefroo *et al.*, Classification and control of the origin of photoluminescence from Si nanocrystals. *Nat. Nanotechnol.* **3,** 174–178 (2008).

119. L. Sun, F. Banhart, J. Warner, Two-dimensional materials under electron irradiation. *MRS Bull.* **40,** 29–37 (2015).

120. J. Jiang, T. Xu, J. Lu, L. Sun, Z. Ni, Review Article Defect Engineering in 2D Materials : Precise Manipulation and Improved Functionalities. **2019,** (2019).

121. Q. Chen, K. He, A. W. Robertson, A. I. Kirkland, J. H. Warner, Atomic Structure and Dynamics of Epitaxial 2D Crystalline Gold on Graphene at Elevated Temperatures. *ACS Nano* **10,** 10418–10427 (2016).

122. P. Xu *et al.*, Self-Organized Platinum Nanoparticles on Freestanding Graphene. *ACS*

Nano **8,** 2697–2703 (2014).

123. A. W. Robertson *et al.,* Atomic Structure and Dynamics of Epitaxial Platinum Bilayers on Graphene. *ACS Nano* **13,** 12162–12170 (2019).

124. W. Xin *et al.,* Graphene template-induced growth of single-crystalline gold nanobelts with high structural tunability. *Nanoscale* **10,** 2764–2773 (2018).

125. W. Xin *et al.,* Ultrasonication-assisted synthesis of high aspect ratio gold nanowires on a graphene template and investigation of their growth mechanism. *Chem. Commun.* **54,** 4124–4127 (2018).

126. W. Xin *et al.,* One-Step Synthesis of Tunable-Size Gold Nanoplates on Graphene Multilayers. *Nano Lett.* **18,** 1875–1881 (2018).

127. Q. Chen *et al.,* Rotating Anisotropic Crystalline Silicon Nanoclusters in Graphene. *ACS Nano* **9,** 9497–9506 (2015).

128. H. Q. Ta *et al.,* Electron-Driven Metal Oxide Effusion and Graphene Gasification at Room Temperature. *ACS Nano* **10,** 6323–6330 (2016).

129. H.-K. Hong *et al.,* Atomic Scale Study on Growth and Heteroepitaxy of ZnO Monolayer on Graphene. *Nano Lett.* **17,** 120–127 (2017).

130. F. Banhart, J. Kotakoski, A. V Krasheninnikov, Structural Defects in Graphene. *ACS Nano* **5,** 26–41 (2011).

131. J. Lee *et al.,* Stabilization of graphene nanopore. *Proc. Natl. Acad. Sci.* **111,** 7522–7526 (2014).

132. J. Zhao *et al.,* Free-standing single-atom-thick iron membranes suspended in graphene pores. *Science* **343,** 1228–1232 (2014).

133. H. T. Quang *et al.,* In Situ Observations of Free-Standing Graphene-like Mono- and Bilayer ZnO Membranes. *ACS Nano* **9,** 11408–11413 (2015).

134. F. Claeyssens *et al.,* Growth of ZnO thin films—experiment and theory. *J. Mater. Chem.* **15,** 139–148 (2005).

135. C. Tusche, H. L. Meyerheim, J. Kirschner, Observation of Depolarized ZnO(0001) Monolayers: Formation of Unreconstructed Planar Sheets. *Phys. Rev. Lett.* **99,** 026102 (2007).

136. J. Nevalaita, P. Koskinen, Stability limits of elemental 2D metals in graphene pores. *Nanoscale* **11,** 22019–22024 (2019).

137. K. Sohlberg, T. J. Pennycook, W. Zhou, S. J. Pennycook, Insights into the physical chemistry of materials from advances in HAADF-STEM. *Phys. Chem. Chem. Phys.* **17,** 3982–4006 (2015).

138. A. B. Yankovich *et al.,* Picometre-precision analysis of scanning transmission electron microscopy images of platinum nanocatalysts. *Nat. Commun.* **5,** 4155 (2014).

139. A. Bin Yousaf, M. Imran, M. Farooq, P. Kasak, Interfacial Phenomenon and Nanostructural Enhancements in Palladium Loaded Lanthanum Hydroxide Nanorods for Heterogeneous Catalytic Applications. *Sci. Rep.* **8,** 4354 (2018).

140. B. Patrick *et al.,* Atomic Structure and Composition of "Pt_3Co" Nanocatalysts in Fuel

Cells: An Aberration-Corrected STEM HAADF Study. *Chem. Mater.* **25,** 530–535 (2013).

141. S. Dai *et al.*, Platinum-trimer decorated cobalt-palladium core-shell nanocatalyst with promising performance for oxygen reduction reaction. *Nat. Commun.* **10,** 440 (2019).

142. D. Su, Advanced electron microscopy characterization of nanomaterials for catalysis. *Green Energy Environ.* **2,** 70–83 (2017).

143. Y. Zhu, M. Xu, W. Zhou, High-resolution electron microscopy for heterogeneous catalysis research. *Chinese Phys. B* **27,** 056804 (2018).

144. H. Fei *et al.*, Single atom electrocatalysts supported on graphene or graphene-like carbons. *Chem. Soc. Rev.* **48,** 5207–5241 (2019).

145. O. Miramontes *et al.*, Ultra-small rhenium clusters supported on graphene. *Phys. Chem. Chem. Phys.* **17,** 7898–7906 (2015).

146. D. A. Bulushev *et al.*, Single Atoms of Pt-Group Metals Stabilized by N-Doped Carbon Nanofibers for Efficient Hydrogen Production from Formic Acid. *ACS Catal.* **6,** 3442–3451 (2016).

147. S. Sun *et al.*, Single-atom Catalysis Using Pt/Graphene Achieved through Atomic Layer Deposition. *Sci. Rep.* **3,** 1775 (2013).

148. N. Cheng *et al.*, Platinum single-atom and cluster catalysis of the hydrogen evolution reaction. *Nat. Commun.* **7,** 13638 (2016).

149. T. Imaoka, T. Toyonaga, M. Morita, N. Haruta, K. Yamamoto, Isomerizations of a Pt_4 cluster revealed by spatiotemporal microscopic analysis. *Chem. Commun.* **55,** 4753–4756 (2019).

150. H. Yi *et al.*, Precisely Controlled Porous Alumina Overcoating on Pd Catalyst by Atomic Layer Deposition: Enhanced Selectivity and Durability in Hydrogenation of 1,3-Butadiene. *ACS Catal.* **5,** 2735–2739 (2015).

151. Z. Zhang, B. Zandkarimi, A. N. Alexandrova, Ensembles of Metastable States Govern Heterogeneous Catalysis on Dynamic Interfaces. *Acc. Chem. Res.* (2020).

152. L. Zhu *et al.*, Tiny Ruthenium-Cobalt-Cobalt Hydroxide Nanoparticles Supported on Graphene for Efficiently Catalyzing Naphthalene Complete Hydrogenation. *ChemistrySelect* **4,** 8394–8397 (2019).

153. M. R. Hauwiller *et al.*, Unraveling Kinetically-Driven Mechanisms of Gold Nanocrystal Shape Transformations Using Graphene Liquid Cell Electron Microscopy. *Nano Lett.* **18,** 5731–5737 (2018).

154. H.-G. Liao, H. Zheng, Liquid Cell Transmission Electron Microscopy. *Annu. Rev. Phys. Chem.* **67,** 719–747 (2016).

155. T. Ngo, H. Yang, Toward Ending the Guessing Game: Study of the Formation of Nanostructures Using In Situ Liquid Transmission Electron Microscopy. *J. Phys. Chem. Lett.* **6,** 5051–5061 (2015).

156. H. Zheng *et al.*, Observation of single colloidal platinum nanocrystal growth trajectories. *Science* **324,** 1309–12 (2009).

157. D. E. McCoy, T. Feo, T. A. Harvey, R. O. Prum, Structural absorption by barbule microstructures of super black bird of paradise feathers. *Nat. Commun.* **9,** 1 (2018).

158. H.-G. Liao, K.-Y. Niu, H. Zheng, in *Liq. Cell Electron Microsc.* 191–209 (Cambridge University Press, 2016).

159. S. Pu, C. Gong, A. W. Robertson, Liquid cell transmission electron microscopy and its applications. *R. Soc. Open Sci.* **7,** 191204 (2020).

160. R. Erni *et al.*, Stability and dynamics of small molecules trapped on graphene. *Phys. Rev. B* **82,** 165443 (2010).

161. M. R. AU - Hauwiller, J. C. AU - Ondry, A. P. AU - Alivisatos, Using Graphene Liquid Cell Transmission Electron Microscopy to Study in Situ Nanocrystal Etching. *JoVE* e57665 (2018).

162. K. Xu *et al.*, Graphene Visualizes the First Water Adlayers on Mica at Ambient Conditions. *Science* **329,** 1188–1191 (2012).

163. J. Park *et al.*, 3D structure of individual nanocrystals in solution by electron microscopy. *Science* **349,** 290–295 (2015).

164. T. Lehnert *et al.*, In Situ Crystallization of the Insoluble Anhydrite AII Phase in Graphene Pockets. *ACS Nano* **11,** 7967–7973 (2017).

165. W. Wei *et al.*, Observing the Growth of Pb3O4 Nanocrystals by in Situ Liquid Cell Transmission Electron Microscopy. *ACS Appl. Mater. & Interfaces* **11,** 24478–24484 (2019).

166. S. M. Ghodsi, S. Anand, R. Shahbazian-Yassar, T. Shokuhfar, C. M. Megaridis, In Situ Study of Molecular Structure of Water and Ice Entrapped in Graphene Nanovessels. *ACS Nano* **13,** 4677–4685 (2019).

167. C. Zhang *et al.*, Recent Progress of In Situ Transmission Electron Microscopy for Energy Materials. *Adv. Mater.* **n/a,** 1904094

168. M. Textor, N. de Jonge, Strategies for Preparing Graphene Liquid Cells for Transmission Electron Microscopy. *Nano Lett.* **18,** 3313–3321 (2018).

169. H. Wang, B. Li, Y.-J. Kim, O.-H. Kwon, S. Granick, Intermediate states of molecular self-assembly from liquid-cell electron microscopy. *Proc. Natl. Acad. Sci.* **117,** 1283–1292 (2020).

170. J. Wu, W. Gao, H. Yang, J.-M. Zuo, Dissolution Kinetics of Oxidative Etching of Cubic and Icosahedral Platinum Nanoparticles Revealed by in Situ Liquid Transmission Electron Microscopy. *ACS Nano* **11,** 1696–1703 (2017).

171. A. Matruglio *et al.*, Graphene liquid cells for multi-technique analysis of biological cells in water environment. *J. Instrum.* **13,** C05016–C05016 (2018).

172. S. M. Ghodsi, C. M. Megaridis, R. Shahbazian-Yassar, T. Shokuhfar, Advances in Graphene-Based Liquid Cell Electron Microscopy: Working Principles, Opportunities, and Challenges. *Small Methods* **3,** 1900026 (2019).

173. W. Krätschmer, L. D. Lamb, K. Fostiropoulos, D. R. Huffman, Solid C60: a new form of carbon. *Nature* **347,** 354–358 (1990).

174. R. Kitaura, H. Shinohara, Endohedral Metallofullerenes and Nano-Peapods. *Jpn. J. Appl. Phys* **46,** 881–891 (2007).

175. M. Inakuma *et al.*, Spectroscopic Properties of Isolated $Sc_3@C_{82}$ Metallofullerene. *J. Phys. Chem* **98,** 8597–8599 (1994).

176. J. Xiao, M. R. Savina, G. B. Martin, A. H. Francis, M. E. Meyerhoff, Efficient HPLC Purification of Endohedral Metallofullerenes on a Porphyrin-Silica Stationary Phase. *J. Am. Chem. Soc.* **116,** 9341–9342 (1994).

177. A. Mishra, Soxhlet Extraction Method- Estimation Of Fat In Food. *Discov. Food Tech* (2017).

178. A. Popov, S. Yang, L. Dunsch, Endohedral Fullerenes. *Chem. Rev.* **113,** 5989–6113 (2013).

179. V. J. Barwick, Sources of uncertainty in gas chromatography and high-performance liquid chromatography. *J. Chromatogr. A* **849,** 13–33 (1999).

180. B. J. Farrington, A tale of two spins: electron spin centre assemblies with $N@C_{60}$ for use in QIP. (2014).

181. D. Liu *et al.*, In situ trapped high-density single metal atoms within graphene: Iron-containing hybrids as representatives for efficient oxygen reduction. *Nano Res.* **11,** 2217–2228 (2018).

182. O. L. Krivanek *et al.*, Atom-by-atom structural and chemical analysis by annular dark-field electron microscopy. *Nature* **464,** 571–574 (2010).

183. Q. D. Truong *et al.*, Inversion domain boundaries in $MoSe_2$ layers. *RSC Adv.* **8,** 33391–33397 (2018).

184. P. E. Vullum *et al.*, Quantitative strain analysis of InAs/GaAs quantum dot materials. *Sci. Rep.* **7,** 45376 (2017).

185. N. Fernández-Delgado *et al.*, Atomic-column scanning transmission electron microscopy analysis of misfit dislocations in GaSb/GaAs quantum dots. *J. Mater. Sci.* **51,** 7691–7698 (2016).

186. M. Haruta, H. Kurata, Direct observation of crystal defects in an organic molecular crystals of copper hexachlorophthalocyanine by STEM-EELS. *Sci. Rep.* **2,** 252 (2012).

187. R. Mishra, R. Ishikawa, A. R. Lupini, S. J. Pennycook, Single-atom dynamics in scanning transmission electron microscopy. *MRS Bull.* **42,** 644–652 (2017).

188. T. Susi *et al.*, Silicon–Carbon Bond Inversions Driven by 60-keV Electrons in Graphene. *Phys. Rev. Lett.* **113,** 115501 (2014).

189. R. E. S. H. W. Kroto, J.R. Heath, S.C. O'Brien, R. F. Curl, C_{60}: Buckminsterfullerene. *Nature* **318,** 162–163 (1985).

190. J. Hawkins, A. Meyer, T. Lewis, S. Loren, F. Hollander, Crystal structure of osmylated C60: confirmation of the soccer ball framework. *Science* **252,** 312–313 (1991).

191. F. Wudl, The Chemical Properties of Buckminsterfullerene (C_{60}) and the Birth and Infancy of Fulleroids. *Acc. Chem. Res* **25,** 157–161 (1992).

192. M. Takata *et al.*, Triangle Scandium Cluster Imprisoned in a Fullerene Cage. *Phys. Rev.*

Lett. **83,** 2214–2217 (1999).

193. C. R. Wang *et al.*, A scandium carbide endohedral metallofullerene: $(Sc_2C_2)@C_{84}$. *Angew. Chemie - Int. Ed.* **40,** 397–399 (2001).

194. T.-S. Wang *et al.*, Russian-Doll-Type Metal Carbide Endofullerene: Synthesis, Isolation, and Characterization of $Sc_4C_2@C_{80}$. *J. Am. Chem. Soc.* **131,** 16646–16647 (2009).

195. S. Stevenson *et al.*, Small-bandgap endohedral metallofullerenes in high yield and purity. *Nature* **401,** 55–57 (1999).

196. M. Krause, F. Ziegs, A. A. Popov, L. Dunsch, Entrapped bonded hydrogen in a fullerene: The five-atom cluster Sc_3CH in C_{80}. *ChemPhysChem* **8,** 537–540 (2007).

197. S. Stevenson *et al.*, A Distorted Tetrahedral Metal Oxide Cluster inside an Icosahedral Carbon Cage. Synthesis, Isolation, and Structural Characterization of $Sc_4(myu_3\text{-}O)_2@I_h\text{-}C_{80}$. *J. Am. Chem. Soc.* **130,** 11844–11845 (2008).

198. L. Dunsch, S. Yang, Metal nitride cluster fullerenes: Their current state and future prospects. *Small* **3,** 1298–1320 (2007).

199. K. Kobayashi, S. Nagase, A stable unconventional structure of $Sc_2@C_{66}$ found by density functional calculations. *Chem. Phys. Lett.* **362,** 373–379 (2002).

200. S. C. Tsang, Y. K. Chen, P. J. F. Harris, M. L. H. Green, A simple chemical method of opening and filling carbon nanotubes. *Nature* **372,** 159–162 (1994).

201. C. S. Allen, Y. Ito, A. W. Robertson, H. Shinohara, J. H. Warner, Two-dimensional coalescence dynamics of encapsulated metallofullerenes in carbon nanotubes. *ACS Nano* **5,** 10084–10089 (2011).

202. A. N. Khlobystov, D. a Britz, G. A. D. Briggs, Molecules in Carbon Nanotubes Molecules in Carbon Nanotubes. *Acc. Chem. Res.* **38,** 901–909 (2005).

203. A. N. Khlobystov *et al.*, Low temperature assembly of fullerene arrays in single-walled carbon nanotubes using supercritical fluids. *J. Mater. Chem.* **14,** 2852 (2004).

204. C. Maddi *et al.*, Nano-Architecture of nitrogen-doped graphene films synthesized from a solid CN source. *Sci. Rep.* **8,** 1–13 (2018).

205. D. Wei, Synthesis of n-doped graphene by chemical vapor deposition and its electrical properties. *Nano Lett.* **9,** 1752–1758 (2009).

206. Z. Luo *et al.*, Pyridinic N doped graphene: Synthesis, electronic structure, and electrocatalytic property. *J. Mater. Chem.* **21,** 8038–8044 (2011).

207. K. Pi *et al.*, Electronic doping and scattering by transition metals on graphene. *Phys. Rev. B - Condens. Matter Mater. Phys.* **80,** 1–5 (2009).

208. J. O. Hwang *et al.*, Workfunction-tunable, N-doped reduced graphene transparent electrodes for high-performance polymer light-emitting diodes. *ACS Nano* **6,** 159–167 (2012).

209. A. Kasry, M. Kuroda, G. Martyna, G. Tulevski, A. Bol, Chemical Doping of Large-Area Stacked Graphene Films for Use as Transparent, Conducting Electrodes.pdf. *Am. Chem. Soc.* **4,** 3839–3844 (2010).

210. K. S. Kim, A. Moradian, J. Mostaghimi, G. Soucy, Modeling of induction plasma process for fullerene synthesis: Effect of plasma gas composition and operating pressure. *Plasma Chem. Plasma Process.* **30,** 91–110 (2010).

211. H. Liu, Y. Liu, D. Zhu, Chemical doping of graphene. *J. Mater. Chem.* **21,** 3335–3345 (2011).

212. R. Lv *et al.*, Nitrogen-doped graphene: Beyond single substitution and enhanced molecular sensing. *Sci. Rep.* **2,** 1–8 (2012).

213. L. Tsetseris, B. Wang, S. T. Pantelides, Substitutional doping of graphene: The role of carbon divacancies. *Phys. Rev. B - Condens. Matter Mater. Phys.* **89,** 3–6 (2014).

214. X. Deng, J. Zeng, M. Si, W. Lu, The mechanism and process of spontaneous boron doping in graphene in the theoretical perspective. *Phys. Lett. Sect. A Gen. At. Solid State Phys.* **380,** 3384–3388 (2016).

215. J. H. Warner, Y. C. Lin, K. He, M. Koshino, K. Suenaga, Stability and spectroscopy of single nitrogen dopants in graphene at elevated temperatures. *ACS Nano* **8,** 11806–11815 (2014).

216. X. Liu *et al.*, Metals on Graphene: Interactions, Growth Morphology, and Thermal Stability. *Crystals* **3,** 79–111 (2013).

217. X. Liu *et al.*, Adsorption and growth morphology of rare-earth metals on graphene studied by ab initio calculations and scanning tunneling microscopy. *Phys. Rev. B - Condens. Matter Mater. Phys.* **82,** 1–7 (2010).

218. B. W. N. H. Hemasiri, J. K. Kim, J. M. Lee, Synthesis and Characterization of Graphene/ITO Nanoparticle Hybrid Transparent Conducting Electrode. *Nano-Micro Lett.* **10,** 1–12 (2018).

219. J. Sloan *et al.*, Imaging the structure, symmetry, and surface-inhibited rotation of polyoxometalate ions on graphene oxide. *Nano Lett.* **10,** 4600–4606 (2010).

220. C. Bosch-Navarro *et al.*, Selective imaging of discrete polyoxometalate ions on graphene oxide under variable voltage conditions. *ACS Nano* **10,** 796–802 (2016).

221. J. H. Warner *et al.*, Rotating fullerene chains in carbon nanopeapods. *Nano Lett.* **8,** 2328–2335 (2008).

222. W. Zhou *et al.*, Direct determination of the chemical bonding of individual impurities in graphene. *Phys. Rev. Lett.* **109,** 2–6 (2012).

223. W. Zhou *et al.*, Atomically localized plasmon enhancement in monolayer graphene. *Nat. Nanotechnol.* **7,** 161–165 (2012).

224. I. F. Crowe *et al.*, Combined super-STEM imaging, EEL and PL spectroscopy of un-doped and Er doped SRSO on Si. *Conf. Optoelectron. Microelectron. Mater. Devices, Proceedings, COMMAD* 163–165 (2008). doi:10.1109/COMMAD.2008.4802117

225. S. Guo, D. Wen, Y. Zhai, S. Dong, E. Wang, Platinum Nanoparticle Ensemble-on- Rapid Synthesis , and Used as New Sensing. *ACS Nano* **4,** 3959–3968 (2010).

226. Y. C. Lin *et al.*, Structural and Chemical Dynamics of Pyridinic-Nitrogen Defects in Graphene. *Nano Lett.* **15,** 7408–7413 (2015).

227. S. Wang *et al.*, Preferential Pt Nanocluster Seeding at Grain Boundary Dislocations in Polycrystalline Monolayer MoS 2. *ACS Nano* **12,** acsnano.8b01418 (2018).

228. Z. Qin, G. Qin, B. Shao, X. Zuo, Unconventional magnetic anisotropy in one-dimensional Rashba system realized by adsorbing Gd atom on zigzag graphene nanoribbons. *Nanoscale* **9,** 11657–11666 (2017).

229. Y. Lu, T. G. Zhou, B. Shao, X. Zuo, M. Feng, Carrier-dependent magnetic anisotropy of Gd-adsorbed graphene. *AIP Adv.* **6,** (2016).

230. M. Alemani *et al.*, Effect of gadolinium adatoms on the transport properties of graphene. *Phys. Rev. B - Condens. Matter Mater. Phys.* **86,** 1–5 (2012).

231. N. V. Bulina *et al.*, Fullerene synthesis in helium flow at atmospheric pressure. *NATO Secur. through Sci. Ser. A Chem. Biol.* 269–274 (2007).

232. G. Churilov *et al.*, Controlled synthesis of fullerenes and endohedral metallofullerenes in high frequency arc discharge. *Fullerenes Nanotub. Carbon Nanostructures* **24,** (2016).

233. C. M. Lieber, C.-C. Chen, in *Solid State Phys.* 109–148 (Elsevier BV, 1994).

234. Z. Wang, H. Omachi, H. Shinohara, Non-Chromatographic Purification of Endohedral Metallofullerenes. *Molecules* **22,** 718 (2017).

235. K. Akiyama *et al.*, Non-HPLC rapid separation of metallofullerenes and empty cages with TiCl4 Lewis acid. *J. Am. Chem. Soc.* **134,** 9762–7 (2012).

236. G. Churilov *et al.*, Controlled synthesis of fullerenes and endohedral metallofullerenes in high frequency arc discharge. *Fullerenes Nanotub. Carbon Nanostructures* **24,** 675–678 (2016).

237. Y. Saito, S. Yokoyama, M. Inakuma, H. Shinohara, An ESR study of the formation of La@C_{82} isomers in arc synthesis. *Chem. Phys. Lett.* **250,** (1996).

238. Y. Lian, S. Yang, S. Yang, Revisiting the Preparation of La@C_{82}(I and II) and La_2@C_{80} : Efficient Production of the. *J. Phys. Chem. B* **106,** 3112–3117 (2002).

239. C. W. Isaacsona, M. Kleberc, J. A. Fielda, Quantitative Analysis of Fullerene Nanomaterials in Environmental Systems: A Critical Review. *Env. Sci Technol.* **43,** 6463–6474 (2009).

240. L. D. Alexey A. Popov, Shangfeng Yang, Endohedral fullerenes. *Chem. Rev.* **113,** 5989–6113 (2012).

241. E. Y. Misochko *et al.*, EPR spectrum of the Y@C_{82} metallofullerene isolated in solid argon matrix: Hyperfine structure from EPR spectroscopy and relativistic DFT calculations. *Phys. Chem. Chem. Phys.* **12,** 8863–8869 (2010).

242. S. Stevenson *et al.*, Isolation and Crystallographic Characterization of Gd_3N@D_2(35)-C_{88} through Non-Chromatographic Methods. *Inorg. Chem* **55,** 62–67 (2016).

243. Z. Wang, Y. Nakanishi, S. Noda, K. Akiyama, H. Shinohara, The Origin and Mechanism of Non-HPLC Puri fi cation of Metallofullerenes with TiCl4. *J. Am. Chem. Soc.* **116,** 15563–25567 (2012).

244. J. Lu *et al.*, Structural and Magnetic Properties of $Gd_3N@C_{80}$. *J. Phys. Chem. B* **110,** 23637–23640 (2006).

245. M. Krause, L. Dunsch, Gadolinium nitride Gd_3N in carbon cages: The influence of cluster size and bond strength. *Angew. Chemie - Int. Ed.* **44,** 1557–1560 (2005).

246. J. M. Cowley, A. F. Moodie, A new formulation of scalar diffraction theory for restricted aperture. *Proc. Phys. Soc.* **71,** 533–545 (1958).

247. P. Stadelmann, Image analysis and simulation software in transmission electron microscopy. *Microsc. Microanal.* **9,** 60–61 (2003).

248. S. Stevenson *et al.*, Pyramidalization of Gd 3 N inside a C 80 cage . The synthesis and structure of $Gd_3N@C_{80}$. 2814–2815 (2004).

249. W. Fang, A. L. Hsu, Y. Song, J. Kong, A review of large-area bilayer graphene synthesis by chemical vapor deposition. *Nanoscale* **7,** 20335–20351 (2015).

250. Y. Kan Koh, M.-H. Bae, D. G. Cahill, E. Pop, Heat Conduction across Monolayer and Few-Layer Graphenes. *Nano Lett.* **10,** 4363–4368 (2010).

251. M.-H. Bae, Z.-Y. Ong, D. Estrada, E. Pop, Imaging, Simulation, and Electrostatic Control of Power Dissipation in Graphene Devices. *Nano Lett.* **10,** 4787–4793 (2010).

252. A. V. Talyzin *et al.*, Reaction of hydrogen gas with C_{60} at elevated pressure and temperature: Hydrogenation and cage fragmentation. *J. Phys. Chem. A* **110,** 8528–8534 (2006).

253. T. Tsukamoto, T. Ogino, Control of graphene etching by atomic structures of the supporting substrate surfaces. *J. Phys. Chem. C* **115,** 8580–8585 (2011).

254. O. Cretu *et al.*, Experimental observation of boron nitride chains. *ACS Nano* **8,** 11950–11957 (2014).

255. J. H. Warner *et al.*, Structural transformations in graphene studied with high spatial and temporal resolution. *Nat. Nanotechnol.* **4,** 500–504 (2009).

256. Q. H. Wang, K. Kalantar-zadeh, A. Kis, J. N. Coleman, M. S. Strano, transition metal dichalcogenides. *Nat. Publ. Gr.* **7,** 699–712 (2012).

257. K. F. Mak, K. He, J. Shan, T. F. Heinz, Control of valley polarization in monolayer MoS_2 by optical helicity. **7,** 494–498 (2012).

258. H. Zeng, J. Dai, W. Yao, D. Xiao, X. Cui, Valley polarization in MoS_2 monolayers by optical pumping. **7,** (2012).

259. D. C. Elias *et al.*, Dirac cones reshaped by interaction effects in suspended graphene. *Nat. Phys.* **7,** 701–704 (2011).

260. B. Radisavljevic, A. Radenovic, J. Brivio, V. Giacometti, A. Kis, Single-layer MoS_2 transistors. **6,** (2011).

261. M. Amani *et al.*, vapor deposition Electrical performance of monolayer MoS_2 field-effect transistors prepared by chemical vapor deposition. **193107,** (2014).

262. R. Ganatra, Q. Zhang, N. Centre, E. Engineering, Few-Layer MoS_2: A Promising Layered Semiconductor. 4074–4099 (2014).

263. R. Lv *et al.*, Transition Metal Dichalcogenides and Beyond : Synthesis , Properties , and Applications of Single- and Few-Layer Nanosheets Published as part of the Accounts of Chemical Research special issue “2D Nanomaterials beyond Graphene ”. (2015).

264. F. Schwierz, J. Pezoldt, R. Granzner, Two-dimensional materials and their prospects in transistor electronics. *Nanoscale* **7,** 8261–8283 (2015).

265. M. Zhou, W. Duan, Y. Chen, A. Du, Single layer lead iodide: Computational exploration of structural, electronic and optical properties, strain induced band modulation and the role of spin-orbital-coupling. *Nanoscale* **7,** 15168–15174 (2015).

266. M. Zhong *et al.*, Large-scale 2D PbI_2 monolayers: Experimental realization and their indirect band-gap related properties. *Nanoscale* **9,** 3736–3741 (2017).

267. A. S. Toulouse *et al.*, Frenkel-like Wannier-Mott excitons in few-layer PbI_2. *Phys. Rev. B* **165308,** 1–5 (2015).

268. X. Liu *et al.*, Whispering Gallery Mode Lasing from Hexagonal Shaped Layered Lead Iodide. *ACS Nano* **9,** 687–695 (2015).

269. Z. Shi, A. H. Jayatissa, Perovskites-Based Solar Cells: A Review of Recent Progress, Materials and Processing Methods. *Materials (Basel)* **11**, 729 (2018).

270. G. Niu, X. Guo, L. Wang, Review of recent progress in chemical stability of perovskite solar cells. *J. Mater. Chem. A* **3,** 8970–8980 (2015).

271. J. Heo, Development of a stable and sensitive semiconductor detector by using a mixture of lead(II) iodide and lead monoxide for NDT radiation dose detection. *JINST* **13,** (2018).

272. X. H. Zhu, Z. R. Wei, Y. R. Jin, A. P. Xiang, Growth and characterization of a PbI 2 single crystal used for gamma ray detectors. *Cryst. Res. Technol.* **42,** 456–459 (2007).

273. J. Greenspan, L. Laperriere, O. Bubon, A. Reznik, Amorphous and Polycrystalline Photoconductors for Direct Conversion Flat Panel X-Ray Image Sensors. *Sensors(Basel)* 5112–5157 (2011).

274. P. A. Beckmann, A review of polytypism in lead iodide. *Cryst. Res. Technol.* **45,** 455–460 (2010).

275. M. Han *et al.*, Two-step vapor deposition of self-catalyzed large-size PbI2 nanobelts for high-performance photodetectors. *J. Mater. Chem. C.* **21,** 5746–5753 (2018).

276. C. Lan *et al.*, Large-Scale Synthesis of Freestanding Layer-Structured PbI 2 and MAPbI 3 Nanosheets for High-Performance Photodetection. *Adv. Mat.* **29,** 1-9 (2017).

277. M. Tan *et al.*, 2D Lead Dihalides for High-Performance Ultraviolet Photodetectors and their Detection Mechanism Investigation. *Small* **13,** 1–8 (2017).

278. W. Zheng *et al.*, High-Crystalline 2D Layered PbI2with Ultrasmooth Surface: Liquid-Phase Synthesis and Application of High-Speed Photon Detection. *Adv. Electron. Mater.* **2,** 1–8 (2016).

279. O. Rybak *et al.*, Luminescent spectra of PbI single crystals doped by 3d-metal impurities. *J. Lumin.* **79,** 257–267 (1998).

280. Y. Chang, R. B. James, Phonon dispersion and polar-optical scattering in 2H PbI_2 *Phys.*

Rev. B. **55,** 8219-8225 (1997).

281. L. Cabana *et al.*, Synthesis of PbI2 single-layered inorganic nanotubes encapsulated within carbon nanotubes. *Adv. Mater.* **26,** 2016–2021 (2014).

282. Q. Fan *et al.*, Liquid Exfoliation of Two-Dimensional PbI2 Nanosheets for Ultrafast Photonics. *ACS Photonics* **6,** 1051–1057 (2019).

283. V. Nicolosi *et al.*, Liquid exfoliation of layered materials. *Science* **340,** 6139 (2013).

284. H. Tao *et al.*, Scalable exfoliation and dispersion of two-dimensional materials-an update. *Phys. Chem. Chem. Phys.* **19,** 921–960 (2017).

285. C. Huo, Z. Yan, X. Song, H. Zeng, 2D materials via liquid exfoliation : a review on fabrication and applications 2D materials via liquid exfoliation : a review on fabrication and applications. *Sci. Bull.* **60,** 1994-2008 (2015).

286. P. May, U. Khan, J. M. Hughes, J. N. Coleman, Role of solubility parameters in understanding the steric stabilization of exfoliated two-dimensional nanosheets by adsorbed polymers. *J. Phys. Chem. C* **116,** 11393–11400 (2012).

287. J. Shen *et al.*, Liquid Phase Exfoliation of Two-Dimensional Materials by Directly Probing and Matching Surface Tension Components. *Nano Lett.* **15,** 5449–5454 (2015).

288. Y. Hernandez, M. Lotya, D. Rickard, S. D. Bergin, J. N. Coleman, Measurement of Multicomponent Solubility Parameters for Graphene Facilitates Solvent Discovery. *Langmuir* **3,** 3208–3213 (2010).

289. K. Manna, H. N. Huang, W. T. Li, Y. H. Ho, W. H. Chiang, Toward Understanding the Efficient Exfoliation of Layered Materials by Water-Assisted Cosolvent Liquid-Phase Exfoliation. *Chem. Mater.* **28,** 7586–7593 (2016).

290. M. Wang *et al.*, Surface Tension Components Ratio: An Efficient Parameter for Direct Liquid Phase Exfoliation. *ACS Appl. Mater. Interfaces* **9,** 9168–9175 (2017).

291. H. Li *et al.*, Atomic Structure and Dynamics of Single Platinum Atom Interactions with Monolayer MoS_2. *ACS Nano* **11,** 3392-3403 (2017).

292. S. Wang *et al.*, Epitaxial Templating of Two-Dimensional Metal Chloride Nanocrystals on Monolayer Molybdenum Disulfide. *ACS Nano* **11,** 6404−6415 (2017).

293. S. Zhou *et al.*, Atomic Structure and Dynamics of Defects in 2D MoS_2 Bilayers. *ACS Omega* **2,** 3315−3324 (2017).

294. M. A. Brogan, A. J. Blake, C. Wilson, D. H. Gregory, Magnesium diiodide, MgI2. *Acta Crystallogr. Sect. C Cryst. Struct. Commun.* **59,** (2003).

295. P. Patnaik, D. Ph, *Handbook of Inorganic Chemicals*. *McGraw-Hill*.

296. H. L. Clever, F. J. Johnston, The solubility of some sparingly soluble lead salts : An evaluation of the solubility in water and aqueous electrolyte solution. *J. Phys. Chem. Ref. Data* **9,** 751 (1980).

297. R. Frisenda *et al.*, Characterization of highly crystalline lead iodide nanosheets prepared by room-temperature solution processing. *Nanotechnology* **28,** 455703 (2017).

298. K. Zhou, N. Mao, H. Wang, Y. Peng, H. Zhang, A Mixed-Solvent Strategy for Efficient Exfoliation of Inorganic Graphene Analogues. *Angew. Chem. Int. Ed.* ***50,*** 10839–10842

(2011).

299. G. Cunningham *et al.*, Solvent Exfoliation of Transition Metal Dichalcogenides : Dispersibility of Exfoliated Nanosheets Varies Only Weakly between Compounds. *ACS* Nanao **6,** 3468–3480 (2012).

300. J. C. Hamill, Y. Loo, In fluence of Solvent Coordination on Hybrid Organic − Inorganic Perovskite Formation. (2018).

301. F. Cataldo, A revision of the gutmann donor numbers of a series of phosphoramides including tepa. *Eur. Chem. Bull.* **4,** 92–97 (2015).

302. C. M. Huggins, G. C. Pimentel, J. N. Shoolery, Proton Magnetic Resonance Studies of Chloroform in Solution: Evidence for Hydrogen Bonding. *J. Chem. Phys.* **23,** 1244-1247 (1955).

303. A. L. McCleallan, S. W. Nicksic, J. C. Guffy, NMR Study of Hydrogen Bonding between Chloroform and Dimethyl. *J. Mol. Spectr.* **348,** 340–348 (1963).

304. S. Wang, A. Robertson, J. H. Warner, A. Robertson, Chem Soc Rev Atomic structure of defects and dopants in 2D layered transition metal dichalcogenides. *Chem. Soc. Rev.* **47,** 6764–6794 (2018).

305. C. Bacaksiz, H. Sahin, Single layer PbI_2: Hydrogenation-driven reconstructions. *RSC Adv.* **6,** 89708–89714 (2016).

306. W. Zhao *et al.*, Metastable MoS_2: Crystal Structure, Electronic Band Structure, Synthetic Approach and Intriguing Physical Properties. *Chem. Eur.J.* **24,** 15942–15954 (2018).

307. M. Ezawa, Peculiar width dependence of the electronic properties of carbon nanoribbons. *Phys. Rev. B.* ***2005***, 1–8 (2006).

308. T. Kawai, Graphitic ribbons without hydrogen-termination : Electronic structures and stabilities. *Phys. Rev. B.* **62,** 349–352 (2000).

309. Y. Li, Z. Zhou, S. Zhang, Z. Chen, MoS 2 Nanoribbons : High Stability and Unusual Electronic and Magnetic Properties. . *J. Am. Chem. Soc.* **130**, 16739–16744 (2008).

310. S. Z. Butler *et al.*, Progress, Challenges, and Opportunities in Two-Dimensional Materials Beyond Graphene. *ACS Nano* **7,** 2898–2926 (2013).

311. S. Wang *et al.*, Atomically Sharp Crack Tips in Monolayer. *ACS Nano* **10**, 9831-939 (2016).

312. S. Wang, H. Sawada, C. S. Allen, A. I. Kirkland, J. H. Warner, Orientation dependent interlayer stacking structure in bilayer MoS_2 domains. *Nanoscale* **9,** 13060–13068 (2017).

313. X. Sang *et al.*, In Situ Edge Engineering in Two-Dimensional Transition Metal Dichalcogenides. *Nat. Commun.* **9,** 2051 (2018).

314. S. Zhou *et al.*, Atomically Sharp Interlayer Stacking Shifts at Anti-Phase Grain Boundaries in Overlapping MoS_2 Secondary Layers. *Nanoscale* **10**, 16692–16702 (2018).

315. Q. Chen *et al.*, Ultralong 1D Vacancy Channels for Rapid Atomic Migration during 2D

Void Formation in Monolayer MoS 2. *ACS Nano* **12,** 7721–7730 (2018).

316. C. J. Russo, J. A. Golovchenko, Atom-by-atom nucleation and growth of graphene nanopores. *PNAS* **109,** 5953–5957 (2012).

317. L. H. Zeng *et al.*, Controlled Synthesis of 2D Palladium Diselenide for Sensitive Photodetector Applications. *Adv. Funct. Mater.* **29,** 1–9 (2019).

318. A. D. Oyedele *et al.*, $PdSe_2$: Pentagonal Two-Dimensional Layers with High Air Stability for Electronics. *J. Am. Chem. Soc.* **139,** 14090–14097 (2017).

319. E. Selb, M. Tribus, G. Heymann, Verbeekite, the Long-Unknown Crystal Structure of Monoclinic $PdSe_2$. *Inorg. Chem.* **56,** 5885–5891 (2017).

320. W. Lei *et al.*, A new 2D high-pressure phase of $PdSe_2$ with high-mobility transport anisotropy for photovoltaic applications. *J. Mater. Chem. C* **7,** 2096–2105 (2019).

321. M. A. ElGhazali *et al.*, Pressure-induced superconductivity up to 13.1 K in the pyrite phase of palladium diselenide $PdSe_2$. *Phys. Rev. B* **96,** 060509 (2017).

322. A. D. Oyedele *et al.*, Defect-Mediated Phase Transformation in Anisotropic Two-Dimensional PdSe2 Crystals for Seamless Electrical Contacts. *J. Am. Chem. Soc.* **141,** 8928–8936 (2019).

323. J. Lin *et al.*, Novel Pd 2 Se 3 Two-Dimensional Phase Driven by Interlayer Fusion in Layered $PdSe_2$. *Phys. Rev. Lett.* **016101,** 1–6 (2017).

324. S. Zuluaga, J. Lin, K. Suenaga, S. T. Pantelides, Two-dimensional $PdSe_2$-Pd_2Se_3 junctions can serve as nanowires. *2D Mater.* **5,** 035025 (2018).

325. O. Torbjorn, R. Erling, G. Fredrik, Phase Relationships of Palladium Selenides. *Acta Chem. Scand. A* **33,** 251–256 (1979).

326. T. Takabatake, M. Ishikawa, J. L. Jorda, Superconductivity and phase relations in the Pd-Se system. *J. Less Common Met.* **134,** 79–89 (1987).

327. H. Okamoto, The pd-se (palladium-selenium) system. *J. Phase Equilibria* **13,** 69–72 (1992).

328. D. Voiry, A. Mohite, M. Chhowalla, Phase engineering of transition metal dichalcogenides. *Chem. Soc. Rev.* **44,** 2702–2712 (2015).

329. W. Lei *et al.*, Ferroelastic lattice rotation and band-gap engineering in quasi 2D layered-structure PdSe2 under uniaxial stress. *Nanoscale* **11,** 12317–12325 (2019).

330. S. E. Offerman *et al.*, Grain Nucleation and Growth During Phase Transformations. *Science* **298,** 1003–1005 (2002).

331. M. I. McMahon, R. J. Nelmes, High-pressure structures and phase transformations in elemental metals. *Chem. Soc. Rev.* **35,** 943–963 (2006).

332. P. Joensen, R. F. Frindt, S. R. Morrison, Single-layer MoS_2. *Mater. Res. Bull.* **21,** 457–461 (1986).

333. B. K. Miremadi, S. R. Morrison, The intercalation and exfoliation of tungsten disulfide. *J. Appl. Phys.* **63,** 4970–4974 (1988).

334. R. A. Gordon, D. Yang, E. D. Crozier, D. T. Jiang, R. F. Frindt, Structures of exfoliated

single layers of WS_2, MoS_2 and $MoSe_2$ in aqueous suspension. *Phys. Rev. B* **65,** 125407 (2002).

335. P. Johari, V. B. Shenoy, Tuning the Electronic Properties of Semiconducting Transition Metal Dichalcogenides by Applying Mechanical Strains. *ACS Nano* **6,** 5449–5456 (2012).

336. S. Cho *et al.*, Phase patterning for ohmic homojunction contact in $MoTe_2$. *Science* **349,** 625 LP – 628 (2015).

337. N. Papadopoulos, J. O. Island, H. S. J. Van Der Zant, G. A. Steele, Investigating Laser-Induced Phase Engineering in MoS_2 Transistors. *IEEE Trans. Electron Devices* **65,** 4053–4058 (2018).

338. F. Bian *et al.*, Ultrasmall Silver Nanopores Fabricated by Femtosecond Laser Pulses. *Nano Lett.* **11,** 3251–3257 (2011).

339. L. Hu, X. Shan, Y. Wu, J. Zhao, X. Lu, Laser Thinning and Patterning of MoS_2 with Layer-by-Layer Precision. *Sci. Rep.* **7,** 15538 (2017).

340. M. Currie *et al.*, Quantifying pulsed laser induced damage to graphene. *Appl. Phys. Lett.* **99,** 211909 (2011).

341. R. Sahin, E. Simsek, S. Akturk, Nanoscale patterning of graphene through femtosecond laser ablation. *Appl. Phys. Lett.* **104,** 053118 (2014).

342. Y. Zhou *et al.*, Microstructuring of Graphene Oxide Nanosheets Using Direct Laser Writing. *Adv. Mater.* **22,** 67–71 (2010).

343. V. Strong *et al.*, Patterning and Electronic Tuning of Laser Scribed Graphene for Flexible All-Carbon Devices. *ACS Nano* **6,** 1395–1403 (2012).

344. R. Sevak Singh, V. Nalla, W. Chen, A. Thye Shen Wee, W. Ji, Laser Patterning of Epitaxial Graphene for Schottky Junction Photodetectors. *ACS Nano* **5,** 5969–5975 (2011).

345. A. Castellanos-Gomez *et al.*, Laser-Thinning of MoS_2: On Demand Generation of a Single-Layer Semiconductor. *Nano Lett.* **12,** 3187–3192 (2012).

346. S. Ghosh *et al.*, Extremely high thermal conductivity of graphene: Prospects for thermal management applications in nanoelectronic circuits. *Appl. Phys. Lett.* **92,** 151911 (2008).

347. D. L. Nika, A. A. Balandin, Two-dimensional phonon transport in graphene. *J. Phys. Condens. Matter* **24,** 233203 (2012).

348. A. A. Balandin, Thermal properties of graphene and nanostructured carbon materials. *Nat. Mater.* **10,** 569–581 (2011).

349. J. Renteria, D. Nika, A. Balandin, Graphene Thermal Properties: Applications in Thermal Management and Energy Storage. *Appl. Sci.* **4,** 525–547 (2014).

350. X. Ling, H. Wang, S. Huang, F. Xia, M. S. Dresselhaus, The renaissance of black phosphorus. *Proc. Natl. Acad. Sci.* **112,** 4523–4530 (2015).

351. G. H. Ryu *et al.*, Striated 2D Lattice with Sub-nm 1D Etch Channels by Controlled Thermally Induced Phase Transformations of $PdSe_2$. **1904251,** 1–7 (2019).

352. J. Sun, H. Shi, T. Siegrist, D. J. Singh, Electronic, transport, and optical properties of bulk and mono-layer $PdSe_2$. *Appl. Phys. Lett.* **107,** 153902 (2015).

353. E. Mostaani, N. D. Drummond, V. I. Fal'ko, Quantum Monte Carlo Calculation of the Binding Energy of Bilayer Graphene. *Phys. Rev. Lett.* **115,** 115501 (2015).

354. Y. Wang, Y. Li, Z. Chen, Not your familiar two dimensional transition metal disulfide: structural and electronic properties of the PdS_2 monolayer. *J. Mater. Chem. C* **3,** 9603–9608 (2015).

355. G. H. Ryu *et al.*, Atomic Structure and Dynamics of Self-Limiting Sub-Nanometer Pores in Monolayer WS_2. *ACS Nano* **12,** 11638–11647 (2018).

356. S. Wang *et al.*, Atomic structure and formation mechanism of sub-nanometer pores in 2D monolayer MoS_2. *Nanoscale* **9,** 6417–6426 (2017).

357. Q. Fu *et al.*, One-Step Synthesis of Metal/Semiconductor Heterostructure NbS_2/MoS_2. *Chem. Mater.* **30,** 4001–4007 (2018).

358. B. Zheng *et al.*, Band Alignment Engineering in Two-Dimensional Lateral Heterostructures. *J. Am. Chem. Soc.* **140,** 11193–11197 (2018).

359. V. Shautsova *et al.*, Direct Laser Patterning and Phase Transformation of 2D $PdSe_2$ Films for On-Demand Device Fabrication. *ACS Nano* **13,** 14162–14171

360. M. Yamada, T. Akasaka, S. Nagase, Endohedral Metal Atoms in Pristine and Functionalized Fullerene Cages. *Acc. Chem. Res* **43,** 92–102 (2010).

361. H. Shinohara *et al.*, Physical Chemistry Spectroscopic Properties of Isolated $Sc_3@C_{82}$ Metallofullerene. *J. Phys. Chem* **98,** 8597–8599 (1994).

362. H. Shinohara *et al.*, Isolation and Spectroscopic Properties of $Sc_2@C_{74}$, SCZ@ C_{82}, and $Sc_2@C_{84}$. *J. Phys. Chem* **97,** 4259–4261 (1993).

363. B.-B. Liu *et al.*, High yield synthesis and extraction of $La@C_{2n}$. *Pergamon Solid State Commun.* **97,** 407–410 (1996).

364. S. Bandow, H. Shinoharat, Y. Saito, M. Ohkohchi, Y. Ando, High Yield Synthesis of Lanthanofullerenes via Lanthanum Carbide. *Phys. Chem. J.* **97,** 6101–6103 (1993).

365. S. W. M. Mark M. ROSS, H. H. Nelson, John H. Callahan, Production and Characterization of Metallofullerenes. *J. Phys. Chem* **96,** 5231–5234 (1992).

366. A. S. Fedorov, P. V. Novikov, G. N. Churilov, Influence of electron concentration and temperature on endohedral metallofullerene $Me@C_{84}$ formation in a carbon plasma. *Chem. Phys.* **293,** 253–261 (2003).

367. A. L. Balch, M. M. Olmstead, Reactions of Transition Metal Complexes with Fullerenes (C_{60}, C_{70}, etc.) and Related Materials. *Chem. Rev.* **98,** 2123–2166 (1998).

368. L. Mu, S. Yang, R. Feng, X. Kong, Encapsulation of Platinum in Fullerenes: Is That Possible? *Inorg. Chem.* **56,** 6035–6038 (2017).

369. T. Pradeep, G. U. Kulkarni, K. R. Kannan, T. N. G. Row, C. N. R. Rao, A novel iron fullerene (FeC_{60}) adduct in the solid state. *J. Am. Chem. Soc.* **114,** 2272–2273 (1992).

370. E. Nishibori, M. Takata, M. Sakata, M. Inakuma, H. Shinohara, Determination of the cage structure of $Sc@C_{82}$ by synchrotron powder diffraction. *Chem. Phys. Lett.* **298,** 79–

84 (1998).

371. C.H. Kiang; P.H.M. Van Loosdrecht; R. Beyers, Novel Structures from Arc-Vaporized Carbon and Metals: Single-layer Carbon Nanotubes and Metallofullerenes. *Surf. Rev. Lett.* **3,** 765–769 (1996).

372. V. Vekselman, M. Feurer, T. Huang, B. Stratton, Y. Raitses, Complex structure of the carbon arc discharge for synthesis of nanotubes. *Plasma Sources Sci. Technol.* **26,** 065019 (2017).

373. H.-J. Qian, Y. Wang, K. Morokuma, Quantum mechanical simulation reveals the role of cold helium atoms and the coexistence of bottom-up and top-down formation mechanisms of buckminsterfullerene from carbon vapor. *Carbon N. Y.* **114,** 635–641 (2017).

374. Shinohara H., Sato H., Ohkohchi M., Encapsulation of Scandium trimer in C_{82}. *Nature* **357,** 52–54 (1992).

375. R. Johnson, M. de Vries, J. Salem, D. S. Bethune, C. S. Yannoni, Electron paramagnetic resonance studies of lathanum-containing C_{82}. *Nature* **355,** 239–240 (1992).

376. C. S. Yannoni *et al.*, Scandium clusters in fullerene cages. *Science* **256,** 1191–1192 (1992).

377. H. Funasaka, K. Sakurai, Y. Oda, K. Yamamoto, T. Takahashi, Magnetic properties of Gd@C_{82} metallofullerene. *Chem. Phys. Lett.* **232,** 273–277 (1995).

378. M. Takata *et al.*, Confirmation by X-ray diffraction of the endohedral nature of the metallofullerene Y@C_{82}. *Nature* **377,** 46–49 (1995).

379. U. Kirbach, L. Dunsch, The Existence of Stable Tm@C_{82} Isomers. *Angew. Chemie Int. Ed. English* **35,** 2380–2383 (1996).

380. J. Ding, S. Yang, Efficient N,N-Dimethylformamide Extraction of Endohedral Metallofullerenes for HPLC Purification. *Chem. Mater.* **8,** 2824–2827 (1996).

381. J. Ding, S. Yang, Isolation and Characterization of Pr@C82 and Pr2@C80. *Am. Chem. Soc.* **118,** 11254–11257 (1996).

382. T. Kodama *et al.*, Structural Study of Three Isomers of Tm@C_{82} by ^{13}C NMR Spectroscopy. *J. Am. Chem. Soc.* **124,** 1452–1455 (2002).

383. V. P. Bubnov *et al.*, Endohedral Metallofullerenes: A Convenient Gram-Scale Preparation. *Chem. Mater.* **14,** 1004–1008 (2002).

384. B. Sun, L. Feng, Z. Shi, Z. Gu, Improved extraction of metallofullerenes with DMF at high temperature. *Carbon N. Y.* **40,** 1591–1595 (2002).

385. R. D. Bolskar *et al.*, First Soluble M@C60 Derivatives Provide Enhanced Access to Metallofullerenes and Permit in Vivo Evaluation of Gd@C_{60}[$C(COOH)_2$]$_{10}$ as a MRI Contrast Agent. *J. Am. Chem. Soc.* **125,** 5471–5478 (2003).

386. Y. Lian, Z. Shi, X. Zhou, Z. Gu, Different Extraction Behaviors between Divalent and Trivalent Endohedral Metallofullerenes. *Chem. Mater.* **16,** 1704–1714 (2004).

387. T. Kodama *et al.*, Selective Extraction of Endohedral Metallofullerenes Using a Mixed Solvent of Triethylamine and Acetone. *Chem. Lett.* **34,** 464–465 (2005).

388. Y. Iiduka *et al.*, ^{13}C NMR spectroscopic study of scandium dimetallofullerene, $Sc_2@C_{84}$ vs. $Sc_2C_2@C_{82}$. *Chem. Commun.* 2057–2059 (2006).

389. Y. S. Grushko *et al.*, MRI-Contrasting System Based on Water-Soluble Fullerene/Gd-Metallofullerene Mixture. *Fullerenes Nanotub. Carbon Nanostructures* **18,** 417–421 (2010).

390. V. S. Kozlov, M. V. Suyasova, V. T. Lebedev, Synthesis, extraction, and chromatographic purification of higher empty fullerenes and endohedral gadolinium metallofullerenes. *Russ. J. Appl. Chem.* **87,** 121–127 (2014).

391. W. Lu, J.-B. Baek, L. Dai, *Carbon nanomaterials for advanced energy systems : advances in materials synthesis and device applications*. John Wiley and Sons.

392. P. I. Kyesmen, A. Onoja, A. N. Amah, Fullerenes synthesis by combined resistive heating and arc discharge techniques. *Springerplus* **5,** 1–7 (2016).

393. G. Kresse, J. Furthmüller, Efficient iterative schemes for ab initio total-energy calculations using a plane-wave basis set. *Phys. Rev. B - Condens. Matter Mater. Phys.* **54,** 11169–11186 (1996).

394. G. Kresse, J. Furthmüller, Efficiency of ab-initio total energy calculations for metals and semiconductors using a plane-wave basis set. *Comput. Mater. Sci.* **6,** 15–50 (1996).

395. P. E. Blöchl, Projector augmented-wave method. *Phys. Rev. B* **50,** 17953–17979 (1994).

396. *Guinness World Records 2006*. (Guinness Media, 2005).

397. E. L. Romero, L. Echegoyen, Electron spin resonance spectroscopy of empty and endohedral fullerenes. *J. Phys. Org. Chem.* **29,** 781–792 (2016).

398. Y. Jiang, Z. Li, J. Zhang, Z. Wang, Endohedral Metallofullerene M2@C80: A New Class of Magnetic Superhalogen. *J. Phys. Chem. C* **124,** 2131–2136 (2020).

399. R. Isaac, W. Wang, G. Aaron, O. Cengiz, O. Mihrimah, Silicon Oxide Contamination of Graphene Sheets Synthesized on Copper Substrates via Chemical Vapor Deposition. *Adv. Sci. Eng. Med.* **6,** (2014).

400. Kresse, G; and J. Joubert, From ultrasoft pseudopotentials to the projector augmented wave method. *Phys. Rev. B* **59,** 1758 (1999).

401. Perdew, J. P.; Burke, K; Ernzerhof, M. Generalized Gradient Approximation Made Simple. *Phys. Rev. Lett.* **77,** 3865 (1996).

402. Grimme, S; Ehrlich, S.; Goerigk, L. Effect of the Damping Function in Dispersion Corrected Density Functional Theory. *J. Comp. Chem.* **32,** 1456 (2011).

403. Sheppard D.; Henkelman, G. Paths to which the nudged elastic band converges. *J. Comp. Chem.* **32,** 1769-1771 (2011).

404. Sheppard, D.; Terrell, R.; Henkelman, G. Optimization methods for finding minimum energy paths, *J. Chem. Phys.* **128,** 134106 (2008).